Bayesian Methods for Gas-Phase Tomography

by
Samuel Jacobi Grauer

A thesis
presented to the University of Waterloo
in fulfilment of the
thesis requirement for the degree of
Doctor of Philosophy
in
Mechanical and Mechatronics Engineering

Waterloo, Ontario, Canada, 2018

Examining Committee Membership

The following served on the Examining Committee for this thesis. The decision of the Examining Committee is by majority vote.

External Examiner	Ashley F. Emery Professor, University of Washington
Supervisor	Kyle J. Daun Associate Professor, University of Waterloo
Internal Member	Serhiy Yarusevych Associate Professor, University of Waterloo
Internal Member	Steven L. Waslander Associate Professor, University of Waterloo
Internal-external Member	Christopher Batty Assistant Professor, University of Waterloo

Author's Declaration

I hereby declare that I am the sole author of this thesis. This is a true copy of the thesis, including any required final revisions, as accepted by my examiners.

I understand that my thesis may be made electronically available to the public.

Abstract

Gas-phase tomography refers to a set of techniques that determine the 2D or 3D distribution of a target species in a jet, plume, or flame using measurements of light, made around the boundary of a flow area. Reconstructed quantities may include the concentration of one or more species, temperature, pressure, and optical density, among others. Tomography is increasingly used to study fundamental aspects of turbulent combustion and monitor emissions for regulatory compliance. This thesis develops statistical methods to improve gas-phase tomography and reports two novel experimental applications.

Tomography is an inverse problem, meaning that a forward model (calculating measurements of light for a known distribution of gas) is inverted to estimate the model parameters (transforming experimental data into a gas distribution). The measurement modality varies with the problem geometry and objective of the experiment. For instance, transmittance data from an array of laser beams that transect a jet may be inverted to recover 2D fields of concentration and temperature; and multiple high-resolution images of a flame, captured from different angles, are used to reconstruct wrinkling of the 3D reacting zone. Forward models for gas-phase tomography modalities share a common mathematical form, that of a Fredholm integral equation of the first-kind (IFK). The inversion of coupled IFKs is necessarily ill-posed, however, meaning that solutions are either unstable or non-unique. Measurements are thus insufficient in themselves to generate a realistic image of the gas and additional information must be incorporated into the reconstruction procedure.

Statistical inversion is an approach to inverse problems in which the measurements, experimental parameters, and quantities of interest are treated as random variables, characterized by a probability distribution. These distributions reflect uncertainty about the target due to fluctuations in the flow field, noise in the data, errors in the forward model, and the ill-posed nature of reconstruction. The Bayesian framework for tomography features a likelihood probability density function (pdf), which describes the chance of observing a measurement for a given distribution of gas, and prior pdf, which assigns a relative plausibility to candidate distributions based on assumptions about the flow physics. Bayes' equation updates information about the target

in response to measurement data, combining the likelihood and prior functions to form a posterior pdf. The posterior is usually summarized by the maximum a posteriori (MAP) estimate, which is the most likely distribution of gas for a set of data, subject to the effects of noise, model errors, and prior information. The framework can be used to estimate credibility intervals for a reconstruction and the form of Bayes' equation suggests procedures for improving gas tomography.

The accuracy of reconstructions depends on the information content of the data, which is a function of the experimental design, as well as the specificity and validity of the prior. This thesis employs theoretical arguments and experimental measurements of scalar fluctuations to justify joint-normal likelihood and prior pdfs for gas-phase tomography. Three methods are introduced to improve each stage of the inverse problem: to develop priors, design optimal experiments, and select a discretization scheme. First, a self-similarity analysis of turbulent jets—common targets in gas tomography—is used to construct an advanced prior, informed by an estimate of the jet's spatial covariance. Next, a Bayesian objective function is proposed to optimize beam positions in limited-data arrays, which are necessary in scenarios where optical access to the flow area is restricted. Finally, a Bayesian expression for model selection is derived from the joint-normal pdfs and employed to select a mathematical basis to reconstruct a flow. Extensive numerical evidence is presented to validate these methods.

The dissertation continues with two novel experiments, conducted in a Bayesian way. Broadband absorption tomography is a new technique intended for quantitative emissions detection from spectrally-convolved absorption signals. Theoretical foundations for the diagnostic are developed and the results of a proof-of-concept emissions detection experiment are reported. Lastly, background-oriented schlieren (BOS) tomography is applied to combustion for the first time. BOS tomography employs measurements of beam steering to reconstruct a fluid's optical density field, which can be used to infer temperature and density. The application of BOS tomography to flame imaging sets the stage for instantaneous 3D combustion thermometry.

Numerical and experimental results reported in this thesis support a Bayesian approach to gas-phase tomography. Bayesian tomography makes the role of prior information explicit, which can be leveraged to optimize reconstructions and design better imaging systems in support of research on fluid flow and combustion dynamics.

Acknowledgements

To begin, I would like to thank Professor Kyle James Daun, noted "really nice person," wizard of inverse analysis, heat transfer expert, proud Manitoban, and benevolent supervisor. Professor Daun, you sold me on Waterloo during our first meeting with your warmth and enthusiasm. When I arrived in Duisburg, I would tell people "you may have met my supervisor, Kyle from Waterloo" and they would light up in recognition and relay some charming anecdote from your last visit. Ditto for the inverse conferences at Michigan State and VMI. Anyone would be glad to leave such an impression. You got me hooked on Bayesian analysis and *ill-posed inverse problems in math and engineering*,[1] which warrants appreciation. I admire your energy and patience, your literary flair, and your deep understanding of applied research. It has been an honour and a pleasure to study under your guidance and I truly cannot thank you enough.

Four other researchers played an outsized role in my trajectory. In chronological order: I thank Prof. Scott Ormiston, for his mentorship during my undergraduate studies. I thank Prof. Mary Wells, for first inviting me to Waterloo and giving me free rein to tackle a challenging problem. I thank Dr. Paul Hadwin, for entertaining my dumb questions and troubleshooting my code; for tolerating my argumentative streak; and for coaching me through my statistics coursework. And I thank Prof. Dr. Khadijeh Mohri, for bringing me to Duisburg. You believed in our project and made sure we saw it through; your determination is remarkable. I have fond memories of our daily run and hope to continue our collaboration.

My labmates have been wonderful and deserve my gratitude, as well. I will name several of you without elaboration, but know that I could (and would) go on at great length, had I the time and motivation. Again chronologically: Etienne Caron, Noel Chester, Kamal Jhajj, Josh Rasera, Cangji Shi, Nigel Singh, Brad Conrad (h.c.), Roger Tsang, Natalie Field, Tim Thompson, Simon Trivett, Tim Sipkens, Sina Talebi Moghaddam, Mohit Verma, Rodrigo Miguel, Cory Yang, and Kaihsiang Lin.[2] Each of you has taught me a great deal and I wish you all the best. To the

[1] To the uninitiated reader, this development has been mostly positive. More *hooked on phonics* than *hooked on drugs*.
[2] Past members are listed in order of their departure; current members are listed by seniority.

Germans—Andreas[3], Johannes, Torsten, Patrick, et al.—you were first-rate hosts and your refusal to jaywalk was delightful.

Some elaboration is in order, of course. Roger, thanks for putting up with me, thanks for your resilience and for the good conversation; you're a tennis trivia champ and you've always got a spot on my team. Natalie, much of the same—sans tennis trivia. And Josh, Alanis Morissette has nothing on you, man. Keep on rockin' in the free world. To Tim, I owe you a swimming pool of ice cream. You have been the consummate roommate and labmate. You are a brilliant researcher and I wish you every success on your journey to Emeritus. I look forward to visiting you in Vancouver and hosting you whenever you're able to make it out my way. To other friends from Waterloo, who know who they are, the pasta parties were a romp and your companionship will be dearly missed. And Emily, the writing cafés were a godsend. Brilliant suggestion (insert OK hand emoji).

Lastly, to my parents, Hermann and Sheryl Grauer, thank you a thousand times. You taught me what is Good and showed me how to live well. You instilled in me a spirit to work hard and serve others. You fostered my curiosity and encouraged me to persist when I did not think I could. I never wanted for love nor support. In return, I love you from the bottom of my heart and it is my greatest ambition to follow in your footsteps. To my siblings, Elizabeth and Joseph (also Grauer), you guys are alright. Thanks for being there.[4]

[3] Andreas[3] refers to Andreases Unterberger, Rittler, and Kempf (Prof. Dr.-Ing.). Incidentally, this is also my third footnote. Sometimes life just works out.

[4] I thought you would find this funny but as you know I love you both and am proud to be your brother.

To Hermann and Sheryl Grauer,
for everything.

Table of Contents

List of Figures

List of Tables

List of Abbreviations

ART	algebraic reconstruction technique
BOS	background-oriented schlieren
BTEX	benzene, toluene, ethylene, and xylene
CARS	coherent anti-Stokes Raman spectroscopy
CCD	charge-coupled device
CFD	computational fluid dynamics
CST	chemical species tomography
DAS	direct absorption spectroscopy
DFB	distributed feedback
DFG	difference frequency generation
DIAL	differential absorption light detection and ranging
DOAS	differential optical absorption spectroscopy
DOE	design-of-experiment
FDS	Fire Dynamics Simulator
FEM	finite element method
FID	flame ionizing detector
FTIR	Fourier transform infrared
HITRAN	high-resolution transmission molecular absorption
IFK	integral equation of the first kind
IID	independent and identically distributed
IR	infrared
LES	large-eddy simulation
LIF	laser-induced fluorescence
LNG	liquefied natural gas
LOS	line-of-sight
LTE	local thermodynamic equilibrium
MAP	maximum a posteriori estimate
MART	multiplicative algebraic reconstruction technique

MLE	maximum likelihood estimate
pdf	probability density function
PIV	particle image velocimetry
PLIF	planar laser-induced fluorescence
RANS	Reynolds-averaged Navier-Stokes
rms	root-mean-square
RTE	radiative transfer equation
SART	simultaneous algebraic reconstruction technique
SCR	selective catalytic reduction
SIRT	simultaneous iterative reconstruction technique
SSIM	structural similarity
TDL	tunable diode laser
TV	total variation
VLIF	volumetric laser-induced fluorescence
VOC	volatile organic compound
WMS	wavelength modulation spectroscopy

List of Symbols

This work draws on physical models and numerical techniques from a wide array of disciplines (radiative transfer, statistical inference, computer vision, etc.), each with a unique set of notation. Where possible, symbols in this document are kept consistent, both internally and with the source literature. Below is a list of symbols used in the thesis, categorized by the context in which the symbols appear.

Radiative transfer

$\mathbf{u}$	Location vector $\mathbf{u} = (x, y, z)^T$
$\mathbf{v}$	Direction vector $\mathbf{v} = (\delta x, \delta y, \delta z)^T$
A	Cross sectional area
Ω	Solid angle
u	Progress scalar
L	Path length
λ	Wavelength
η	Wavenumber
I_η	Spectral intensity
$I_{\mathrm{b},\eta}$	Blackbody intensity
Q_η	Spectral energy
κ_η	Absorption coefficient
β_η	Extinction coefficient
τ_η	Spectral transmittance
S_η	Radiative source term

Subscripts

abs	Absorption
emit	Emission
in	In-scattering
out	Out-scattering

Radiative transfer state

χ	Volume fraction
p	Pressure
T	Temperature
N	Number density

Spectral lines

E_i	Internal energy
S_{ij}	Line intensity
f	Lineshape
A_{ji}	Einstein A coefficient
B_{ij}, B_{ji}	Einstein B coefficient
τ_{ji}	Transition-specific lifetime

Subscripts

i, j	Energy states
ij	Transition from i to j
L	Lorentzian profile
D	Doppler profile
V	Voigt profile

Analytic reconstruction

f	Unknown distribution (continuous)
b	Projection
F, B	Fourier transform
x, y	Physical coordinates
u, v	Frequency coordinates
s, θ	Sinogram coordinates
ω	Spatial frequency
$\mathscr{R}f$	Radon transform
K	Kernel

Algebraic reconstruction

Ω	Physical domain
$\delta\Omega$	Element
Φ	Basis
ϕ_j	Basis function
α_j	Coefficient for ϕ_j
$\mathbf{r}_i$	Indicator function
x, y	Physical coordinates
ξ, η	Element coordinates
$C_{\delta\Omega}$	Element-wise path length
$S_{\delta\Omega}$	Element-wise normalization constant
N_i	Shape function
n	Number of basis functions
m	Number of optical paths
$\mathbf{A}$	Ray-sum matrix
$\mathbf{a}_i$	Ray-sum row vector
$\mathbf{b}$	Projection data
$\mathbf{x}$	Unknown distribution (discrete)
$\mathbf{e}$	Error
λ	Regularization parameter (Tikhonov)
β	Diffusion parameter (TV)

Subscripts

i	Optical path
j	Basis function
c	Constant shape function
l	Linear shape function
q	Quadratic shape function

Statistical reconstruction

$\pi(\cdot)$	Probability density function
$\pi(\mathbf{x}\|\mathbf{b})$	Posterior pdf
$\pi(\mathbf{b}\|\mathbf{x})$	Likelihood pdf
$\pi_{\text{pr}}(\mathbf{x})$	Prior pdf
$\pi(\mathbf{b})$	Evidence pdf
μ_n	n^{th} moment of $\pi(\cdot)$
$\boldsymbol{\mu}$	Mean distribution
$\boldsymbol{\Gamma}$	Covariance matrix
$\mathbf{L}$	Cholesky factor of $\boldsymbol{\Gamma}^{-1}$
$\mathbf{v}$	Variance vector
$\mathbf{S}$	Standard deviation matrix (diagonal)
σ	Standard deviation
$\mathbf{y}$	Continuous projection (modelled)

Subscripts and Superscripts

exact	Ideal projection/measurement
MAP	MAP estimate
disc	Discretization error
noise	Measurement noise
int	Noise-model error interaction
appx	Approximation error
sq	Square-exponential structure
smp	Sample-based quantity
est	Mean/covariance estimate

Self-similarity analysis

$\mathbf{u}$	Velocity vector $\mathbf{u} = (u, v, w)^T$
$\mathbf{x}$	Position vector $\mathbf{x} = (x, r, \theta)^T$
c	Concentration
t	Time
$\bar{\cdot}$	Mean component
$\cdot'$	Fluctuating component
U	Velocity scale
U'	Velocity fluctuation scale
C	Concentration scale
C'	Concentration fluctuation scale
L	Length scale
ξ	Dimensionless radius
ψ	Streamline function
f	Mean velocity scale
g	Reynolds stress scale
h	Mean concentration scale
m	Rms concentration scale
$\beta_0, \beta_1, \beta_2$	Scale function parameters
u_0	Velocity source
c_0	Concentration source
A_0	Inlet cross sectional area

Design-of-experiments

F_{D1}	Resolution norm DOE function
F_{D2}	Grid weight DOE function
F_{D3}	Collinearity DOE function
F_{B1}	Bayesian DOE function (A-optimal)
F_{B2}	Bayesian DOE function (D-optimal)
$\mathbf{O}$	Ray-sum outer projections

Spectroscopic models

E_i	Internal energy at state i
ε_i	Normalized energy (in wavenumbers)
I	Moment of inertia
I_A, I_B, I_C	Principal moments of inertia
r_{eq}	Rotor length
m	Particle mass
μ	Reduced mass (system)
ω	Angular velocity
$\mathbf{P}$	Angular momentum vector
F_{vib}	Spring force
k_{vib}	Spring constant
x_c	Anharmonicity constant
J	Rotational quantum number
B	Rotational constant
v	Vibrational quantum number
Ψ	Wavefunction
U	Potential field
θ	Characteristic temperature
σ_{sym}	Symmetry factor
Q	Total internal partition sum
γ	Collisional broadening HWHM

Subscripts

eq	Equilibrium length
rot	Rotational system/energy
vib	Vibrational system/energy

Model selection

M_i	Model
B_{ij}	Bayes factor
$\pi(\mathbf{b}\|M_i)$	Model likelihood
L_i	Log-scale model likelihood
V_i	Measurement credence
D_i	Data fit
P_i	Prior fit
C_{sys}	System constant

Broadband absorption CST

P	Power
Tr	Transmittance
τ_η	Spectral transmittance
C_{det}	Detector constant
C_η	Spectral shape function
G	Emissions burden
G^{-1}	Transfer function

Subscripts

abs	Absorption measurement
ref	Reference measurement

Deflection sensing

I	Intensity field
I_x, I_y, I_t	Differential intensity $I_x = \delta I/\delta x$
u, v	Pixel velocity
α	Horn-Schunck regularization parameter
$\boldsymbol{\delta}$	Deflection vector $\boldsymbol{\delta} = (\delta_x, \delta_y, \delta_z)^T$
$\mathbf{p}_u$, $\mathbf{p}_v$	Background plane basis vectors

BOS tomography

$\mathbf{u}$	Position vector $\mathbf{u} = (x, y, z)^T$
$\mathbf{v}$	Local ray direction $\mathbf{v} = (\delta x, \delta y, \delta z)^T$
ds	Differential path length
n	Index of refraction
d	Distance to target
$\mathbf{S}$	Voxel ray-sums
$\mathbf{D}_x$, $\mathbf{D}_y$, $\mathbf{D}_z$	1D finite difference matrices
$\mathbf{V}$	Background basis
$\mathbf{P}$	Projection matrix
$\mathbf{A}$	Deflection operator
$\mathbf{x}$	Unknown refractive index
$\mathbf{b}$	Deflections
$\mathbf{x}^{(k)}$	kth iteration of TV estimate

Camera calibration

$\mathbf{K}$	Intrinsic matrix
$\mathbf{M}$	Extrinsic matrix
$\mathbf{R}$	Rotation matrix
$\mathbf{t}$	Translation vector
$\mathbf{c}$	Camera position
$\mathbf{q}$	Sensor coordinates $\mathbf{q} = (u, v)^T$
$\mathbf{r}$	Ray vector

Soot parameters

f_v	Soot volume fraction
E	Soot absorption fraction
m	Complex index of refraction
n	Index of refraction
k	Extinction coefficient

Physical constants

h	Planck's constant
c	Speed of light
k_B	Boltzmann constant
c_1	First radiation constant
c_2	Second radiation constant

Operators

$\langle \cdot, \cdot \rangle$	Inner product
$E[\cdot]$	Expectation
$\det(\cdot)$	Determinant
$\mathrm{tr}(\cdot)$	Trace
$\mathrm{chol}(\cdot)$	Cholesky factor
$\mathrm{rank}(\cdot)$	Matrix rank

Chapter One
Introduction to Gas Sensing by Tomography

Gas-phase tomography is a class of imaging tools which estimate the spatial distribution of a target species using optical instruments placed around the periphery of a flow area. Quantities of interest may include the volume fraction, temperature, pressure, mass density, refractive index, or bulk velocity of a gas, depending on the measurement modality. All forms of gas tomography are based on a model of radiative transport through a participating medium. Measurement models for the techniques discussed in this dissertation simplify to a common integral equation, which enables a unified approach to imaging. The aim of this work is to advance the Bayesian framework for this class of problems by way of theoretical developments and practical demonstrations.

Gas sensing technologies feature widely in science and engineering. Details about the motivation for spatially-resolved gas diagnostics are discussed below, followed by an overview of alternative techniques. The story of tomography is told through a historical survey of its medical and mathematical foundations along with a comprehensive review of the literature on gas-phase applications. The introduction closes with a summary of the structure and purpose of subsequent chapters.

1.1 Motivation for Gas-Phase Tomography

1.1.1 Researching turbulence

First, and most basically, gas tomography is used to aid the fundamental study of turbulence. Turbulent phenomena are ubiquitous in natural fluid flow and engineering environments; turbulent flows are marked by tumultuous motion—rotational, diffusive, and dissipative [1]—with random, coherent structures that span many scales of length and time. Research on turbulence has prompted

famous unsolved questions that lie at the heart of mathematics and elegant engineering simulations that predict fluid motion with a high degree of accuracy. Most models of turbulent behaviour follow from the Navier-Stokes equations, which describe the changing state of an idealized continuum fluid subject to viscous forces. Mass, momentum, and scalar conservation are enforced by a set of coupled partial differential equations, where the motion, scalars, and turbulent stresses within a fluid are unknown, resulting in an underdetermined system.

Numerous closures to the Navier-Stokes equations have been proposed for specific flow regimes. Closures developed for numerical solutions, such as large-eddy simulations (LESs), average the Navier-Stokes equations in space to facilitate discrete representation of the flow field and reduce the computational cost of simulation. In Reynolds-averaged Navier-Stokes simulation (RANS), the equations are averaged in time to simplify turbulent stresses.[5] Averaged equations in LES and RANS involve subgrid or Reynolds stress terms that must be modelled. Historically, the development of turbulence models has been driven by empirical observation: these models feature constants that need to be specified by experimental data or direct numerical simulation [2]. Moreover, the vorticity fluctuations that constitute turbulence induce 3D variation and, as a result, instantaneous turbulent dynamics are inherently 3D [3]. Statistical approaches to the simulation of turbulence, such as those based on probability density functions (pdfs) [4] and "smart" subgrid stress [5] methods, require time-resolved measurements of flow quantities. Tomographic methods can realize the high spatiotemporal resolution required to devise and specify models of turbulence. Furthermore, multi-modal experiments that include a tomographic component can provide data on several variables, simultaneously, used to generate conditional statistics for a conditional moment closure [6].

1.1.2 Characterizing combustion

Second, and closely related to the first motivation, gas tomography is applied to characterize and control reacting flows: principally those involving combustion. Understanding flame dynamics poses challenges beyond turbulence modelling per se and has major implications for energy consumption patterns. Combustion is the primary source of energy for transportation and a leading source of electricity. Improving the conversion efficiency of combustion through the design of

[5] Direct numerical simulation is an alternative to LES and RANS where the timestep and grid resolution are sufficiently small to fully resolve a continuum model of turbulent flow [365]. However, the substantial computational burden of this approach limits the range of practical applications.

novel devices lowers transportation and electricity costs, thereby improving standards of living [7–9]. Moreover, developments such as pressure gain combustors [10], coal gasifiers [11], and alternative clean fuels [12] reduce targeted products of combustion (i.e., pollutants), which have harmful health and environmental effects. Simulations of turbulent flames are key to the design and operation of commercial combustion devices [13,14], but combustion modelling involves substantial challenges. Difficulties arise from the strong non-linear coupling of kinetic and transport mechanisms, called turbulence-chemistry interactions, due to overlapping timescales [15]. Similar complexities are introduced by the interdependence of reaction mechanisms, scalar transport, and radiative heat transfer, called turbulence-radiation interactions [16].

Industrial engines, boilers, and turbines are designed to promote turbulent combustion to improve mixing and heat transfer. Turbulence-chemistry and turbulence-radiation interactions are key to flame ignition and stabilization; the formation of NO_x and soot; the onset of flash back, engine knock, and cyclic variations in gas turbines; and the overall efficiency of energy conversion. Burner performance depends on these effects. Accurate simulations are therefore required to optimize burner design. Flame simulations are compared to experimental data from representative lab-scale flames in order to ensure validity. These data are obtained from a variety of diagnostics, including gas tomography [17].[6]

1.1.3 Monitoring emissions

Finally, gas tomography is a key tool for remote sensing of hazardous or environmentally-harmful emissions. The need for remote sensing is driven by the increased production of gas-phase pollutants that impact human health and safety, ecological stability, and long-term climate patterns. Examples include the aerosolized SO_2 and NO_2 generated by fossil fuel power stations, which are converted to sulphuric and nitric acids that further decompose into toxic compounds [18]. Sulphuric aerosols cause human respiratory morbidity; and subsequent acidic products damage nearby soil [19]. Power stations must scrub and monitor effluent gas flows to minimize these effects. Anthropogenic sources of hydrocarbon gasses, owing largely to the extraction, processing, and consumption of fossil fuels, contribute positive radiative forcing due to the greenhouse effect—amplified by feedback mechanisms [20]. Atmospheric CO_2 is of primary interest since it

[6] Validation data sets include mean and fluctuating components of velocity, temperature, and species concentrations; power spectra thereof; and quantities that require spatially-resolved measurements such as gradients (to gauge dissipation), length scales, and strain, vorticity, and dilation fields.

is the principal product of combustion and exhibits a long atmospheric lifetime. There is also a significant focus on CH_4 and NO_2 emissions, as their mass-based greenhouse warming potential is 86 and 268 times greater than that of CO_2 over a 20-year period, respectively [21]. National regulatory agencies such as the EPA have issued rules to limit emissions of CH_4, NO_2, volatile organic compounds (VOCs), and other toxic molecules: to promote health and meet global climate commitments [22]. Regulations mandate that polluters monitor their emissions to ensure compliance. Reported emissions inform inventories, themselves used to benchmark climate models. Primary targets of industrial regulation include emissions from factory chimneys, flare stacks, and landfills. These flows are often intermittent, spatially distributed, and physically inaccessible. Optical tools to quantify emissions are thus required to measure the release of hazardous gasses, inform scientific models of plume dispersion, and devise mitigation strategies.

1.2 Gas Flow Measurement Technologies

Numerous diagnostics have been developed to measure the presence and state of a gaseous species: to aid the fundamental study of turbulence, validate combustion simulations, and quantify harmful emissions. What follows is an outline of these tools, with attention to their advantages and drawbacks relative to tomography, and an overview of a central technology: chemical species tomography (CST).

1.2.1 Invasive probes

High-precision measurements of a gas are often made with an invasive device which is physically inserted into the flow field. Such probes are typically responsive to local quantities, though some record bulk measurements, instead.

Most invasive sensors record an electrical gradient due to a pressure difference, heat flux, or mechanical motion to infer a gas parameter. A multiplicity of techniques are available to fluid dynamists and combustion modellers to measure quantities of interest. For instance, velocity data may be obtained by hot wire anemometry, in which convective heat losses from a wire to a surrounding flow are used to calculate the fluid velocity, or with a pitot tube, where the gauge pressure at the inlet of a small pipe is related to velocity along the inflow direction. Measurements of temperature are typically made with a fine-wire thermocouple, electrical resistance device, or thermistor. Thermocouples have two wires, made of different metals, which generate a voltage difference across a reference junction in proportion to the temperature of the thermocouple. By contrast, electrical resistance devices and thermistors measure temperature using a circuit with a

temperature-dependent resistor and constant current source. Gas concentration data may be determined through contact methods—e.g., using a ceramic semiconductor sensor, pellistor, or electrochemical sensor—or by processing a sample of the fluid with a flame ionization detector or photoionization detector.

Physical methods to probe a gas suffer from a common set of drawbacks, reflecting the fact that the presence of a probe in the flow field perturbs the quantity of interest [23]. Under some circumstances, the probe has a predictable effect on measurements that is counteracted with a correction factor. For instance, pitot tubes displace a portion of the flow, thereby changing its velocity at the tube inlet. A correction term is derived from analysis of the streamline gradients about the entry nozzle [24]. Similarly, thermocouples measure their own temperature—not that of the surrounding fluid—and heat transfer at the interface must be modelled to obtain a fluid temperature. Other forms of interference are more severe. Wires for thermometry and ceramic semiconductors introduce thermal and catalytic disturbances in a flame, altering the local balance of turbulent transport, chemical kinetics, and radiative transfer. These effects may quench the flame around a sensor, substantially altering temperature and concentration measurements. Moreover, flames are frequently stabilized by recirculation currents; probes can interrupt this motion and cause a global instability. Further forms of physical interference include the accumulation of particulate matter on a sensor—such as soot, which builds up a thermal resistance—and devices can be degraded or destroyed by a harsh environments: high temperature, highly corrosive, large loads, and so on.

More fundamentally in the context of 2D and 3D measurement, invasive probe data are inherently local, or else relay aggregate quantities (e.g., bulk velocity in pipe flow). Key distributions must be found by interpolation between multiple measurements, which exacerbates the perturbation effects and often prevents instantaneous measurement, altogether. Statistical techniques such as kriging have been used to interpolate point data but these procedures are subject to considerable spatial uncertainty [25,26]. Non-invasive methods are thus employed to obtain comprehensive spatial information about gas parameters without disturbing the flow field or damaging the measurement apparatus.

1.2.2 Line-of-sight absorption spectroscopy

Advances in laser technology and spectral light sensing have enabled a suite of optical diagnostics for gas and combustion processes—many quantitative and most non-invasive. These tools offer

high-sensitivity to the target species; fast response times, appropriate for real-time control; and non-invasive in situ measurement capabilities. Spectroscopy operates on the principles of light-matter interaction, based on quantum interactions and governed in aggregate by the radiative transfer equation (RTE). Light travelling through a gas is absorbed, emitted, and scattered as a function of its wavelength and the state of the medium. Optical line-of-sight (LOS) measurements are combined with a model of the target species to infer parameters of interest.

Photonic absorption and emission by a gas molecule are related to its chemical structure and internal energy. Transitions between rotational, vibrational, and electronic states give rise to spectral lines. Light is measured in the UV/visible, mid-infrared (IR), or near-IR range, depending on the target.[7] In LOS absorption spectroscopy, emission and in-scattering are negligible and the RTE simplifies into the Beer-Lambert law, which describes the attenuation of monochromatic light by an absorbing medium in terms of a local spectral absorption coefficient (itself a function of the molecular composition and thermodynamic state). Illumination from a background source or ambient light is recorded by a photon detector and measurements comprise a reference signal, made without the absorbing species, and attenuated signal. The path-integrated absorption coefficient between the source and detector is calculated from the ratio of the reference intensity to the attenuated intensity. Key parameters of a gas process are inferred from the mean coefficient. Moreover, additional components of the RTE may be included as required, as emission and scattering become salient.

Measurements for LOS gas sensing are either spectrally resolved, monochromatic, or broadband in nature. Costs typically scale with increasing spectral resolution (and spatial resolution in the case of imaging devices) and the optimal modality depends on the application. For instance, single-species measurements of concentration in an isothermal, isobaric environment can be made with a broadband source and detector, e.g., a thermal lamp and photon detector. Most such arrangements are enclosed, as in Ref. [27], but open path broadband systems have also been demonstrated, e.g., Ref. [28]. A majority of open path devices are spectrally-resolved in order to minimize the effects of interference by an unknown absorber. These systems are either *active*, with illumination provided by the experimental apparatus, or *passive*, using ambient light (e.g., solar radiation). Differential optical absorption spectroscopy (DOAS) is an example of Beer-Lambert-

[7] See Chapter 5 for a detailed discussion of absorption transitions and the calculation of spectral lineshapes.

type detection that features spectral measurements made with an array of solid state photon detectors or a Fourier transform IR (FTIR) spectrometer [29]. Differential absorption light detection and ranging (DIAL) is another high-precision form of LOS spectroscopy, based on backscattered laser light [30]. In DIAL, a laser and detector are collocated and pointed towards the atmosphere. The laser is pulsed and some of its light collides with target molecules; a portion of scattered light returns to the source. Scattering can alter the wavelength of light, depending on the nature of the collision (elastic or inelastic); and the wavelength and travel time are used to gauge the state of a target and the distance to a gas feature, respectively. DOAS and DIAL systems have been used to measure NH_3, NO_2, SO_2, and VOCs in the C_2 to C_{22} range, including alkanes, alkenes, aromatics, benzene, and toluene [31–37].

High-temperature scenarios—e.g., products in a shock tube, coal gasifier, or ram jet—require coefficient data for at least two wavelengths to disambiguate the effects of temperature and concentration. Two-line thermometry uses the ratio of line strengths from two transitions to obtain a gas temperature. Given the temperature, either line may be used to calculate the species concentration. Today, this method is conducted with multiplexed lasers or a tunable diode laser (TLD) [38]. TDLs generate monochromatic light at a wavelength that scans a spectral range in response to an *injection current*. Direct absorption spectroscopy (DAS) features a simple injection current (with a ramp or sinusoidal function); and wavelength modulation spectroscopy (WMS) consists in modulating the injection current and taking the ratio of the measurement signal's first and second harmonics, obtained with a lock-in device [39]. WMS harmonics are sensitive to the curvature of absorption features rather than absolute absorption, as in DAS. The modulation technique is robust to beam distortion, window fouling, and thermal noise, all typical of harsh high-temperature, high-pressure environments [40]. Fluctuations in the gas state may be combined with knowledge about the measurement environment to infer velocity and mass flux data. Recent experiments include the measurement of density, velocity and mass flux of air in a gas turbine [41], temperature and concentration of H_2O from engine exhaust [42], mass flux of O_2 in a wind tunnel [43], and in situ concentration and temperature of H_2O in an optical engine [44,45].

Line-of-sight spectroscopy can generate accurate data about jets, plumes, and flames, including the line-averaged composition, pressure, temperature, velocity, or mass flux of a process. The technique has been deployed for remote sensing over very long distances as well as the in situ characterization of combustors. However, the single-LOS approach to spectroscopy is limited by

strong assumptions about the distribution of gas along the measurement path. The absorption coefficient is presumed to be uniform throughout the target, either throughout the path or within a finite slab (as in DIAL, for instance). When the distribution is non-uniform and the temperature is constant, estimates of volume fraction correspond to a path-integrated mean along a LOS. But in the case of a non-uniform gas in a variable-temperature environment—common to reacting flows—the line-averaged absorption coefficient resists easy interpretation because of the non-linear effects of temperature and pressure on absorption spectra. Spatial resolution is required to extract local estimates with a clear physical meaning.[8]

1.2.3 Laser-induced fluorescence

Fluorescence is the emission of light by a molecule that has been excited by radiation. Laser light energizes an orbital electron, which jumps to an elevated state without changing its spin. There are several mechanisms by which the electron may return to its ground state, including vibrational relaxation, electronic transfer to a colliding molecule, and spontaneous photonic emission (i.e., fluorescence).[9] Laser-induced fluorescence (LIF) is a mature gas and combustion diagnostic in which a short laser pulse excites a target species and cameras record the resulting fluorescence. Several arrangements of LIF have been demonstrated, which feature point, planar (PLIF), and, recently, volumetric (VLIF) measurement [46–48]. In PLIF, a system of lenses forms light from the laser into a sheet to simultaneously stimulate molecules in a plane that transects the gas/flame. Fluorescence from this plane is captured by a camera facing the laser sheet. The resulting image is a near-instantaneous cross section of the excited species. VLIF entails mechanized optics that sweep the laser sheet through a volume of the domain while the camera records successive planes. Alternatively, VLIF can be achieved by using lenses to form the laser light into a volume; multiple cameras image emission this volumetric emission from different perspectives and a computed tomography algorithm is employed to resolve the 3D source distribution.

Laser-induced fluorescence has been employed to study intermediate radicals in hydrocarbon combustion such as OH^*, CH^*, and HCO^*, which provide a measure of turbulent chemistry at the flame front [49]. CN [50] and NO [51] intermediates reveal the progression of nitrogen reactions; and further PLIF studies have focused on CH_2O^* [52], H_2^* [53], and O_2^* [54]. Recent advances in

[8] Under idealized (exceedingly rare) conditions—i.e., a gas of uniform composition that varies only in temperature—rich, spectrally-resolved LOS data for a single path can be used to recover the distribution of temperature along the path [366]. This is made possible by the directional-dependence of self-absorption effects.

[9] Additional mechanisms involved in the relaxation of excited electrons are described in Schulz and Sick [367].

LIF include the use of a wavelength modulated laser pulse [55]. PLIF and VLIF require considerable optical access since the combustion must be open to the laser sheet and cameras. While this approach is feasible for laboratory flames and special optical engines, many combustors cannot be modified to accommodate spatially-resolved LIF. Moreover, the introduction of a tracer can influence combustion through the formation or vapourization of droplets and LIF poses considerable costs and safety hazards relative to non-laser based alternatives.

1.2.4 Raman-Rayleigh scattering and CARS

Scattering phenomena are also exploited for quantitative gas sensing. During collisions between a photon and molecule, an orbital electron may "assume" an intermediate quantum state known as a virtual state. Electrons transition through virtual states, returning to a ground state; the molecule effectively absorbs and instantaneously emits a photon, which is said to have been "scattered." Most electrons return to their original state such that incident and scattered photons have the same energy—this exchange amounts to an elastic collision called *Rayleigh scattering*. Some electrons relax to an elevated energy level, scattering a photon with less energy than the incident photon, which yields a *Stokes line*. Other electrons relax to a less energetic state, scattering a more energetic photon that yields an *anti-Stokes* line. Collisions that result in Stokes and anti-Stokes lines entail net energy transfer between the molecule and photon and are said to be inelastic. Inelastic scattering of this type is called *Raman scattering.* The relative intensity of light due to Rayleigh scattering and Stokes and anti-Stokes lines depends on the energy of incident light and the state and molecular structure of gas molecules at the measurement point. The abundance of target molecules is thus inferred from the spectral signature of scattered light.

Electrons preferentially absorb light aligned with an electronic transition, jumping to an elevated state rather than interacting with a virtual state to scatter a photon. Absorption is followed by vibrational relaxation and fluorescence, which is more efficient than scattering, thereby corrupting the Rayleigh signal. However, scattering may occur whether or not incident light is aligned with a valid transition. Interference by fluorescence is commonly overcome by tuning the laser to avoid valid transitions. At the same time, the efficiency of scattering through a virtual state is proportional to λ^{-4}, where λ is the wavelength of incident light. Increasing power to the TDL therefore reduces the probability of Rayleigh and Raman scattering. Some experiments use a multi-pass approach to resolve this issue [56], with many optical paths intersecting the measurement point, or temporal gating to avoid measurement of the relatively fast fluorescence signal [57].

The molecular number density and temperature of a target can be computed from a Rayleigh line, alone [58]. However, the spectral characteristics of Raman scattering are highly-sensitive to the mixture composition, temperature, and pressure at the measurement location. Combined Raman-Rayleigh diagnostics are employed to obtain robust concentration data for multiple species as well as temperature and pressure [59]. More recently, the Raman-Rayleigh technique has been combined with PLIF, called *Raman-Rayleigh-LIF*. Raman-Rayleigh measurement yields absolute data at a reference point, which anchors the scale of PLIF images. The result is simultaneous, quantitative, 2D images of temperature and key radical number densities [60].

Coherent anti-Stokes Raman spectroscopy (CARS) is a related diagnostic that uses the same transition mechanisms as basic Raman-Rayleigh devices. In CARS, *pump* and *stokes* lasers are multiplexed; the laser wavelengths are tuned such that their beat frequency is aligned with the energy difference between a ground state and vibrational eigenstate. These states become coupled as a result and molecules in the measurement area exists in a coherent superposition of the ground and elevated states. A third laser—or *probe beam*—excites the coherent system, scattering through a virtual state to produce an anti-Stokes line. These anti-Stokes lines are more energetic than standard Rayleigh lines, which are filtered out in CARS. The resulting signal omits the fluorescence that corrupts Raman-Rayleigh data. CARS is widely used to obtain point-measurements of volume fraction, temperature and pressure in laboratory experiments and has been applied to turbines, industrial combustors, and natural gas engines [61].

Raman-Rayleigh scattering and CARS are used to obtain high-precision, non-invasive measurements of number density and temperature in reacting flows. However, these diagnostics feature limited spatial resolution on their own and multi-diagnostic setups are incredibly expensive: with multiple lasers, beam splitters, interferometers, and high-speed cameras required as well as full optical access to the probe volume. Spatially-resolved spectroscopy with a Raman-Rayleigh component is normally restricted to advanced applications in specialized labs.

1.2.5 Schlieren imaging

Schlieren imaging refers to a suite of optical tools that take advantage of the refraction of light through a variable index flow field to visualize density gradients. The speed of light in a medium is given by its refractive index (or “optical density”), which depends on the medium’s local mass density and chemical composition. Fermat’s principle holds that the travel time of a photon between two points is invariant to small changes in the path. From this statement it can be deduced

that smooth variation in the refractive index generates curved photon trajectories. Rays bend away from regions of higher density or towards lower density. As a fluid fluctuates, the phase of light can be seen to shift in response. These "streaks" of visible light are recorded and give the schlieren imaging its name.[10]

Several optical arrangements have been devised to record the schlieren effect for the purpose of flow visualization.[11] The standard approach aligns the flow with the Fourier plane of a Fourier optical correlator. A knife edge is placed at the focus of the second lens, in front of a camera, to mask half of the spatial frequency spectrum, making phase differences visible in the image. Lens-and-grid schlieren apparatuses shine light through a large grid of lenses and then through the flow. The light is received by a secondary system of lenses, with a negative cut-off grid positioned within the latter system to filter half the spatial frequencies. Alternatively, shadowography is based on the direct observation of shadows cast by refraction in a fluid onto a distant background plane. And background-oriented schlieren (BOS) uses time-resolved images of a background plane with a printed pattern, positioned behind the flow, in combination with image processing tools to infer disruption of the image by the fluid.

Early developments in the method were limited to the qualitative assessment of fluid structures made visible by the schlieren effect. In the 1930s, Hubert Schardin proposed a theoretical foundation for schlieren phenomena, used for quantitative analysis [62]. A straightforward approach to quantitative schlieren involves tracking the size and movement of fluid structures with computer vision tools for velocimetry. For instance, Hargather et al. [63] conducted schlieren-based velocimetry of a boundary layer in a supersonic wind tunnel. Rich data about density and temperature can be inferred from the refractive index field. Geometric optics relates gradients in optical density to the magnitude of light deflections and the Gladstone-Dale equation describes the relationship between mass and optical density. Deflections can be determined in several ways: with monochromatic light and reference measurements to relate intensity to the refractive index [64]; by replacing the knife edge with a colour-grid cut-off, such that the magnitude of the phase shift correlates to colour in the image, called rainbow schlieren

[10] The name schlieren derives from *schliere*, the German word for streak, first used to describe deflectometry by August Toepler in the 1860s.

[11] Notably, the first of schlieren technique was reported by Robert Hooke in 1665 [330]. The apparatus used a large lens to focus light from a candle through the flow field (a hot air plume above another candle) and small viewing aperture. Inhomogeneities in the heated plume were visibly apparent through the viewing window.

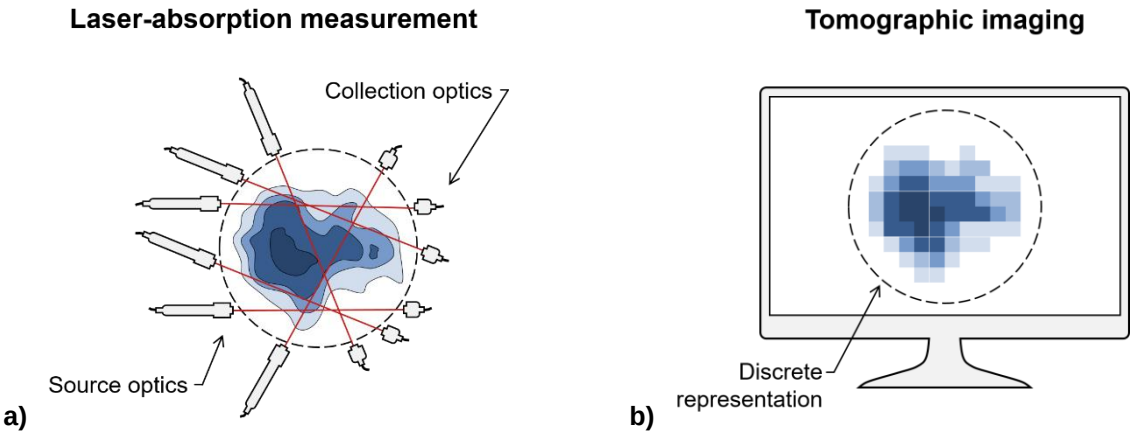

Figure 1.1: Sample schematic for absorption CST: a) measurement of light attenuation by a gas and b) reconstruction using a discrete representation of the target.

[65]; or by directly measuring deflections, as in BOS [66]. These techniques have been applied to study supersonic flow around a 2D wedge plate [67], the density of a microjet [68], and the oscillating wave structure in the wake behind a sphere [69], among other applications.

1.2.6 Chemical species tomography

Gas-phase tomography is an imaging technique that generates 2D or 3D estimates of a gas distribution using multiple LOS measurements, each tracing a unique path through the flow area. Under minimal scattering conditions,[12] measurements of light are governed by a Fredholm IFK. Non-scattering LOS tomography of this kind is called *hard-field tomography*, or *chemical species tomography* in the gas sensing context.[13] Path-integrated measurements in gas tomography share a mathematical form with the X-ray measurements of medical imaging. As a result, the standard approach to computed tomography can be used to reconstruct the spectral absorption coefficient or emission source term. Reconstructed quantities are related in turn to the concentration, temperature, or pressure of a target species. Figure 1.1 shows a sample schematic for 2D CST, with LOS measurements over a ground truth distribution and discrete reconstruction.

Chemical species tomography is flexible with respect to the number of measurements required to image a flow field and compatible with a broad range of existing optical diagnostics. Two-dimensional gas distributions can be computed from as few as 20-40 optical paths, which enables

[12] Such conditions are achieved when the signal is dominated by the absorption of background light (typically light from an active source) or radiative emission from the gas.

[13] CST is a term for hard-field gas-phase tomography that originates with Carey et al. [130]. Alternative terms include agile tomography, line-of-sight-absorption infrared tomography, etc.—each with a somewhat distinct meaning. CST is general, grouping diagnostics by their mathematical properties, and neatly divides into modality- and algorithm-based categories. This document employs “CST” to refer to non-scattering gas tomography based on coupled IFKs.

quantitative imaging of an enclosed process or large-scale emissions flux with minimal instrumentation. Alternatively, a laboratory camera array—where each pixel constitutes a measurement, resulting in a total of ~10^5-10^6 equations—can generate time-resolved 3D reconstructions with sub-millimetre resolution. CST algorithms accommodate non-scattering forms of LOS spectroscopy, flame chemiluminescence, and LIF measurements. Furthermore, there is a direct relationship between CST and gas-phase tomography by schlieren imaging, discussed in Chapter Six. CST devices are categorized in terms of their measurement principle. Systems that measure attenuated light are termed *absorption* CST and those based on images of thermal emission by gas molecules, chemiluminescence, or LIF are called *emission* CST.

Industrial applications and scientific campaigns that make use of CST are more and more common. The technique is adopted because it generates accurate images of internal flow structures, robust to the availability of optical access, at a relatively low cost, due to the advent of inexpensive opto-electronic components. Moreover, the powerful computing resources now available permit real-time monitoring of a gas process by CST. This unique set of advantages renders gas-phase tomography well-suited to the study of turbulent transport and flame dynamics, control of industrial processes, and quantitative measurement of hazardous emissions.

This dissertation reports the application of Bayesian inference, a statistical framework for inverse analysis, to CST. Furthermore, two novel applications of gas-phase tomography are discussed. Readers will learn of the utility of Bayesian algorithms compared to state-of-the-art classical alternatives: for optimizing beam arrays, selecting an appropriate discretization scheme, and generating accurate images of a turbulent flow. Moreover, broadband absorption CST is presented as a novel low-cost approach to emissions measurement. Finally, BOS tomography is applied to combustion imaging for the first time.

1.3 Survey of Gas-Phase Tomography

Modern tomographic imaging spans applications from fundamental combustion research [70] to crack detection in concrete [71], from 3D cell microscopy [72] to the characterization of quantum states [73]. These techniques are diverse in their targets and modes of operation but united in form: all tomography consists in the reconstruction of a function from its projections, where the function represents a physical quantity of interest and projected data is generated by a penetrating wave (i.e., electromagnetic radiation). The first application of tomography was medical imaging, which brought together 2D radiography, advances in mathematical transformations, and computer

technology. The fundamental research was conducted first by mathematicians, who were unaware of the technological implications of their work, and subsequently by medical physicists, in fierce competition to engineer a viable commercial device. Gas-phase tomography is a direct product of this history and shares a mathematical foundation with medical imaging. A brief digression on the discoveries and developments leading up to CST is thus worthwhile. This survey of CST begins with a historical account of tomography, followed by an overview of reconstruction and a comprehensive account of absorption and emission experiments. Finally, the outlook for gas-phase tomography is discussed, with particular attention on the contributions of this dissertation.

1.3.1 Origins of tomography

Simple tomographic systems are based on measurements of the transmission or emission of light along a straight path. Measurements from multiple perspectives are combined to produce an image of the unknown distribution.

Johann Radon proposed a transform of an arbitrary function—in 2D or 3D, based on line integrals of the function—as well as the corresponding inversion in 1917 [74]. Today, these are called the *Radon* and *inverse Radon* transforms. The Radon transform can be interpreted as a mathematical representation of tomographic measurement; the inverse transform is thus applied to reconstruct an unknown function from its projections.[14] Similarities between the Radon transform and X-ray measurements were noticed early on by medical researchers who had spent the past few decades experimenting with radiography. X-rays were first reported by Wilhelm Röntgen in 1895 and the phenomenon was quickly adopted by physicians to assist medical diagnoses. Early attempts to extract 3D information from X-ray images employed multiple images, captured by manually moving an X-ray tube and film cassette around a target—e.g., published in 1915 by Carlo Baese and in 1922 by Andre Bocage—but these experiments failed to resolve internal structures from projection data.

Years later, in 1957 (though not published until 1963), Allan Cormack united of X-ray imaging with the mathematical inversion of Radon. Motivated by the potential radiological applications, Cormack developed a version of the inverse Radon transform that was subject to the physical constraints of X-ray imaging. He then built a device to measure projections,

[14] It is noteworthy that Radon's motivation was entirely mathematical, concerning partial differential equations; potential physical applications were not apparent to him [79]. The first application of the Radon transform on record was an initial value problem, concerning hyperbolic homogeneous equations with constant coefficients [368].

reconstructing an aluminum cylinder in 1957 and pork cutlet with aluminum inserts in 1963. Independent of Cormack, Godfrey Hounsfield devised an approach to reconstruction using a pixelated representation of the X-ray target and a series of linear equations to approximate the coupled path integrals. Hounsfield assembled the first computed tomography scanner in 1967. The inaugural test of this device made 28,000 measurements through a preserved brain—a task that took over nine days to complete! Instead of using a transform-based algorithm like Cormack, Hounsfield opted for an algebraic algorithm, similar in form to the algebraic algorithms used in most contemporary tomography experiments. Reconstruction was carried out on an EMIDEC 1100 transistor computer, lasting 2.5 hours, resulting in an 80×80 pixel image. The reconstruction bore a clear resemblance to the preserved brain tissue, a major achievement in the progression of tomographic imaging.

Subsequent developments in the technology were rapid, driven in large part by the substantial commercial incentives. By the mid-1970s, manufacturing conglomerates like General Electric had begun to produce tomographic X-ray scanners at scale. These scanners were used as non-invasive means to identify lesions, tumors, blood clots, and other ailments. In 1979, the significance of computed tomography was acknowledged with the awarding of a Nobel Prize to Cormack and Hounsfield. The 1980s saw advances in laser diagnostics and imaging technologies; researchers in other fields began to realize the potential for computed tomography as a scientific diagnostic and experimental demonstrations soon followed.

1.3.2 Reconstruction algorithms

Measurements in gas-phase tomography are line-integrated quantities that depend on the unknown distribution of an absorption coefficient or radiative source term. Reconstruction of the unknown function from line-integrated data is an ill-posed inverse problem, meaning the problem is either underdetermined, in which case infinitely many images can fully explain the projections, or sensitive to small changes in the data, such that measurement noise produces large perturbations which distort the image.

This section reviews the techniques devised to address ill-posedness in gas-phase tomography, which divide into analytical and algebraic algorithms. Mathematical details that are relevant to this thesis are presented in Chapter Two.

1.3.2.1 Analytical techniques

Analytical techniques derive from the inverse Radon transform and express the reconstruction as a direct function of the projections. Colloquially, *back projection* is said to "smear" the data back along the measurement line. Projections are combined to form an image of the object in sinogram space, which corresponds to a Radon transform of the unknown distribution. A complete Radon transform requires an infinite set of line-integrals so interpolation is required to supplement the sinogram data. Back projection approximates the hypothetical integral over the full set of projections from the inverse Radon transform with a sum over the actual measurements. The sum features a frequency filter to reduce blurring and noise amplification, which are inherent to the inversion. As a result, the approach is often called *filtered back projection*.

Back projection was independently developed by Bracewell and Riddle in 1967 [75] and Ramachandran and Lakshminarayanan in 1971 [76]. Shepp and Logan later introduced a widely-used low-pass filter (as well as the famous phantom of a head section) [77].[15] The text of Herman [78] is frequently cited in CST papers as the source of the back projection algorithm; and readers of this thesis are directed to the text of Deans [79] for a complete account of analytical algorithms for tomography. Analytical algorithms require a dense measurement array with regular projections, typically using a fan-beam or parallel-beam arrangement. It is challenging to achieve the setup required for analytical back projection in gas-phase tomography; and few such algorithms have been developed for gas imaging with a limited field of view. Therefore, when CST practitioners employ back projection, they normally adopt algorithms from the medical imaging literature.

1.3.2.2 Algebraic techniques

Algebraic algorithms formulate projection as matrix-vector multiplication, starting with discretization of the flow field. The domain is represented using a finite basis—typically square pixels that contain a uniform concentration of gas, by assumption—and a discrete measurement operator is constructed, accordingly. The result is a linear system of equations, with one variable per basis function and one equation per measurement, which is iteratively solved. Stefan Kaczmarz proposed an iterative solution to matrix systems called the *method of projections* in 1937 [80]. The procedure was independently discovered by Gordon et al. [81] in 1970 for the purpose of medical imaging. They christened their method the *algebraic reconstruction technique* (ART), which has

[15] "Phantom" refers to a ground truth distribution.

become the standard term of art. Algebraic reconstruction is similar in effect to back projection: each iteration distributes a measurement residual along the corresponding LOS. The approach offers several advantages over analytical algorithms in the gas sensing context. The ART can be used for reconstruction regardless of the arrangement of optical paths; the technique is more robust to measurement noise; and ART algorithms are more-readily adapted to incorporate prior information about the measurements and gas process.

Reconstruction by the ART, alone, yields sparse, non-physical solutions under limited-data conditions that are common in CST. As such, numerous modifications have been proposed, many of which are specific to a restricted set of experimental conditions. For instance, Shepp and Vardi [82] formulated reconstruction as a stochastic problem to account for measurement noise. However, their algorithm did not alter information about the target distribution and the results were substantially similar to ART reconstructions [83]. Multiplicative ART (MART) was proposed alongside the ART by Gordon et al. [81]. MART modifies the ART using an exponential weighting of the residual, which has been shown to maximize the entropy of the reconstructed image, effectively promoting smoothness [84]. Numerous other iterative algorithms that promote smooth solutions have been proposed, e.g., Refs. [85–89]. Additional techniques include a wavelet algorithm [90], level-set approach [91], statistical methods [92], and a non-linear technique that incorporates hyperspectral features of the measurement [93].

1.3.3 Experiments in absorption tomography

1.3.3.1 Initial developments

Two-dimensional gas tomography with lasers was first proposed by Chen and Goulard [94] and Wang [95] in 1976. The authors described the similarity between the extinction of X-rays in medical imaging and absorption of light by gas molecules; both papers proposed a two-step procedure to determine the temperature and concentration of a target using a Boltzmann ratio (i.e., two-line thermometry). Chen and Goulard [94] and Wang [95] each used an algebraic algorithm, tailored to their study, and numerically demonstrated their approach. Four years later, Emmerman et al. [96] reported the first experimental test of absorption CST. The authors probed a free-shear turbulent jet, composed of 90%-10% CH_4-Ar, with a 3.39 μm He-Ne laser. They spread the laser into a horizontal sheet and attenuated light was resolved into LOS measurements by an uncooled Pb-Se detector array. This procedure was repeated at 12 equally-spaced projection angles and the mean absorption coefficient was reconstructed using filtered back projection. Other early

experiments include that of Santoro et al. [97] in 1981 and Bennett et al. [98] in 1984. Santoro's group [97] conducted another experiment with a He-Ne laser and CH_4-Ar jet while Bennett et al. [98] reconstructed I_2 vapour in a free-shear jet. They measured attenuation of an Ar^+ laser, divided into a fan-beam array, and reconstructed the I_2 distribution with a back projection algorithm for fan-beam projections from the medical imaging literature.

Ray and Semerjian [99] were the first researchers to report the results of flame imaging by absorption tomography. The pair used a continuous-wave dye laser to determine the temperature and concentration of Na in a seeded premixed flat flame. Hall and Bonczyk [100] detected the temperature and volume fraction of soot produced by a C_8H_{18}-air diffusion flame from the absorption of near-IR radiation. Broadband light from a W filament lamp was detected at 1,000 nm to avoid scattering by the soot; reconstructions were obtained using a Fourier algorithm with a modified Shepp-Logan filter. Spectral scanning with a TDL was introduced to absorption CST in 1992 with the work of Ouyang et al. [101], who imaged CO_2 above an axisymmetric flame. TDLs enable spectrally-resolved measurements of a molecule's transition features, improving reliability over monochromatic data. Kauranen et al. [102] modulated their TDL signal (as in WMS) to further improve the accuracy of absorption data. The authors report 2D distributions of O_2 in an air jet.

Innovations that refined the spectral resolution of CST data were accompanied by efforts to improve temporal resolution. In 1992, Beiting [103] engineered a device to record data from multiple fan-beam projections in 200 ns, which he deployed for time-resolved 2D absorption tomography. Light from Nd:YAG and tunable dye lasers was multiplexed and measured with a lock-in detector to obtain the two spectral intensity values required for two-line thermometry. He reconstructed the distribution of $C_4H_6O_2$ in an atmospheric plume using filtered back projection. During the remainder of the 1990s, several other groups established and honed absorption CST experiments. Shimizu and Saki [104] measured temperature and number density above a premixed C_3H_8-air flame, Chung et al. [105] and Torniainen and Gouldin [106] reconstructed a CH_4 jet, McNesby et al. [107] and Baum et al. [108] investigated CO products in and above flames by absorption tomography, Kessler et al. [109] used a TDL for CST of O_2 (reconstructing temperature and concentration), and Greenberg and Ku [110] imaged the soot volume fraction in a cross section of a laminar diffusion flame.

1.3.3.2 Laboratory-scale jets and flames

Continued work on laboratory-scale absorption CST has focused on reconstructing multiple parameters, simultaneously, and improving accuracy.

High-enthalpy flows have been the primary target of recent absorption tomography experiments. Following Refs. [104,107,108,110], Wondraczek et al. [111] and Villarreal and Varghese [112] imaged CH_4-air flames from a flat flame burner. Wondraczek et al. [111] constructed an apparatus for 2.5D tomography using a difference frequency generation (DFG) laser to measure mean absorption on a plane-by-plane basis;[16] and Villarreal and Varghese [112] used a TDL with a modulated injection current to resolve the temperature and volume fraction of CO_2. Kasyutich and Martin [113] mounted a distributed feedback (DFB) laser and scanning mirror on movable carriages, equipped with servo motors. They generated five fan-beam projections with 11 beams, each, and estimated the distribution of H_2O. Bryner et al. [114] and Busa et al. [115] reported the construction of an absorption CST device at the University of Virginia, for use in a scramjet combustor. Bryner et al. [114] tested the system on a flat flame burner and Busa et al. [115] combined the device with stereoscopic PIV to measure the mass flux of vapour. Song et al. [116] multiplexed the signals from DFB lasers at 1344.9 and 1388.1 nm to image temperature above a gas-field furnace. The authors attached the furnace to a stepper motor, moving the furnace between measurements, and obtained time-averaged data for 49 paths. Similar such experiments were conducted by Wang et al. [117], using a square burner; Liu et al. [118], who reported real-time imaging of a turbulent swirl flame; and a number of studies of CH_4-air combustion: from a Bunsen flame [119] or flat flame burner [120–123].

Non-linear algorithms are increasingly applied to reconstruct multiple parameters from instantaneous spectrally-resolved measurements. Ma et al. [124] deployed the first CST system designed for non-linear reconstruction. Light was generated by a TDL scanning from 1,333 to 1,377 nm at 200 Hz, resulting in dense spectral data. Six beams were shone through a plane above the square flame target, produced by a H_2-air Hencken burner and encased in a N_2 coflow. Simulated annealing was used to obtain 2D distributions of water vapour and temperature. The authors' objective function was the residual between spectral data for all six paths and a discrete Beer-Lambert model, parametrized by temperature and concentration vectors. An et al. [125]

[16] In 2.5D CST, slices of a volume are treated independently and a 3D reconstruction is built-up from 2D images.

improved the resolution of this device, using 30 beams to acquire 15×15 pixel images of temperature and water vapour. Later, An et al. [126] modified the algorithm, introducing a compressed sensing technique and testing the device on a high-temperature water vapour flow. Much subsequent research has focused on non-linear algorithms, which are discussed in Chapter Two.

Several papers feature non-reacting turbulent gas jets, including Rahim et al. [127] and Wang et al. [128]. The former seeded an air jet with plastic baffles and measured the line-average density of baffles along 76 lines-of-sight. Wang et al. [128] swept light from four TDLs along an 11° arc in 100 ms to generate intersecting fan-beam projections. They used this system to measure instantaneous distributions of NH_3 based on an absorption feature at 1,500 nm. Recent work by Halls et al. [129] used an Nd:YAG burst mode laser to illuminate a free-shear air jet, seeded with acetone tracer. The scene was imaged with seven high-speed cameras and the authors computed time-resolved sequences of the jet to follow the evolution of turbulent structures. Free-shear turbulent gas jets, as in Refs. [103,106,127–129], support the fundamental study of turbulence and are ideal targets for the covariance estimation method described in Chapter Three.

1.3.3.3 In situ tomography of combustors and exhaust monitoring

Combustion efficiency depends on ignition timing and the relative abundance of air and fuel throughout a combustion cycle. Information about mixing is critical to the design and operation of internal combustion engines, gas turbines, and commercial boilers, but these devices are enclosed, which limits visibility. Moreover, modifying combustors to obtain optical access with full-field diagnostics like LIF can alter mixing characteristics and engine performance and restricts the maximum pressure. As a result, significant effort has been devoted to minimally-invasive in situ combustion imaging by absorption CST.

Internal combustion engines have been a particular focus of this research. Carey et al. [130] developed a system for in situ CST of the air/fuel ratio in a piston using micro-optic components to access the chamber. The group constructed a pressurized chamber for the combustion of C_8H_{18}. Fiber cables directed multiplexed light at 1,550 and 1,700 nm from custom diode lasers to the piston and then from the piston to a data acquisition system. The collimating lens and detection optics were embedded in the piston wall to minimize alterations to the chamber geometry. McCann et al. [131] and Hindle et al. [132] reported early applications of the device in 2001, featuring the algebraic reconstruction of data from 33 and 32 optical paths, respectively. In 2005, Wright et al.

[133] improved the signal reliability and measurement frequency, introduced a modified Landweber reconstruction algorithm, and fitted their system to a production engine [134]. Subsequently, Wright et al. [135] reported in situ reconstructions of the air/fuel ratio in a four cylinder production engine, resolved at 3° crank angles. More recently, in 2015, Terzija et al. [136] used this in-cylinder device to image fuel droplets and vapour concentration distributions a direct injection system; and in 2017 Tsekenis et al. [137] adapted the system to monitor LNG combustion in a large-bore piston from a marine engine. Independent of the group of McCann, Kawazoe and Whitelaw [138] used a He-Ne laser to probe the gas distribution in a cylinder outfitted with quartz windows.

Absorption CST has also been applied to other types of combustors. Gillet et al. [139] developed a system for in situ CST in the premixing chamber of a gas turbine in 2004. Light at 3.39 μm was generated by a He-Ne laser and shone through the enclosure, accessed through large sapphire windows. Six projections, each with 25 parallel optical paths, were imaged with a CCD camera; CH_4 distributions were algebraically reconstructed. In 2008, Lindstrom et al. [140] measured the shock train structure of supersonic combustion in a research cell from two view angles. Because of the view restriction, measurement data was severely limited. The authors supplemented their experimental data with eigenfunctions from a CFD simulation (similar to the approach of Torniainen and Gouldin [106]). Following developments made by the laser diagnostics group at the University of Virginia, Busa et al. [141,142] tested a coupled CST-stereoscopic PIV device to measure the mass flow of water vapour in a scramjet to diagnose combustion efficiency.

Species concentration and temperature data for exhaust from an engine can also be used to gauge the quality of combustion. Hot spots indicate problems with mixing and exhaust temperature is correlated with the formation of pollutants like NO_x. Moreover, distributions of NH_3 following urea injection in an exhaust aftertreatment indicate the efficiency of a selective catalytic reduction (SCR). Kamimoto and Deguchi [143] detected the concentration and temperature of H_2O in exhaust from a gasoline generator. Ma et al. [144] used their non-linear CST device to resolve temperature and H_2O volume fraction in the exhaust of a J85 jet engine at 50 kHz. More recently, the FLITES consortium—convened by researchers at the Universities of Manchester, Edinburgh, Southampton, and Strathclyde, along with industrial partners and the EPSRC—developed a system for high-speed imaging of CO_2 and temperature in the exhaust of a commercial jet engine. They

constructed a 126-beam measurement array with a modulated TDL source and applied their system to experimental phantoms and jet engine exhaust [145–148]. Recently, Stritzke et al. [149] used a DFB laser to monitor NH_3 in the SCR system of a commercial diesel engine by absorption CST.

1.3.3.4 Environmental monitoring

Demand for remote sensing tools has grown in response to research on radiative forcing by greenhouse gasses and the health effects of toxic emissions such as VOCs. As a result, absorption CST devices have been developed to quantify emissions fluxes distributed over large areas as well as to monitor volcanic activity.

Cuccoli et al. [150] first remarked on the possibility of using TDLs for large-scale CST, motivated by the need to monitor urban pollution. They proposed a suitable suite of molecular targets, instrumentation, and an experimental setup and then simulated the diagnostic. Shortly thereafter, in 2003, Belotti et al. [151] applied the technique to map the distribution of CO_2 above Solfatara, a volcanic crater near Naples. The authors measured the transmission of IR radiation at 1,580 nm over 15 paths—each roughly 1 km long. A TDL and photodiode detector were collocated at one end of the path with a retroreflector at the other end: to return light from the laser to the detector. Mean transmittance data was algebraically reconstructed. The group of Platt at the University of Heidelberg has since made considerable contributions to DOAS tomography. Pundt et al. [152] carried out an experimental campaign using multiple long-path DOAS devices to map NO_2 emissions along a highway in southwest Germany in 2005. Pundt and Mettendorf [152] designed an active DOAS system for this study: with a halogen lamp to produce light, spectrometers for detection, and retroreflectors to focus light from the source back towards the detectors. General et al. [153] modified the device for airborne tomography (i.e., measurements were conducted inside an airplane). Heue et al. [154] used this approach for airborne mapping of NO_2 in an industrial region of South Africa. And Frins et al. captured the atmospheric distribution of NO_2 over Heidelberg [155] and distributions of NO_2 and SO_2 over Montevideo [156–158] by long-path DOAS tomography.

DOAS tomography has been deployed by a number of other groups to monitor volcanic emissions. Kazahaya et al. [159] reported the use of a passive system with spectrometers designed to measure UV/visible light. They mapped SO_2 concentrations over the Miyakejima volcano. Wright et al. [160] measured the distribution of SO_2 over Mt. Etna, and Johansson et al. [161] measured SO_2 and NO_2 emissions—at Mt. Etna and then at a power plant in Aragon, Spain.

Krueger et al. [162,163] visualized volcanic emissions of SO_2 and SiF_4 at Popocatépetl in Mexico. They used a scanning interferometer, articulated with stepper motors, for measurement and reconstructed the emissions with a Tikhonov-based smoothing algorithm. Further measurements of CO_2 emissions at Solfatara were carried out by Queißer et al. [164].

A number of additional CST experiments with environmental targets have been reported in the literature. Rusch and Harig developed a system to capture spectrally-resolved 2D IR images of a scene using a scanning mirror and interferometer [165]. The authors used this device to record NH_3 plumes emanating from an industrial stack from two vantage points. These views were combined to reconstruct the 3D plume structure [166] with a novel CST algorithm [167]. Dobbler et al. [168,169] described a set of TDLs and retroreflectors that can generate 40 paths across a carbon storage field. They measured the spatial distribution of time-averaged CO_2 emissions over an area of approximately 1 km^2 and period of 200 hrs. Seidel et al. [170] deployed another TDL system to measure the H_2O released by permafrost. And CST was again used to detect a CO_2 source by Levine et al. [171] with the system of Dobbler et al. [168]. The largest application of CST to date, in terms of spatial scale, has been the aerosol reconstruction experiment of Garay et al. [172]. This group used IR data from NASA's Terra satellite to image a smoke plume from a wildfire in California and compared their results to data from a ground-based LIDAR experiment. There were 337 paths through 441 pixels, each 1.1 km^2 in size. The group used an algorithmic reconstruction approach and reported results that were in good agreement with the LIDAR measurements.

1.3.3.5 Other applications

Additional applications of absorption tomography are worth mentioning and feature less common targets. Zhang et al. [173] reconstructed the temperature and atomic number density of Ar in the exhaust plume of a 3 kW arcjet thruster. They used a diode laser, tuned to 810 nm, to probe the plume. The laser-detector pair was mounted on a translation stage, moved during the experiment to obtain projections through three axial planes. Zhang et al. [173] assessed the response of Ar emissions to the arcjet's discharge current and mass flow rate.

Absorption CST was applied to measure the concentration of water vapour in a packed bed adsorption column by Salem et al. [174] in 2005. They split light from a TDL into three sheets with equiangular spacing, resolved into 384 measurements by a set of InGaAs detector arrays. Images of the vapour temperature and concentration were obtained by algebraic reconstruction. A

3D version of this diagnostic was developed by tSaoir et al. [175,176], who used the technique to monitor a vapour-phase hydrogen isotope exchange.

Multi-phase flow is another CST target: Schleicher et al. [177] devised a system to resolve dye in single-phase flow with a tracer as well as phases in a bubbly flow. The probe volume was illuminated by a system of 256 LEDs; transmitted light was recorded by 32 detectors at 4.5 kHz. Chen et al. [178] measured phase distributions in a multi-phase flow, as well, using the attenuation of light from a near-IR laser source.

1.3.4 Experiments in emission tomography

Emission CST uses measurements of light to estimate the 2D or 3D radiative source term distribution in a reacting gas. Light from the flow field is primarily generated by thermal emission or the relaxation of radicals produced by intermediate chemical reactions. The dominant source depends on the nature of the flow and spectral range of the data.

1.3.4.1 Thermal emission

The first papers on thermal emission tomography were those of Uchiyama et al. [179] and Hino et al. [180], published in 1985 and 1987, respectively. Uchiyama et al. [179] measured IR emission from a CH_4-air flame generated by a circular burner. They used a mechanical chopper and lock-in detector to isolate the signal, detected by a photoconductive sensor, from light between 1,000 and 5,000 nm. Intensity in this band was reconstructed by back projection. The resulting "intensity source" distribution was correlated to a flame temperature using thermocouple data from discrete locations. The intensity source map was converted to a temperature distribution using this correlation. Uchiyama et al. [179]'s semi-empirical technique was justified by assuming an optically thin flame with negligible variation in the absorption coefficient over the spectral range of the detector and temperature range of the flame.[17] Hino et al. [180] reconstructed visible radiative emission from plasmas in a fluorescent lamp and Geissler tube. The lamp served as a test case, based on visible emission by Hg; the Geissler tube was pressure-controlled and emission by N_2 molecules was collected with and without a magnet beside the tube, to disturb the discharge condition. Average intensity was detected by a CCD array from 68 projection angles. Spectral

[17] The spectral absorption coefficient is expected to vary considerably throughout this flame due to variation in composition (with the additional complication of collision broadening) and temperature. Breakdown of the author's assumption can be seen in the graph of measured temperature vs. reconstructed intensity (Fig. 9). However, the paper merits recognition as the first attempt at emission tomography.

profiles of Hg and N_2 emission were used to select the measurement wavelengths—isolated with an interferometric filter—and data were algebraically reconstructed. Later, in 2004, Wan et al. [181] conducted 3D plasma tomography based on thermal emission from an Ar-arc plasma. They used a novel algebraic algorithm with a smoothing component to reconstruct the UV source at 420 and 425.9 nm. The authors calculated the temperature and number density of Ar^+ throughout the volume in a post-processing stage.

Much of the research on emission CST has focused on the pyrometry of sooting flames. In this work, thermal emission from soot particles at two or more wavelengths is fit to Planck's distribution to infer the temperature and density of soot particles.[18,19] Early experiments normally featured an axisymmetric flame, though many already employed a general 2D algorithm for reconstruction. Fischer and Burkhardt [182] used CCD cameras equipped with a filter to image a candle flame in the visible RBG bands, reporting a 3D estimate of the temperature distribution; Ha and Choi [183] used a similar approach, only with a C_3H_8-air flame. Best et al. [184] and Bates et al. [185] documented early uses of FTIR measurement for emission CST in 1991 and 1993, respectively. Dense spectral data was transformed into mean volume fraction distributions of soot and other species (e.g., CO_2, C_2H_2). Both tests were conducted on a laminar C_2H_4-air diffusion flame. These papers all used a cold, dark environment, assuming negligible background illumination. In 2001, Correia et al. [186,187] modified the tomography algorithm to account for radiation from a furnace wall; they also applied a correction for self-absorption, relaxing the assumption of an optically thin medium. The authors computed 3D temperature distributions for an axisymmetric flame in a semi-industrial furnace, with a single CCD array, and unsteady flame in open air, with four cameras. Luo and Zhou [188] and Huajian et al. [189] deployed a similar system on two occasions: using four cameras to estimate a 2D temperature distribution in a pulverized coal combustor in 2005 [188] and 11 cameras to capture the 3D distribution of temperature in an arch-fired coal furnace in 2009 [189].

During the mid-2000s, researchers developed sensors for time-resolved measurement of 3D flame fronts based on broadband measurements of emission. Most of these studies looked at visible

[18] The procedure assumes that the optical properties of soot cancel out in the ratio of spectral intensity data. However, soot is known to have complex spectral properties and the assumption can break down, considerably affecting reconstructions of temperature and volume fraction.

[19] In the two-wavelength case, an analytic formula for two-line thermometry may be used (i.e., the Boltzmann ratio).

emission by the flame, thus combining thermal emission and chemiluminescence. Ihrke and Magnor [190] reconstructed emission source data for a small laboratory flame using eight cameras with a RGB sensor; results were used to generate realistic flames for computer visualizations. Bheemul et al. [191–193] imaged a similar target with three equally-spaced monochromatic CCD devices. They subsequently employed this data to quantify geometric features of the reaction zone (volume, length, circularity, surface area, and orientation). In 2005, Brisley et al. [194] used a monochromatic CCD to capture instantaneous distributions of temperature in a C_4H_{10}-air flame by two-line thermometry. And, in 2005 and 2007, Gilabert et al. [195,196] simulated back projection and algebraic algorithms and used the system of Bheemul et al. [191] to reconstruct temperature in coal- and gas-fired combustion processes. More recently, in 2012, Huang et al. [197] built a system to measure emission by soot at multiple wavelengths from two angles with a high-speed camera. Their 3D reconstruction algorithm included a correction for self-absorption and resolved the temperature and volume fraction of soot in an unsteady C_3H_8-air diffusion flame.

1.3.4.2 Chemiluminescence emission

In 1988, shortly after the introduction of thermal emission tomography by Uchiyama et al. [179] and Hino et al. [180], Hertz and Faris [198] conducted the first emission CST experiment, focused on the radiation emitted by excited radicals in a flame. The authors restricted measurements to a narrow spectral range with a 410 nm bandpass filter. This range was selected to isolate emissions from excited CH^* in the reaction zone of two premixed flames: with CH_4-O_2 fuel and C_3H_8 fuel. Three projections were simultaneously measured with a single intensified diode array by multiplexing the emission signals. An algebraic technique was employed to reconstruct the flame fronts. Leipertz et al. [199,200] then created a system to limit NO_x generation in a brown coal firing process. The system used CST images of the flue gas to diagnose the abundance of NH^* and CN^*, which are intermediate components in the liberation of nitrogen and thereby correlate to the formation of NO. Measurements were obtained with a cooled CCD array and UV filter; reconstructed 2D distributions were generated for CH^*, OH^*, CN^*, and C_2^*.

Chemiluminescence-based CST began to proliferate in the mid-2000s due to the decreased price of camera and computing resources. In 2005, Ishino and Ohiwa [201] devised a custom multi-lens system with a broadband CCD (400 to 600 nm, detecting mostly OH^*) to image chemiluminescence from a turbulent flame. They achieved 40 simultaneous views at 500 Hz. High-speed 2D imaging of OH^* in a turbulent diffusion flame was later conducted by Anikin et al.

in 2010 [202] and 2012 [203] using Kepler telescopes, arranged in a semicircle, to direct emission from the flame onto a CCD detector. Worth and Dawson [204] imaged the OH^* distribution of two interacting flames with 15 cameras. The authors validated their reconstructions with cross sectional images from a parallel OH-PLIF experiment. And Floyd et al. [205,206] used commercial cameras and mirrors to generate time-resolved 3D estimates of a CH_4-O_2 flame from a matrix burner and turbulent opposed jet flame. The authors imaged CH^* instead of OH^*, which is corrupted by self-absorption because of the longevity of ground state OH outside the reacting zone.

The group of Ma at Virginia Tech has conducted a large number of emission CST experiments. Beginning in 2013, Cai et al. [207] established an emission CST device and investigated the effects of viewing angles on reconstruction accuracy. Kang et al. [208] conducted a similar study in 2014, using fiber-based endoscopes instead of CCDs to capture chemiluminescence. And, also in 2014, Li and Ma [209] reported 3D CST images of CH^* from a highly-turbulent swirl flame using five cameras. Their system had a temporal resolution of 1 kHz. The group has conducted emission CST in parallel with Mie scattering [210] and PLIF measurements [211] to cross-validate these diagnostics. Another group that is active in emission CST of chemiluminescence is that of He at the Nanjing University of Science and Technology. Since 2015, they have established a multi-camera system for CST [212], at first using 12 cameras and later 15; devised a numerical procedure to compensate for overexposure [213]; applied a correction to the measurement model [214]; and developed a custom filter to simultaneously image CH^* and C_2^* with an RGB sensor [215]. The latter development is particularly significant as the point-wise ratio of chemiluminescence from different radicals correlates to the local heat release rate, which permits quantitative heat release rate imaging via chemiluminescence CST. He's group used an unsteady premixed C_3H_8-air diffusion flame to test their system.

Other CST experiments featuring chemiluminescence include the reconstruction of CH^* in the CH_4-air flame from a Meker burner [216]; OH^* in a laminar premixed H_2-air flame [217]; and CH^* in a turbulent swirl flame [218]. Further work, published by Wiseman et al. [219], described a novel approach to quantifying the flame front geometry with emission CST data. And Alviso et al. [220] used a CST apparatus with an intensified CCD camera and system of narrow band filters to simultaneously reconstruct distributions of OH^*, CH^*, and C_2^*.

1.3.4.3 Aerospace applications

Emission CST has been most frequently applied to the study of phenomena in laboratory-scale flames but can also be used for in situ monitoring and on-line control purposes. In particular, numerous aerospace applications have been reported. Herding et al. [221] imaged OH^* emission in a shear coaxial injector to investigate flame structure and stability near the injector. Sivathanu et al. [222] used two imaging spectrometers to measure light along fan-beam paths through a solid rocket propellant plume above an Al diffusion flame. Their spectral measurements, resolved over from 1,300 to 4,800 nm, were used to reconstruct radiation from particulate matter in the plume. And Ma et al. [223] investigated the shape of the ignition kernel and combustion stability in a Mach-2 cavity combustor, subject to two fuel conditions. Ma's system used eight lenses, positioned throughout the combustor, and two fiber-based endoscopes, with an exposure time of 49 μs and measurement frequency of 20 kHz.

1.4 Outlook for CST

The trend in gas-phase tomography is towards increasing the number of optical paths, precision of measurements, and temporal resolution of the data. Recent publications feature novel modalities [224] and applications [225], high resolution images [219], and irregular domains that resist easy optical access [149]. This progress was enabled by the decreasing cost of the electronics, optical components, and computing resources needed for tomographic imaging—trends that are expected to continue. As a result, while there were only a handful of gas tomography experiments reported in the 1980s, well over one hundred papers on CST have been published since 2010. Current efforts in CST research are focused on the development of sophisticated algorithms, to incorporate specific information about a flow field into reconstructions, and the formal quantification of uncertainty. Statistical imaging methods are well-suited to meet these research challenges.

1.5 Overview of the dissertation

This work reports developments and applications of the Bayesian framework for gas-phase tomography over the course of seven chapters. Following on from the introduction, Chapter Two reviews the physics of measurement and mathematics of reconstruction for gas tomography and presents the Bayesian framework for CST.

Bayesian imaging begins with likelihood and prior pdfs, predicated on the assumption that accurate pdfs will yield accurate reconstructions. Chapter Three presents a justification for joint-normal priors in the context of turbulent targets. Moreover, a theoretical analysis of self-similarity

in turbulent jets is employed to construct an advanced prior for round free-shear flow. The form of Bayes' equation suggest methods for model selection and designing experiments: Chapter Four develops these ideas to fruition for hard-field tomography. Bayesian functions for optimal experimental design are proposed and compared to existing deterministic criteria. Following this, a statistical approach to model comparison is introduced to select a discretization scheme, mode of interpolation, and prior from measurement data in a numerical experiment.

Chapters Two through Four focus on the fundamentals of Bayesian tomography. The dissertation continues with experimental developments, conducted in a Bayesian way. Broadband absorption CST is a new technique, intended for quantitative emissions detection using spectrally-convolved absorption signals. Chapter Five provides a theoretical basis for the method and reports the results of a proof-of-concept emissions detection experiment. Chapter Six concerns BOS tomography, in which the refractive index of a fluid is reconstructed from measurements of beam steering. The diagnostic is enhanced with a modification to measurement model and applied to combustion imaging for the first time.

Finally, Chapter Seven provides a synopsis of the theoretical and experimental contributions described in this work. The case for Bayesian methods in gas-phase tomography is recapitulated and the dissertation closes with recommendations for future work.

Chapter Two
Bayesian Chemical Species Tomography

Tomography is a canonical inverse problem. Projections are an indirect observation of the quantity of interest (the forward problem) and a mathematical model of projection is inverted to estimate this quantity from a set of observations (the inverse problem). The forward problem in gas-phase tomography is the calculation of intensity at a detector for a known distribution of gas. The inverse problem—*reconstruction*—involves estimating the gas distribution from a set of intensity data. Gas-phase tomography requires an equation to describe radiative transfer in the medium as well as a finite representation of the gas. CST divides into absorption and emission modalities and emission CST is further divisible into thermal and chemical modes. This chapter begins with a detailed summary of the measurement physics for absorption and emission CST, which simplify into a unitary forward model.

Direct inversion of the forward model is either underdetermined or unstable, meaning the measurements are insufficient in themselves to obtain a realistic reconstruction. Consequently, CST algorithms need supplemental information about the measurements and flow field to generate physically-plausible images of the gas parameters. Classical techniques of computed tomography implicitly include this information, by regularizing measurements in frequency space, with analytical algorithms, or physical space, with algebraic algorithms. This chapter describes both methods, paying particular attention to the inherent role of prior assumptions. Following the introduction to classical reconstruction, the ill-posed nature of tomography is proved.

Statistical inversion is an alternative approach to inverse analysis in which the assimilation of measurement data and prior assumptions is explicit. The method employs Bayes' equation to

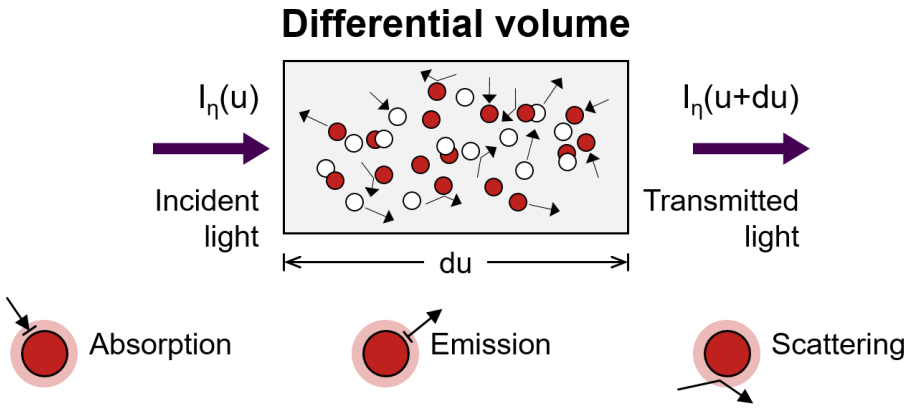

Figure 2.1 Schematic of the radiative energy balance in a differential volume along a LOS, showing absorption, emission, and in- and out-scattering; adapted from Ref. [226].

incorporate prior knowledge into the reconstruction procedure in a statistically-robust manner. Critically, the form of Bayes' equation itself suggests methods for: *improving reconstructions* through advanced priors, discussed in Chapter Three; *designing experiments*, discussed in Chapter Four; and *selecting models*, also discussed in Chapter Four. The final section of this chapter reviews the philosophical foundations and formalisms of Bayesian tomography.

2.1 Measurement Physics for Gas-Phase Tomography

2.1.1 Radiative transfer in a participating medium

Engineering analyses that involve radiative transfer through a participating medium commonly employ the RTE to compute aggregate light-matter behaviour. In classical form, the RTE is a first-order integral-differential equation that accounts for the accumulation and attenuation of intensity along a path by photonic absorption, emission, and scattering. The intensity of light, I, is parametrized by its wavelength, λ, or wavenumber, $\eta = \lambda^{-1}$; location, $\mathbf{u}$; and direction, $\mathbf{v}$. $I_\eta(\mathbf{u},\mathbf{v})$ is the spectral radiative intensity—that is, radiative power per unit area along $\mathbf{v}$, solid angle Ω, and wavenumber η [227]. Figure 2.1 shows a differential control volume and the light-matter interactions involved in the RTE.

The change in radiative energy through a differential volume, $\Delta Q_\eta = [I_\eta(u + du,\mathbf{v}) - I_\eta(u,\mathbf{v})]dAd\Omega$, equals the sum of gains and losses due to absorption, emission, and in- and out-scattering: $\Delta Q_{\eta,\text{abs}} + \Delta Q_{\eta,\text{emit}} + \Delta Q_{\eta,\text{in}} + \Delta Q_{\eta,\text{out}}$. Attenuation along the element by absorption and out-scattering events is given by $\Delta Q_{\eta,\text{abs}} = -\kappa_{\text{a},\eta} I_\eta(u,\mathbf{v})dudAd\Omega$ and $\Delta Q_{\eta,\text{out}} = -\kappa_{\text{s},\eta} I_\eta(u,\mathbf{v})dudAd\Omega$, respectively, where $\kappa_{\text{a},\eta}$ and $\kappa_{\text{s},\eta}$ are the spectral absorption and scattering coefficients [226]. (The extinction coefficient, $\beta_\eta = \kappa_{\text{a},\eta} + \kappa_{\text{s},\eta}$, makes the final expression more compact.) Kirchhoff's law states that the spectral absorption coefficient and emissivity are equal when a medium is in local

thermal equilibrium (LTE).[20] Given $\varepsilon_\eta = \kappa_{a,\eta}$, the expression for emission in the volume is $\Delta Q_{\eta,\text{emit}} = \kappa_{a,\eta} I_{b,\eta}[T(\mathbf{u})] du dA d\Omega$, where $I_{b,\eta}$ is the spectral emission at η from a blackbody at temperature T. Scattering behaviour is characterized by a phase function, $\Phi_\eta(\mathbf{v}\cdot\mathbf{v}')$, which describes the solid angle-weighted portion of light traveling along $\mathbf{v}$ that scatters in the direction $\mathbf{v}'$. The contribution of in-scattering is found by integrating the incident intensity at u that is redirected along $\mathbf{v}$,

$$\Delta Q_{\eta,\text{in}} = \frac{\kappa_{s,\eta}}{4\pi} \int_{4\pi} I_\eta(u, \mathbf{v}') \Phi_\eta(\mathbf{v}\cdot\mathbf{v}') d\Omega' ds dA d\Omega \,. \tag{2.1}$$

Finally, the RTE combines these terms into a single expression,

$$\frac{dI_\eta(u,\mathbf{v})}{du} + \beta_\eta I_\eta(u,\mathbf{v}) = \kappa_{a,\eta} I_{b,\eta}\left[T(u)\right] + \frac{\kappa_{s,\eta}}{4\pi} \int_{4\pi} I_\eta(u, \mathbf{v}') \Phi_\eta(\mathbf{v}\cdot\mathbf{v}') d\Omega' ds dA d\Omega \,. \tag{2.2}$$

Evaluating the RTE is greatly complicated by scattering. The scattering coefficient and phase function depend on the scattering regime, which changes with the size of a particle, its molecular structure, and the wavelength of incident light. Hard-field gas tomography features molecular gasses and IR or UV/visible light; measured wavelengths thus greatly exceed the particle size.[21] As a result, scattering is negligible, $\beta_\eta \approx \kappa_{a,\eta}$, and $\Delta Q_{\eta,\text{in}} \approx 0$. The scattering coefficient, $\kappa_{s,\eta}$, is unused so the absorption coefficient, $\kappa_{a,\eta}$, is denoted κ_η for the remainder of this dissertation. Moreover, when scattering is neglected, the remaining terms in Eq. (2.2) are directionally-aligned so the directional dependence of I_η is dropped from the notation, as well. The non-scattering RTE is integrable along a LOS from $u = 0$ to L, resulting in the expression

$$I_\eta(L) = \overbrace{I_\eta(0) \exp\left\{-\int_0^L \kappa_\eta(u) du\right\}}^{\text{Absorption of background radiation}} + \overbrace{\int_0^L S_\eta(u) \underbrace{\exp\left\{-\int_u^L \kappa_\eta(u') du'\right\}}_{\text{Re-absorption}} du}^{\text{Spontaneous emission}} , \tag{2.3}$$

where S_η is a radiative source term that combines thermal emission and spontaneous emission due to the relaxation of excited electronic states. Equation (2.3) is further simplified and rearranged to obtain modality-specific measurement models for absorption and emission CST.

[20] LTE assumes that spatial and temporal temperature are small enough to preserve the formal definition of temperature. More precisely, in volume elements on the scale of spatial temperature gradients, molecular velocities roughly adhere to a Maxwell-Boltzmann distribution. LTE is a realistic assumption for most CST experiments.

[21] Soft-field tomography features a high-energy source with rays that are subject to scattering by a molecular target. For instance, terahertz-based atmospheric tomography or medical imaging with X-rays. In transitional cases, in-scattering remains negligible and scattered rays are filtered out by the detector. Hard-field reconstruction techniques are thus used in transitional scenarios [369].

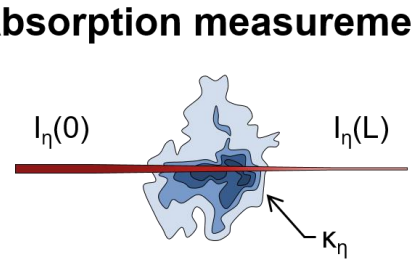

Figure 2.2: Absorption measurement along a LOS showing attenuation of the source intensity by the absorption coefficient, κ_η. Absorption CST reconstructs the spatial distribution of κ_η, which is post-processed to determine physical parameters (e.g., volume fraction, temperature, pressure).

2.1.2 Absorption CST

Absorption tomography involves the attenuation of light by a cold gas, meaning thermal emission from the gas is negligible compared to the source intensity at the measurement wavenumber. Figure 2.2 depicts the attenuation of a background source by a gas. In this scenario, the RTE reduces to the *Beer-Lambert law*,

$$I_\eta(L) \approx I_\eta(0) \exp\left\{-\int_0^L \kappa_\eta(u)du\right\}. \tag{2.4}$$

Equation (2.4) is re-arranged to form a Fredholm IFK, which defines an absorption measurement,

$$b \equiv \ln\left[\frac{I_\eta(0)}{I_\eta(L)}\right] \approx \int_0^L \kappa_\eta(u)du\,. \tag{2.5}$$

The kernel of this IFK is unity, which enables the analytical inversion of coupled measurements. I_η at L is the active measurement and I_η at 0 is a reference intensity, produced by a calibrated light source (such as a TDL) or background illumination. Measurement paths extend from a source at $u = 0$ to a detector at $u = L$;[22] reference measurements are made without the gas so κ_η is null along the LOS. Tunable and two-colour systems can infer $I_\eta(0)$ from the intensity at a nearby wavenumber such that $I_\eta(0)$ and $I_\eta(L)$ are simultaneously recorded. This procedure mitigates the effects of beam steering, window fouling, and fluctuations in the source intensity.

The spectral absorption coefficient is the reconstructed parameter in absorption CST but is not itself the quantity of interest. Two- or three-dimensional estimates of κ_η must be related to the distribution of physical properties by spectroscopic modelling. Typically, the composition,

[22] Some DOAS devices use ambient light that originates far away from the detector, in which case a "fictional" source is located immediately outside the imaging domain.

temperature, and pressure of a mixture are of primary interest, though some practitioners use absorption CST in tandem with PIV to estimate the velocity and mass flux of a flow [142].

Gas molecules can transition between a large variety of energy states, with translational, rotational, vibrational, electronic, and nuclear components.[23] Of these, rotational and vibrational transitions are the most salient to absorption CST. The former component relates to the angular momentum of a molecule while the latter refers to the vibration of atoms in a polyatomic system. Rotational and vibrational transitions are often coupled and referred to as *rovibrational* transitions. Molecules may absorb an incident photon and jump to a higher state, provided the energy of the photon is aligned with the difference between energy levels of the transition. Potential transitions are clustered around specific energies that reflect the structure and state of interacting molecules. Distinct transitions result in a spectral line, with a finite width and distinct shape, and the bond energies and geometric configurations of different species result in a unique pattern of lines. These "spectral signatures" form the basis of spectroscopy—described in detail in Chapter Five.

Line-by-line parameters for rovibrational and electronic transitions are used to calculate the absorption coefficient for a gas based on its temperature and partial pressure. The reconstructed coefficient, κ_η, is thereby used to infer the gas state. Spectroscopic models specify transitions between a lower state, i, and an upper state, j, designated ij for absorption or ji for emission. Transitions are described in terms of their overall line intensity, S_{ij}, and lineshape, f. Typically, η is the measurement wavenumber; η_{ij} is the centreline, equal to the transition energy in wavenumbers ($E_j - E_i = hc\eta_{ij}$, where c is the speed of light and h is Planck's constant); and χ, p, and T are the mole fraction, pressure, and temperature of the molecule.

The centreline indicates the characteristic energy of a transition but there is a non-zero probability that photons with an energy close to η_{ij} will be absorbed due to *line broadening* effects. Several mechanisms contribute to broadening and determine the lineshape of a transition. Natural broadening is a consequence of Heisenberg's uncertainty principle, which limits the combined precision of the energy and lifetime of an excited state. This effect is minimal on its own but is amplified through molecular collisions, which reduce the lifetime of excited states. Collisional broadening depends on the frequency of collisions and composition of a mixture. Doppler broadening is predominantly a high-temperature phenomenon. The wavelength of light is relative

[23] Translational energy is bulk molecular motion; electronic energy depends on the orbital position and spin of electrons in the gas; and the nuclear component refers to energy levels in the nucleus (spin energies, etc.).

to the velocity of colliding particles. As a result, the distribution of molecular velocities, which depends on their temperature, affects the photon energies associated with a transition.[24] Pressure and Doppler effects also shift the centreline of a transition. Chapter Five provides further details on these phenomena and gives their lineshape functions.

Reconstructed values of κ_η reflect the sum of absorption coefficients for molecules present in a mixture. Species-specific coefficients are themselves a sum of transition-specific coefficients, $\kappa_{\eta,ij}$: $\kappa_\eta = \Sigma_{ij}(\kappa_{\eta,ij})$ gives the rate of absorption of incident intensity at η. Transition-specific coefficients equal

$$\kappa_{\eta,ij} = S_{ij}(T)\, f(\eta) \frac{\chi p}{k_B T}, \tag{2.6}$$

where k_B is the Boltzmann constant.[25] The total absorption coefficient for a species is proportional to the species concentration (i.e., $\kappa_\eta \propto \chi$) and the ratio of two lines is independent of concentration and pressure. CST experiments often feature a target that is roughly isothermal and isobaric, in which case the volume fraction of the target is $\chi = (k_B T/S_{ij} f)\cdot\kappa_\eta$.

Significant temperature variation in the target gas is common in absorption CST of flames and exhaust gasses. Data about the concentration and temperature of a target species can be extracted by careful selection of one or more measurement wavenumbers. Two-line thermometry—based on the temperature dependence of the ratio of spectral lines—is often used to calculate a gas state. The spectral line intensity is

$$S_{ij}(T) = I_a \frac{A_{ji}}{8\pi c \eta_{ij}^2} \frac{g_i}{Q(T)} \exp\left\{-\frac{c_2 E_j}{T}\right\}\left(1-\exp\left\{-\frac{c_2 \eta_{ij}}{T}\right\}\right), \tag{2.7}$$

where I_a is the natural terrestrial isotopic abundance, A_{ji} is the Einstein A coefficient, g_j is the statistical upper weight of the transition, Q is the total internal partition sum, $c_2 = h/k_B T$ is the second radiation constant, and E_i is the lower-state energy [228]. In order to determine a local temperature, one takes the ratio of κ_η at two lines, η_1 and η_2: $R = \kappa_{\eta 2}/\kappa_{\eta 1}$. An expression for

[24] Natural, collisional, and Doppler broadening are local effects. Collisions also induce narrowing [370], which is only observable under rare conditions. Nearby molecules (usually in a liquid or solid state) can alter the spacing of energy levels, e.g., in ionic liquids. And full-field electric effects such as Stark broadening can alter the lineshape, as well. Collision and Doppler broadening dominate in the CST context.

[25] Equation (2.6) expresses the line intensity as a function of temperature and lineshape as a function of the measurement wavenumber but in reality both values are complex functions of the energy states in a transition, temperature and pressure of the gas, and molecular composition of a mixture.

temperature is derived by substituting Eqs. (2.6) and (2.7) into R and re-arranging the result to isolate T,

$$T = \frac{c_2(E_{i,\eta 2} - E_{i,\eta 2})}{\ln[R] + \ln\left[\frac{S_{\eta 2}(T_{\text{ref}})}{S_{\eta 1}(T_{\text{ref}})}\right] + c_2 \frac{E_{i,\eta 2} - E_{i,\eta 2}}{T_{\text{ref}}}}, \tag{2.8}$$

where T_{ref} is a reference temperature (typically 296 K) [229]. Finally, the target concentration is calculated using either wavenumber,

$$\chi = \frac{\kappa_{\eta 1}}{S_{\eta 1} p} \text{ or } \frac{\kappa_{\eta 2}}{S_{\eta 2} p}. \tag{2.9}$$

Estimating pressure requires a two-step procedure [230]. The first step involves hyperspectral reconstruction, where images of κ_η are computed for many wavenumbers. Second, the reconstructed absorption spectra at each basis function is used to estimate χ, p, and T by non-linear regression.

2.1.3 Emission CST

Emission tomography is based on the conversion of thermal or electronic energy in a fluid into light by spontaneous emission, illustrated in Figure 2.3. Background radiation over the spectral range of the detector is typically neglected (i.e., $I_\eta(0) \approx 0$) and the RTE reduces to

$$I_\eta(L) = \int_0^L S_\eta(u) \exp\left\{-\int_u^L \kappa_\eta(u')du'\right\} du. \tag{2.10}$$

The nested integral in Eq. (2.10) accounts for the absorption of radiation emitted in the probe volume, usually due to self-absorption,[26] which depends on the optical density of the medium. CST of thermal emission and chemiluminescence are both prone to self-absorption effects, though experiments are designed to mitigate this effect. Optically thin media satisfy

$$\int_0^L \kappa_\eta(u)du \ll 1. \tag{2.11}$$

[26] Self-absorption refers to emission and re-absorption by molecules from the same species. It is possible but uncommon for emission produced by intermediate radicals to be attenuated by a broadband absorber outside the reaction zone. Self-absorption is difficult to model as the distribution of a ground state species is not easily detected by emission CST.

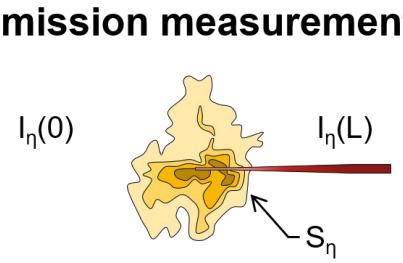

Figure 2.3: Emission measurement along a LOS showing the accumulation of intensity due to the radiative source, S_η. Emission CST reconstructs the spatial distribution of S_η, which reveals combustion structures and may be post-processed to determine physical parameters (e.g., soot volume fraction).

A good heuristic in the CST context is to assume the target is thin when this integral is less than 0.025. Under these conditions, the measurement model is

$$b \equiv I_\eta(L) \approx \int_0^L S_\eta(u)du\,, \tag{2.12}$$

which is the same Fredholm IFK as the equation for absorption CST. In contrast to absorption tomography, Eq. (2.12) does not transform of the detected quantity with a logarithm so broadband emission signals are linear. Parameters of interest in emission CST include the temperature and volume fraction of soot, geometry of a reaction zone, and local heat release rate. The relationship between these properties and the radiative source term depends on the mode of emission.

2.1.3.1 Thermal emission

Random molecular motion due to thermal energy results in a large number of collisions that follow a predictable distribution. Photonic emission is a mechanism for energy conservation and the acceleration and deceleration of charge associated with thermal motion produces thermal emission. Thermal radiation from an ideal emitter (or a blackbody) is given by Planck's law,

$$I_{b,\eta}(T) = \frac{c_1\eta^3}{\exp\{c_2\eta/T\}-1} \approx c_1\eta^3 \exp\left\{-\frac{c_2\eta}{T}\right\}, \tag{2.13}$$

where $c_1 = 2hc^{-2}$ and c_2 are the first and second radiation constants. Equation (2.13) also shows Wien's approximation, which holds at high temperatures. Emission for a non-ideal body is the product of blackbody emission and a spectral emissivity, which equals the spectral absorption coefficient per Section 2.1.1. Measurements of thermal radiation for emission CST are made in the near-IR and visible range at wavenumbers selected to limit interference by chemiluminescence. Therefore, the source term for thermal emission CST is $S_\eta = \kappa_\eta\, I_{b,\eta}$.

Soot temperature and volume fraction are the primary quantities of interest in thermal emission scenarios [197]. Both properties are inferred from S_η by modelling κ_η. The spectral absorption coefficient of soot is approximated by the Rayleigh equation,

$$\kappa_\eta = 6\pi f_v \eta E(m), \tag{2.14}$$

where f_v is the volume fraction, $E = [(m^2 - 1)/(m^2 + 2)]$ is the soot absorption fraction, and $m = n - ik$ is the complex index of refraction.[27] Typically, the refractive index, n, and extinction coefficient, k, are computed with a curve fit (e.g., Huang et al. [197] use fits from Chang and Charalampopoulos [231]). Next, the radiative source is reconstructed at two wavenumbers, η_1 and η_2, which are converted to a temperature by a two-colour method—similar to Eq. (2.8). In this approach, the ratio $S_{\eta 1}/S_{\eta 2}$ is expressed using Wien's approximation and re-arranged to isolate T,

$$T = \frac{c_2(\eta_1 - \eta_2)}{\ln\left[\dfrac{S_{\eta 2}/E_{\eta 2}(m)}{S_{\eta 1}/E_{\eta 1}(m)}\right] - 4\ln\left[\dfrac{\eta_2}{\eta_1}\right]}. \tag{2.15}$$

Finally, the volume fraction is determined by solving Eq. (2.14) for f_v at either measurement wavenumber,

$$f_v = \frac{S_{\eta 1}\exp\{c_2\eta_1/T\}}{6c_1E_{\eta 1}(m)\eta_1^{\,2}} \text{ or } \frac{S_{\eta 2}\exp\{c_2\eta_2/T\}}{6c_1E_{\eta 2}(m)\eta_2^{\,2}}. \tag{2.16}$$

There is considerable uncertainty about the optical properties of soot, particularly at high temperatures, which affects the accuracy of temperature and volume fraction estimates based on Eqs. (2.15) and (2.16) [232]. Moreover, detecting S_η requires κ_η to be large, contradicting the assumption of an optically thin medium.[28] Several studies have introduced modifications to the tomography algorithm to approximate Eq. (2.10), such as Refs. [189,197,223]. Historically, most researchers have not employed a correction procedure, however, and reconstructions based on Eq. (2.12) do not compare favourably to thermocouple data.

[27] Equation (2.14) applies to soot aggregates that are much smaller than the measurement wavelength, which holds true in the near-IR-to-visible range.

[28] That is, if κ_η is small enough to satisfy Eq. (2.11) then the accumulation of intensity from a source where $S_\eta = \kappa_\eta I_{b,\eta}$ is difficult to detect.

2.1.3.2 Chemiluminescence emission

The other source of radiation in emission CST is chemiluminescence, which consists of light produced by the relaxation of reaction intermediates rather than heat. Chemiluminescence requires an exothermic reaction—to supply the energy required to yield excited intermediates—and chemical pathways that produce radicals with limited opportunities for thermal relaxation. Some such molecules quickly emit a photon in order to return to their ground state (chemiluminescence); others may be de-excited by collisional quenching. Emission from the radical, *i*, is governed by a rate equation,

$$I_{\eta,i} = A_i N_i \,. \tag{2.17}$$

where A_i and N_i are the Einstein *A* coefficient and molar density of *i*, respectively [233]. Here, $I_{\eta,i}$ is the photon emission intensity, which has units u/cm^3-s (where u is a mole of photons). Transitions in chemiluminescence involve the same energy states as absorption. As with absorption lines, the emission intensity is distributed about a narrow spectral band, centred on η, which depends on the chemical properties of *i*. The emission energy, $hc\eta$, equals the energy of transition between the radical's ground and excited states. (Combustion radicals typically emit chemiluminescence in the UV/visible range.) Cumulative intensity along a LOS is given by the line integral over $I_{\eta,i}$. Provided the target is optically thin, the radiative source term is $S_\eta = I_{\eta,i}$, where η is tuned to image a particular intermediate.

Chemiluminescence tomography is primarily a combustion diagnostic and considerable attention has focused on characterizing the relationship between select intermediates and flame properties. The most common radicals in hydrocarbon flames are OH^*, CH^*, C_2^*, and CO^*. Emission from these species centres on multiple peaks, the bulk of which lie in between 275 to 525 nm. Several prominent CH^* and C_2^* peaks reside in the visible spectrum and can be imaged by commercial cameras.

Excited combustion radicals exist at low concentrations due to the small volume of the reaction zone and high rate of collisional quenching. The population of an excited species is thus limited by the production rate and quantitative information can, in principle, be extracted from the intensity. However, in practice, unknown distributions of the corresponding ground state

molecules and variable quenching rates render this inference intractable.[29] Nevertheless, the ratio of excited radicals is highly correlated to the local heat release rate, which is an important variable in the study of combustion. The correlation depends on the fuel and mode of combustion. Simulation of common pathways (such as $CH + O_2 \rightarrow CO + OH^*$, $C_2 + OH \rightarrow CO + CH^*$, etc. [234]); 1D flamelet data are used to model this correlation and extract information from the ratio of local chemiluminescence data. Recent progress in chemiluminescence tomography has demonstrated the simultaneous 3D reconstruction of multiple radicals [215], clearing a path for quantitative tomographic imaging of the heat release rate in a turbulent flame.

2.2 Classical Reconstruction Algorithms

Governing equations for absorption and emission CST have the same mathematical form, which they share with the X-ray attenuation equation used in medical imaging. Classical reconstruction algorithms from the computed tomography literature can therefore be applied to both CST modalities. This section presents reconstruction with respect to projections of an arbitrary 2D function, f, which represents either κ_η or S_η.

2.2.1 Analytical algorithms

2.2.1.1 Fourier slice theorem

Analytical expressions for reconstruction exploit the relationship between an unknown distribution in physical space and its projections, which are the measured quantity in tomography. This connection is helpfully illustrated by the Fourier slice theorem—itself closely connected to the Radon transform, discussed in Chapter One. Moreover, the Fourier slice theorem provides the basis for filtered back projection.

The theorem considers a function, f, and its projections. Figure 2.4 depicts a sample function with a set of parallel-beam projections for a fixed view (i.e., variable axial distances, s, at a fixed angle, θ). Measurements of f, denoted b, are line integrals akin to Eqs. (2.5) and (2.12). For convenience, these measurements are represented in terms of an integration over the entire domain,

$$b(s,\theta) = \iint_{\mathbb{R}^2} f(x,y)\delta(x\cos(\theta) + y\sin(\theta) - s)dxdy\,, \tag{2.18}$$

where δ is the Dirac delta function and the coordinates (s, θ) pick out a LOS through f, as illustrated in Figure 2.4. The 1D Fourier transform of a projection is

[29] As an example, while OH^* emits a strong signal, ground state OH is plentiful outside the flame front, resulting in self-absorption and a corrupted signal.

$$B(\omega,\theta)=\int_{\mathbb{R}} b(s,\theta)\exp\{-2\pi i\cdot\omega s\}\,ds\,. \tag{2.19}$$

Next, the definition of a projection is substituted into Eq. (2.19). Note that Eq. (2.19) is only nonzero when s equals $x\cdot\cos(\theta) + y\cdot\sin(\theta)$, which is the distance from the origin at (x, y). As such, s can be replaced with this distance, resulting in an explicit transform of the projections in terms of f,

$$B(\omega,\theta)=\iint_{\mathbb{R}^2} f(x,y)\exp\{-2\pi i\cdot[\omega x\cos(\theta)+\omega y\sin(\theta)]\}\,dxdy\,. \tag{2.20}$$

Equation (2.20) employs a continuous set of projections along s in $(-\infty, \infty)$ at a fixed view angle. Computing B for $\theta \in [0, \pi]$ yields a full transformation of the function. By definition, the 2D Fourier transform of f is

$$F(u,v)=\iint_{\mathbb{R}^2} f(x,y)\exp\{-2\pi i\cdot(ux+vy)\}\,dxdy\,. \tag{2.21}$$

From Eqs. (2.20) and (2.21) it can be seen that the 1D Fourier transform of a projection, B, contains the same information as the 2D Fourier transform of f: $B(\omega, \theta) = F[\omega\cdot\cos(\theta), \omega\cdot\sin(\theta)]$. Equation (2.20) thus implies that projections along a view angle correspond to a line in the Fourier transform of f and the relationship between (u, v) and (ω, θ) indicates a coordinate transform that relates these quantities. The unknown function can thus be recovered from its projections by taking the inverse 2D Fourier transform of the full set of projections. It is worth mentioning that this set of projections amounts to a Radon transform, $\mathscr{R}f$, which is expressed in terms of the (s, θ) coordinate system; moreover, $\mathscr{R}f(s, \theta) = b(s, \theta)$.

Intuitively, the discrete sinogram of a function can be constructed by sampling projections at dense, regular intervals of s and θ. This sinogram can then be transformed back into a spatial

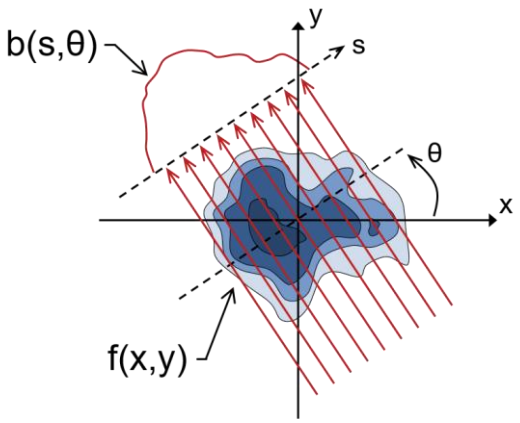

Figure 2.4: 2D schematic of projection measurements for an arbitrary function, f(x,y), which represents κ_η or S_η.

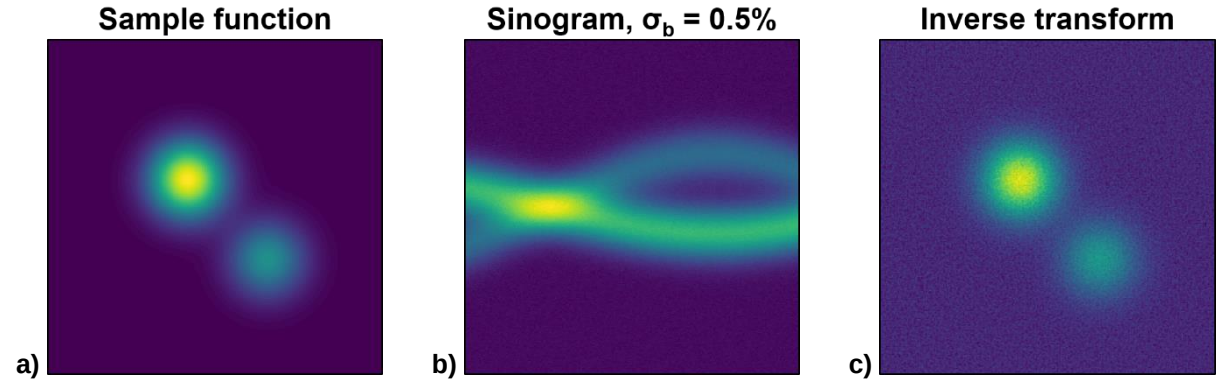

Figure 2.5: Overview of analytic reconstruction: a) a 2D sample function, f(x,y); b) the Radon transform of f in sinogram space (s,θ), with 0.5° spacing between projections and 0.5% Gaussian noise; and c) the inverse Radon transform.

function. Figure 2.5 depicts this progression with a sample distribution; its discrete Radon transform, constructed from noisy projections; and an estimate of *f*, recovered by way of the inverse Radon transform. The procedure illustrates the key insight of tomography: radiative projections can be mathematically manipulated to reveal the internal structure of an object. However, the exact inverse Radon transform requires an infinite set of projections and the inverse transform is corrupted by noise—even minimal noise. Therefore, in practice, analytic algorithms must employ a filtered representation of the sinogram.

2.2.1.2 Filtered back projection

Filtered back projection can be derived from the Fourier slice theorem by applying a coordinate transform and simplifying the inverse operation to account for the symmetry of projections. Cai and Kaminsky [235] present a single expression that includes both the projection model and filtered inversion,

$$f(x,y) = \underbrace{\int_0^{\pi} \underbrace{\int_{\mathbb{R}} \underbrace{\int_{\mathbb{R}} b(s,\theta) \exp\{-2\pi i \cdot \omega s\}\, ds}_{\text{Fourier transform of a projection}} \overbrace{|\omega|}^{\text{Filter}} \exp\{2\pi i \cdot \omega s\}\, d\omega}_{\text{Inverse Fourier transform}}\, d\theta}_{\text{Back projection}}, \tag{2.22}$$

where $|\omega|$ acts a ramp filter in frequency space.[30] Back projection amounts to "smearing" measurements back along the corresponding lines-of-sight. On its own, this procedure reconstructs

[30] The frequency term arises from the transformation of the integral to frequency coordinates: $dudv = \omega d\omega d\theta$. The absolute value function follows from $b(s,\theta+\pi) = b(-s,\theta)$ and $B(\omega,\theta+\pi) = B(-\omega,\theta)$. These relationships permit the integration over θ to be restricted to $[0,\pi]$ given $|\omega|$.

bulk features of an image but is subject to blurring. Blur arises due to the finite nature of the projection data. Low-frequency components of the sinogram are oversampled relative to high-frequency components, themselves overwhelmed by noise, which further contributes to blur. Hence, filter functions are used to regularize the data in sinogram space.

In practice, the number of measurement angles are limited and individual lines-of-sight have finite width. Integrals over sinogram space are thus replaced by summation over the projections. Shepp and Logan [77] proposed an analytical solution,

$$f(x,y) = \frac{a}{2JK}\sum_{j=1}^{J}\sum_{k=1}^{K} b(s_k,\theta_j)\phi(x\cos(\theta_j) + y\sin(\theta_j) - s_k), \tag{2.23}$$

where J is the number of measurement angles, K is the number of projections for a given view, a is the axial spacing between projections, and the function ϕ weights the contribution of data from each beam at (x, y).[31] Equation (2.23) requires a dense set of projections to adequately sample the sinogram space and estimates remain sensitive to measurement noise, regardless—as can be seen in Figure 2.5. Various filters have been developed to overcome these limitations. However, it is difficult to establish a filter's effect on the spatial characteristics of reconstructions and the analytical approach does not generalize to arbitrary measurement setups. These factors motivate algebraic techniques.

2.2.2 Algebraic methods

2.2.2.1 Discretization

Algebraic reconstruction requires a finite representation of the unknown quantity to enable computational solutions. The CST equations are linear so the set of integral equations for a system of optical paths can be approximated by matrix-vector multiplication. Basis functions are selected to represent the gas and support the measurement operator. The most common CST bases are square pixels and cubic voxels in 2D and 3D domains, respectively. By assumption, pixels and voxels contain a uniform concentration of the unknown distribution. Numerous alternative schemes have been proposed and the ideal grid resolution and mode of interpolation depends on the measurement array and application. Chapter Four discusses high-order interpolation in CST and introduces a technique for basis selection.

[31] Several ϕ functions have been proposed and similar expressions to Eq. (2.23) have been derived for fan- and cone-beam arrangements. See Herman [78] for an overview of analytical algorithms for computed tomography.

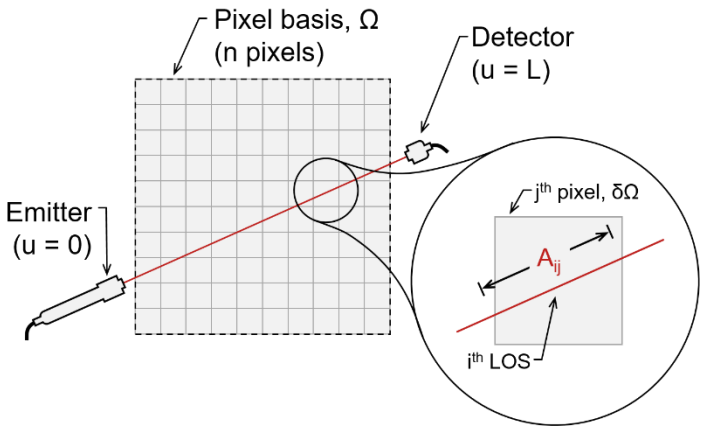

Figure 2.6: Discrete absorption CST domain, Ω, with pixelated elements, δΩ, and the LOS between an emitter and detector.

Figure 2.6 shows a pixelated 2D CST domain along with an emitter-detector pair. The domain, Ω, is defined as a separable Hilbert space and the unknown distribution, x, is a Ω-valued vector that represents κ_η or S_η.[32] By construction, pixels are orthonormal and span Ω. The resulting basis, $\Phi^{(n)}$, consists of n basis functions, ϕ_j. In a pixel-wise basis, ϕ_j equals 1 inside the jth pixel and 0 elsewhere. The continuous distribution, x, is approximated by a low-dimensional representation,

$$x \approx \sum_{j=1}^{n} \alpha_i \phi_i \,, \tag{2.24}$$

where α_j is a coefficient that gives the value of x in the jth pixel.[33] Distributions are described by the vector $\mathbf{x} \in \mathbb{R}^n$, where $\mathbf{x} = \{\alpha_j\}$. Projection of x onto an n-dimensional subspace, $\Phi^{(n)}$, is given by the coefficients $\alpha_j = \langle x, \phi_j \rangle$, where $\langle \cdot, \cdot \rangle$ is the inner product operator.

Equations (2.5) and (2.12) are linear IFKs and therefore compatible with the summation in Eq. (2.24). CST measurements for the discrete distribution, $\mathbf{x}$, are approximated by summing the path integrals along a LOS for each basis function, called a *ray-sum*,

$$b_i \approx \sum_{j=1}^{n} \alpha_j \int_0^L \phi_j \left[\mathbf{r}_j(u) \right] du \,, \tag{2.25}$$

where u is a position along the ith LOS from 0 to L and $\mathbf{r}_i$ is an indicator function that relates the location u along the ith path to a position in the element ϕ_j. The vector $\mathbf{b} \in \mathbb{R}^m$, where $\mathbf{b} = \{b_i\}$,

[32] This definition enables rigorous classification of alternative bases, which is useful when comparing discretization schemes, as in Chapter Four.

[33] Pixels and other finite element schemes employ basis functions with compact support such that the coefficients have a straightforward physical interpretation (i.e., α_j gives the value of x at some location). However, this is not always the case, as in radial basis functions and sample-based eigenfunctions.

gives the set of projections that correspond to the *m* optical paths in a CST system. For pixels and voxels that contain a uniform concentration of *x*, the path integral in Eq. (2.25) equals the chord length of the *i*th LOS through the *j*th pixel: A_{ij}, as shown in Figure 2.6.[34]

Line integrals over the basis functions are carried out for each optical path to construct a discrete measurement operator,

$$A_{ij} = \int_0^L \phi_j \left[\mathbf{r}_i(u)\right] du \,. \tag{2.26}$$

Computing Eq. (2.26) for each of the functions for each LOS yields the *ray-sum matrix*, $\mathbf{A} \in \mathbb{R}^{m \times n}$. The result is a linear system, $\mathbf{Ax} = \mathbf{b}$, and algebraic reconstruction consists in the inference of a gas state, defined by the vector $\mathbf{x}$ and basis Φ, subject to an observation, $\mathbf{b}$.

2.2.2.2 Algebraic reconstruction technique

Algebraic reconstruction refers to a class of algorithms that reconstruct a function in discrete form from its sinogram, $\mathbf{b}$. The basic formula proceeds from an initial guess, $\mathbf{x}^{(0)}$ (often a zeros vector), which is iteratively updated,

$$\mathbf{x}^{(k+1)} = \mathbf{x}^{(k)} + \lambda \frac{b_i - \mathbf{a}_i^T \mathbf{x}^{(k)}}{\mathbf{a}_i^T \mathbf{a}_i} \mathbf{a}_i \,, \tag{2.27}$$

where k is the current iteration, λ is a relaxation parameter, b_i is the ith projection, and $\mathbf{a}_i$ is the ith row of $\mathbf{A}$, arranged as a column vector. Each iteration of Eq. (2.27) propagates the ith residual back along the corresponding LOS, similar to filtered back projection. Therefore, only pixels transected by a beam will change from the initial guess. This simple form of the ART is not ideal for applications where the number of pixels exceeds the number of projections.

The ART converges to the minimum norm least squares solution, $\mathbf{x}^{\mathrm{LS}} = \mathbf{A}^{\#}\mathbf{b}$, where $\mathbf{A}^{\#} = (\mathbf{A}^T\mathbf{A})^{-1}\mathbf{A}^T$ is the pseudoinverse of $\mathbf{A}$. However, for dense arrays with an overdetermined ray-sum matrix, the least squares solution is subject to noise-related artifacts, similar to back projection algorithms. Early iterations contribute low-frequency components to $\mathbf{x}$. Spatial frequencies in updates, $\mathbf{x}^{(k+1)} - \mathbf{x}^{(k)}$, progressively increase as the measurement residual approaches zero. This progression results in a phenomenon called semi-convergence. Elfving et al. [236] analytically demonstrated that high-frequency contributions from later iterations are more noise-affected than

[34] The cross section of a beam in the probe volume may be non-trivial, depending on the modality. In such a case, the integral yields the fraction of a pixel's area or voxel's volume that is transected by a beam.

contributions from early steps. Moreover, since early iterations of $\mathbf{x}^{(k)}$ are smooth they are likely to exhibit spatial features that are typical of gasses. Practitioners halt Eq. (2.27) prior to convergence to improve the accuracy of a reconstruction. However, it is difficult to establish the optimal stopping criteria without prior knowledge that is specific to experimental conditions (e.g., the number and arrangement of beams, spatial frequencies expected of **x**, etc.).

Two modifications of the ART bear mentioning. First, iterations of the simultaneous ART (SART) update $\mathbf{x}^{(k)}$ with information from all of the residuals, at once, with an emphasis on corrections to the centre of the domain [237]. This approach enables fast ART-type convergence without explicit computation of the inverse operator. It is advantageous to avoid calculation of $\mathbf{A}^{\#}$ in cases where the dimension of the problem is very large, as in the 3D systems in Chapter Six. For such arrangements, the convergence time of Eq. (2.27) is prohibitively long and neither $\mathbf{A}^{\#}$ nor its factorizations can be stored in memory, which prevents LU- and QR-type solutions to the matrix system. Second, the multiplicative ART was devised to maximize the information entropy of reconstructions. Smooth distributions have greater information entropy than discontinuous distributions and, as a result, the MART promotes realistic physical features in CST images.[35] By introducing an assumption about the relationship between elements of **x**, MART serves as a precursor to the Bayesian method introduced at the end of this chapter.

2.2.2.3 Limited-data and full-rank tomography as ill-posed inverse problems

It has been mentioned several times that tomographic reconstruction is an ill-posed inverse problem. The concept of an ill-posed problem is implicit in the definition of a well-posed problem, commonly understood in terms of the criteria set out by Jacques Hadamard in 1902 [238]. According to Hadamard, a problem is well-posed if it meets the following conditions:

1. *Existence*: a solution must exist;
2. *Uniqueness*: the solution must be unique; and
3. *Stability*: the solution must change continuously with changes to the initial conditions.[36]

Tomographic reconstruction necessarily violates the last two criteria in one way or another, which is why additional measures must be taken to ensure the accuracy of reconstructions. Chapter One

[35] There is a noteworthy connection, here, between the information and thermodynamic entropy of a distribution. This relationship can be seen in the formal definitions of both forms of entropy, which are both proportional to the expectation of $\log(p_i)$, where p_i is the probability of the ith state.

[36] That is, small changes in the data should not yield disproportionately-large changes in the solution.

introduced the categories of limited-data and full-rank CST, which are ill-posed for distinct reasons.

Limited-data CST features fewer projections than basis functions, typically having $m < 100$ measurements because of optical access restrictions, high equipment costs, or both. At the same time, instantaneous estimates of κ_η or S_η in an unsteady flow require a large number of basis functions to properly represent the gas dynamics. When the number of basis functions is small—for instance, a 10×10 pixel basis, $\Phi^{(100)}$—features of the flow are poorly-resolved in the projection of x onto Φ, called $\mathbf{x}^{\text{exact}}$, which is the best-case reconstruction using Φ. Moreover, for a pixel- or voxel-wise basis, such as $\Phi^{(100)}$, the assumption of a uniform concentration of gas within the pixels breaks down and $\mathbf{x}^{\text{LS}}$ is unlikely to resemble $\mathbf{x}^{\text{exact}}$. However, given a large number of pixels, adequate to capture the flow field dynamics but exceeding the number of measurements, $\mathbf{A}$ must be underdetermined. Formally, $\text{rank}(\mathbf{A}) \leq m < n$. Rank-deficiency means that $\mathbf{A}$ has a non-trivial null space and an infinite set of candidate vectors, $\{\mathbf{x}\}$, can fully explain any data vector, $\mathbf{b}$. Limited-data CST thus violates *uniqueness*, Hadamard's second criterion.

Full-rank CST, as its name implies, features a dense measurement array, arranged in such a way that $\text{rank}(\mathbf{A}) = n$. Since the system is full-rank, there is a unique least squares solution and the inference of $\mathbf{x}$ for $\mathbf{A}$ and $\mathbf{b}$ will satisfy Hadamard's *existence* and *uniqueness* criteria. However, full-rank CST operators must be overdetermined due to the geometry of ray-sums (i.e., many nearly-collinear rays are required to get independent information about interior basis functions). Moreover, projections are subject to noise and thus imply incompatible information about the domain. The measurement IFKs damp frequencies in x and therefore amplify frequencies when inverted, resulting in large artifacts.

To illustrate this damping effect, consider the definition of an IFK,

$$b(s) = \int_{t_0}^{t_n} K(s,t)\, f(t)\, dt\,, \tag{2.28}$$

where b is the data, K is a kernel that incorporates the measurement physics, and f is the unknown function [239]. (In CST, $K = 1$.) Next, consider the function $f_p(t) = \sin(2\pi p t)$, where $p = 1, 2, \ldots$ Irrespective of the kernel, the Riemann-Lebesgue lemma demonstrates that

$$b_p(s) = \int_{t_0}^{t_n} K(s,t)\, f_p(t)\, dt \to 0 \text{ as } p \to \infty\,. \tag{2.29}$$

That is, the map from *f* to *b* diminishes high-frequency components such that *b* is smoother than *f* [239]. Accordingly, the inverse map from *b* to *f* necessarily amplifies frequencies in *b*; frequency amplification for the near-collinear ray-sums implies that **A** has a very large condition number. Measurements are always noise-laden and discretization implies a model error, which has a similar effect to noise. Simple least squares inversion is therefore subject to non-physical artifacts that arise from small perturbations in **b**. In this way, full-rank CST necessarily violates *stability*, Hadamard's third criterion.

Both limited-data and full-rank CST fall short of the criteria for of a well-posed problem. Conceptually, ill-posed inverse problems lack sufficient information to obtain a unique, stable solution. Either there are too few measurements or noise eradicates necessary components of the signal. In this light, regularization amounts to the inclusion of additional information about a problem, implicitly or explicitly, to improve the accuracy of solutions. The challenge of reconstruction in CST can be described as an information deficit that must be supplemented by prior assumptions.

2.3 Bayesian Framework for Tomographic Imaging

Statistical inversion is an approach to inverse problems in which prior information about an observed system is brought to bear on estimates of the system parameters using Bayesian statistics. Inverse problems are formulated in epistemic terms: information is extracted from measurements to update one's existing knowledge of the system parameters [240]. In this framework, all quantities—inferred parameters, measurements, physical constants, and so on—are conceived as random variables with an associated pdf. Randomness represents both variation that is inherent to the physical system, such as the probabilistic emission of a photon or turbulent fluctuations in a fluid, and epistemic uncertainty: about the system state, the mathematical form of physical models, fundamental parameters, and the like. This approach is well-suited to ill-posed inverse problems because the information used to regularize an inversion is given explicit representation. Researchers can directly interrogate the assumptions used to generate a reconstruction in Bayesian CST and quantify the uncertainty of an estimate. Moreover, the Bayesian framework itself suggests possibilities for regularizing and optimizing experiments, demonstrated in later chapters of this work.

This section introduces the concept of Bayesian updating, in which prior assumptions about a flow field are brought into line with measurement information. Updating requires likelihood and

prior pdfs to calculate a posterior distribution and likelihood and prior pdfs for CST are described, below. Finally, the posterior pdf is sampled to come up with a representation of the target distribution, akin to classical reconstruction. The chapter ends with a brief discussion of Bayesian reconstruction for gas-phase tomography.

2.3.1 Bayesian updating

Probability density functions characterize the behaviour of a continuous random variable. The function, $\pi(y)$, returns the relative likelihood that a random process, Y, will result in a specific outcome, y.[37] Pdfs have inverse units to y and integration of $\pi(y)$ over a subset of Y's possible outcomes, e.g., $[y_1, y_2]$, gives the probability that $y \in [y_1, y_2]$. Integration over all possible realizations of Y must equal unity, called the *law of total probability*. In Bayesian statistics, knowledge about a random process (such as the distribution of a gas in CST) is quantified with a prior pdf, $\pi_{\text{pr}}(\mathbf{x})$. The prior describes the relative likelihood of candidate vectors, $\mathbf{x}$, based on a priori information about the gas, which can include previous measurements. For instance, $\pi_{\text{pr}}(\mathbf{x})$ may assign a greater value to smooth distributions or promote discontinuities, predetermined spectral features, etc. In principle, the prior should account for all relevant knowledge about the system parameters.

Following an observation, $\mathbf{b}$, information about $\mathbf{x}$ is updated according to Bayes' equation,

$$\pi(\mathbf{x}\,|\,\mathbf{b}) = \frac{\pi(\mathbf{b}\,|\,\mathbf{x})\pi_{\text{pr}}(\mathbf{x})}{\pi(\mathbf{b})} \propto \pi(\mathbf{b}\,|\,\mathbf{x})\pi_{\text{pr}}(\mathbf{x}), \tag{2.30}$$

where $\pi(\mathbf{x}|\mathbf{b})$, $\pi(\mathbf{b}|\mathbf{x})$, and $\pi(\mathbf{b})$ are the posterior, likelihood and evidence functions. The likelihood pdf encodes the measurement model: i.e., $\pi(\mathbf{b}|\mathbf{x})$ returns the chance of observing $\mathbf{b}$ when the system state equals $\mathbf{x}$, reflecting the uncertainty about $\mathbf{b}$ due to noise and accuracy of the measurement model. Since $\mathbf{b}$ has already been observed, $\pi(\mathbf{b})$ is a constant scalar that normalizes the numerator to conserve total probability,

$$\pi(\mathbf{b}) = \int_{\mathbf{x}} \pi(\mathbf{b}\,|\,\mathbf{x})\pi_{\text{pr}}(\mathbf{x})d\mathbf{x}\,. \tag{2.31}$$

The posterior, $\pi(\mathbf{x}|\mathbf{b})$, gives the probability density for a set of parameters, $\mathbf{x}$, given the measurement data, $\mathbf{b}$, subject to prior information about the gas.

[37] This relative likelihood may be called a probability density or density or, in less formal terms, a chance or likelihood (both of which are also understood in a relative sense).

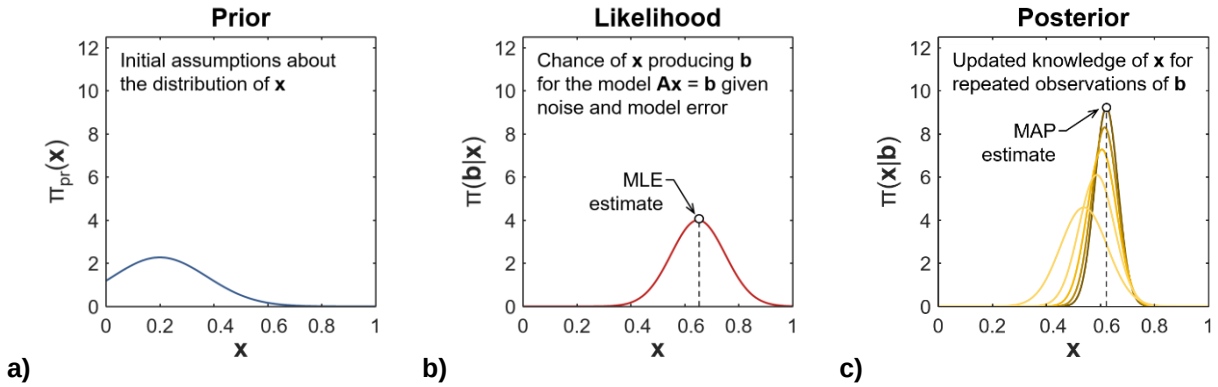

Figure 2.7: Sample 1D Bayesian update: a) prior information about x; b) probability of observing b for different values of x, maximized by the maximum likelihood estimate (MLE); and c) successive posterior distributions for five observations of b, along with the MAP estimate.

Equation (2.30) updates information in the prior based on measurement data, illustrated in Figure 2.7 for a 1D system. The update is properly-weighted to account for variance in the measurement process and one's confidence in the prior information. Posterior probabilities describes the information one has about a system following an observation; $\pi(\mathbf{x}|\mathbf{b})$ is considered a comprehensive solution to the inverse problem in itself. However, in high-dimensional problems—such as tomographic imaging—it is difficult to represent the posterior in a comprehensible manner. Point estimates of $\mathbf{x}$ are used to visualize $\pi(\mathbf{x}|\mathbf{b})$, such as the MAP estimate shown in Figure 2.7.

2.3.2 Likelihood functions

The likelihood pdf specifies the chance of observing the data based on a presumed system state by way of the measurement model. Measurements are subject to noise and model error, both of which affect parameter estimates. Noise refers to random signal perturbations caused by physical processes in the system, itself, and measurement electronics. Model error arises from the discretization scheme and simplifications applied to the governing equations. These phenomena are grouped together in an overall error term, $\mathbf{e} \in \mathbb{R}^m$, where $\mathbf{e} = \mathbf{e}^{\text{noise}} + \mathbf{e}^{\text{model}}$. Due to the cumulative effects of error, there is some chance that a range of system states, $\{\mathbf{x}\}$, will yield the observation $\mathbf{b}$, quantified by $\pi(\mathbf{b}|\mathbf{x})$. Key factors that contribute to $\mathbf{e}^{\text{noise}}$ and $\mathbf{e}^{\text{model}}$ are enumerated below to motivate an explicit form for the likelihood pdf.

Gas-phase tomography features noise from three types of physical variation. Fluctuations in the light source in absorption CST; shot noise, produced by quantization of the source medium,

detector mechanism, and gas; and thermal motion in the circuitry of amplifiers.[38] Variation in the optical power of a laser, called relative intensity noise, can arise due to cavity vibrations and quantization effects in the gain medium. Relative intensity noise occurs in state-of-the-art TDLs, regardless of variation in the injection current, though current controllers can contribute to the effect. The power spectrum of this source exhibits $1/f$ behaviour; and, while relative intensity noise is best modelled as a pink source, normally-distributed (white) noise serves as a conservative baseline [241].

Shot noise is a consequence of the discrete nature of electric charge and photonic interactions with the light source, photodetectors, and gas. Emission and absorption are inherently probabilistic and natural variation in the number events over a measurement interval affects the number of photons incident on a detector. Moreover, the quantized nature of absorption, emission, and detection resembles a discrete counting process. Processes of this sort follow a Poisson distribution, the limit of which is a Gaussian distribution with a mean and variance equal to the rate constant (in this case, the number of detected photons).[39] Shot noise can have a similar effect to relative intensity noise at very high frequencies (~1 MHz). However, shot noise exhibits a current density orders of magnitude below that of relative intensity noise at lower frequencies (< 1 kHz) [241].

Thermal noise, also called Johnson-Nyquist noise, arises due to the disruption of electrons in a system's circuitry by random thermal motion in the wires. At any given instant, these disruptions add up to a net charge with a magnitude proportional to the wire's temperature (effectively independent of the signal). The power spectrum of thermal noise is relatively constant—approximating white noise—but eventually decays to zero. However, the decay occurs at a frequency far higher than those resolved in CST measurements, with an onset around 50 GHz. Johnson-Nyquist noise is close in form to an independent and identically distributed (IID) normal random variable [242]. The influence of thermal noise is typically less than that of shot noise though similar in magnitude [241].

Finally, model error comes from: i) differences between the measurement model and physical process of measurement; and ii) the projection of x onto a finite subspace. Certain aspects of (i)

[38] Electromagnetic interference is another form of noise that is marginal in the context of gas-phase tomography due to the frequencies of interest and typical data acquisition electronics.

[39] Incident photons are distributed as a Poisson random variable, scaled by the detector's quantum efficiency.

are knowable, in principle—e.g., error due to simplification of the RTE into the Beer-Lambert law. However, scientific models are coarse-grained descriptions of reality and some measure of residual uncertainty will inherent limit any inference. More practically, (ii) is the dominant source of model error in CST and can be quantified using an approximation errors approach. Approximation errors are discussed in Chapter Four; for the purposes of this section, it is sufficient to note that one can numerically assess their magnitude and distribution.

Aggregate error in hard-field tomography is treated as an additive process [240],[40] which corresponds to the model $\mathbf{b}^{\text{mod}} = \mathbf{Ax} + \mathbf{e}$. Subject to the hypothesis that the system state is $\mathbf{x}$, $\mathbf{b}^{\text{mod}} = \mathbf{b}^{\text{meas}}$ and

$$\mathbf{e} = \mathbf{b}^{\text{meas}} - \mathbf{A}\mathbf{x}^{\text{exact}}. \tag{2.32}$$

The Bayesian paradigm treats error as a random variable and assumptions about the distribution of noise and model error are used to construct an explicit likelihood pdf. The form of this pdf is typically joint-normal. Gaussian distributions are ubiquitous in statistical inference, both because they are easy to manipulate and as a consequence of the central limit theorem.[41] The corresponding likelihood pdf is

$$\pi(\mathbf{b} \mid \mathbf{x}) = \det(2\pi\boldsymbol{\Gamma}_{\mathbf{e}})^{-1/2} \exp\left\{-\frac{1}{2}\left\|\mathbf{Ax}-\mathbf{b}\right\|_{\mathbf{L}_{\mathbf{e}}}^{2}\right\}. \tag{2.33}$$

where $\boldsymbol{\Gamma}_{\mathbf{e}}$ is the covariance of error vector; $\mathbf{L}_{\mathbf{e}} = \text{chol}(\boldsymbol{\Gamma}_{\mathbf{e}}^{-1})$, where chol(·) returns the Cholesky factor; and det(·) is the determinant operator.

Error is often assumed to be IID with model error as the leading source of uncertainty, in which case $\boldsymbol{\Gamma}_{\mathbf{e}} = \sigma^2\mathbf{I}$, where σ is the standard deviation of error. (For an IID model of $\mathbf{e}$, absent an estimate of $\text{var}(\mathbf{e}^{\text{model}})$, σ can be selected such that variation in $\mathbf{e}$ overwhelms correlations observed in the noise.) However, Eq. (2.33) can accommodate other forms of noise and model error, approximating non-Gaussian noise with the addition of a mean error, $\bar{\mathbf{e}}$, and complex covariance structure. This flexibility, in conjunction with the fact that uncertainty about $\mathbf{x}$ dominates overall uncertainty, justifies the use of Eq. (2.33) for the tomography likelihood.

[40] Other treatments are possible but uncommon. These include multiplicative error, $\mathbf{b}^{\text{mod}} = \mathbf{AxE}$, where $\mathbf{E}$ is a diagonal matrix with the vector $\mathbf{e}$ along the diagonal, and an arbitrary error function, in which $\mathbf{e} = \mathbf{b}^{\text{meas}} - f(\mathbf{x},\mathbf{e})$ [240].

[41] The central limit theorem states that the mean of a population drawn from an arbitrary distribution with a finite variance will be normally distributed.

2.3.2.1 Prior functions

Constructing a prior is the most critical step in Bayesian CST, and often the most challenging. The prior contains explicit assumptions about variation in the gas; developing a formal model of the system that conforms to the definition of a pdf disciplines inverse analysis. But knowledge about an experiment is frequently qualitative in nature, and it can be difficult to systematically synthesize a priori information. Fortunately, considerable effort has been devoted to developing Bayesian functionals for prior pdfs in gas-phase tomography. Practitioners can thus begin their analysis with an established prior, making modifications as additional information accumulates.

Turbulent behaviour is a focus of much CST research. Flow and combustion variables in flame fronts, free-shear jets, internal pipe flows, and the like exhibit stable mean distributions. However, high-intensity flow fields feature instantaneous distributions, subject to random instabilities, and turbulent fluctuations are properties of interest in fundamental turbulence modelling and combustion simulation. Turbulent variables are commonly considered as a random process [2]. Ideally, given perfect knowledge of the flow conditions, the prior would conform to the distribution of these fluctuations. Motivated by this observation, gas processes are modelled as a joint-normal variable, which can be made to closely resemble the behaviour of turbulent flows. Chapter Three discusses the validity of this approximation at length.

By assumption, $\mathbf{x} \sim \mathcal{N}(\boldsymbol{\mu}, \boldsymbol{\Gamma}_\mathbf{x})$, where $\boldsymbol{\mu}$ and $\boldsymbol{\Gamma}_\mathbf{x}$ are the mean and spatial covariance of $\mathbf{x}$, respectively. Knowledge of $\mathbf{x}$ is necessarily incomplete so one must rely on estimates of $\boldsymbol{\mu}$ and $\boldsymbol{\Gamma}_\mathbf{x}$. Uncertainties in $\boldsymbol{\Gamma}_\mathbf{x}$ are amplified to account for epistemic uncertainty. The joint-normal treatment of $\mathbf{x}$ results in a standard form for the prior pdf,

$$\pi_{\text{pr}}(\mathbf{x}) = \det(2\pi\boldsymbol{\Gamma}_\mathbf{x})^{-1/2} \exp\left\{-\frac{1}{2}\|\mathbf{x}-\boldsymbol{\mu}\|_{\mathbf{L}_\mathbf{x}}^2\right\}, \tag{2.34}$$

where $\mathbf{L}_\mathbf{x} = \text{chol}(\boldsymbol{\Gamma}_\mathbf{x}^{-1})$, as with $\mathbf{L}_\mathbf{e}$. Absent specific information about the flow field, $\boldsymbol{\mu}$ is initialized with a zeros vector.

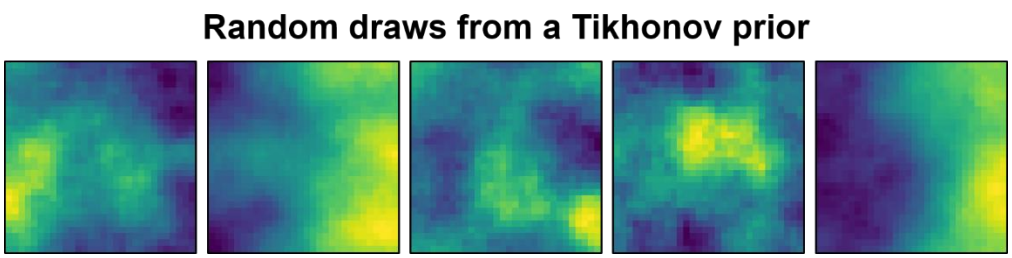

Figure 2.8: Random draws from a Tikhonov prior (λ = 10) on a 30×30 square-pixel grid.

The distribution of variance should also conform to information about the gas. Spatial smoothness is a common starting point when the structure of $\mathbf{\Gamma_x}$ is unknown. Daun [88] proposed a smoothness prior for CST with a covariance structure based on the first-order Tikhonov matrix. In this approach, the Cholesky factorization of $\mathbf{\Gamma_x}$ is directly constructed. For a pixel basis, the element-wise definition of $\mathbf{L_x}$ is

$$L_{ij} = \sigma_x^{-1} \begin{cases} 1, & i = j \\ -n_i^{-1}, & d_{ij} = 1 \\ 0, & \text{otherwise} \end{cases}, \tag{2.35}$$

where n_i is the number of pixels bordering the ith pixel, d_{ij} is the pixel-wise distance from i to j, and σ_x is the presumed average standard deviation of the flow. $\mathbf{L_x}$ is symmetric so $\mathbf{\Gamma_x} = \mathbf{L_x}^{-2}$, and Figure 2.8 gives a qualitative sense of the spatial information of a Tikhonov prior with five random draws on a 30×30 grid with λ = 10. As with the $\boldsymbol{\mu}$, more sophisticated covariance data can incorporated into the prior as it becomes available.

2.3.3 Visualizing the posterior pdf: Bayesian reconstruction

It was noted above that the posterior pdf is considered the solution to an inverse problem in statistical inversion. This section includes brief notes on the representation, calculation, and interpretation of the posterior, along with a sample reconstruction.

Joint-normal likelihood and prior pdfs are desirable—provided they can adequately characterize the measurement error and variation in a system—because they result in a tractable expression for the posterior. Equations (2.33) and (2.34) are joint-normal pdfs, the product of which is also joint-normal, and there is an explicit formula for $\pi(\mathbf{x}|\mathbf{b})$ as a result. Substituting $\pi(\mathbf{b}|\mathbf{x})\cdot$and $\pi_{\text{pr}}(\mathbf{x})$ into Eq. (2.30) gives an expression that is proportional to the posterior pdf,

$$\pi(\mathbf{b}\,|\,\mathbf{x})\pi_{\text{pr}}(\mathbf{x}) = \det(2\pi\mathbf{\Gamma_e})^{-1/2}\det(2\pi\mathbf{\Gamma_x})^{-1/2}\exp\left\{-\frac{1}{2}\|\mathbf{b}-\mathbf{A}\mathbf{x}\|_{\mathbf{L_e}}^2 - \frac{1}{2}\|\mathbf{x}-\boldsymbol{\mu}\|_{\mathbf{L_x}}^2\right\}. \tag{2.36}$$

It is not always possible to derive such a formula in Bayesian inference. (In fact, analytical expressions for the posterior are uncommon in large-scale inverse problems.) For instance, hierarchical Bayesian estimation infers prior parameters (such as σ_x) along with $\mathbf{x}$, simultaneously. As a result, the *form* of $\pi(\mathbf{x}|\mathbf{b})$ depends on the data and is not known, a priori. Sampling methods are therefore required to populate a discrete representation of the probability space. (These methods include Markov chain Monte Carlo sampling with a Metropolis Hastings kernel, Gibbs

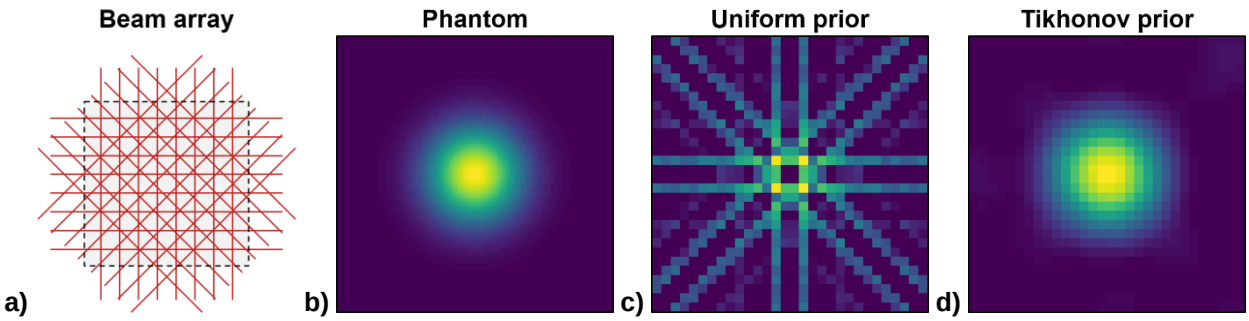

Figure 2.9: Sample estimates based on measurements from a limited-data array (m = 32) using a 30×30 pixel grid. Reconstructions were computed with an IID prior and Tikhonov prior (λ = 10).

sampling, etc.) Discrete representation of the posterior, like analytical expressions, are difficult to interpret.

Point estimates of the posterior pdf are routinely employed to represent the posterior pdf. Bimodal posterior distributions are uncommon in Bayesian CST and mean measures of the posterior over-smooth features of interest (especially in the limited-data context due to the flexibility of the likelihood function). This dissertation employs the MAP estimate, $\mathbf{x}^{\text{MAP}}$, to visualize the posterior. The MAP estimate is the value of $\mathbf{x}$ that maximizes $\pi(\mathbf{x}|\mathbf{b})$ and is the most common point-estimate in Bayesian CST. For a joint-normal likelihood and prior, the MAP estimate also maximizes Eq. (2.36),

$$\pi(\mathbf{x}\,|\,\mathbf{b}) \propto \exp\left\{-\frac{1}{2}\left\|\begin{bmatrix}\mathbf{L}_e\mathbf{A}\\ \mathbf{L}_x\end{bmatrix}\mathbf{x}-\begin{bmatrix}\mathbf{L}_e\mathbf{b}\\ \mathbf{L}_x\boldsymbol{\mu}\end{bmatrix}\right\|_2^2\right\}. \tag{2.37}$$

The Euclidean norm in Eq. (2.37) is non-negative and contains all instances of $\mathbf{x}$ in the expression for the posterior, minimizing the argument of the norm will maximize $\pi(\mathbf{x}|\mathbf{b})$. Therefore, the MAP is found by least squares minimization of an augmented linear system,

$$\mathbf{x}^{\text{MAP}} = \left(\begin{bmatrix}\mathbf{L}_e\mathbf{A}\\ \mathbf{L}_x\end{bmatrix}^T\begin{bmatrix}\mathbf{L}_e\mathbf{A}\\ \mathbf{L}_x\end{bmatrix}\right)^{-1}\begin{bmatrix}\mathbf{L}_e\mathbf{A}\\ \mathbf{L}_x\end{bmatrix}^T\begin{bmatrix}\mathbf{L}_e\mathbf{b}\\ \mathbf{L}_x\boldsymbol{\mu}\end{bmatrix}. \tag{2.38}$$

Equation (2.38) is the Bayesian form of reconstruction for CST with joint-normal likelihood and prior pdfs.

Figure 2.9 shows a set of sample reconstructions, computed with Eq. (2.38) for a limited-data array using an independent uniform prior and Tikhonov smoothness prior. The uniform prior contains no information about the mean of $\mathbf{x}$ or correlation between the pixels. As a result, only pixels that are transected by a beam are updated (as with the simple ART). By contrast, the

Tikhonov prior promotes smooth distributions, as can be seen in the random draws in Figure 2.8. Clearly, bringing the prior into line with expectations about the flow field increases the accuracy of reconstructions.

Following reconstruction, the posterior covariance matrix can be computed to determine credibility intervals for **x** (see Chapters Four and Five). It is worth emphasising that this procedure does not imply that the true mean of **x** will fall in the 95% confidence interval 95% of the time, however. The posterior represents an epistemic position, based on strong modelling assumptions. Confidence intervals reflect one's state of knowledge about the flow field but do not guarantee the accuracy of the inference. As such, some caution against over-interpreting $\pi(\mathbf{x}|\mathbf{b})$ is warranted. Nevertheless, the Bayesian approach to CST is a powerful lens. The remainder of this thesis illustrates how a statistical frame of mind, based on the techniques introduced in this chapter, can suggest modes of regularizing and designing experiments that improve on state-of-the-art classical techniques.

Chapter Three
Covariance Estimation for Tomography of a Turbulent Flow

Turbulent behaviour is a common feature of fluid flows in natural and engineering environments. Dispersion models of turbulent plumes are used to monitor emissions and detailed simulations of turbulent combustion enable the design of efficient IC engines. A large number of CST experiments require instantaneous images of turbulent flows to inform models and simulations. Turbulence is marked by chaotic motion that spans a range of length and time scales: vortices roll up into large coherent eddies that dissipate energy down to smaller and smaller scales until ultimately depleted by viscous forces. The study of turbulence is largely probabilistic in nature because statistical properties of the flow field remain steady and predictable in spite of erratic fluctuations, which are difficult to forecast. Statistical regularities of turbulent phenomena can be exploited to improve tomography of an unsteady flow. This chapter illustrates the synergy between probabilistic descriptions of turbulence and Bayesian imaging in two ways. First, it is shown how moments of the pdfs in a self-preserving flow are related, which informs CST imaging of a free-shear jet. Second, the quasi-joint-normal distribution of fluctuations is established, a fact that is subsequently used to estimate the variance of a complex process.

The concept of self-similarity in free-shear flow is a major finding of research on fluid dynamics with direct implications for CST. Self-similarity applies to the pdf of dynamic variables in fully-developed jets and plumes, suggesting a connection between the mean of a target (which is relatively easy to reconstruct) and higher moments of the pdf. In particular, the variance of a quantity can be inferred from the mean distribution and subsequently incorporated into the prior to improve the accuracy of future estimates. This chapter begins with a review of the theoretical

framework for self-similarity along with experimental evidence from the fluid mechanics literature. Later in the chapter, a procedure is developed to leverage self-similarity in the pdf of a passive scalar for Bayesian CST. First, it is noted that the combined effects of advection and diffusion imply a smooth average flow field; this observation is used to compute a robust estimate of the mean from time-averaged LOS data. Next, mean concentration data are mapped to the variance of scalar fluctuations. The distribution of variance is used to build a covariance matrix for the prior. Finally, instantaneous estimates of the gas parameters are computed with this prior.

More generally, following on the discussion of Chapter Two, it is argued that the distribution of fluctuations projected onto a CST basis will be roughly joint-normal. This form is especially advantageous given the joint-normal likelihood pdf. Gaussian distributions are self-conjugate and the combination of a joint-normal likelihood and prior yields a joint-normal posterior pdf. Computation of the MAP estimate is linear as a consequence of this shared form, resulting in an analytic expression for the posterior covariance. The linear formulation of CST is essential to full-rank covariance estimation; and the posterior covariance matrix is the basis for the Bayesian design-of-experiment and model selection techniques developed in Chapter Four.

Reconstructions obtained by direct inversion of a full-rank operator are corrupted by noise and model error. High-frequency components in the data are amplified by the inverse smoothing kernel—a problem compounded by the nearly-collinear nature of full-rank arrays—and prior information is required for reconstruction. Complex structures are a common occurrence in full-rank CST studies: the probe volume may feature interacting flames or mixing behaviour near an inlet, which do not satisfy to the assumptions made in self-similar covariance estimation. Nevertheless, statistical properties of the LOS data converge over time, and the target covariance can be directly estimated due to the linear system that follows from the joint-normal pdfs. A method is presented to approximate model errors and estimate the covariance matrix in full-rank CST. This estimate is included in a prior—as in the self-similar case—which is used to reconstruct successive measurements.

Numerical experiments were conducted to demonstrate the effect of the prior covariance on reconstruction errors in gas-phase tomography. Bayesian estimates of concentration in a turbulent jet and the reaction rate in a turbulent flame were compared to ground truth distributions in terms of the normalized Euclidean distance. Moreover, the structural similarity (SSIM) index was introduced as an alternative measure of quality for CST images. Both metrics established that

reconstructions informed by an estimate of the covariance matrix were more accurate than reconstructions obtained with a smoothing prior. The SSIM index distinguished the accuracy of CST images better than the Euclidean distance. Increased accuracy due to the use of a covariance estimate was especially dramatic in the test designed to mimic a real-time industrial imaging scenario, relevant to many CST practitioners.

3.1 Turbulence Theory for CST

Several aspects of turbulence theory are important to CST practitioners. This section begins with an account of self-similar behaviour in turbulent jets followed by a review of their governing equations. Analytical scale functions for the scalar field are presented, including a novel expression of the variance distribution in terms of the mean profile. Empirical measurements that verify the existence of a self-similar regime are used to fit the analytical profiles. Finally, arguments are presented to justify the use of a joint-normal prior pdf in gas-phase tomography.

3.1.1 Phenomenology of self-preserving jets

Self-similarity, also called *self-preservation*, refers to a dynamic equilibrium where the mean and higher-order moments of flow variables evolve together. When this occurs, dynamic variables (velocity, temperature, etc.) have the same relative value at the same relative location [243]. Profiles of velocity, temperature, and the like can therefore be expressed in terms of scale functions that only depend on one dimension of the flow. Correspondingly, the governing equations become independent of this dimension. When the conservation and transport equations are 2D or axisymmetric, for a semi-infinite or round flow, respectively, they simplify into ordinary differential equations. Manipulation of the governing equations in self-similar form can reveal important relationships between flow variables. These results are used to predict characteristics of a turbulent fluid flow's asymptotic state.

There are a broad range of conditions under which a turbulent flow approaches a self-preserving or partially self-preserving equilibrium. Properties that are subject to a similarity analysis usually include mean and root-mean-square (rms) distributions of velocity, temperature and transported scalars. More fundamentally, pdfs of fluctuating variables become self-preserving, themselves, along with power spectra, dissipation rates, and correlation functions. Self-preservation of these latter quantities implies self-preservation in the mean and rms profiles of a fluid. Crucially, once the lower moments of a turbulent pdf attain similarity, they can be incorporated into a Bayesian prior to improve the accuracy of CST images. Two canonical

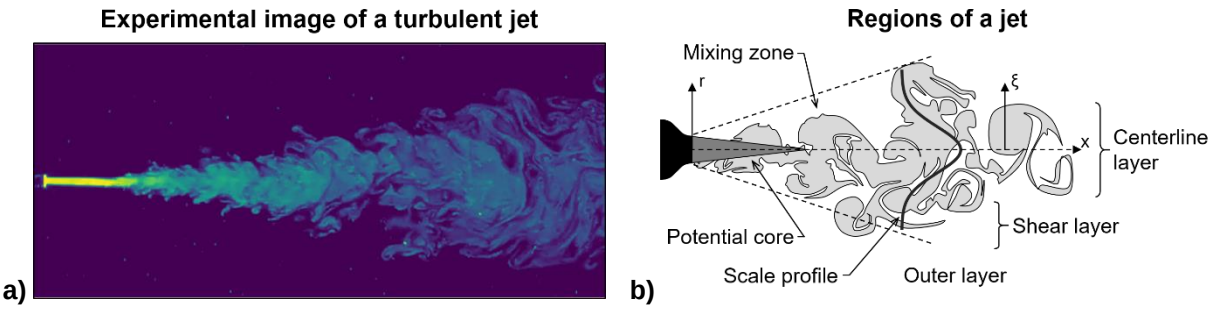

Figure 3.1: Cross sections of a round turbulent jet: a) PLIF image from Ref. [244]; and b) schematic of a round jet showing its development and constituent regimes, adapted from Ref. [245].

examples of self-similar flows are free-shear jets and wakes, which are common laboratory fluid targets and feature widely in industrial settings. The phenomenology of turbulent jets is of particular interest in the CST context. Therefore, self-similarity in gas-phase jets is the principal focus of this chapter.

Figure 3.1 shows a cross section of a round turbulent jet issuing into a quiescent medium and a schematic that illustrates jet flow regimes. Jets are divided into three axial zones [2]. The jet develops from a potential core in the *near field*, surrounded by an annular mixing region; near field behaviour is a strong function of the inlet conditions. Once the mixing region subsumes the core, the jet is said to have entered a *transitional state* or *intermediate region*. Finally, the jet reaches a self-similar equilibrium that defines the *far field*, in which axial gradients are dominated by radial gradients. The onsets of transitional and fully-developed behaviour are characterized in terms of an axial distance normalized by the nozzle diameter, called a *relative diameter*. These transitions typically occur about 7 and 70 diameters downstream from the inlet, respectively [245]. Jets are also divided into three concentric regions: the centerline, shear, and outer region. Flow along the centerline is predominantly axial while the shear region involves substantial radial motion. The near field shear region has a strong radial gradient around the potential core, resulting in vortex generation and roll-up. Vortices combine in the intermediate field to form large, visible eddies that decay into smaller eddies and eventually vanish. The transition to complete self-preservation is marked by successive similarity in the jet's moments [243]. Mean profiles of velocity become similar early on, followed by transported scalars, then rms profiles, and so on with higher-order

moments.[42] Experimental measurements have shown that mean and rms distributions can achieve weak self-preservation in the near field [246].[43]

Transition dynamics and the evolution towards a jet's equilibrium state depend on the rate of entrainment of ambient fluid at the shear layer. Classical descriptions of turbulent jet flow are based on Kolmogorov's theory of turbulence, which supposes that small-scale turbulence is statistically isotropic [247]. On this model, turbulent phenomena are inherently local and jets continually readjust towards a universal equilibrium, which only depends on the rate of momentum addition. (Townsend [247] famously summarized this view with the phrase "turbulence forgets its origins.") Therefore, classical jets are modelled in terms of a point source of momentum at a virtual origin with no mass flux, regardless of the actual inflow conditions. Governing equations for an axisymmetric jet are transformed, accordingly, using appropriate scale functions for mean and rms distributions, resulting in a set of ordinary differential equations. The scale functions contain empirical constants which ought to be identical for all jets that share a momentum flux. Careful studies have found that a large range of round jets are well-modelled by the classical approach [248]. However, further reviews of experimental data noted inconsistent similarity parameters in some jets, attributable to differences in their initial conditions [243,245,249]. In particular, variation in the mass flux, inflow velocity profile, and global density ratio can affect the location of the virtual origin, rate of axial expansion, and constants in the scale functions [250,251].[44] Based on these observations, it has been widely accepted that the classical description of self-preservation presents an incomplete picture of jet dynamics.

In light of the evidence against universal self-similar jet dynamics, George [243] re-analyzed self-preservation in turbulent jets and wakes with an explicit focus on the initial conditions. He proposed three forms of self-similarity:

1. Jets may be fully self-preserving at all orders of turbulent moments and scales of motion;
2. Jets may be partially self-preserving, up to a certain moment or spatial scale; or

[42] The scalar field approaches self-preservation more slowly than do velocity components as the former is more sensitive to turbulent structures. According to Sreenivasan and Antonia [273], "in homogeneous shear flows the scalar field attains a semblance of universality only if the velocity field in its entirety is universal (not just one of its components)."

[43] Here, *weak similarity* refers to a condition where flow variables can be collapsed onto a scale distribution but the scale functions are not necessarily in sync with one another.

[44] The boundary layer thickness at the origin determines the nature of vortex generation and thereby roll-up, pair-up, and eddy characteristics, which propagate through the jet. Or, per Nathan et al. [250], "a jet never forgets."

3. Jets may be locally self-preserving, in which case the profiles scale with local quantities but the governing equations do not admit to a self-preserving solution [243].

By conjecture, all turbulent jets will approach one of these three states, determined by the initial conditions. On this view, the surplus spreading observed in some jets is thought to arise from additional shear at the nozzle. For instance, a smooth contraction nozzle results in a quasi-uniform (i.e., top hat) profile while a long straight pipe yields fully-developed inflow. The top hat profile features greater shear at the interface, which promotes the formation of vortices in the near field. These vortices are thought to roll-up into eddies that propagate throughout the flow, causing stronger engulfment of ambient fluid in the far field [245].

Intuitively, according to George [243], jets can only enter a fully self-preserving equilibrium when the classical self-similar solution satisfies the governing equations.[45] Nevertheless, absent such conditions, jets tend as close as possible towards full self-preservation. At a minimum, jets approach local self-preservation, in which scale functions describe the far field profiles but their relative balance is not necessarily synchronous. When similarity profiles are out of sync, the axial form of the scale variable cannot be analytically determined and must be measured, instead. As will be shown later, all three forms of self-preservation are suitable for covariance estimation.

3.1.2 Self-similar governing equations

The Reynolds decomposition is used to analyze turbulence in terms of mean variables and their fluctuating components. For instance, the velocity vector, $\mathbf{u}(\mathbf{x}, t)$, is decomposed into $\bar{\mathbf{u}}(\mathbf{x}, t) + \mathbf{u}'(\mathbf{x}, t)$, where $\bar{\mathbf{u}}$ and $\mathbf{u}'$ are the mean and fluctuating quantities of $\mathbf{u} = (u, v, w)^T$ at a certain location, $\mathbf{x} = (x, r, \theta)^T$, and time, t.[46] Mean variables are an idealized quantity, defined as the average value in an ensemble, which is a hypothetical set of duplicate flows with identical boundary conditions. (Ensemble statistics converge on the corresponding pdf.) For instance, the mean velocity is

$$\bar{\mathbf{u}} = E[\mathbf{u}] \equiv \int_{-\infty}^{\infty} \mathbf{u}\pi(\mathbf{u})d\mathbf{u}, \tag{3.1}$$

[45] Self-similar solutions do not exist when the density varies appreciably across the flow. However, as a jet develops, density gradients diminish and ultimately disappear. As such, density gradients become buoyancy-driven, which renders self-similar solutions mathematically tractable (realized via the Boussinesq approximation).

[46] The overbar and prime notation designate the mean and fluctuating elements of a flow variable. Moreover, it should be noted that this section features some overlap in notation. Flow field notation introduced in Section 3.1.2 does not carry on throughout the text.

where E is the expectation operator and $\pi(\mathbf{u})$ is the pdf of $\mathbf{u}$.[47] More generally, the shape of a turbulent pdf is characterized in terms of its moments,

$$\mu_n \equiv \int_{-\infty}^{\infty} (x-\mu_1)^n \pi(x) dx, \tag{3.2}$$

where μ_1 is the mean and μ_n is the nth moment for $n > 1$. The mean is taken about zero, as in Eq. (3.1), and successive moments are taken about the mean. These describe the spread of a distribution (variance, μ_2), its lopsidedness (skewness, μ_3), flatness (kurtosis, μ_4), and so on. For a statistically stationary process, $\bar{\mathbf{u}}$ is a function of location, only.

This chapter considers tomographic reconstruction of a passive scalar, transported by a round, incompressible, momentum-driven jet. Lubbers et al. [252] presented a standard similarity analysis for this class of fluid flow, adapted below. Similar analyses can be found in the work of Dahm and Dimotakis [253], Richards and Pitts [248], Mi et al. [254], Carazzo et al. [255], and Shin et al. [256], among others. First, governing equations are derived for the jet from the cylindrical form of the Navier-Stokes equations by neglecting viscous and body forces, applying the boundary layer approximation, and averaging. The resulting expressions for continuity and momentum are

$$\frac{\partial \bar{u}}{\partial x} + \frac{1}{r}\frac{\partial (r\bar{v})}{\partial r} = 0 \text{ and } \bar{u}\frac{\partial \bar{u}}{\partial x} + \bar{v}\frac{\partial \bar{u}}{\partial r} = -\frac{1}{r}\frac{\partial (r\overline{u'v'})}{\partial r}, \tag{3.3}$$

where u and v are the axial and radial components of velocity and the averaged product of u' and v' is a Reynolds stress term. The same procedure is applied to the scalar transport equation,

$$\bar{u}\frac{\partial \bar{c}}{\partial x} + \bar{v}\frac{\partial \bar{c}}{\partial r} = -\frac{1}{r}\frac{\partial (r\overline{v'c'})}{\partial r}. \tag{3.4}$$

By definition, dynamic variables in a self-similar flow can be collapsed using scale functions. The scale functions of a round jet are expressed in terms of a dimensionless radius, $\xi = r/L(x)$ (shown in Figure 3.1b), where L is a characteristic length scale. Typically, for a round jet, L is the radial distance that satisfies $\bar{u}(x, r) = \bar{u}(x, 0)/2$. Alternatively, per George [243], L can be derived in terms of the momentum flux and inlet profile; the scale may also be an arbitrary local value.

The functional form of similarity profiles are largely empirical but it is possible to comment on the existence, structure, and interrelation of self-similar variables by manipulating Eqs. (3.3)

[47] By contrast, actual estimates of $\bar{\mathbf{u}}$ are from multiple measurements of $\mathbf{u}$ in a single flow at different times or locations.

and (3.4). Towards this end, velocity and Reynolds stress terms are written as the product of an axial scale and dimensionless radial function,

$$\bar{u}(x,\xi) = U(x)\, f(\xi) \text{ and } \overline{u'v'}(x,\xi) = U'(x) g(\xi), \tag{3.5}$$

where U and U' are scales for the mean velocity and velocity fluctuations. Typically, U is taken to be the mean centreline velocity. The streamfunction, ψ, is defined by the relations

$$\bar{u} = -\frac{1}{r}\frac{\partial \psi}{\partial x} \text{ and } \bar{v} = \frac{1}{r}\frac{\partial \psi}{\partial r} \tag{3.6}$$

and can be expressed in terms of a jet's scales and scale functions: $\psi(x, \xi) = UL(x)^2 \cdot F(\xi)$, where $F'(\xi)/\eta = f(\xi)$. Substituting the streamline function into Eqs. (3.3) and (3.4) and rearranging the result yields a statement of momentum conservation in terms of the scale functions,

$$-\frac{1}{\xi}\frac{d(\xi g)}{d\xi} = -\frac{U^2}{U'^2}\frac{\partial L}{\partial x}\left[\frac{F}{\xi}\frac{d}{d\xi}\left(\frac{F'}{\xi}\right) + \left(\frac{F'}{\xi}\right)^2\right]. \tag{3.7}$$

Integrating the momentum equation across an axial plane generates an expression for the conservation of axial momentum flux. Namely: the product function $UL(x)$ must be a constant. Moreover, it can be shown that Eq. (3.7) only admits to a solution when

$$\left(\frac{U}{U'}\right)^2 \frac{\partial L}{\partial r} = c_1, \tag{3.8}$$

where c_1 is a constant [2]. Equation (3.8) is a formal expression of the classical assumption that turbulent jets exhibit a constant, linear spreading rate in the self-similar regime. According to Tennekes and Lumley [3], the mean velocity and velocity fluctuation scales are approximately equal, i.e., $U = U'$, resulting in a universal spreading rate that coheres with classical theory. By contrast, the analysis of George [243] and a large body of observations suggest that, in fact, the mean and fluctuating velocity scales are not necessarily equal and c_1 is replaced with some function of x that depends on the inlet velocity profile.

Next, scale functions are introduced to collapse the scalar concentration and corresponding turbulent stress, h and k. Here, $\xi_c = r/L_c(x)$ is introduced, where L_c is a radial length scale for the concentration field. The mean passive scalar and turbulent stress terms are modelled as

$$\bar{c}(x,\xi_c) = C(x) h(\xi_c) \text{ and } \overline{v'c'}(x,\xi_c) = U'C'(x) k(\xi_c), \tag{3.9}$$

where C and C' scale the mean scalar and scalar fluctuation profiles. The net scalar flux is found by integrating Eq. (3.4) across an arbitrary axial plane,

$$\int_0^\infty \overline{uc}\, 2\pi r dr = \frac{u_0 c_0}{A_0}, \tag{3.10}$$

where u_0 and c_0 are the mean velocity and concentration at the inlet and A_0 is the area of the nozzle exit. The similarity profiles in Eqs. (3.5) and (3.9) are inserted into Eq. (3.10). Based on this expression, the radial length scale for concentration, L_c, must equal the radial velocity length scale, L, in order for a self-similar solution to exist. Rather, $\xi_c = \xi$, meaning concentration and velocity will exhibit the same spreading rate. This model is useful for multi-modal tomographic reconstruction; e.g., simultaneous CST and PIV [142]. Next, velocity and concentration terms in Eq. (3.4) are replaced with their self-preserving equivalents. Simplification of this expression results in a transport equation for the concentration profile,

$$\frac{U}{C}\frac{C'}{U'}\frac{d(Fh)}{d\xi} = \frac{1}{c_2}\frac{d(\xi k)}{d\xi}, \tag{3.11}$$

where c_2 is a constant. Concentration dynamics in the far field become independent of the inlet conditions when Eq. (3.11) admits to a self-similar solution, which requires $U = U'$ and $C = C'$ such that c_2 is a universal constant [2].

Estimating a covariance matrix in Bayesian CST requires a variance scale function. The quantity of interest in this case is the transported scalar, c, and its variance. In the boundary layer approximation, the transport of scalar fluctuations is governed by

$$\bar{u}\frac{\partial \overline{c'c'}}{\partial x} + \bar{v}\frac{\partial \overline{c'c'}}{\partial r} = -2\overline{v'c'}\frac{\partial \bar{c}}{\partial r} - \frac{\partial \overline{v'c'c'}}{\partial r} - X, \tag{3.12}$$

where X is the molecular destruction of scalar fluctuations,

$$X \equiv 2D\overline{(\nabla c')^2}, \tag{3.13}$$

and D is a diffusion constant. As with preceding similarity variables, the scale functions, m and n, are introduced to collapse the distribution of scalar fluctuations, resulting in

$$\overline{c'c'}(x,\xi) = C'C'(x)m(\xi) \text{ and } \overline{v'c'c'}(x,\xi) = U'C'C'(x)n(\xi). \tag{3.14}$$

Finally, substitution of these functions into Eq. (3.12) gives the transport equation of scalar variance in terms of self-similar profiles,

$$\frac{L}{CU'\xi}\left[2U\frac{dC'}{dx}F'm+C'\frac{dU}{dx}Fm'\right]=-2kh'+\frac{C'}{C}n'+\frac{LX}{UC'^2}. \tag{3.15}$$

As with Eqs. (3.7) and (3.11), solutions to Eq. (3.15) are only possible for a constant spreading rate and comparable mean and fluctuating scales: $U = U'$ and $C = C'$ [2]. When jets do tend towards a fully self-preserving equilibrium, a suitable function, m, will express the distribution of variance in the radial direction throughout the jet and scale with $C'C'$. However, even when jets do not approach such a state, concentration fluctuations remain well-modelled by m, according to George [243], scaled by an arbitrary local variable instead of $C'C'$.

3.1.3 Analytic scale functions

Evolution of a round, isothermal jet transporting a passive scalar is governed by Eqs. (3.3) and (3.4). Equations (3.7), (3.11), and (3.15) describe the velocity, concentration, and concentration fluctuations in the jet as members of a self-preserving equilibrium. According to George [243], jets converge towards this equilibrium when the governing equations are solved by self-similar profiles that are consonant with Eqs. (3.5), (3.9), and (3.14). Of particular interest in Bayesian CST are the functions h and m, which correspond to the structure of the first two moments of the concentration pdf and can be used to develop a prior. Section 3.1.2 demonstrated constraints on the existence of a self-similar solution. Further analysis of the governing equations reveals the expected form of and relationship between concentration scale functions, later used for covariance estimation.

3.1.3.1 Mean profiles for velocity and concentration

Early solutions to the mean jet equations were based on the turbulence models of Prandtl and Taylor. Prandtl [257] assumed conservation of momentum in the jet during mixing, resulting in an eddy viscosity term, ε. He proposed two equations for ε, relating the Reynolds stress terms to mean flow properties. Tollmien [258] used Prandtl's first mixing length model to solve the jet equations. The model predicted that the kinematic eddy viscosity would vanish at the centre of the jet (i.e., $\varepsilon_{P1} = l_P^2|d\bar{u}/d\eta|$, where l_P is Prandtl's mixing length), contradicted by experimental findings. Görtler [259] derived the velocity profile for Prandtl's second equation, which has a constant eddy viscosity (i.e., $\varepsilon_{P2} = k\cdot\bar{u}_0\cdot b(x)$, where k is a constant of proportionality and b scales the inlet velocity). Taylor's closure was based on the assumption of vorticity conservation in the jet, producing an eddy viscosity term, analogous to Prandtl's only applied to vorticity transport (i.e., $\varepsilon_T = l_T^2|\nabla\bar{u}|$, where l_T is a vorticity mixing length). Howarth [260] used this approach to calculate

velocity and temperature fields for a turbulent jet. Distributions based on the theories of Prandtl and Taylor roughly capture mean jet behaviour, and mixing length models remain important in turbulence education. However, the solutions of Tollmien [258], Görtler [259], and Howarth [260] neglect the variance of axial velocity in the momentum equations, which has been shown to play a substantial role in the evolution of turbulent jets and wakes.

Reichardt [261] reformulated the governing equations by averaging them without applying a Reynolds decomposition; he thereby avoided explicitly modelling fluctuations. The resulting expressions for momentum and scalar transport are

$$\frac{\partial \overline{u^2}}{\partial x} + \frac{1}{r}\frac{\partial (r\overline{uv})}{\partial r} = 0 \text{ and } \frac{\partial \overline{uc}}{\partial x} + \frac{1}{r}\frac{\partial (r\overline{vc})}{\partial r} = 0 . \tag{3.16}$$

He made the assumption that

$$\overline{uv} = -\Lambda_u \frac{\partial \overline{u^2}}{\partial r} \text{ and } \overline{cv} = -\Lambda_c \frac{\partial \overline{uc}}{\partial r} , \tag{3.17}$$

where Λ_u and Λ_c are axial scale functions for velocity and concentration, given by

$$\Lambda_u = \frac{b_u}{2}\frac{db_u}{dx} \text{ and } \Lambda_c = \frac{b_c}{2}\frac{db_c}{dx} . \tag{3.18}$$

The constants b_u and b_c scale the velocity and concentration similarity profiles. In the previous section, it was remarked that scales that share the form of b_u and b_c must be proportional to x in order to permit a self-preserving solution. A physical basis for Eqs. (3.17) and (3.18) can be derived from three assumptions about the jet: i) the mean flow is predominantly axial, ii) the turbulent intensity is small, and iii) radial velocity fluctuations are proportional to the mean velocity [262]. Substituting Eqs. (3.17) and (3.18) into Eq. (3.16) yields a system of differential equations,

$$\frac{\partial \overline{u^2}}{\partial x} = \frac{\Lambda_u}{r}\frac{\partial}{\partial r}\left(r\frac{\partial \overline{u^2}}{\partial r}\right) \text{ and } \frac{\partial \overline{uc}}{\partial x} = \frac{\Lambda_c}{r}\frac{\partial}{\partial r}\left(r\frac{\partial \overline{uc}}{\partial r}\right) . \tag{3.19}$$

Equation (3.19) is solved by functions of the form $K/b \cdot \exp\{-(r/b)^2\}$, with a constant, K, that depends on the corresponding source strength (momentum for K_u, concentration for K_c). Radial scale functions are obtained by normalizing this solution by the mean centreline value, which cancels out source-related terms,

$$f(\xi) = h(\xi) = \exp\left\{-\beta_0 \xi^2\right\} , \tag{3.20}$$

where β_0 is an empirical constant, related to the jet's radial length scale.[48] (The constant, β_0, includes the axial scale, b_u or b_c, and is not necessarily the same for the scale functions f and h.)

3.1.3.2 Profile for scalar fluctuations

Chatwin and Sullivan [263] proved the existence of a family of solutions for the scalar variance profile, m. These functions depend on the mean concentration and nature of molecular diffusion in a jet. The solutions are predicated on the assumption of uniform concentration at the outlet, c_0, and negligible molecular diffusion. (The latter assumption is physically untenable, but is relaxed following the derivation.) Under these conditions, the pdf of concentration is

$$\pi_c(y) = \theta(x,\xi)\delta(y-c_0) + \left[1-\theta(x,\xi)\right]\delta(y), \tag{3.21}$$

where the argument, y, is a concentration and θ is an intermittency indicator, defined as the probability that $c(x, \xi) > 0$. The mean concentration is calculated using Eqs. (3.1) and (3.21),

$$\begin{aligned}\overline{c} &= \int_0^\infty y\pi_c(y)dy \\ &= \int_0^\infty y\left\{\theta\delta(y-c_0) + \left[1-\theta\right]\delta(y)\right\}dy = c_0\theta\end{aligned}. \tag{3.22}$$

Similarly, the scalar variance is

$$\begin{aligned}\overline{c'c'} &= \int_0^\infty (y-\overline{c})^2\pi_c(y)dy = \int_0^\infty y^2\pi_c(y)dy - \overline{c}^2 \\ &= \int_0^\infty y^2\left\{\theta\delta(y-c_0) + \left[1-\theta\right]\delta(y)\right\}dy - \overline{c}^2 \\ &= c_0^2\theta - \left[c_0\theta\right]^2 = c_0^2\theta(1-\theta)\end{aligned}. \tag{3.23}$$

It follows from Eq. (3.22) that $\theta = \overline{c}/c_0$, which can be substituted into the expression for variance,

$$\overline{c'c'} = c_0^2\left(\overline{c}/c_0\right)(1-\overline{c}/c_0) = \overline{c}(c_0-\overline{c}) = \frac{c_0^2}{4} - \left(\overline{c} - \frac{c_0}{2}\right)^2. \tag{3.24}$$

Equation (3.24) is maximized when $\overline{c} = c_0/2$, which is offset from the centreline. This behaviour coheres with empirical scale profiles for $c'c'$. However, as mentioned above, Eq. (3.24) neglects diffusion, which counteracts the production of fluctuations and augments pressure scrambling

[48] The Gaussian form for f and h is ubiquitous in the literature on self-similar jets. However, Pope [2] suggests the form $f(\xi) = (1 + \beta\xi^2)^{-2}$, based on the solution of Görtler [259]. This choice leads to an analytical solution for the mean radial velocity but underpredicts mean axial velocity at the edge of the jet.

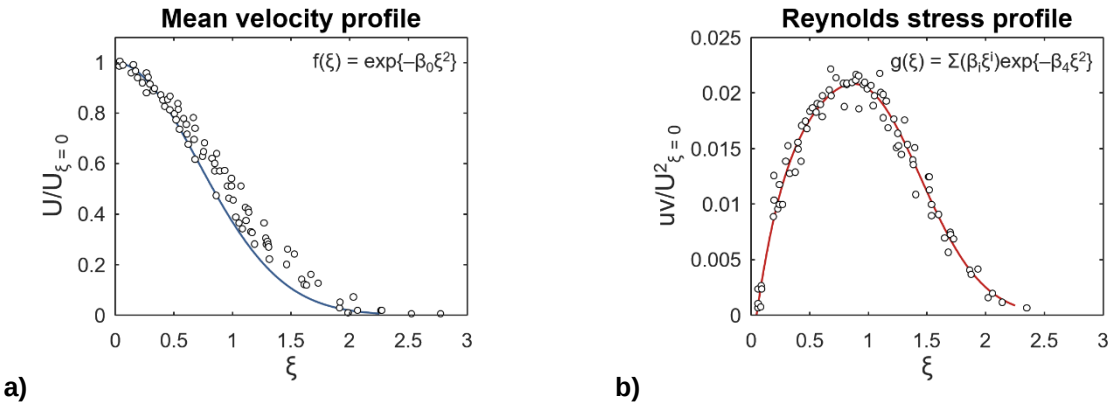

a) b)

Figure 3.2: Empirical scale profiles for a round turbulent jet: a) mean velocity profile and b) Reynolds stress profile; showing data from Antoine et al. [264].

[264]. Therefore, Chatwin and Sullivan [263] proposed a pair of constants: β_1, to account for the effects of diffusion on mean flow properties; and β_2, to account for statistical properties of the velocity field. The authors' diffusion-adjusted equation for scalar variance is

$$\overline{c'c'}(x,\xi) = \beta_2 \bar{c}(x,\xi)\left[\beta_1 C(x) - \bar{c}(x,\xi)\right], \tag{3.25}$$

where C is the axial concentration scale from Section 3.1.2. Since $h = \bar{c}/C$ and $m = c'^2/C^2$, Eq. (3.25) can be adapted into a novel expression of m in terms of h,

$$m(\xi) = \beta_2\left[\beta_1 h(\xi) - h^2(\xi)\right]. \tag{3.26}$$

3.1.4 Empirical scale functions

Numerous studies have reported experimentally- and numerically-derived self-preserving distributions for turbulent jets. Figure 3.2 and Figure 3.3 present the standard forms of f, g, h, and m, derived from the work of Birch et al. [265], Dowling and Dimotakis [249], Panchapakesan and Lumley [266], Antoine et al. [264], and references therein. These papers report experimental data

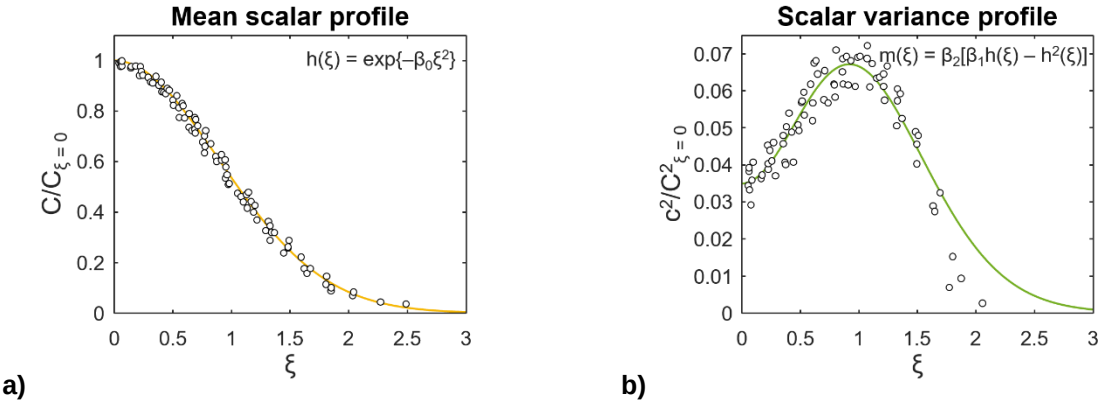

a) b)

Figure 3.3: Empirical scale profiles for a round turbulent jet: a) mean scalar profile and b) scalar variance profile; showing data from Antoine et al. [264].

for jets of water, heated air, He, CH_4, C_2H_4, C_3H_6, and C_3H_8; issued into a reservoir of water, air, or N_2, resulting in a range of Schmidt numbers;[49] and having a Reynolds number from 5,000 to 50,000.[50] Several inlet velocity profiles were tested by alternatively using a smooth contraction, convergent, or long pipe nozzle. Measurements of concentration, temperature, and velocity were made using tracer LIF, Rayleigh laser thermometry, hot-wire anemometry, resistance thermocouples, or oil smoke light scattering; and radial distributions of key quantities were measured at multiple axial planes, located 10 to 105 diameters downstream from the inlet.

Equations (3.20) and (3.26) were used to plot *f*, *h*, and *m* in Figure 3.2 and Figure 3.3, with $\beta_0 = 0.813$ for *f* and $\beta_0 = 0.622$, $\beta_1 = 1.181$, and $\beta_2 = 0.192$ for *h* and *m*.[51] Data in these figures demonstrate that scaled quantities of velocity and concentration are consistent across a wide range of conditions and measurement positions, even for measurements in the intermediate field. The existence of robust scale functions confirms the self-preserving nature of round, free-shear turbulent jets and support the use of self-similarity for covariance estimation.

3.1.5 Gaussian form of the pdf

Thus far, this chapter has demonstrated that self-similar profiles can describe the variance of a scalar quantity in a free-shear jet in terms of the mean profile. A full pdf is necessary to calculate the posterior distribution in Bayesian CST, which constitutes a quantitative measure of uncertainty about the parameters of interest. Ideally, given perfect knowledge about the macroscopic boundary conditions of a turbulent flow, the prior would assume the form of turbulent fluctuations about the mean distribution. Therefore, it is instructive to consider the characteristics of fluctuations in a typical gas process. Chapter Two presented Bayesian CST with a joint-normal prior pdf; justification for this choice is presented below.

It has been widely observed in research on turbulence that fluctuating quantities follow a distribution that is near-Gaussian [267].[52] Under certain conditions, fluctuations may exhibit sub- or hyper-Gaussian behaviour, in which the tails are under- or over-pronounced [268]; the distribution of certain quantities may also be skewed. Deviations from Gaussian distribution are

[49] The Schmidt number is the dimensionless ratio of the viscous to molecular diffusion rates, $Sc = \mu/\rho D$.

[50] The Reynolds number is the (dimensionless) ratio of inertial to viscous force, $Re = \rho u L/\mu$.

[51] The Reynolds stress scale function was fit to a polynomial-exponential function suggested by Hussein et al. [371], which was not analytically motivated: $g(\zeta) = (0.103\zeta^3 - 0.101\zeta^2 + 0.082\zeta - 0.004)\cdot\exp\{-1.361\zeta^2\}$.

[52] See the temperature and velocity distributions reported by Tavoularis and Corrsin [372] (Figures 21 and 22) and the scalar pdfs in Dowling and Dimotakis [249] (Figures 27 to 29).

commonly observed in turbulent stresses, fluctuations that are orthogonal to the primary flow direction, and double correlations. The mechanisms responsible for these distributions are not always clear, though many instances of non-Gaussianity arise due to *external intermittency*—i.e., interaction with an erratic boundary condition [269]—and *internal intermittency*, associated with non-isotropic features at very small scales. The choice of a Gaussian prior is typically well supported, even in the case of non-Gaussian fluctuations, because projection of the flow field onto a basis amounts to an averaging procedure.

Batchelor [267] summarized the traditional argument for normally-distributed fluctuations and presented experimental evidence. He showed how simple assumptions about the Fourier coefficients of a turbulent variable could be combined with the central limit theorem to establish an idealized model of Gaussian fluctuations. The analysis makes use of the integral timescale, T, based on the autocorrelation function, R, defined as

$$R(\tau) = E[c'(\mathbf{x},t)\cdot c'(\mathbf{x},t+\tau)] \text{ and } T = \frac{1}{R(0)}\int_0^\infty R(\tau)d\tau\,. \tag{3.27}$$

First, a large number of measurements of a scalar concentration, $c(\mathbf{x}, t)$, are made over the interval $0 \le t \le t_n$, where the measurement interval is much longer than T. The Fourier expansion of the scalar fluctuations is

$$c'(\mathbf{x},t) = \sum_{n=1}^{\infty} a_n(c')\cos\left(\frac{2\pi nt}{t_n}\right) + b_n(c')\sin\left(\frac{2\pi nt}{t_n}\right). \tag{3.28}$$

According to Brun and Pumir [270], the Fourier coefficients, a_n and b_n, are normally distributed though not necessarily independent. This result is illustrated by considering the definition of the coefficients (here the argument for a_n will stand in for both),

$$a_n(c') = \frac{2}{t_n}\int_0^{t_n} c'(\mathbf{x},t)\cos\left(\frac{2\pi nt}{t_n}\right)dt\,. \tag{3.29}$$

Equation (3.29) is equivalent to a sum of m integrals,

$$a_n(c') = \frac{2}{t_n}\sum_{i=1}^{m}\int_{(i-1)t_n/m}^{it_n/m} c'(\mathbf{x},t)\cos\left(\frac{2\pi nt}{t_n}\right)dt = \frac{2}{t_n}\sum_{i=1}^{m} a_{n,i}(c')\,, \tag{3.30}$$

where $1 << m$. The terms $a_{n,i}$ and $b_{n,i}$ are independent averages of the nth frequency component of the scalar fluctuations, provided the segment duration, t_n/m, is sufficiently long relative to T. Long wavelength modes (i.e., $n \approx 1$) may be correlated, reflecting the presence of integral-scale

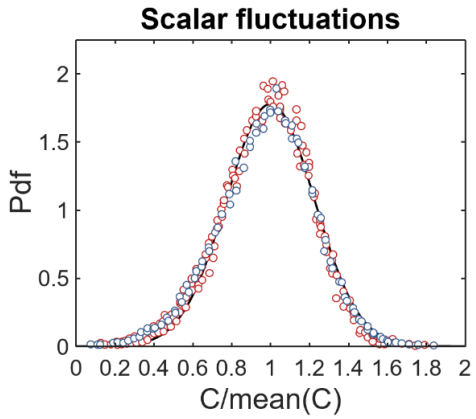

Figure 3.4: Pdf of the normalized centreline concentration in a C_2H_4 jet (Re = 5,000, measured at x/d = 20, 40, 60, and 80), indicated with blue dots, and C_3H_6 jet (Re = 16,000, measured at x/d = 30 and 90), indicated with red dots; data from Ref. [249].

structures advecting through the measurement position. However, as the interval, t_n, approaches infinity, integral-scale coefficients decay to zero, leaving only terms that are effectively independent random variables. The sum of a large number of independent random variables is normally distributed, per the central limit theorem. Therefore, a_n and b_n are necessarily Gaussian. Moreover, it has been shown that var$\{a_n\}$ = var$\{b_n\}$ = E_n, which is the turbulent energy at the wavelength corresponding to the nth mode of the Fourier expansion [271].

The characteristic functions of $a_n(c')\cos(2\pi nt/t_n)$ and $b_n(c')\sin(2\pi nt/t_n)$ are denoted $G_n^{(a)}$ and $G_n^{(b)}$. Manipulation of $G_n^{(a)}$ and $G_n^{(b)}$ can reveal the distribution of scalar fluctuations; these functions are defined as

$$G_n^{(a)}(k) = \exp\left\{-\frac{k^2}{2}E_n\cos^2\left(\frac{2\pi nt}{t_n}\right)\right\} \text{ and } G_n^{(b)}(k) = \exp\left\{-\frac{k^2}{2}E_n\sin^2\left(\frac{2\pi nt}{t_n}\right)\right\}, \quad (3.31)$$

respectively, where $E_n\cdot\cos2(2\pi nt/t_n)$ and $E_n\cdot\sin^2(2\pi nt/t_n)$ are the variance of the cosine and sine terms in Eq. (3.28). Since a_n and b_n are independent, the characteristic function of the concentration fluctuations, $G^{(c)}$, is the product of $G_n^{(a)}$ and $G_n^{(b)}$ for n from 1 to infinity. This product can be expanded in logarithmic scale, corresponding to a sum,

$$\ln\left[G^{(c)}\right](k) = \sum_{n=1}^{\infty}\ln\left[G_n^{(a)}\right] + \sum_{n=1}^{\infty}\ln\left[G_n^{(b)}\right] = -\frac{k^2}{2}\sum_{n=1}^{\infty}E_n\,. \quad (3.32)$$

Equation (3.32) is the characteristic function of a Gaussian variable having a variance equal to the sum of E_n for n from 1 to infinity. As such, assuming a sufficiently long measurement interval, the scalar fluctuations should follow a normal distribution with zero mean.

Figure 3.4 shows normalized concentration pdfs for a C_2H_4 jet with a Reynolds number of 5,000 and C_3H_6 jet with a Reynolds number of 16,000 [249]. The data exhibit the predicted Gaussian behaviour. Fully-developed turbulence features large-scale eddies that are random in nature and effectively uncorrelated. As a result, the Fourier coefficients are approximately independent and the assumption of Gaussian scalar fluctuations is valid for several standard deviations [271]. The jets measured to generate the data for Figure 3.4 exemplify the ideal conditions that result in normally-distributed fluctuations.

Lockwood and Moneib [272] measured the first four moments of temperature pdfs at numerous positions throughout a self-similar jet. (The temperature pdf is a good surrogate for the pdf of transported scalars.) They found the flatness and skewness parameters approached Gaussian values of zero and three (i.e., $\mu_3 = 0$ and $\mu_4 = 3$ for a normal distribution) as the jet transitioned into its self-preserving equilibrium. But the scalar pdfs deviated from a normal distribution in some regions—i.e., μ_3 and μ_4 deviated substantially from zero and three—particularly in the near field of the jet and far from the centreline. Internal intermittency, a major cause of non-Gaussian fluctuations, is associated with the presence of small-scale coherent structures such as vortex tubes [273]. Typically, these structures produce sub-Gaussian tails [268]; however, in the presence of a large mean gradient, the combined effects of advection and molecular diffusion can yield a scalar pdf with exponential tails [274–276]. Large scale structures that arise due to interaction with external features can also generate fat-tailed distributions.

Non-Gaussian behaviour of this kind is observed in high-frequency, high-precision point-measurements. However, the target variable in gas-phase tomography is projected onto a finite basis, where each basis function effectively averages the flow. Fluctuations are correlated in space and time so the effect of projection on the distribution of fluctuations is not directly analogous to the central limit theorem—though it is directionally similar. For instance, the sum of perfectly correlated random variables will follow the same distribution as the variables, per se, while the sum of IID random variables will converge towards a normal distribution. Sums of correlated variables with finite variance will interpolate between these limiting conditions, depending on the correlation function and extent of averaging. Turbulent fluctuations have a pdf that is reasonably close to Gaussian, to begin with, and this averaging effect will diminish non-Gaussian features.

In summary, there are strong reasons to prefer the joint-normal form for prior pdfs in gas-phase tomography:

1. Simple assumptions about the nature of turbulent variables suggest a Gaussian distribution of fluctuations, a priori;
2. Experimental evidence confirms that scalar pdfs in jets tend towards a Gaussian distribution as the flow asymptotes towards its self-similar equilibrium;
3. Non-Gaussianity predominantly features in the tails of scalar pdfs, and tail probabilities play a small role in the joint-estimation of a large number of spatial variables that span the entire flow field;
4. Projection of the target variable onto a basis is akin to an averaging procedure that will diminish non-Gaussian aspects of a turbulent pdf; and
5. Insofar as the precise distribution of fluctuations projected onto the basis is unknown, the normal distribution is an appropriate, high-entropy choice that reflects general knowledge about the variation of turbulent quantities and uncertainty about the true distribution.

3.2 Estimating covariance structure in gas-phase tomography

Gas-phase tomography is an ill-posed inverse problem that requires prior information to obtain accurate estimates of $\mathbf{x}$ at an acceptable spatial resolution, even if the linear system is fully-determined. Bayesian CST incorporates additional knowledge about a process into reconstructions by way of a prior pdf. It has been argued here that passive scalars in a turbulent flow, projected onto a finite basis, roughly follow a joint-normal distribution about $\boldsymbol{\mu} \in \mathbb{R}^n$, where $\boldsymbol{\mu} = E[\mathbf{x}]$, with covariance $\boldsymbol{\Gamma}_\mathbf{x} \in \mathbb{R}^{n \times n}$, where $\boldsymbol{\Gamma}_\mathbf{x} = E[\mathbf{x}\mathbf{x}^T]$. As a result, $\pi_{\text{pr}}(\mathbf{x})$ should take the joint-normal form and, together, the arguments $\boldsymbol{\mu}$ and $\boldsymbol{\Gamma}_\mathbf{x}$ fully specify the prior. Basic covariance relationships can be derived from first principles; for instance, a smoothness prior, where $\boldsymbol{\Gamma}_\mathbf{x}$ is obtained from the first-order Tikhonov matrix, and total variation (TV) prior, which promotes smooth regions separated by sharp discontinuities. Advanced numerical simulations that mirror experimental conditions can also be used to produce a covariance matrix. But simple priors often lack the specificity needed to resolve salient flow features and simulation may require more detailed information about the target than is known.

Covariance estimation in CST consists in approximating $\boldsymbol{\Gamma}_\mathbf{x}$ from time-resolved measurements, generating an estimate of $\boldsymbol{\mu}$ in the process. Like instantaneous reconstruction, covariance estimation requires LOS data as well as with supplemental information in order to determine the mean vector and covariance matrix. Fortunately, the statistical nature of $\boldsymbol{\mu}$ and $\boldsymbol{\Gamma}_\mathbf{x}$ enables the use of constraints derived from the fluid mechanics literature: in particular, the self-

preserving scale functions from Section 3.1.3 and Gaussian fluctuations from Section 3.1.5. Estimates of the mean and covariance are inferred from multiple measurements and subsequently used for instantaneous imaging. Covariance estimation produces a prior that is at once theoretically-motivated and specific to the flow conditions. Techniques for estimating $\boldsymbol{\mu}$ and $\boldsymbol{\Gamma}_{\mathbf{x}}$ depend on the nature of the information deficit (i.e., the rank of the tomography system) and class of fluid flow. This section presents two methods to estimate the covariance of a passive target, both viable in the limited-data context; and a general method for covariance estimation in full-rank CST, which can be applied to irregular flow structures.

3.2.1 Limited-data covariance estimation

Limited-data tomography is characterized by rank($\mathbf{A}$) < n such that an infinite set of vectors can minimize the forward model. It is always possible to introduce a coarse basis for which $\mathbf{A}$ is full-rank (in the extreme case: a single pixel will always be full-rank) but this is a superficial solution because low-resolution images cannot represent features of interest in the flow and model error substantially corrupts coarse systems, regardless. At first glance, limited-data covariance estimation should pose a greater challenge than instantaneous reconstruction because $\boldsymbol{\Gamma}_{\mathbf{x}}$ has n^2 parameters—by comparison the inference of $\mathbf{x}$ has n unknowns. One solution involves constructing an approximate covariance matrix from K estimates, for $\mathbf{b}^{(1)}$, $\mathbf{b}^{(2)}$, …, $\mathbf{b}^{(K)}$,

$$\boldsymbol{\Gamma}_{\mathbf{x}} \approx \frac{1}{K}\sum_{k=1}^{K} \mathbf{x}^{(k)}[\mathbf{x}^{(k)}]^{T} , \tag{3.33}$$

where $\mathbf{x}^{(k)}$ is the kth reconstruction. However, some previous estimate of $\boldsymbol{\Gamma}_{\mathbf{x}}$ is required to obtain $\mathbf{x}^{(k)}$ and the covariance produced by Eq. (3.33) will reflect errors that stem from the initial prior.[53] Clearly, inferring $\boldsymbol{\Gamma}_{\mathbf{x}}$ with an underdetermined operator is a hopeless task absent substantial information about the true covariance structure.

Many CST experiments feature a momentum-driven free-shear target (e.g., Refs. [103,106,127–129,141]). Section 3.1 provides theoretical and experimental evidence that members of this class of fluid flow progress towards a self-preserving equilibrium. Fully-preserving equilibria are marked by similarity in all moments of pdfs for the dynamic variables, which are interrelated. Moreover, it is possible to obtain a robust estimate of the mean distribution—i.e., the

[53] This approach incorporates information from multiple measurements to reconstruct a single shot and seemingly could improve the quality of limited-data CST images. However, the covariance information used to reconstruct $\mathbf{x}^{(k)}$—implicit or explicit—dominates the structure of the covariance estimate from Eq. (3.33).

first moment—by limited-data gas-phase tomography. Therefore, an estimate of the mean, $\boldsymbol{\mu} \approx \bar{\mathbf{x}}$, can be combined with similarity relations to estimate $\boldsymbol{\Gamma}_\mathbf{x}$. This section describes two procedures to determine the spatial distribution of variance, $\mathbf{v} \in \mathbb{R}^n$, where $v_j = \mathrm{var}(x_j)$, followed by a technique to determine $\boldsymbol{\Gamma}_\mathbf{x}$ from $\mathbf{v}$.

3.2.1.1 Estimating variance in terms of scale functions

Covariance estimation takes advantage of the stability of statistical properties in turbulent flow. For high-speed gas-phase tomography, this assumption is valid so long as changes to the inflow conditions and ambient environment occur at the integral timescale. The scale function approach to covariance estimation requires an additional assumption: the target must issue from a round (or small) nozzle into a quiescent medium. In this case, it is possible to parametrize the flow with the mean scale, h, to estimate the mean target distribution, $\boldsymbol{\mu}$. According to Eq. (3.9), the distribution of concentration can be represented as $C(x)h(\xi)$. Neither C nor the precise size and position of the jet are known, but these parameters can be determined from LOS data by imposing a subspace restriction on the inference via h.

To begin, the mean scalar profile for a single jet or plume is expressed in terms of an arbitrary position and scale within the measurement plane. Equation (3.20) is re-written for a CST domain,

$$h(x, y; x_0, y_0, L) = \exp\left\{-\beta_0 \frac{(x-x_0)^2 + (y-y_0)^2}{L^2}\right\}, \tag{3.34}$$

where (x, y) is a position in the domain, (x_0, y_0) is the axial centre of the flow, and L is the radial length scale. Next, ray-sums are computed using Eq. (3.34) as a basis, resulting in the operator $\mathbf{A}(x_0, y_0, L)$. Since reconstructions are linear, the average scalar distribution can be directly inferred from mean LOS data,

$$\bar{\mathbf{b}} = \frac{1}{K}\sum_{k=1}^{K} \mathbf{b}^{(k)}, \tag{3.35}$$

where K is the number of measurement shots. Parameters for the mean profile are found by non-linear regression,

$$(C, x_0, y_0, L) = \underset{C, x_0, y_o, L}{\arg\min}\left\{\left\|\bar{\mathbf{b}} - \mathbf{A}(x_0, y_0, L)C\right\|_2^2\right\}. \tag{3.36}$$

It is not necessary to specify the spreading coefficient since β_0 and L^2 are perfectly convolved in this expression (i.e., the fraction β_0/L^2 is sufficient for covariance estimation). Equation (3.36)

involves the inference of four parameters from time-averaged LOS data. For any practical measurement array, the inference will be overdetermined. Results from Eq. (3.36) are used to estimate the mean: $\boldsymbol{\mu} \approx C\mathbf{h}$.

Ray-sums can be computed by high-order integration over Eq. (3.34), but this is a computationally-demanding procedure. An alternative approach is to precompute ray-sums for a finite basis, $\Phi^{(n)}$, which yields the operator $\mathbf{A}^{(n)}$. A discrete form of h, $\mathbf{h}(x_0, y_0, L) = \{h_j\}$, is calculated by projecting Eq. (3.34) onto $\Phi^{(n)}$

$$h_j = \left\langle \phi_j, h \right\rangle \approx h(x_j, y_j), \tag{3.37}$$

where (x_j, y_j) is the centre of mass of the jth basis function; the approximation holds for high-resolution bases with compact support. Using Eq. (3.37) to obtain $\mathbf{h}$, ray-sums across the mean scale function are computed by matrix-vector multiplication, $\mathbf{A}^{(n)}\mathbf{h}$. Computing $\mathbf{A}(x_0, y_0, L)$ in this way is generally faster than the direct numerical approximation and results in minimal error, given a high-resolution basis.

Following estimation of the target's axial centre and radial scale, the relationship between h and m in Eq. (3.26) is used to calculate the distribution of variance in the measurement plane. Similar to $\mathbf{h}$, a discrete form of the variance scale function, $\mathbf{m} = \{m_j\}$, is populated with elements given by the scale function,

$$m_j \approx \beta_2 \left(\beta_1 \exp\left\{-\xi_j^2\right\} - \exp\left\{-2\xi_j^2\right\} \right), \tag{3.38}$$

where $\xi_j^2 = [(x_j - x_0)^2 + (y_j - y_0)^2] \cdot \beta_0 / L^2$. If the measurement plane is well past the near field, β_1 and β_2 can be determined by regressing Eq. (3.26) to empirical variance data, as in Section 3.1.4 (i.e., $\beta_1 = 1.181$, and $\beta_2 = 0.192$). Otherwise, these coefficients are included in the regression to scale $\boldsymbol{\Gamma}_{\mathbf{x}}$, described below. Finally, the variance of the target is

$$\mathbf{v} = C'^2 \mathbf{m}, \tag{3.39}$$

where C'^2 is an unknown scale. The variance scale vector, $\mathbf{m}$, is valid for jets and plumes that have achieved similarity in the first two moments of the concentration pdf, which may occur in the near field in some instances. However, Eq. (3.39) does not require a universal spreading rate nor an analytical solution for the axial scale since C'^2 is treated as an arbitrary parameter. As such, this procedure applies to all three similarity regimes proposed by George [243].

The procedure described thus far concerns a single jet or plume. Extending the technique to multiple sources is achieved by the principle of superposition. The scalar diffusion equation is linear so the mean and variance of a passive scalar may be approximated by a linear combination of scalar profiles [277]. The mean distribution of K sources is given by summation,

$$h_j = \sum_{k=1}^{K} \exp\left\{-\beta^{(k)}\left[(x_j - x_0^{(k)})^2 + (y_j - y_0^{(k)})^2\right]\right\}, \tag{3.40}$$

where $(x_0^{(k)}, y_0^{(k)})$ is the axial position of the kth source and $\beta^{(k)}$ is a convolved spreading parameter/radial scale. The variance scale function is extended in a similar way. The minimization based on Eq. (3.40) has $4K$ parameters, which would normally be smaller than the typical number of beams, even in limited-data CST. However, when the number of sources is unknown, hierarchical estimation of **h** and **m** becomes ill-posed because any single source is closely approximated by the sum of several sources and vice versa. As a result, the stability of a multi-source regression is a strong function of the measurement arrangement, number of sources, and prior knowledge about the target.

3.2.1.2 Estimating variance by assuming a proportional relationship

Environmental applications of CST frequently feature emissions from a distributed area or unknown number of point sources. Profiles for any given source may be distorted by a crosswind. As a result, scale functions from the self-similarity analysis in the beginning of this chapter cannot be employed to estimate **v**. However, it remains possible to estimate the variance with a simple model of the flow field.

The model assumes the second moment of the scalar pdf will be a function of the square of the first moment. Regions of high concentration deviate the most from ambient conditions and must be maintained by some momentum- or buoyancy-driven source, upstream from the measurement plane, resulting in a relatively large mass flux. By contrast, regions of low concentration are nearer to the entrainment zone and feature lower-magnitude velocity fluctuations. Gradients of the mean and rms velocity fields feature in the scalar variance production term. High scalar variance should therefore track regions of high concentration. Equation (3.25) suggests that this relationship will take the form $v_j \propto \beta + (\beta/2 - \bar{x}_j)^2$, where the parameter β has a complex relationship to the source of the target. Absent detailed information about the inflow conditions and velocity field, a simple assumption is suggested: $\beta = \max(\bar{x}_j^2)$ and

$$\mathbf{v} = C'^2 \max\left\{\beta + (\beta/2 - \bar{\mathbf{x}})^2, \beta/8\right\}. \tag{3.41}$$

The minimum value of $\beta/8$ is selected to prevent non-physical (i.e., negative) values of $\mathbf{v}$ and to account for uncertainty about the precise edge of the flow.

Equation (3.41) requires an estimate of the mean distribution, $\bar{\mathbf{x}}$, which can be reconstructed from time-averaged data, $\bar{\mathbf{b}}$, and a smoothness prior. The initial structure of $\mathbf{\Gamma_x}$ is thus determined by Eq. (2.35); $\bar{\mathbf{x}}$ is the MAP estimate, based on $\bar{\mathbf{b}}$ and calculated with Eq. (2.38); $\boldsymbol{\mu} \approx \bar{\mathbf{x}}$; and $\mathbf{v}$ is found with Eq. (3.41).

3.2.1.3 Completing an estimate of the covariance matrix

Estimates of $\mathbf{v}$ computed with Eq. (3.39) or (3.41) include a constant of proportionality, C'^2, which remains to be determined, and the variance does not itself account for the flow's correlation structure. The correlation matrix implicit in a Tikhonov prior exhibits full field covariance, where variables are substantially correlated with each other variable. This behaviour is not representative of autocorrelation functions observed in fluid flows. Instead, Vecherin et al. [278] suggest the use of a square-exponential autocorrelation matrix, $\mathbf{\Gamma}_{\text{sq}}$,

$$\Gamma_{\text{sq},ij} = \exp\left\{-\frac{d_{ij}^2}{\hat{b}^2}\right\}, \tag{3.42}$$

where d_{ij} is the physical distance between the centre of mass of the functions ϕ_i and ϕ_j and $\hat{b}$ is a correlation length: $\hat{b} = b/[-\ln(c)]^{1/2}$, where $c \in (0, 1)$ is the correlation between fluctuations separated by the physical distance, b.

The variance is divided into a diagonal standard deviation matrix, $\mathbf{S}$, with elements $s_{jj} = v_j^{1/2}/C'$. Correspondingly, $\mathbf{\Gamma_x} \propto \mathbf{S}\mathbf{\Gamma}_{\text{sq}}\mathbf{S}^T$, where C'^2 is the unknown constant of proportionality. This constant should be selected to ensure that the measurement variance implied by $C'^2\mathbf{S}\mathbf{\Gamma}_{\text{sq}}\mathbf{S}^T$ matches the observed variance, $\mathbf{\Gamma_b} = E[\mathbf{b}\mathbf{b}^T] - \bar{\mathbf{b}}\bar{\mathbf{b}}^T$. A relationship between the measured and modelled covariance is inferred from the relationship $E[\mathbf{b}\mathbf{b}^T] \approx E[(\mathbf{A}\mathbf{x})(\mathbf{A}\mathbf{x})^T] = \mathbf{A}(\boldsymbol{\mu}\boldsymbol{\mu}^T + \mathbf{\Gamma_x})\mathbf{A}^T$. The trace operator is employed to match the total variance of these quantities, which results in a final estimate of the covariance of $\mathbf{x}$,

$$\mathbf{\Gamma_x} \approx \left[\frac{\text{tr}\left(\mathbf{\Gamma_b}\right)}{\text{tr}\left(\mathbf{A}(\mathbf{S}\mathbf{\Gamma}_{\text{sq}}\mathbf{S}^T)\mathbf{A}^T\right)}\right]\mathbf{S}\mathbf{\Gamma}_{\text{sq}}\mathbf{S}^T. \tag{3.43}$$

Both limited-data techniques require an estimate of $\boldsymbol{\mu}$ to estimate the covariance matrix. Together, $\boldsymbol{\mu}$ and $\boldsymbol{\Gamma}_{\mathbf{x}}$ complete the prior pdf. While this procedure is designed for limited-data tomography—as limited-data experiments are more likely to feature self-similar targets—it can also be employed in the full-rank context.

3.2.2 Full-rank covariance estimation

Full-rank gas-phase tomography involves a dense measurement array and basis arranged such that rank($\mathbf{A}$) = n. The measurement operator must be overdetermined because the ray-sums include multiple overlapping components by construction: i.e., a large number of similar paths is required to obtain a linearly-independent combination of functions near the centre of the measurement plane. The overdetermined system and unstable inverse smoothing kernel of a full-rank system yield an ill-conditioned operator. Measurement noise and model error cannot be avoided; reconstructions obtained by direct pseudoinversion are therefore corrupted by non-physical artifacts. Bayesian inference diminishes this effect and improves the accuracy of CST images by incorporating a priori information about the flow field into the reconstruction procedure. The previous section describes a technique to estimate $\boldsymbol{\mu}$ and $\boldsymbol{\Gamma}_{\mathbf{x}}$ if the target is a passive scalar and transport is governed by advection and diffusion. Full-rank CST systems are often used to image turbulent flames (e.g., Refs. [186,187,191,192,202–206]), which violate the assumptions made in Section 3.2.1. Tomography of a complex process with a dense measurement array thus calls for a unique approach to covariance estimation.

Covariance estimates are predicated on the stability of flow field statistics. Ideally, absent measurement noise and model error, when rank($\mathbf{A}$) = n, the covariance matrix can be expressed in terms of the mean data, $\bar{\mathbf{b}}$, and measurement covariance, $\boldsymbol{\Gamma}_{\mathbf{b}}$,

$$\begin{aligned}\boldsymbol{\Gamma}_{\mathbf{x}} &= E[\mathbf{x}\mathbf{x}^T] - \boldsymbol{\mu}\boldsymbol{\mu}^T = E[(\mathbf{A}^{\#}\mathbf{b})(\mathbf{A}^{\#}\mathbf{b})^T] - \boldsymbol{\mu}\boldsymbol{\mu}^T \\ &= \mathbf{A}^{\#}(\bar{\mathbf{b}}\bar{\mathbf{b}}^T + \boldsymbol{\Gamma}_{\mathbf{b}})(\mathbf{A}^{\#})^T - \boldsymbol{\mu}\boldsymbol{\mu}^T = \mathbf{A}^{\#}\boldsymbol{\Gamma}_{\mathbf{b}}(\mathbf{A}^{\#})^T\end{aligned}. \tag{3.44}$$

Unfortunately, Eq. (3.44) is prone to the same sources of error as $\mathbf{x}^{\mathrm{LS}} = \mathbf{A}^{\#}\mathbf{b}$; only more so because the pseudoinverse is squared. Close inspection of $\boldsymbol{\Gamma}_{\mathbf{b}}$ explicates the effects of discretization error and noise on direct covariance estimation, which can be counteracted.

Conceptually, the data is decomposed in terms of *exact* and *error* components,

$$\mathbf{b} = \mathbf{b}^{\mathrm{exact}} + \mathbf{e}^{\mathrm{disc}} + \mathbf{e}^{\mathrm{noise}}, \tag{3.45}$$

where $\mathbf{b}^{\text{exact}}$ is the product of $\mathbf{A}$ and $\mathbf{x}^{\text{exact}}$, itself the projection of x onto Φ; $\mathbf{e}^{\text{disc}}$ is the discretization error, i.e., the difference between a hypothetical noise-free measurement and $\mathbf{b}^{\text{exact}}$; and $\mathbf{e}^{\text{noise}}$ is the measurement noise. Regularization adds information that improves the direct inversion, pushing solutions from $\mathbf{A}^{\#}\mathbf{b}$ towards $\mathbf{A}^{\#}\mathbf{b}^{\text{exact}}$; meanwhile, reconstruction errors derive from $\mathbf{A}^{\#}(\mathbf{e}^{\text{disc}} + \mathbf{e}^{\text{noise}})$. While the vectors $\mathbf{e}^{\text{disc}}$ and $\mathbf{e}^{\text{noise}}$ are unobservable, a large set of measurement data can be used to infer average properties of $\mathbf{e}^{\text{disc}}$ and $\mathbf{e}^{\text{noise}}$. Information about these vectors can be used, in turn, to augment Eq. (3.44) and stabilize the direct estimation of $\mathbf{\Gamma_x}$.

For a stationary process, the observed measurement covariance will asymptote towards the true value. That is, given a sufficiently long interval, noise has a minimal effect on estimates of $\mathbf{\Gamma_b} \approx \Sigma_k(\mathbf{b}^{(k)}[\mathbf{b}^{(k)}]^T)/K - \bar{\mathbf{b}}\bar{\mathbf{b}}^T$. The number of measurements required for adequate convergence depends on the intensity of noise, variance of the process, and discretization scheme. The expected outer product, $E[\mathbf{b}\mathbf{b}^T]$, can be broken up into its constituent parts per Eq. (3.45),

$$\begin{aligned} E[\mathbf{b}\mathbf{b}^T] &= E[(\mathbf{b}^{\text{exact}} + \mathbf{e}^{\text{disc}} + \mathbf{e}^{\text{noise}})(\mathbf{b}^{\text{exact}} + \mathbf{e}^{\text{disc}} + \mathbf{e}^{\text{noise}})^T] \\ &= \bar{\mathbf{b}}\bar{\mathbf{b}}^T + \mathbf{\Gamma}_{\text{ex}} + \mathbf{\Gamma}_{\text{disc}} + \mathbf{\Gamma}_{\text{noise}} \\ &\quad + 2E[\mathbf{b}^{\text{exact}}(\mathbf{e}^{\text{disc}})^T] + 2E[\mathbf{b}^{\text{exact}}(\mathbf{e}^{\text{noise}})^T] \\ &\quad + 2E[\mathbf{e}^{\text{disc}}(\mathbf{e}^{\text{noise}})^T] \end{aligned} \quad . \tag{3.46}$$

The interaction between the idealized data, $\mathbf{b}^{\text{exact}}$, and the discretization error, $\mathbf{e}^{\text{disc}}$, is denoted $\mathbf{E}_{\text{int}}$. For centred, IID noise, Eq. (3.46) simplifies further,

$$E[\mathbf{b}\mathbf{b}^T] \approx \bar{\mathbf{b}}\bar{\mathbf{b}}^T + \mathbf{\Gamma}_{\text{ex}} + \mathbf{\Gamma}_{\text{disc}} + \mathbf{\Gamma}_{\text{noise}} + \mathbf{E}_{\text{int}} . \tag{3.47}$$

Under noise-free conditions, the spatial and measurement covariance are related by the expression $\mathbf{\Gamma_x} = \mathbf{A}^{\#}\mathbf{\Gamma}_{\text{ex}}(\mathbf{A}^{\#})^T$. In reality, noise corrupts estimates of $\mathbf{\Gamma}_{\text{ex}}$ due to the ill-conditioned operators. However, provided that $\mathbf{\Gamma_b}$ has converged, suitable models of $\mathbf{\Gamma}_{\text{disc}}$, $\mathbf{\Gamma}_{\text{noise}}$, and $\mathbf{E}_{\text{int}}$ can be devised to better approximate $\mathbf{\Gamma}_{\text{ex}}$. Using this approach, estimates of $\mathbf{\Gamma_x}$ are found by

$$\mathbf{\Gamma_x} \approx \mathbf{A}^{\#}(\mathbf{\Gamma_b} - \mathbf{\Gamma}_{\text{disc}} - \mathbf{\Gamma}_{\text{noise}} - \mathbf{E}_{\text{int}})(\mathbf{A}^{\#})^T . \tag{3.48}$$

Measuring the covariance of electronic noise from a data acquisition device is straightforward. Recording data for an empty domain (for absorption CST) or steady phantom (for emission CST) yields a measurement covariance matrix that approximates $\mathbf{\Gamma}_{\text{noise}}$, which is typically much smaller than $\mathbf{\Gamma_b}$ for an active process. Far more important, however, are the covariance matrix that characterizes discretization error, $\mathbf{\Gamma}_{\text{disc}}$, and $\mathbf{E}_{\text{int}}$, the expected interaction between $\mathbf{b}^{\text{exact}}$ and $\mathbf{e}^{\text{disc}}$.

Approximation errors and model reduction are used to estimate $\mathbf{\Gamma}_{\text{disc}}$ and $\mathbf{E}_{\text{int}}$ [279]. Similar to the "proportional variance" procedure in Section 3.2.1.2, the first step involves reconstruction of a large set of estimates using a smoothness prior and non-negativity constraint. The resulting population of estimates is $\mathbf{X} = \{\mathbf{x}^{(k)}\}$ for $k = 1, \ldots, K$. These reconstructions feature artifacts, either due to noise or over-smoothing, and do not capture the flow field statistics with a high degree of precision. However, even rough approximation errors can stabilize the inference [240]. Next, spline interpolation is used to project $\mathbf{X}$ onto a high-resolution basis; the projected population is called $\tilde{\mathbf{X}}$ (with realizations $\tilde{\mathbf{x}}^{(k)}$). The quasi-continuous operator, $\tilde{\mathrm{A}}$, returns ray-sums across $\tilde{\mathbf{x}}^{(k)}$ by high-order interpolation. For $\mathbf{y}^{\text{meas}} = \tilde{\mathrm{A}}(\tilde{\mathbf{x}}^{(k)})$ and $\mathbf{y}^{\text{exact}} = \mathbf{A}\mathbf{x}^{(k)}$, discretization error vectors and the corresponding covariance are estimated using $\mathbf{e}^{\text{appx}} = \mathbf{y}^{\text{meas}} - \mathbf{y}^{\text{exact}}$ and

$$\mathbf{\Gamma}_{\text{disc}} \approx E[d^2 \mathbf{e}^{\text{appx}} (\mathbf{e}^{\text{appx}})^T], \tag{3.49}$$

where d is a constant that scales the discretization errors. Likewise, the interaction matrix is roughly given by

$$\mathbf{E}_{\text{int}} \approx E[d \mathbf{y}^{\text{exact}} (\mathbf{e}^{\text{appx}})^T], \tag{3.50}$$

where d is the same constant. Error vectors in Eqs. (3.49) and (3.50) have been centred.

The structure of $\mathbf{\Gamma}_{\text{disc}}$ and $\mathbf{E}_{\text{int}}$, computed using Eqs. (3.49) and (3.50), should tend towards that of the true discretization error and its expected interaction with $\mathbf{b}^{\text{exact}}$. However, the constant d is not known. As with the limited-data technique, a suitable scale for the parameter is identified using observed variance and covariance data,

$$d = \arg\min_{d} \left\{ \left\| \begin{array}{l} \bar{\mathbf{b}}\bar{\mathbf{b}}^T + \mathbf{\Gamma}_{\mathbf{b}} - \mathbf{\Gamma}_{\text{noise}} \\ -\left(\bar{\mathbf{y}}\bar{\mathbf{y}}^T + E[d^2 \mathbf{e}^{\text{disc}} (\mathbf{e}^{\text{disc}})^T] + E[d^2 \mathbf{y}^{\text{exact}} (\mathbf{e}^{\text{disc}})^T] \right) \end{array} \right\|_2^2 \right\}. \tag{3.51}$$

Finally, an estimate of $\mathbf{\Gamma}_{\mathbf{x}}$ is produced by first using Eq. (3.51) to solve for d and then substituting the products of Eqs. (3.49) and (3.50) into Eq. (3.48). However, the correlation structure of this estimate is less robust than the variance so the structure of $\mathbf{\Gamma}_{\text{sq}}$ is employed, instead. This procedure allows CST practitioners to exploit the covariance data present in a large set of measurements to improve instantaneous reconstructions.

3.3 Numerical validation of covariance estimation

3.3.1 Measurement arrays

Two beam arrangements and bases were devised to represent limited-data and full-rank CST experiments, typical of those found in the literature. The limited-data arrangement is depicted in Figure 3.5a, with four projections of six paths, rotated by 45° increments, and a beam spacing of 1/8th the domain width. This setup was designed to resemble an emitter-detector pair for absorption CST, such as those of Wright et al. [133] or An et al. [125]. The full-rank arrangement in Figure 3.5b simulated a row of pixels from a semicircle of CCD arrays, as in Upton et al. [280] or Lv et al. [217]. Thirty cameras were spaced 8.3° apart, collecting light from a 12° fan, resolved into 45 paths per camera.

Square-pixel bases were employed to represent both estimates. The coarse basis, $\Phi^{(a)}$, comprised a 400 pixel grid; the fine basis, $\Phi^{(b)}$, had 900 pixels. The latter can alternatively represent a 2D plane or slice of voxels from a quasi-3D (or 2.5D) experiment. Operators correspond to a beam arrangement and basis, indicated in the superscript in that order: e.g., $\mathbf{A}^{(1a)}$ is the operator for the limited-data arrangement with support $\Phi^{(a)}$. The rank of each operator was numerically verified: $\text{rank}(\mathbf{A}^{(1a)}) = \text{rank}(\mathbf{A}^{(1b)}) = 24$, $\text{rank}(\mathbf{A}^{(2a)}) = 400$, and $\text{rank}(\mathbf{A}^{(2b)}) = 900$, confirming that operators for the dense array spanned both bases.

Ground truth measurements were calculated by high-order interpolation of vertex data from a LES and IID noise was added to generate $\mathbf{b}$. Noise vectors were drawn from a normal distribution with zero mean and a standard deviation equal to 1% of $\max(\bar{\mathbf{b}})$ (in effect, a conservative approximation to Poisson noise). Ground truth vectors were obtained by projecting vertex data from a LES onto the appropriate basis at each timestep.

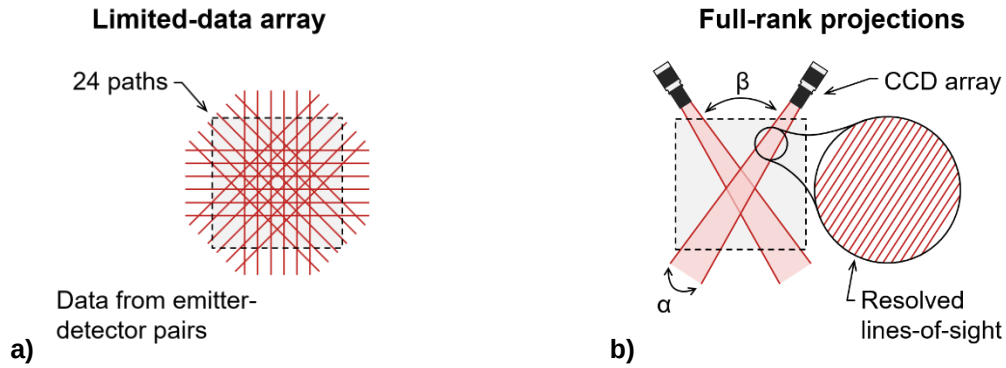

Figure 3.5: Beam arrangement schematics: a) 24-projection limited-data arrangement and b) two projections from a full-rank arrangement with array geometry shown, where *α* is the angular projection width and *β* is the angular spacing between projections.

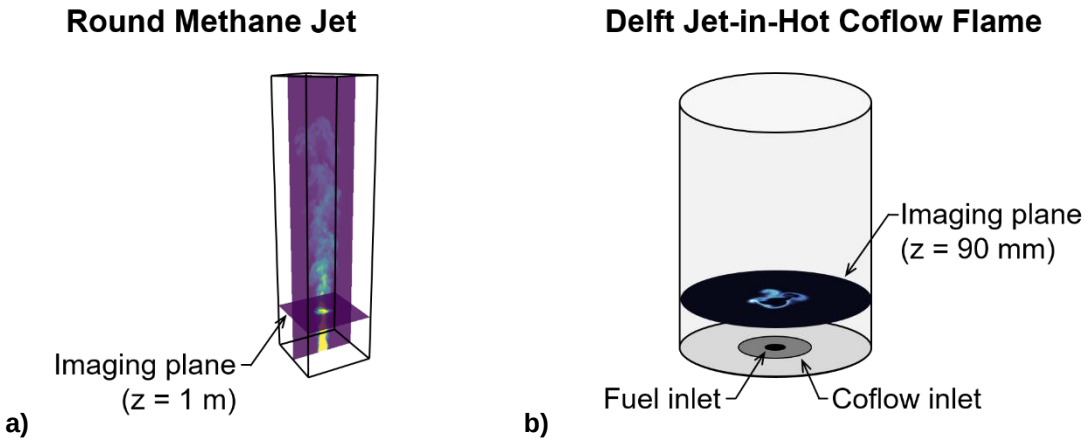

Figure 3.6: Computational domains to generate phantoms for CST by LES: a) FDS domain for an axisymmetric momentum-driven jet and b) OpenFOAM® domain for a Delft jet-in-hot coflow flame.

3.3.2 Round free-shear turbulent jet

The first set of phantom data was obtained from a LES of a free-shear momentum-driven jet of CH_4 flowing into a reservoir of quiescent N_2. The simulation was conducted for this thesis with Fire Dynamics Simulator (FDS) [281] using the domain pictured in Figure 3.6a. The domain was a 6 m rectangular prism with a 1.5 m square base at standard pressure and temperature. CH_4 entered the domain through a 0.2 m circular port at the centre of the base with an inlet Reynolds number of 3,000. The computational grid comprised 4 million cubic voxels, with open surfaces applied to the boundaries; the Dynamic Smagorinsky approach was used to model subgrid-scale diffusion. Concentration data at the voxel vertices in a measurement plane, located 1 m upstream from the entrance, was reported at 0.01 s intervals. Thirty seconds of data was collected (i.e, 3,000 shots), beginning at 3.75 s in physical time, at which point the jet was fully-developed in the measurement plane.

Numerous simulations were conducted to ensure that integral-scale features in the jet phantoms were emblematic of turbulent jet structures. Grids of increasing resolution were tested, with inner diameter-to-grid width ratios of $ID/\Delta x$ = 5, 10, 15, and 20. Distributions of CH_4 were projected onto $\Phi^{(a)}$ and $\Phi^{(b)}$ to verify that the jet statistics were constant in the tomography domain. An analysis of the power spectra of concentration fluctuations revealed the expected -5/3 decay slope, showing that fluctuations were resolved well into the inertial subrange, below the resolution of the tomography bases. Finally, comparisons were made to the experimental measurements of Birch et al. [265]. The centreline and axial decay of mean and fluctuating components of CH_4 in the LES were in good agreement with the trends reported in Ref. [265].

3.3.3 Delft jet-in-hot-coflow flame

The second phantom set represented a turbulent flame target, with reaction rate distributions from the LES of Labahn and Devaud [282]. The simulation used conditional source-term estimation of a Delft jet-in-hot coflow flame, benchmarked against experimental data from Oldenhof et al. [283]. The computational domain, shown in Figure 3.6b, was a 0.225 m tall cylinder with a 0.08 m radius. Inlet conditions were derived from experimental mean velocity and temperature conditions with a no slip boundary applied to the cylinder wall. The grid consisted of 1.5 million non-uniform cells, concentrated around the centreline—near the nozzle, in particular—resulting in a filter width below the Kolmogorov length scale. Turbulent features in the measurement plane were judged to be well-resolved. Vertex data of the methane reaction rate (a proxy for the intensity source term) was reported at 284 timesteps.

3.3.4 Test matrix

Four tests were devised to assess the limited-data and full-rank covariance estimation techniques. The first two tests resembled a limited-data CST study of jet behaviour. *Test 1* used phantoms from the CH_4 jet, measured with the limited-data beam arrangement. CH_4 distributions were projected onto $\Phi^{(a)}$ to establish ground truth vectors and reconstructions were computed with $\mathbf{A}^{(1a)}$. In this test, a non-negativity prior was employed to compare the limited-data covariance estimation technique to best-practice Tikhonov reconstruction [88]. Due to the large dimension of $\mathbf{x}$, computation time for the constrained least squares algorithm exceeded the typical duration of a CST measurement interval, preventing real-time applications. *Test 2* duplicated the conditions of Test 1, only excluding the non-negativity prior such that reconstructions could be quickly computed, in sync with the measurements.

Two further tests were devised to evaluate the full-rank technique for covariance estimation. *Test 3* considered phantoms from the CH_4 jet, measured with the full-rank array (similar to the full-rank jet study of Wang et al. [128]). Covariance data was estimated for experiments of increasing duration, lasting 0.1, 2.5, and 30 s, to test the hypothesis that converged measurement statistics enable full-rank covariance estimation. Plots of $\mathbf{\Gamma}_{\text{disc}}$ and $\mathbf{E}_{\text{int}}$ and successive estimates of $\mathbf{\Gamma}_{\mathbf{x}}$ were generated using $\Phi^{(a)}$ to illustrate key trends (corresponding matrix plots for $\Phi^{(b)}$ were too dense to visually distinguish the salient features). Next, the full-rank procedure from Section 3.2.2 was conducted in full with $\mathbf{A}^{(2b)}$. Finally, *Test 4* simulated emission tomography to demonstrate the utility of covariance estimation for a complex process. The test was carried out with CH_4

reaction rate phantoms from the flame LES and measured with the full-rank array; reconstructions were computed with $\Phi^{(b)}$. Since the number of snapshots in the flame LES was limited, noise was added to the true $\mathbf{\Gamma}_{\text{noise}}$ and $\mathbf{E}_{\text{int}}$ matrices, based on the quality of those estimates in Test 3, to approximate the estimates that could be obtained in a long experiment. Corrupted matrices were used to calculate $\mathbf{\Gamma}_{\mathbf{x}}$ via Eq. (3.48) and reconstructions were carried out with $\mathbf{A}^{(2b)}$. In addition to the covariance estimate and smoothing priors, Tests 3 and 4 featured reconstructions for an IID (or *uniform*) prior. The uniform prior illustrated the amplification of noise and model error by pseudoinversion of a full-rank operator.

3.3.5 Error metrics for numerical studies of gas-phase tomography

The standard measure of accuracy in gas-phase tomography is the normalized Euclidean distance between the ground truth and reconstructed images,

$$e(\mathbf{x},\mathbf{y}) = \frac{\left\|\mathbf{x}-\mathbf{y}\right\|_2^2}{\left\|\mathbf{x}\right\|_2^2}, \tag{3.52}$$

where $\mathbf{x}$ and $\mathbf{y}$ correspond to $\mathbf{x}^{\text{exact}}$ and $\mathbf{x}^{\text{MAP}}$, respectively. However, the utility of distance metrics is considerably reduced with increasing dimension. In particular, the Euclidean distance of out-of-flow artifacts diminishes relative to the magnitude of $\mathbf{x}^{\text{exact}}$ with additional parameters. This is a classic problem in computer vision and other fields that model large data sets (e.g., deep learning). Numerous alternative metrics have been developed to address this concern.

One such alternative is the SSIM index. This measure was designed to reflect apparent changes in image quality by emphasizing differences in the structural information of a scene. The index compares the variance and covariance of windows in an image,

$$\text{SSIM}(\mathbf{x},\mathbf{y}) = \frac{(2\mu_x\mu_y + c_1)(2\sigma_{xy} + c_2)}{(\mu_x^2 + \mu_y^2 + c_1)(\sigma_x^2 + \sigma_y^2 + c_2)}, \tag{3.53}$$

where $\mathbf{x}$ and $\mathbf{y}$ are $\mathbf{x}^{\text{exact}}$ and $\mathbf{x}^{\text{MAP}}$, interchangeably (as the SSIM index is symmetrical). In Eq. (3.53), μ_x is the mean of $\mathbf{x}$, μ_y is the mean of y, σ_x^2 is the variance of $\mathbf{x}$, σ_y^2 is the variance of $\mathbf{y}$, and σ_{xy}^2 is the covariance of $\mathbf{x}$ and $\mathbf{y}$. The constants, $c_1 = (k_1 L)^2$ and $c_2 = (k_2 L)^2$, stabilize the denominator, where $L = 2^{b-1}$ is range([$\mathbf{x}$; $\mathbf{y}$]) and b is the number of bits per element. Typically, $k_1 = 0.01$ and $k_2 = 0.03$ [284]. The SSIM index was designed to be sensitive to apparent structural differences between high-dimensional vectors, including low-contrast features, which makes the metric well-suited to fluid applications. The index has also been shown to track perceptive

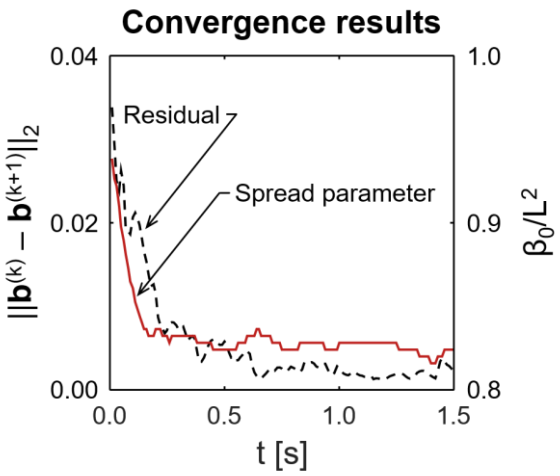

Figure 3.7: Running residual of the average data and the radius used to scale h. The estimate converged after 0.5 s of physical time.

similarity [285]. Note that $e \in [0, \infty)$, where smaller scores are better, and SSIM $\in [0, 1]$, where higher scores are better.

3.4 Results and discussion

3.4.1 Limited-data covariance estimation

Covariance estimation for Tests 1 and 2 began with a minimization of the residual between ray-sums over the scaled similarity profile, $C' \cdot h(x, y; \beta_0/L^2)$, and the time-averaged data, $\bar{\mathbf{b}}$. This was accomplished by minimizing Eq. (3.36) for a small set of measurements. Figure 3.7 shows the mean data residual, $\|\bar{\mathbf{b}}^{(k+1)} - \bar{\mathbf{b}}^{(k)}\|_2$, where $\bar{\mathbf{b}}^{(k)}$ is the average data from the first shot to the kth shot. Also depicted is the spreading parameter from the regression, β_0/L^2. This figure illustrates that convergence of the residual is a proxy for convergence of the regression, as expected. Covariance estimation is performed once $\bar{\mathbf{b}}$ has stabilized.[54] The spreading parameter in Figure 3.7 and empirical constants from Section 3.1.4—β_0 and β_1 and β_2, respectively—were used to compute the scalar variance profile, $\mathbf{m}$. Next, Eq. (3.43) was employed to estimate $\boldsymbol{\Gamma}_\mathbf{x}$. Finally, estimates in Test 1 were computed with MATLAB's *lsqnonneg* function and estimates in Test 2 were computed by simple matrix-vector multiplication.

Convergence of the mean data residual is a function of the variance of the jet and number and position of measurements. The scale function parameters stabilized after 0.5 s of physical time. Reconstructions were carried out in MATLAB, run on an Intel® Core™ i7-4600U CPU at 2.10 GHz. The net estimation time was 3.29 s, including the duration of physical measurement (from

[54] The procedure may be repeated to update $\boldsymbol{\mu}$ and $\boldsymbol{\Gamma}_\mathbf{x}$ if drift is observed in the mean measurement.

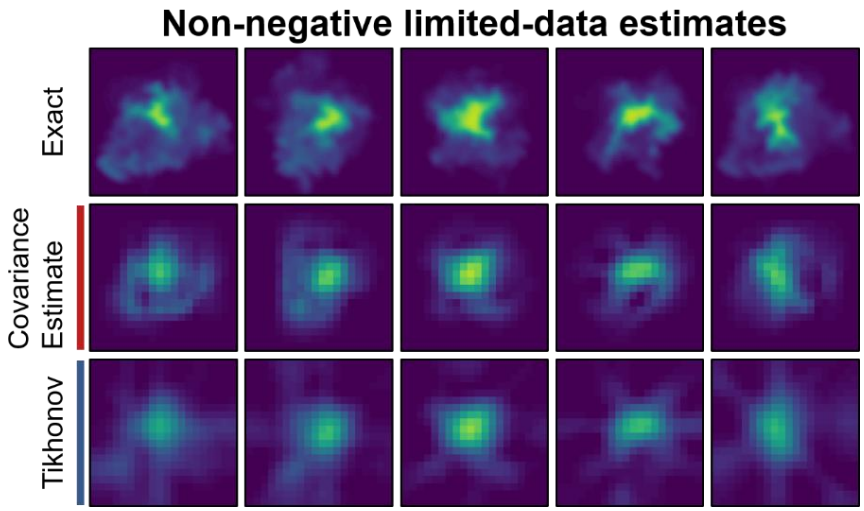

Figure 3.8: Representative estimates from Test 1, reconstructions with a covariance estimate captured jet structures better than Tikhonov estimates.

the LES) and the time required to compute $\boldsymbol{\mu}$, $\boldsymbol{\Gamma}_{\mathbf{x}}$, and $\mathbf{L}_{\mathbf{x}}$. Mean reconstruction times for the different priors were comparable in all cases. Test 1 reconstructions took 2.75 s using the covariance estimate and 2.76 s using the smoothness prior. Test 2 reconstructions took $3.25 \cdot 10^{-4}$ s using the covariance estimate and $1.71 \cdot 10^{-4}$ s using the smoothness prior. Computation times for Test 2 fell well within the interval required to resolve integral-scale features of interest. As such, statistics from the Test 2 results reflect accuracies that can be achieved in real-time limited-data CST (which may be used for online feedback and control purposes).

Table 3.1: Euclidean Distance and SSIM Distributions for Tests 1 and 2

Prior	**Test 1**				**Test 2**			
	Euclidean		*SSIM*		*Euclidean*		*SSIM*	
	Mean	*Dev.*	*Mean*	*Dev.*	*Mean*	*Dev.*	*Mean*	*Dev.*
Cov. Est.	0.181	0.033	0.842	0.041	0.182	0.034	0.832	0.048
Tikhonov	0.232	0.043	0.643	0.367	0.367	0.063	0.375	0.055

Figure 3.8 and Figure 3.9 show representative images from the non-negative and real-time limited-data tests, respectively, and Table 3.1 lists the reconstruction accuracy statistics. Tomographic images based on the self-similarity prior captured considerably more detail than Tikhonov reconstructions in both tests, which is readily apparent in the figures. Both error metrics reflect this difference, though the SSIM index showed greater sensitivity than the normalized Euclidean distance. Tikhonov images lacked the inner-jet structure apparent in covariance estimate

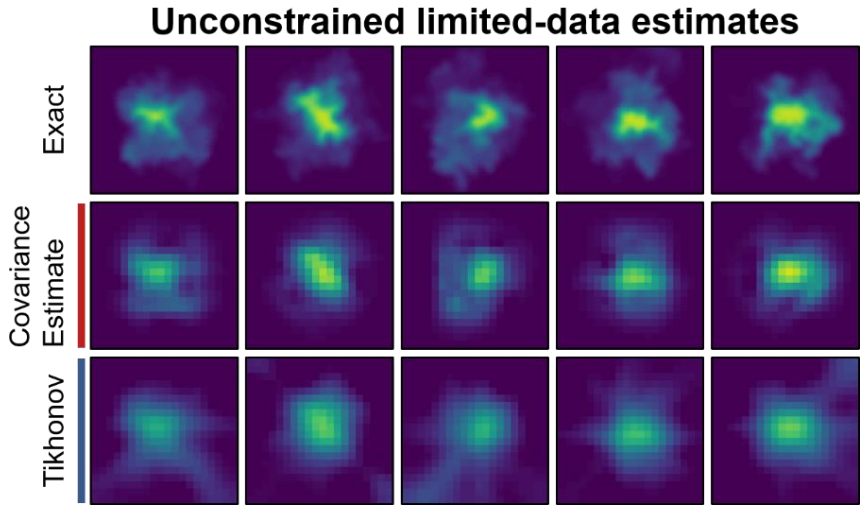

Figure 3.9: Representative estimates from Test 2; as with Test 1, the use of a covariance estimate improved the accuracy of reconstructions. Computation times for Test 2 were well within 100 Hz, sufficient for real-time applications.

images; and out-of-jet artifacts in the Tikhonov results overstate the flow area. The quality of reconstructions obtained with a data-based estimate of $\mathbf{\Gamma}_\mathbf{x}$ is particularly noteworthy considering the extremely-limited measurement information. Only 24 lines-of-sight were used to specify the prior and estimate instantaneous distributions of CH_4. Estimating $\mathbf{\Gamma}_\mathbf{x}$ under these conditions was made possible by the subspace restriction used to calculate $\bar{\mathbf{x}}$ and the relationship between the first two moments of the jet's CH_4 concentration pdf.

Results from the limited-data tests illustrate the utility of the Bayesian framework. Reconstruction accuracy improved as the prior covariance was brought in line with the true jet statistics, using a procedure made possible by fluid mechanics theory. This finding held true with and without a non-negativity prior. Moreover, estimating $\mathbf{\Gamma}_\mathbf{x}$ considerably reduced the penalty of removing the non-negativity prior, improving the quality of reconstruction under realistic on-line imaging conditions.

3.4.2 Full-rank covariance estimation

Full-rank tests began with approximation of the model error covariance and interaction terms. First, the population of reconstructions, $\mathbf{X}$, was obtained for the full set of measurements using smoothing and non-negativity priors. Reconstructions were then projected onto a high-fidelity mesh of vertices by spline interpolation, resulting in a quasi-ground truth population, $\tilde{\mathbf{X}}$. Differences between modeled measurements for the coarse grid, $\mathbf{y}^{\text{exact}} = \mathbf{A}\mathbf{x}^{(k)}$, and relatively continuous grid, $\mathbf{y}^{\text{meas}} = \tilde{\mathbf{A}}(\tilde{\mathbf{x}}^{(k)})$, were used to estimate $\mathbf{\Gamma}_{\text{disc}}$ and $\mathbf{E}_{\text{int}}$ via Eqs. (3.49) and (3.50).

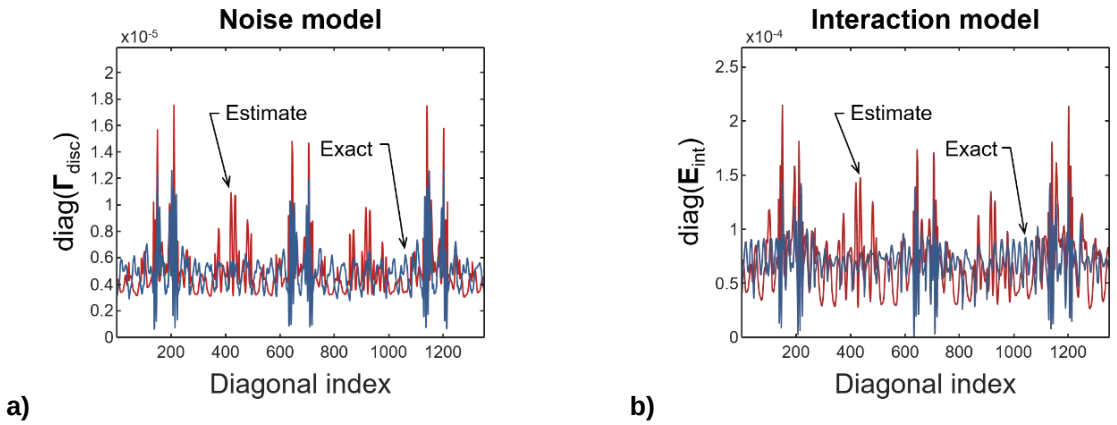

Figure 3.10: Approximating model error: a) diagonal of exact and estimated $\mathbf{\Gamma}_{disc}$ matrices and b) diagonal of exact and estimated $\mathbf{E}_{int}$ matrices. Models captured the salient bulk structure (location of peaks), with a normalized Euclidean distance error of 0.35 and 0.36 for $\mathbf{\Gamma}_{disc}$ and $\mathbf{E}_{int}$.

Figure 3.10 shows diagonal terms of the ground truth and approximate covariance matrix, $\mathbf{\Gamma}_{disc}$, and interaction matrix, $\mathbf{E}_{int}$. Key features of the true bulk structure were effectively recovered by the interpolation procedure. Peaks in $\mathbf{\Gamma}_{disc}$ represent pixels in which substantial fluctuations are distorted by the basis and peaks in $\mathbf{E}_{int}$ connect this distortion to variation in the continuous measurement operator. Together, these matrices relate fluctuations in the data to expected reconstruction errors due to the discretization scheme. $\mathbf{\Gamma}_{disc}$ and $\mathbf{E}_{int}$ were used to inform an estimate of $\mathbf{\Gamma_x}$ via Eq. (3.48). The accuracy of $\mathbf{\Gamma_x}$ is related to the stability of $\mathbf{\Gamma_b}$; estimates of $\mathbf{\Gamma_b}$ for a stationary progress towards the expected value as the measurement interval increases. Given a converged measurement covariance and suitable models of $\mathbf{\Gamma}_{disc}$ and $\mathbf{E}_{int}$, Eq. (3.48) should produce viable estimates of $\mathbf{\Gamma_x}$.[55]

Covariance estimates were computed for numerical tests of increasing duration. Figure 3.12 illustrates the effect of test duration on the accuracy of $\mathbf{\Gamma_x}$. The results show a clear trend: continued measurement stabilized the inversion in Eq. (3.48) and improved the accuracy of covariance estimates. Noise has a persistent effect, however, and the approximation error procedure is imperfect. As a result, minor inaccuracies persist in the covariance estimate, regardless of the test duration (these inaccuracies can be seen in Figure 3.12c). Nevertheless, the final estimate of $\mathbf{\Gamma_x}$ closely matched ground truth statistics of the flow field, showing that it is possible to recover the spatial covariance matrix from LOS data in a long experiment with a full-rank system.

[55] Note that reconstruction artifacts were present in both $\mathbf{X}$ and its projections, $\tilde{\mathbf{X}}$, affecting estimates of $\mathbf{\Gamma}_{disc}$ and $\mathbf{E}_{int}$. However, these effects were secondary compared to the benefits of capturing the general structure of such errors and their interaction with the discretization scheme [279].

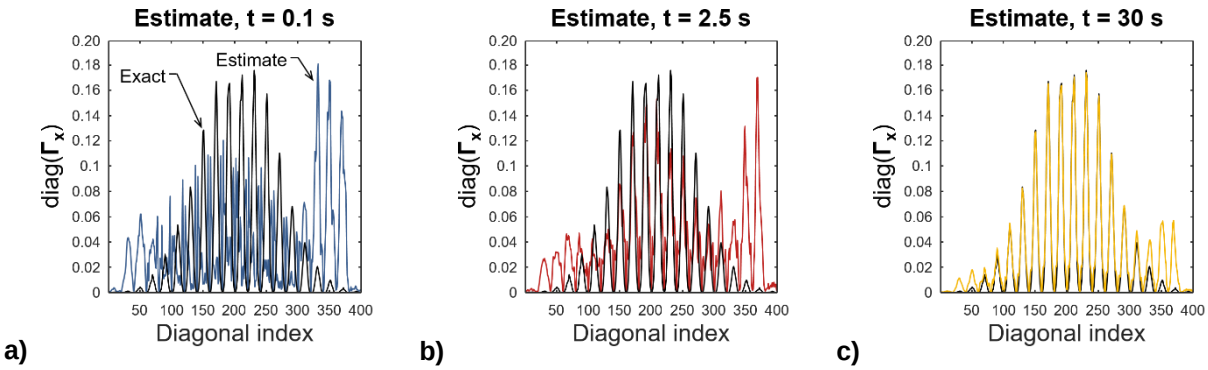

Figure 3.12: Covariance estimates for experiments of increasing duration, lasting a) 0.1 s, b) 2.5 s, and c) 30 s. Accuracy improved with additional data, with a normalized Euclidean distance error of 1.20, 0.66, and 0.21 for (a), (b), and (c), respectively.

Practitioners can monitor the difference between $\mathbf{\Gamma_b}^{(k+1)}$ and $\mathbf{\Gamma_b}^{(k)}$ in real time to ensure that the measurement covariance has converged. The utility of $\mathbf{\Gamma_b}$ relates to the condition number of $\mathbf{A}$, which is a function of the measurement array and basis. Ideally, the experiment should continue until $\sigma_{b1}{}^{-1/2}$ is less than the condition number of $\mathbf{A}$, where σ_{b1} is the first singular value of the residual matrix, $\mathbf{\Gamma_b}^{(k+1)} - \mathbf{\Gamma_b}^{(k)}$. (The inverse square of the condition number is a good tolerance since Eq. (3.48) features left- and right-multiplication by $\mathbf{A}^{\#}$.)

Images from Tests 3 and 4 are shown in Figure 3.12 and Figure 3.11 and Table 3.2 gives statistics for the reconstruction errors. Images obtained using the full-rank covariance estimate

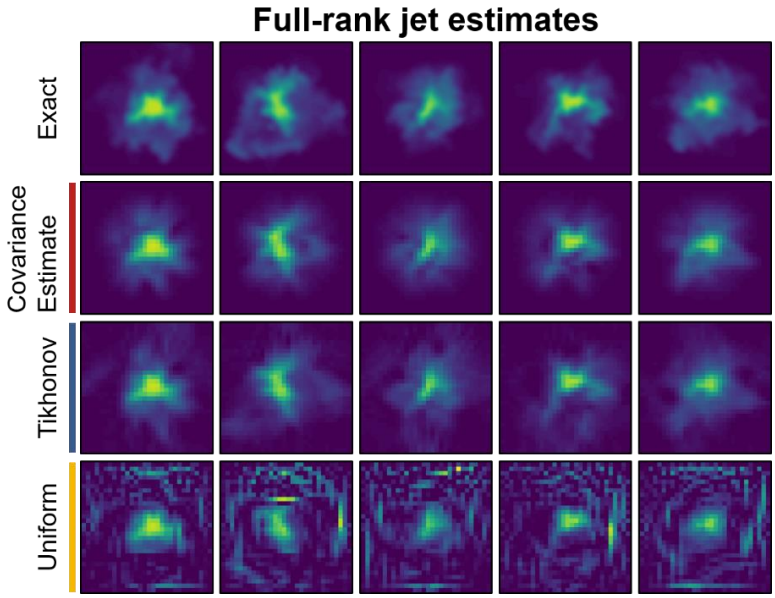

Figure 3.11: Representative estimates from Test 3; the use of a covariance estimate produced the best results while the smoothing prior blurred features about the jet's edge. Pseudoinversion of the full rank operator amplified noise.

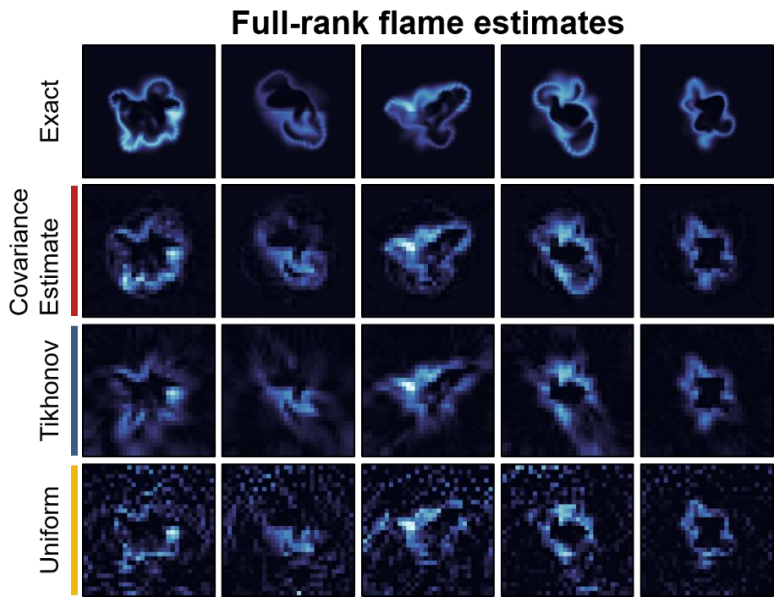

Figure 3.13: Representative estimates from Test 4; results were similar to Test3: the covariance estimate gave the best reconstructions, Tikhonov estimates were over-smoothed, and uniform estimates generally failed to resolve the flame front.

outperformed the smoothing prior Tests 3 and 4; moreover, both of these priors outperformed the uniform prior. Artifacts due to Tikhonov regularization were qualitatively-similar in the limited-data and full-rank simulations. Tikhonov errors are marked by over-smoothing of internal structures and over-estimation of the target boundary, which reflects the full-field covariance implicit in the Tikhonov matrix. By contrast, reconstructions informed by an estimate of $\mathbf{\Gamma}_x$ captured accurate detail throughout the flow, especially at the periphery.

Table 3.2: Euclidean Distance and SSIM Distributions for Tests 3 and 4

Prior	**Test 3**				**Test 4**			
	Euclidean		*SSIM*		*Euclidean*		*SSIM*	
	Mean	*Dev.*	*Mean*	*Dev.*	*Mean*	*Dev.*	*Mean*	*Dev.*
Cov. Est.	0.167	0.051	0.842	0.040	0.300	0.064	0.614	0.058
Tikhonov	0.173	0.043	0.657	0.056	0.433	0.085	0.284	0.039
Uniform	0.743	0.152	0.230	0.056	0.742	0.102	0.195	0.027

Results from the final test reinforce the findings of the limited-data tests. Accurate covariance information improves the quality of reconstructions, especially in the case of a complex process. Differential performance of the covariance estimate and Tikhonov priors was more pronounced with increasing complexity of the flow field. This trend is due to the full-field covariance implicit

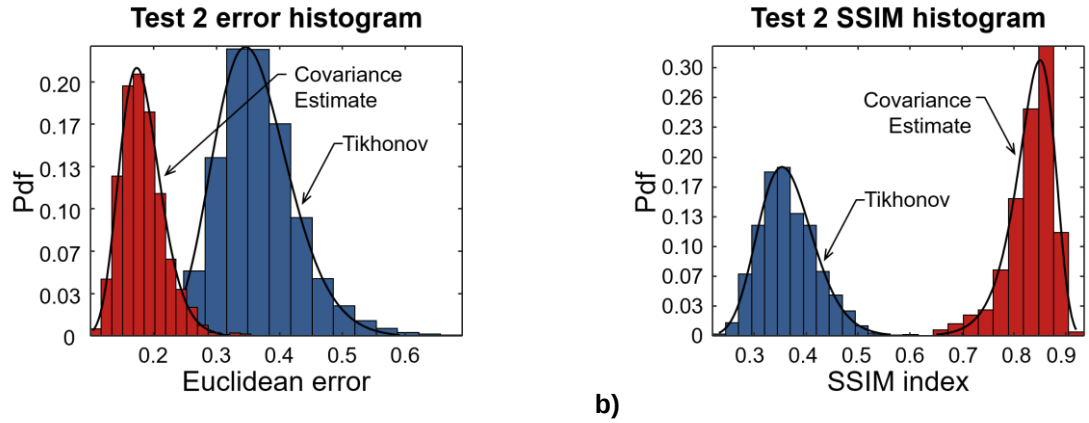

Figure 3.15: Histograms of a) Euclidean distances and b) SSIM indices for Test 2 reconstructions.

in the Tikhonov matrix, which was less compatible with sharp discontinuities in the flame front phantoms than with the smooth jet structures. (Neither flow is well-modelled by a full-field covariance, however.) Taken together, results from the jet and flame studies suggest that covariance data from the measurements should be incorporated into CST reconstructions.

3.4.3 Comparing accuracy metrics for a CST study

The normalized Euclidean distance between image vectors is the standard measure of error in CST. Distance metrics diminish the impact of structural perturbations that may be of interest to CST practitioners. The SSIM index is an alternative to the Euclidean distance, which remaps errors to emphasize structural differences between images, even in low-contrast regions. Errors in CST include low-contrast blurring of internal flow structures and poorly-resolved flow boundaries, readily apparent in the reconstructions in Figure 3.8, Figure 3.9, Figure 3.11, and Figure 3.13. It was hypothesized that the SSIM index could better identify such errors than the normalized Euclidean distance.

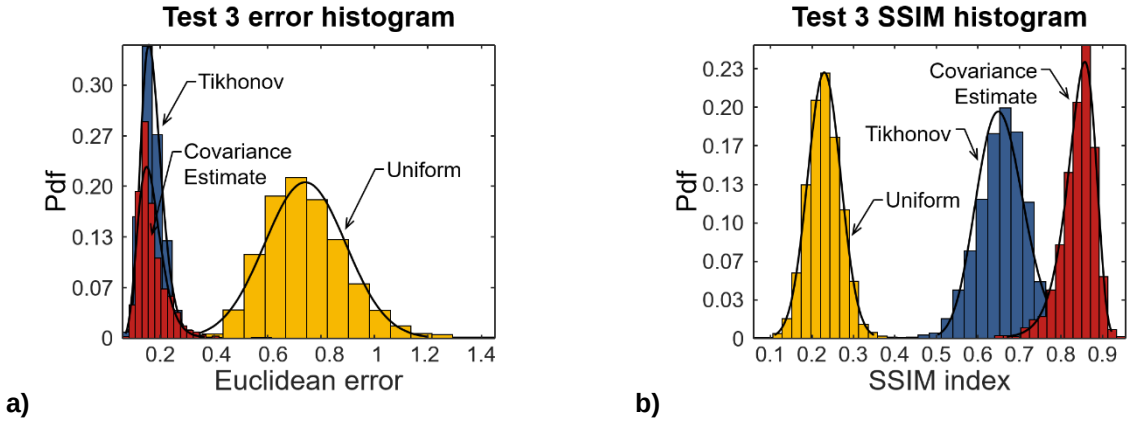

Figure 3.14: Histograms of a) Euclidean distances and b) SSIM indices for Test 3 reconstructions.

Table 3.1 and Table 3.2 show significant differences between the mean SSIM indices for covariance estimate and Tikhonov-based reconstructions in all four tests. These results agree with the qualitative differences apparent in the reconstructions. The same pattern held for Euclidean distances in the full-rank tests, though Euclidean distance scores for the covariance estimate and Tikhonov reconstructions were considerably more similar in Tests 1 and 3. Histograms of the normalized Euclidean distance and SSIM index for Test 2 are shown in Figure 3.15; Figure 3.14 shows the same histograms for Test 3. These plots illustrate the ability of the SSIM index to discriminate structural differences that are clearly visible in the reconstructions.

The utility of an error metric in CST depends on the objective of an experiment. However, it is generally desirable for quality metrics to be sensitive to common forms of error. The normalized Euclidean distance becomes less useful with increasing resolution and clearly neglects important errors in CST reconstructions. Moreover, these errors are clearly captured by the SSIM index, as evidenced by the qualitative reconstruction quality and spread of SSIM indices. It is therefore suggested that the SSIM index is often a preferable measure of accuracy in the CST context, relative to the normalized Euclidean distance.

3.5 Conclusions

A large portion of CST experiments feature turbulent jets and flames. Turbulence is often characterized by unstable fluctuations and stable statistical properties. The statistical regularities of turbulent flows can be useful in the context of Bayesian gas-phase tomography, which requires a prior pdf to quantify assumptions about the target. Ideally, given full knowledge about a flow's boundary and initial conditions, the prior pdf should assume the form of turbulent fluctuations. As such, estimates of the distribution of fluctuations in a flow can be used to construct a prior that will improve the accuracy of Bayesian reconstructions. This chapter began with an overview of self-similarity in turbulent jets, which is a classic finding of research on turbulence. An extended argument was presented in support of the assumption that fluctuations, projected onto the basis, will follow a joint-normal distribution. Together, these results were used to develop procedures for estimating the covariance matrix of a target in limited-data and full-rank scenarios. Four numerical tests were conducted to verify the performance of reconstructions based on these procedures.

Self-preserving jets feature pdfs that have a consistent structure, which stretches out as the flow evolves. The scale profiles derived in Section 3.1.3 enable CST practitioners to image the

variance of scalar fluctuations via LOS data. First, a regression is performed to locate the position and scale of the mean distribution of concentration. Next, the relationship between the first two moments of the scalar pdf are leveraged to estimate the target variance. This structure is combined with a square-exponential autocorrelation function to complete an estimate of the covariance matrix, which is finally scaled using the measurement covariance. An extension of this method is proposed for multiple sources and an alternative approach is developed for an arbitrary first moment. Two limited-data tests were conducted to verify the covariance estimation procedure based on self-similar scale functions. Reconstructions were compared to Tikhonov estimates (i.e., a smoothness prior) with and without a non-negativity constraint. Images reconstructed with a self-similarity covariance estimate were more accurate than Tikhonov reconstructions in both tests. Moreover, improvements were especially pronounced absent the non-negativity prior, which resembles real-time imaging conditions.

Covariance estimation for a gas jet or plume based on scale functions can be conducted regardless of the rank of the tomography system. However, CST experiments commonly target turbulent flames, which exhibit sharp discontinuities at the flame front and are not amenable to a similarity analysis. These experiments typically feature a dense measurement array, resulting in a full-rank system. Reconstructions obtained by direct inversion of a full-rank operator are corrupted by noise so prior information is still required and covariance estimation can be used to improve the prior. Therefore, a method was developed using approximation errors to stabilize direct estimation of the target covariance. As with the limited-data case, numerical tests were conducted to verify the algorithm's performance. LES phantoms of a turbulent jet and flame were measured using a dense array and reconstructions were performed with a covariance estimate, Tikhonov matrix, and uniform prior. Images computed with the covariance estimate were superior in both tests. Moreover, differences between the accuracy of jet and flame reconstructions showed that the utility of accurate covariance data increased with the complexity of the target.

Finally, the standard error metric in CST (the normalized Euclidean distance) was compared to the structural similarity index. Distance metrics are known to become less useful as the dimension of vectors is increased. By contrast the SSIM index remaps the classic CST error to emphasize structural differences between the ground truth and reconstructed vectors. Both metrics verified the superior performance of reconstructions based on a covariance estimate. However, the

SSIM index was shown to better distinguish the visual quality of CST images than did the normalized Euclidean distance.

Chapter Four
Statistically-Optimal Gas-Phase Tomography

Reconstruction accuracy in gas-phase tomography depends on the arrangement of optical paths in the probe volume, magnitude of model error, and validity of the prior information associated with the inverse algorithm. Each of these elements interacts with the discretization scheme in a complex manner. The freedom to adjust the measurement operator, beam arrangement, finite basis, and prior pdf in CST results in a large design space, featuring numerous convoluted trade-offs. Previous research on the design of measurement systems for gas-phase tomography has applied classical objective functions to choose between candidate beam arrays; and studies that compare discretization schemes have been observational in nature. Bayesian updating is an approach to inverse analysis that can be used to re-interpret classical design-of-experiment (DOE) techniques, taking account of parameter uncertainty and including prior information. This chapter first demonstrates how the statistical approach to tomography improves objective functions for experimental design by incorporating information about the reconstruction algorithm and target distribution into the function. In the second section, a rigorous mathematical framework is developed from Bayes' equation to compare alternative bases for reconstruction.

Research on experimental design in industrial tomography is driven by advances in opto-electronic components, which have made it possible to instrument fluid enclosures with a flexible arrangement of measurement paths at a low cost. For instance, Carey et al. [130] multiplexed modulated diode lasers; shone the light through a piston along 28 paths using fiber optic cables and micro-optic lenses, embedded in the chamber wall; and recovered the absorption signals with lock-in detectors. The number of paths through such a domain is restricted by the need to preserve

the piston's structural integrity and heat transfer properties but the precise arrangement of beams is relatively unconstrained. Salem et al. [174], Terzija et al. [89], and Stritzke et al. [149] provide further examples of limited-data CST experiments: on a packed bed adsorber, lab-scale plume, and exhaust system, respectively. Motivated by this work, considerable attention has focused on the mathematics of optimal experiments in limited-data CST. Reconstruction with a rank-deficient operator is a strong function of the regularization scheme and previous approaches to choosing the beam array neglected the crucial role of a prior information. The first section of this chapter reviews the existing literature on DOE in CST and presents a Bayesian algorithm to optimize the position of optical paths in limited-data tomography. Structural relationships between the deterministic and Bayesian objective functions are noted and numerical tests are presented to verify the superior performance of the Bayesian algorithm.

Some initial discretization scheme, or set of candidate discretizations, is required to optimize the measurement array for CST imaging. Upon the selection of an arrangement and completion of an experiment, however, the discretization basis is free to vary. The ideal basis to represent a gas-phase flow field depends on the scale of structures in the gas and density of measurement paths. These aspects of an experiment are not known with perfect precision prior to measurement and may deviate from prior expectations in actuality. For this reason, the optimal basis for an experiment can depart from the initial choice. Ideally, data from the experiment could be combined with prior information about the flow field to select an appropriate basis to estimate the target distribution during reconstruction. However, no general method has been proposed to establish the relative utility of discretization schemes for a set of measurement vectors in limited-data CST.

Reconstruction accuracy is also sensitive to the discretization scheme in full-rank experiments. Full-rank systems are necessarily overdetermined due to their large number of collinear ray-sums, which are required to obtain unique information about internal basis functions. Dense arrays are implemented by placing multiple cameras around the flow field, e.g., the 24-camera setup of Mohri et al. [218], or directing laser light through a domain with scanning optics and mirrors, described in detail by Tsekenis and Polydorides [286]. The relative position of optical paths in a full-rank CST system is not easily modified, but the condition of the measurement operator can be changed by adjusting the grid resolution. Previous studies examined the relationship between the discretization scheme, number of views, and accuracy, by comparing experimental reconstructions [218]. However, the space of possible bases and views is infinite and

most CST practitioners employ heuristic methods to discretize the probe volume. Therefore, as with limited-data CST, a mathematically-rigorous approach to discretization in full-rank CST is desired in order to navigate the trade-offs between resolution and accuracy in the context of posterior uncertainty.

The second section of this chapter addresses the need to quantify the utility of finite bases in limited-data and full-rank CST. Together, the discretization scheme, measurement operator, and likelihood and prior pdfs constitute a model of the flow field. Bayesian inference can be conditioned on the model, which is treated as an unknown quantity. Different models are then compared using a Bayes factor, which is a ratio of the candidate models' *model likelihood*. This chapter describes the first application of Bayesian model comparison to CST: to select a measurement operator and grid resolution for reconstruction. Moreover, as the prior is itself a component of the model, it is shown how Bayesian model comparison, informed by measurement data, can be applied to identify the covariance structure of a target. The technique is demonstrated with numerical tests based on an advanced simulation of a catalytic reduction. This scenario is motivated by the recent CST experiment of Stritzke et al. [149], which featured extremely restricted measurement conditions. Model likelihoods are presented in logarithmic form and decomposed. Finally, it is shown how components of the model likelihood relate to reconstruction accuracy.

Results from the DOE and model selection tests demonstrate how Bayesian imaging can be used to obtain accurate reconstructions, even under restrictive measurement conditions. The Bayesian framework for CST implies a statistical approach to experimental design and model selection, which improve on classical techniques and support the use of Bayesian methods in gas-phase tomography.

4.1 Design of Limited-Data Tomography Experiments

4.1.1 Deterministic design-of-experiment techniques

Several methods have been proposed to assess the quality of limited-data arrays in hard-field tomography. These include qualitative methods, equations based on intuition about the reconstruction algorithm, and advanced metrics that follow from a formal derivation. Existing procedures for beam optimization, summarized below, are united by the fact that they neglect prior information about the flow field.

4.1.1.1 Uniform sinogram sampling

Rattey and Lindgren [287] presented a Fourier analysis of the 2D Radon transform to identify an appropriate grid and measurement spacing for medical imaging by limited-data X-ray tomography. Their results were obtained for a regular array of optical paths, i.e., a parallel- or fan-beam arrangement. Terzija et al. [89] interpreted this analysis for irregular beam arrangements in gas-phase tomography, where the target is more amenable to simple priors (such as a smoothness prior) and the fluid area may be enclosed, which prevents periodic sampling by a mobile measurement hub (typical of medical imaging devices). Based on their interpretation of Rattey and Lindgren [287], Terzija et al. [89] argued that reconstruction with the modified Landweber algorithm effectively interpolates data in sinogram space.

As discussed in Chapter Two, each optical path is associated with a set of sinogram coordinates, (s, θ), and Terzija et al. [89] sought measurement arrays that uniformly-sampled a large region of sinogram space. They conducted tests of candidate beam arrangements with a series of phantoms. The authors considered uniform and irregular 32-beam arrays and an irregular 27-beam array, all shown in Figure 4.1 with the corresponding sinogram coordinates. Euclidean distance statistics were computed for these systems and the relationship between the sinogram

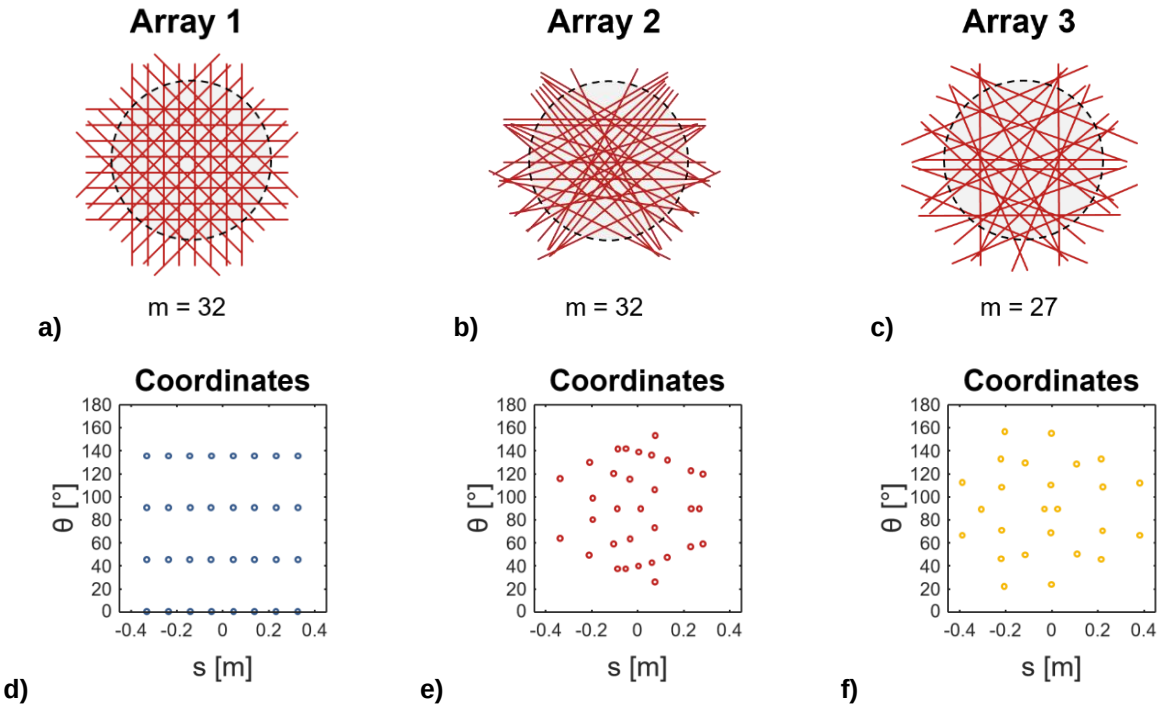

Figure 4.1: Beam geometry (a-c) and sinogram plots (d-f) for three limited-data measurement arrays from Terzija et al. [89]: a,d) a regular 32-beam array, b,e) an irregular 32-beam array, and c,f) an irregular 27-beam array.

plots and reconstruction accuracy was discussed in qualitative terms. The authors concluded that the performance of an array was related to its coverage of sinogram space.

Terzija et al. [89] presented their beam selection procedure as a heuristic method but did not propose a metric to quantify the coverage of sinogram space by candidate arrays. Daun [288] analyzed the sinogram point plots in Figure 4.1 using a point set discrepancy, which measures the uniformity of a distribution of points. He computed the discrepancy for each array and reconstructed Gaussian phantoms with Tikhonov and modified Landweber algorithms. There was no correspondence between the discrepancy rank and reconstruction statistics, irrespective of the algorithm used for reconstruction.

4.1.1.2 Minimizing regularization error with the resolution matrix

The concept of a resolution matrix is based on a perturbation analysis, in which the regularized inversion of a linear system is manipulated to explicitly attribute reconstruction errors to noise and regularization. Twynstra and Daun [289] derived a resolution matrix for Tikhonov-regularized CST. First, they presented the regularized inverse,

$$\mathbf{A}^{\#} = (\mathbf{A}^T\mathbf{A} + \lambda^2\mathbf{L}^T\mathbf{L})^{-1}\mathbf{A}^T, \tag{4.1}$$

where $\mathbf{L}$ is the first-order Tikhonov matrix from Chapter Two and λ is a regularization parameter. The reconstruction, $\mathbf{x}^{\text{TK}}$, is found by right-multiplying the data by the regularized inverse, $\mathbf{x}^{\text{TK}} = \mathbf{A}^{\#}\mathbf{b}$. The noisy data, $\mathbf{b}$, can be decomposed,

$$\mathbf{b} = \mathbf{b}^{\text{exact}} + \mathbf{e}^{\text{meas}} = \mathbf{A}\mathbf{x}^{\text{exact}} + \mathbf{e}^{\text{meas}}, \tag{4.2}$$

where $\mathbf{b}^{\text{exact}}$ is an idealized measurement, defined as $\mathbf{A}\mathbf{x}^{\text{exact}}$, and $\mathbf{e}^{\text{meas}}$ is a general error term, given by the residual $\mathbf{b} - \mathbf{b}^{\text{exact}}$.[56] As in Chapter Three, $\mathbf{x}^{\text{exact}}$ is the projection of the ground truth distribution onto the basis. Using Eqs. (4.1) and (4.2), the Tikhonov estimate is found to be

$$\mathbf{x}^{\text{TK}} = \mathbf{A}^{\#}\mathbf{A}\mathbf{x}^{\text{exact}} + \mathbf{A}^{\#}\mathbf{e}^{\text{meas}} = \mathbf{R}\mathbf{x}^{\text{exact}} + \mathbf{A}^{\#}\mathbf{e}^{\text{meas}}, \tag{4.3}$$

where $\mathbf{R} = \mathbf{A}^{\#}\mathbf{A}$ is the resolution matrix. This quantity describes how the measurement operator and Tikhonov matrix modify the idealized projection, $\mathbf{x}^{\text{exact}}$, in reconstruction. Next, the residual, $\mathbf{e}^{\text{TK}}$, is presented in terms of the resolution matrix,

$$\mathbf{e}^{\text{TK}} = \mathbf{x}^{\text{exact}} - \mathbf{x}^{\text{TK}} = (\mathbf{I} - \mathbf{R})\mathbf{x}^{\text{exact}} - \mathbf{A}^{\#}\mathbf{e}^{\text{meas}}. \tag{4.4}$$

[56] By this definition, $\mathbf{e}^{\text{meas}}$ contains both noise and model error.

The first term in Eq. (4.4) describes the direct contribution of regularization to reconstruction error and the second term describes the amplification of measurement error by $\mathbf{A}^{\#}$. Amplification errors can also be expressed in terms of the resolution matrix: $-\mathbf{R}\mathbf{A}^T(\mathbf{A}\mathbf{A}^T)^{-1}\mathbf{e}^{\text{meas}}$.

The measurement array determines the structure of the resolution matrix, which plays a role in regularization error and the amplification of measurement noise. In a full-rank experiment, there is a trade-off between regularization and amplification errors. By contrast, in limited-data tomography, the operator has a non-trivial null space and $\mathbf{e}^{\text{TK}}$ is dominated by $(\mathbf{I} - \mathbf{R})\mathbf{x}^{\text{exact}}$. Twynstra and Daun [289] conjectured that reconstruction accuracy in limited-data CST would be maximized by selecting a measurement array to minimize $(\mathbf{I} - \mathbf{R})\mathbf{x}^{\text{exact}}$, which suggests a "resolution matrix objective function,"

$$F_{D1}(\mathbf{A}) = \left\| \mathbf{I} - \mathbf{R}(\mathbf{A}) \right\|_2^2 . \tag{4.5}$$

The authors used a set of LES phantoms to test parallel-beam, fan-beam, and unstructured arrays. Reconstructions were computed by first-order Tikhonov regularization and errors were compared to Eq. (4.5). Twynstra and Daun [289] found that beam arrangements selected according to F_{D1} tracked reconstruction errors.

4.1.1.3 Maximizing physical coverage with a grid weight

Algebraic reconstruction, used in most CST experiments (and almost all limited-data scenarios), effectively distributes measurements back along the corresponding optical path. Each sweep of the basic ART algorithm updates pixels once for each beam that that transects the pixel. Following this observation, Song et al. [290] reasoned that candidate beam arrays should be compared in terms of their coverage of pixels. The authors proposed an objective function to quantify this coverage,

$$F_{D2}(\mathbf{A}) = \frac{1}{n}\sum_{j=1}^{n}\sum_{i=1}^{m(j;\mathbf{A})}\frac{1}{2^{i-1}} = 2 - \frac{1}{n}\sum_{j=1}^{n} 2^{1-m(j;\mathbf{A})} , \tag{4.6}$$

where n is the number of pixels and $m(j; \mathbf{A})$ is the number of beams transecting the jth pixel.[57,58] F_{D2} maximized by beams that effectively cover the measurement plane. The effect of this metric can be understood by considering an individual optical path. Rays contribute to F_{D2} by transecting

[57] The function $m(j; \mathbf{A})$ returns the number of non-zero entries in the jth column of $\mathbf{A}$.

[58] Song et al. [290] present the double summation in Eq. (4.6), which is equivalent to the simplified expression on the right-hand side.

pixels; but the marginal contribution of this intersection to F_{D2} is diminished as more measurement paths cross a pixel. In contrast to the work of Terzija et al. [89], F_{D2} promotes broad coverage of the flow field in physical space as opposed to sinogram space.

Equation (4.6) was motivated by the concept of back projection but the precise form of the F_{D2} was not derived by mathematical analysis of the ART. Song et al. [290] simulated their approach with a Gaussian phantom and modified ART, with smoothing applied to **x** at each step. They found their objective function was maximized by the beam arrangement that minimized reconstruction error. However, the correlation between F_{D2} and the reconstruction statistics was not reported.

4.1.1.4 Minimizing the collinearity of ray-sums

Ray-sums in gas-phase tomography are a linear approximation to the measurement operator, specific to the reconstruction basis. The maximum rank of the ray-sum matrix for a set of *m* beams in a limited-data system is *m*, but an infinite set of arrangements can share this rank. Optical paths with similar sinogram coordinates have many near-parallel ray-sums, which can be problematic in reconstruction because similar row vectors are susceptible to noise in inversion, even if the primary source of reconstruction error is regularization. Moreover, collinear rows contain redundant information. Arrays with unnecessary collinear beams fail to capitalize on information that could potentially be extracted by a better arrangement with the same number of rays.[59] Yu et al. [291] proposed a metric to minimize the angle between rows of the ray-sum matrix (i.e., the angle between the vectors with support Φ),

$$F_{D3}(\mathbf{A}) = \max\left\{\mathbf{O}(\mathbf{A}) - \mathbf{I}\right\}, \tag{4.7}$$

where $\mathbf{O} \in \mathbb{R}^{m\times m}$ contains the cosine of the angle between ray-sums with each other sum, θ_{ij}. The element-wise definition of **O** is

$$O_{ij} = \cos(\theta_{ij}) = \frac{\mathbf{a}_i \mathbf{a}_j^{\,T}}{\left\|\mathbf{a}_i\right\| \cdot \left\|\mathbf{a}_j\right\|}, \tag{4.8}$$

where $\mathbf{a}_i$ and $\mathbf{a}_j$ are the *i*th and *j*th row of **A**. F_{D3} is zero for a set of orthogonal ray-sums and unity for any arrangement with a set of duplicate rays.

[59] Alternatively: nearly-collinear ray-sums can be eliminated with minimal effect on the reconstruction accuracy. This can significantly reduce the cost of measurement in scenarios that require modifications to a fluid enclosure, as in the experiments of Carey et al. [130] and Stritzke et al. [149].

Yu et al. [291] conducted numerical tests using three phantoms: a superposition of two Gaussian peaks, separated by a random offset; a Gaussian peak and square platform; and a third phantom, devised to resemble a turbulent flame. A large number of random arrays were generated and reconstructions were computed with a simple ART algorithm as well as Tikhonov regularization. The authors compared the quality of reconstructions to Eqs. (4.5) and (4.7) and concluded that the collinearity metric was a better predictor of accuracy than the resolution matrix function, F_{D1}.

4.1.2 Bayesian approach to the design-of-experiments

Design-of-experiment techniques in the previous section were all motivated by the reconstruction algorithm in some way, but do not reflect expectations about the experiment. Yet some information about the target process and geometry of the probe volume is always known, and this knowledge can be usefully incorporated into the objective function. The Bayesian formulation of tomography is predicated on the role of prior information and Bayes' equation suggests a superior approach to experimental design.

Conceptually, optimal beam arrays for tomography are those that maximize confidence in the reconstructed image, based on a statistical model of tomographic inversion. Bayesian DOE begins with an expression for the posterior covariance, which quantifies joint-uncertainties in the reconstructed parameters as a function of the measurement array and prior pdf. Next, an appropriate mapping is selected to generate a scalar summary of the posterior. Ideally, this metric (or *summary statistic*) corresponds to one's overall confidence in the reconstructions. The summary statistic is calculated for candidate arrangements using a fixed prior;[60] it is hypothesized that the posterior confidence will track the average accuracy of CST images. This section describes the calculation of a posterior covariance matrix and traditional summary statistics, used to construct a Bayesian objective function. Finally, Bayesian DOE formulas are compared to the deterministic objective functions from the previous section.

4.1.2.1 Calculating a posterior covariance matrix

Bayesian reconstruction yields a posterior pdf, $\pi(\mathbf{x}|\mathbf{b})$, which quantifies the relative probability of candidate vectors subject to an observation and prior assumptions about the flow field. Chapter

[60] Experiments are designed before measurement so the prior must be constant (whereas the prior may be updated between reconstructions in real time imaging or post-processing). As such, the differential uncertainty between the prior and posterior covariance is only due to the information gained from a measurement.

Two presented joint-normal likelihood and prior pdfs for gas-phase tomography, $\pi(\mathbf{b}|\mathbf{x})$ and $\pi_{pr}(\mathbf{x})$, which were further explored in Chapter Three. The joint-normal prior is conjugate to the joint-normal likelihood such that the posterior is also joint-normal. One important consequence of this shared form is that analytic expressions of the posterior mean and covariance can be expressed in terms of the likelihood and prior parameters. The posterior pdf is

$$\pi(\mathbf{x}\,|\,\mathbf{b}) = \det(2\pi\boldsymbol{\Gamma}_{\mathbf{x}|\mathbf{b}})^{-1} \exp\left\{-\frac{1}{2}\left\|\mathbf{x}-\mathbf{x}^{\mathrm{MAP}}\right\|_{\mathbf{L}_{\mathbf{x}|\mathbf{b}}}^2\right\}, \tag{4.9}$$

in which the MAP estimate is the mean, $\boldsymbol{\Gamma}_{\mathbf{x}|\mathbf{b}}$ is the posterior covariance, and $\mathbf{L}_{\mathbf{x}|\mathbf{b}} = \mathrm{chol}(\boldsymbol{\Gamma}_{\mathbf{x}|\mathbf{b}}^{-1})$. According to Bayes' equation, the posterior pdf is proportional to the product of $\pi(\mathbf{b}|\mathbf{x})$ and $\pi_{pr}(\mathbf{x})$,

$$\pi(\mathbf{x}\,|\,\mathbf{b}) \propto \det(2\pi\boldsymbol{\Gamma}_{\mathbf{e}})^{-1/2} \det(2\pi\boldsymbol{\Gamma}_{\mathbf{x}})^{-1/2} \exp\left\{-\frac{1}{2}\left\|\mathbf{b}-\mathbf{A}\mathbf{x}\right\|_{\mathbf{L}_{\mathbf{e}}}^2 - \frac{1}{2}\left\|\mathbf{x}-\boldsymbol{\mu}\right\|_{\mathbf{L}_{\mathbf{x}}}^2\right\}. \tag{4.10}$$

Arguments in Eqs. (4.9) and (4.10) all reside in the exponential terms and must be equal to satisfy the proportionality in Eq. (4.10). The L-norm notation signifies a square system,

$$\left\|\mathbf{x}-\boldsymbol{\mu}\right\|_{\mathbf{L}_{\mathbf{x}}}^2 = (\mathbf{x}-\boldsymbol{\mu})^T(\mathbf{L}_{\mathbf{x}}{}^T\mathbf{L}_{\mathbf{x}})(\mathbf{x}-\boldsymbol{\mu}) = (\mathbf{x}-\boldsymbol{\mu})^T\boldsymbol{\Gamma}_{\mathbf{x}}{}^{-1}(\mathbf{x}-\boldsymbol{\mu}), \tag{4.11}$$

which implies that

$$(\mathbf{x}-\mathbf{x}^{\mathrm{MAP}})^T\boldsymbol{\Gamma}_{\mathbf{x}|\mathbf{b}}{}^{-1}(\mathbf{x}-\mathbf{x}^{\mathrm{MAP}}) = (\mathbf{b}-\mathbf{A}\mathbf{x})^T\boldsymbol{\Gamma}_{\mathbf{e}}{}^{-1}(\mathbf{b}-\mathbf{A}\mathbf{x}) + (\mathbf{x}-\boldsymbol{\mu})^T\boldsymbol{\Gamma}_{\mathbf{x}}{}^{-1}(\mathbf{x}-\boldsymbol{\mu}). \tag{4.12}$$

Terms in Eq. (4.12) are expanded and regrouped by order of $\mathbf{x}$ multiplication, which yields an explicit expression for the posterior,

$$\boldsymbol{\Gamma}_{\mathbf{x}|\mathbf{b}} = \left(\mathbf{A}^T\boldsymbol{\Gamma}_{\mathbf{e}}{}^{-1}\mathbf{A} + \boldsymbol{\Gamma}_{\mathbf{x}}{}^{-1}\right)^{-1}. \tag{4.13}$$

Substituting $\boldsymbol{\Gamma}_{\mathbf{x}|\mathbf{b}}$ into Eq. (4.12) and solving for $\mathbf{x}^{\mathrm{MAP}}$ results in an alternative equation for Bayesian MAP estimates,

$$\mathbf{x}^{\mathrm{MAP}} = \boldsymbol{\Gamma}_{\mathbf{x}|\mathbf{b}}\left(\mathbf{A}^T\boldsymbol{\Gamma}_{\mathbf{e}}{}^{-1}(\mathbf{b}-\bar{\mathbf{b}}) + \boldsymbol{\Gamma}_{\mathbf{x}}{}^{-1}\boldsymbol{\mu}\right). \tag{4.14}$$

The posterior covariance in Eq. (4.13) is only a function of the measurement operator, error model, and prior covariance. It should be noted that the data is not included in this expression and, as a result, Bayesian functions to optimize the beam arrangement can be developed using $\boldsymbol{\Gamma}_{\mathbf{x}|\mathbf{b}}$.

4.1.2.2 Summary statistics of the posterior

Bayesian DOE proceeds by first quantifying the information that can be extracted from an observation (relative to prior assumptions about the inference) and then adjusting the measurement

setup to maximize this information—thereby maximizing the accuracy of parameter estimates. One resource for characterizing informative gain is the posterior covariance matrix. Values of $\mathbf{\Gamma_{x|b}}$ account for variance and correlation that is: i) inherent in the parameters of interest, encoded in the prior, and ii) propagated through to parameter estimates by inversion, originating from noise and model error. It can be difficult to comprehend the implications of $\mathbf{\Gamma_{x|b}}$ as a whole, especially if there are many parameters, the parameters of interest are intrinsically correlated, or the measurement operator convolves information about individual parameters. Each of these complications arises in gas-phase tomography so an appropriate summary of the posterior covariance is necessary to quantify the informative of CST measurements.

Several criteria have been developed to relate $\mathbf{\Gamma_{x|b}}$ to statistical attributes of the parameter estimates. The most prevalent of these are A-optimality, which minimizes the average variance of the MAP estimate, and D-optimality, which minimizes the spread of the posterior ellipse, accounting for both the variance and covariance of estimates. Further alternatives are available. For instance, E-optimality assigns a relative importance to the parameters, G-optimality minimizes the maximum variance of estimates, and so on. See Atkinson et al. [292] for a complete overview of optimality criteria in statistical experimental design. The Bayesian objective function for A-optimality is

$$F_{B1}(M) = \mathrm{tr}\left[\mathbf{\Gamma}_{\mathbf{x|b}}(M)\right] \tag{4.15}$$

and the D-optimality function is

$$F_{B2}(M) = \det\left[\mathbf{\Gamma}_{\mathbf{x|b}}(M)\right]. \tag{4.16}$$

Equation (4.16) accounts for parameter correlations that stem from the prior or ray-sums, where the latter convolves information about elements of $\mathbf{x}$. However, in limited-data CST, the operator is rank deficient by definition and the prior covariance is often degenerate. In this case, Eq. (4.13) must be approximated by pseudoinversion. F_{B1} is more robust to numerical artifacts in the posterior covariance than F_{B2} and, for this reason, the former criterion is preferred for the design of limited-data CST systems. Examples of degenerate priors include sample-based priors in which the flow does not occupy every pixel; first-order Tikhonov regularization (i.e., a smoothness prior); and linear approximations to the TV norm, discussed in Chapter Six.[61] In cases

[61] The presence of a degenerate prior does not pose a problem for CST imaging because reconstruction is based on the augmented system, which is overdetermined when the measurement operator and prior are combined.

where a suitable positive-definite prior is available, the determinant of $\mathbf{\Gamma_{x|b}}$ is a superior metric to the trace.

4.1.2.3 Relationship to deterministic techniques

Equations (4.5) to (4.7) were not developed to accommodate specific information about the flow field, whereas Eqs. (4.15) and (4.16) are explicit functions of the prior covariance matrix. Priors can be constructed to reflect the assumptions used to derive F_{D1} and F_{D3}; the resulting functions, F_{B1} and F_{B2}, can be compared to their deterministic counterparts. Doing so reveals similarities between the deterministic and Bayesian metrics and highlights the latter's ability to augment F_{D1} and F_{D3} with flow-specific information.

Twynstra and Daun [289] obtained an expression of the resolution matrix for CST with Tikhonov regularization, often employed in the Bayesian framework as a smoothness prior. Adopting this prior, the corresponding posterior covariance is

$$\mathbf{\Gamma}_{\mathbf{x|b}} = \left(\begin{bmatrix} \mathbf{L_e A} \\ \lambda \mathbf{L} \end{bmatrix}^T \begin{bmatrix} \mathbf{L_e A} \\ \lambda \mathbf{L} \end{bmatrix} \right)^{-1}, \tag{4.17}$$

where $\mathbf{L_e}$ is the Cholesky factor of the error covariance matrix and $\mathbf{L}$ is the first-order Tikhonov matrix. Equation (4.17) is substantially similar to the resolution matrix, though F_{D1} and F_{B1} differ in several ways. First, F_{B1} is weighted by the effects of noise and model error while F_{D1} is not; and second, there is no clear statistical interpretation of the norm of $\mathbf{I} - \mathbf{R}$, whereas the trace of Eq. (4.17) minimizes the variance of parameter estimates, by construction (insofar as $\mathbf{L}$ conforms to the spatial covariance of the flow). As such, while F_{B1} with a smoothness prior and F_{D1} will exhibit broadly similar trends, the Bayesian metric can be expected to provide some improvement over the resolution matrix. Moreover, since specific information about the distribution of variance in the flow field is almost always known, it is preferable to employ F_{B1} using an estimate of $\mathbf{\Gamma_x}$ that features a more realistic distribution of variance than the Tikhonov prior.

Comparison of the Bayesian functions with F_{D2} and F_{D3} is also instructive. F_{D1} assumes spatial smoothness whereas F_{D2} and F_{D3} make no assumptions about the flow field, which is equivalent to an IID prior covariance in Bayesian CST. (This prior is also realized by zeroth-order Tikhonov regularization, in which $\mathbf{\Gamma_x} = \lambda^{-2}\mathbf{I}$, where λ^{-2} is the average variance of the flow field.) Consistent with the minimal assumptions implicit in F_{D2} and F_{D3}, using $\sigma_m^2 = \lambda^{-2} = 1$ such that $\mathbf{L_e} = \mathbf{L_e} = \mathbf{I}$, the Bayesian functions become

$$F_{B1} = \mathrm{tr}\left[(\mathbf{A}^T\mathbf{A} + \mathbf{I})^{-1}\right] \text{ and } F_{B2} = \det\left[(\mathbf{A}^T\mathbf{A} + \mathbf{I})^{-1}\right]. \quad (4.18)$$

F_{D2} effectively counts the number of beams crossing each pixel, discounting duplicate beams in a heuristic manner. The Bayesian functions in Eq. (4.18) consider the outer product of ray-sums, $\mathbf{A}^T\mathbf{A}$,[62] which also tabulates the contribution of ray-sums at each pixel. However, A- and D-optimality measures of $\mathbf{A}^T\mathbf{A} + \mathbf{I}$ are statistically-motivated whereas Eq. (4.6) does not follow from a principled derivation. Rather than discounting additional beams in an arbitrary way, the outer product of $\mathbf{A}$ considers the length of beams throughout the pixels such that linearly-independent rows of $\mathbf{A}$ are explicitly preferred.

The matrix $\mathbf{O}$ of F_{D3} can be found by normalizing the elements of $\mathbf{A}\mathbf{A}^T$ by $\|\mathbf{a}_i\|\cdot\|\mathbf{a}_j\|$. This procedure neglects the length of rays through the domain, considering only their relative direction in $\mathbb{R}^m$. Beams that cross a single pixel are considered no worse than beams that traverse the entire domain.[63] Moreover, the max operator in Eq. (4.7) eliminates most of the information about the beam arrangement that is encoded in $\mathbf{O}$. F_{D3} only considers the most collinear pair of rays, which results in a non-convex objective function that may feature a non-unique minima, depending on the basis and number of rays. As such, while $\mathbf{O}$ contains useful information about the general suitability of a measurement array, the information is underutilized by F_{D3}; similar information is naturally incorporated in the Bayesian framework.

Deterministic objective functions for DOE in limited-data CST are motivated by the reconstruction algorithms but are not readily-adapted to specific information about the flow field. By contrast, the Bayesian objective functions are designed to maximize the informative content of CST measurements in the context of prior knowledge about a process. F_{B1} and F_{B2} share key structural features with each of the deterministic functions, which can be seen by substituting minimally-informative priors into Eqs. (4.15) and (4.16). Moreover, the trace and determinant of $\mathbf{\Gamma}_{\mathbf{x}|\mathbf{b}}$ relate to statistical attributes of the reconstructions, while the norm and max operators do not. All of these observations lend support to the use Bayesian functions in the design of CST experiments.

[62] Ray-sums are row vectors so $\mathbf{A}^T\mathbf{A}$ is an outer product of the rays while $\mathbf{A}\mathbf{A}^T$ is an inner product.

[63] For instance: beams crossing a single corner pixel are orthogonal to any beam that does not intersect that corner and nearly-orthogonal to all other beams. F_{D3} does not penalize such rays though they self-evidently represent a poor choice of position.

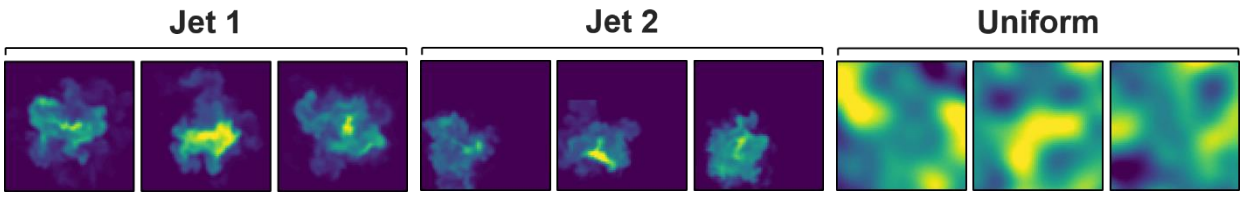

Figure 4.2: Three sample concentration distributions from each phantom set.

4.1.3 Simulating experimental design for limited-data CST

Three sets of phantoms were developed to represent a turbulent target: two iterations of a turbulent jet, called *jet* 1 and *jet* 2, and draws designed to mimic large-scale isotropic turbulence, called *uniform*. Figure 4.2 shows random draws that typify the phantom sets. Measurements for candidate arrays were obtained by high-order interpolation of the ground truth phantoms and reconstructions were computed with a 400-pixel basis. Deterministic objective functions were compared to Tikhonov-based reconstruction errors and the A-optimal Bayesian DOE function was compared to Bayesian reconstruction errors. The same prior was used for optimization and reconstruction.

Two scenarios were devised to appraise the performance of DOE functions. First, structured arrays were optimized with the deterministic functions and F_{B1}. Beams were arranged into conventional fan-beam and parallel-beam projections, parametrized by a single variable. The second test featured unstructured arrays, providing a useful test of the objective functions by exploring a large space of arrangements. Beam positions in the unstructured arrays were free to vary, independently, so long as each path transected the measurement plane. A genetic algorithm was developed to reduce the chance of stopping at a local minima.

4.1.3.1 Generating the turbulent phantoms sets

Jet phantoms were based on the LES from Chapter Three, which featured a round, momentum-driven CH_4 jet. Two separate simulations were started from a unique random seed and run for 20 s with a reporting timestep of 0.01 s. Both phantom sets contained 1,000 frames, from t = 3.75 s to 13.75 s in physical time, projected onto a 2,500-pixel ground truth basis. The 3.75 s delay represented several flow-through periods, selected to ensure fully-developed flow in the measurement plane. Phantoms for jet 1 were taken directly from the FDS output files, with no modifications made to the flow field. CH_4 distributions for jet 2 were scaled by 50% and offset from the centre of the measurement plane by $\Delta x = \Delta y = -0.25$ m. The second jet was transformed to test the effects of large-scale structure and asymmetry in the probe volume on the opjective functions' performance.

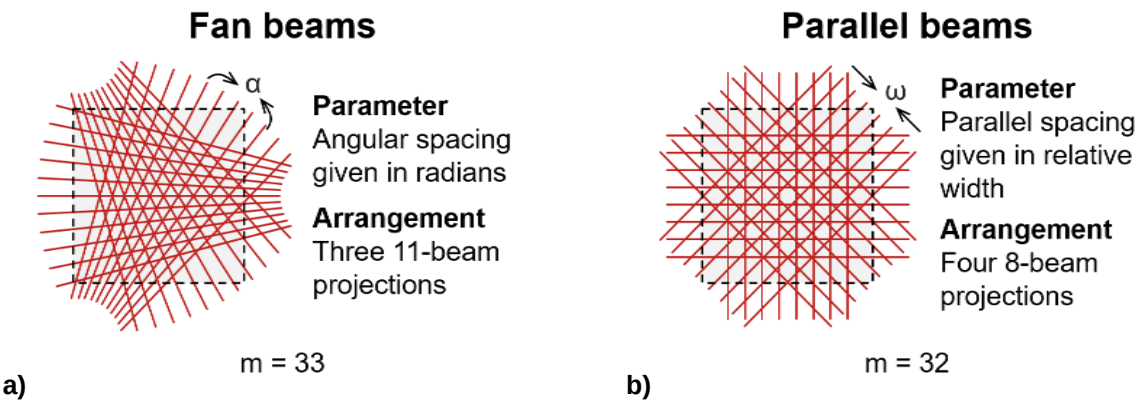

Figure 4.3: Structured array geometry: a) a three-projection fan-beam array with an angular spacing parameter, α, and b) a four-projections parallel-beam arrangement with a spacing parameter, ω.

Uniform phantoms were intended to resemble a large-scale quasi-isotropic flow field, reminiscent of an emissions tomography scenario (e.g., Vecherin et al. [278]). Moreover, spatial homogeneity is an ideal test case for the Tikhonov reconstruction algorithm and deterministic objective functions, which effectively presume spatial invariance in all moments of the target pdf. Isotropic distributions were drawn from a Gaussian random field with a uniform mean of 0.5 (interpreted as a CH_4 mole fraction) and square-exponential covariance. Elements of the covariance matrix were

$$\Gamma_{U,ij} = 0.2^2 \exp\left\{-\frac{\sqrt{-\ln(0.05)}}{21.5} d_{ij}^2\right\}, \tag{4.19}$$

where 0.2 is a pixel-wise standard deviation, 0.05 is the correlation over 21.5 pixels, and d_{ij} is the distance between the centroid of pixels i and j. As with jets 1 and 2, the uniform set comprised 1,000 phantoms, supported by the same 2,500-pixel basis.

All three phantom sets were divided into two, equally-sized subsets. The first subset, called the *sample-based subset*, was used to generate sample-based priors; the second, called the *reconstruction subset*, was used to simulate CST experiments. Slice data from the jet simulations was sequential whereas uniform phantoms were independent in time. This difference did not affect the results, however, since both algorithms were stationary.

4.1.3.2 Optimization of structured beam arrays

Figure 4.3 shows the structured measurement arrays from Twynstra and Daun [289]. In the first array, three 11-beam fan projections were rotated in 120° increments. The spread of the fan was parametrized by the angle α. A second format consisted of four 8-beam parallel projections, rotated

in 45° increments. Beam positions were determined by a spacing parameter, ω, which represented a fraction of the domain width. Fifty uniformly-spaced values of $\alpha \in [0.01, 0.07]$, in radians, and $\omega \in [0.075, 0.125]$ were scored using all three deterministic functions as well as F_{B1}, calculated with a sample-based prior.

4.1.3.3 Optimization of unstructured beam arrays

Unstructured measurement arrays with 32 beams were scored using F_{D1}, F_{D2}, F_{D3}, and F_{B1} for all three phantom sets. Beam positions were defined by sinogram coordinates. The space of possible arrangements was explored using a genetic algorithm, tailored to the study.

The genetic algorithm was initialized with a random arrangement of optical paths, called a *seed*, which was systematically modified to form a population of *spawn arrays*. The combination of the seed and spawn arrays formed a *generation*. Measurement arrays in each generation were assigned a fitness score by the DOE functions and the array with the best score was chosen to seed the next generation. This process was repeated until a single array was selected to seed 50 successive generations. Generations comprised 33 unique arrangements, including the seed. Spawn arrays were constructed as follows: one randomly-selected beam was adjusted in the first spawn, two randomly-selected beams in the second, and so on, with all 32 beams repositioned in the final spawn. All rays had equal probability of being repositioned; if selected, rays were assigned a new orientation by uniform draws of s and θ, from $(-0.5, 0.5)$ and $(0, \pi)$, respectively.

Four unstructured optimizations were run with the genetic algorithm. In the first test, F_{D1} was used to select the array and reconstructions were calculated for all three phantom sets. In the next three tests, F_{B1} was used to score arrays with a sample-based prior for the jet and uniform phantoms, separately. Every seed and spawn in every test was assigned a fitness score with F_{D1}, F_{D2}, F_{D3}, and F_{B1}. Two hundred and fifty phantoms were reconstructed for each candidate array using both the Tikhonov regularization and Bayesian techniques. The genetic algorithm was designed to explore a large space of beam arrangements and reconstruction statistics were compared to the DOE functions for different flow conditions and prior assumptions. Results were used to gauge the general correspondence between F_{D1}, F_{D2}, F_{D3}, and F_{B1} and the accuracy of CST images.

4.1.4 Results and discussion

4.1.4.1 Structured projection tests

The deterministic objective functions do not consider flow-specific prior information so each function exhibits a single trend with α and ω, irrespective of the target. Plots of F_{D1}, F_{D2}, and F_{D3} vs. α and ω are shown in Figure 4.4, along with the corresponding reconstruction errors for jet 1. The objective functions were normalized by their range and F_{D2} was inverted to illustrate the relevant trend, as this function was designed to be maximized. Also shown in Figure 4.4 are correlations between each objective function n and the mean reconstruction errors for jet 1. Statistics for all three phantom sets are presented below in Table 4.1.

Low values of the reconstruction error represent narrow projections; beams were more evenly-spaced across the domain at maximum values of α and ω. Performance of the structured arrays in a deterministic setting improved as α and ω were increased, increasing coverage of the domain by the optical paths in turn. This trend was captured by the resolution matrix function of Twynstra and Daun [289] and grid weight function of Song et al. [290], both of which exhibited correlations greater than 0.9 for all three flows. However, there was little correspondence between the maximum collinearity function of Yu et al. [291] and reconstruction error, regardless of the target. F_{D1} and F_{D2} prefer beam arrangements that broadly cover the measurement plane, which are ideal when little information about the flow is known. By contrast, F_{D3} only depends on the most collinear pair of ray-sums and does not directly relate to coverage of the domain. This metric was

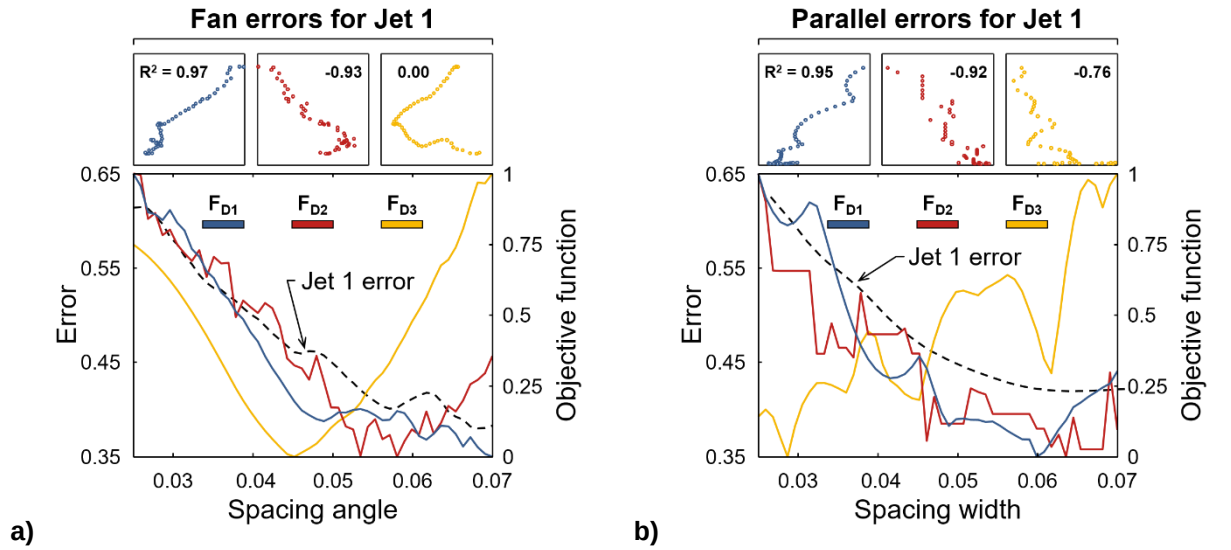

Figure 4.4: Comparison of the deterministic DOE functions and reconstruction statistics for jet 1 obtained with the a) three-projection fan-beam arrangement and b) four-projections parallel-beam.

quite sensitive to the transition of paths across pixel boundaries, which produced a superposition of consistent but opposing trends with the accuracy metric. Figure 4.4a shows that the maximum collinearity decreased from α = 0.01 to 0.045 rad but increased thereafter, resulting in zero correlation between F_{D3} and $\|\mathbf{e}\|_2$. F_{D3} was significantly correlated to reconstruction error for the parallel projections; but the correlation was negative, opposite the intended relationship.

Table 4.1: Reconstruction Statistics for the Fan- and Parallel-Beam Optimization Tests

Case		Jet 1			Jet 2			Uniform		
		$\|\mathbf{e}^{opt}\|_2$	R^2	*Diff.*	$\|\mathbf{e}^{opt}\|_2$	R^2	*Diff.*	$\|\mathbf{e}^{opt}\|_2$	R^2	*Diff.*
F_{D1}	*Fan*	0.383	0.971	32%	0.431	0.967	43%	0.135	0.965	12%
	Par.	0.342	0.954	31%	0.410	0.947	41%	0.140	0.904	9%
F_{D2}	*Fan*	0.614	-0.931	58%	0.793	-0.934	69%	0.252	-0.924	53%
	Par.	0.444	-0.918	47%	0.598	-0.927	60%	0.195	-0.914	35%
F_{D3}	*Fan*	0.461	0.001	58%	0.667	-0.184	50%	0.182	-0.041	35%
	Par.	0.426	-0.764	47%	0.409	-0.767	56%	0.186	-0.841	32%
F_{B1}	*Fan*	0.260	0.717	-	0.246	0.947	-	0.119	0.886	-
	Par.	0.237	0.998		0.242	0.893		0.127	0.960	

Figure 4.5 shows the Bayesian DOE function and mean reconstruction errors for all three target flows using both projections. Statistics for these tests are included in Table 4.1 along with the deterministic results. Unlike the deterministic functions, trends in F_{B1} depend on explicit prior assumptions about the flow. When the spatially-uniform sample-based prior was employed, F_{B1} reproduced the results of F_{D1} and F_{D2}. This correspondence supports the analysis in Section 4.1.2.3

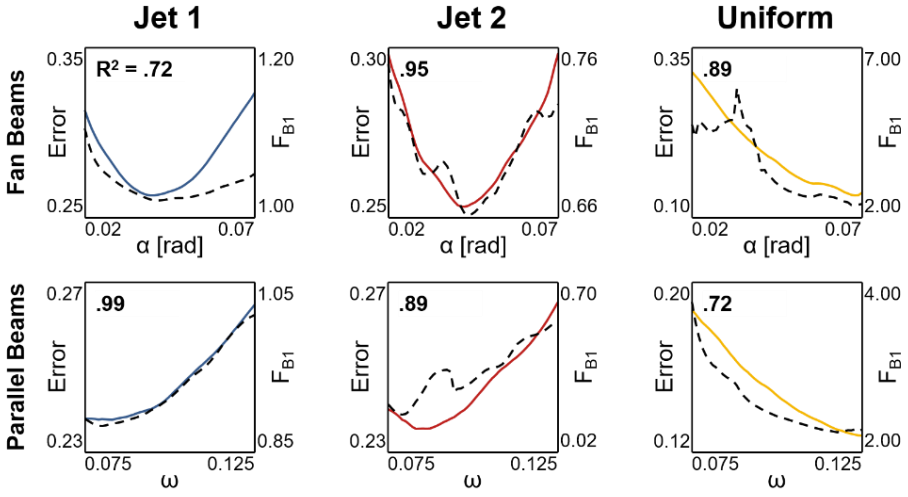

Figure 4.5: F_{B1} vs. reconstruction error for the fan-beam and parallel-beam projections.

that shows a close connection between the deterministic and Bayesian DOE functions, assuming minimal prior information.[64] By contrast, the Bayesian function exhibited unique trends over α and ω for the jets. Sample-based priors imply approximate bounds for the target, and F_{B1} acted to align the spread and width of the fan and parallel projections within the flow area. F_{B1} and the reconstruction error were highly-correlated for each target set. Moreover, the Bayesian algorithm improved the accuracy of reconstructions across the entire parameter space for both arrangements compared to Tikhonov regularization. Table 4.1 summarizes the percentage difference in reconstruction error between optimal deterministic and Bayesian arrangements, identified by F_{D1}, F_{D2}, F_{D3}, and F_{B1}.

In several cases, the correlation between the reconstruction error and F_{B1} was slightly lower than the same correlations for F_{D1} and F_{D2}. The most significant such instance occurred for jet 1, where F_{B1} had a correlation of 0.72 compared to 0.97 and -0.93 for F_{D1} and F_{D2}, respectively (a maximum difference of 26%). The remaining lower correlations for F_{B1} were within 8% of the resolution norm correlation. Several factors mitigate the importance of differences between these correlations. First, trends in the Bayesian reconstruction errors were non-linear; nevertheless, F_{B1} captured the salient features of $\|\mathbf{e}\|_2$ vs. α and ω. Moreover, the correlation statistic understates the correspondence between reconstruction accuracy and F_{B1} in such cases, as in the fan-beam test for jet 1. This feature was illustrated by the fact that F_{B1}-based optimization approximately identified the optimal spacing parameter for each combination of projection type and prior, regardless of the correlation. Second, the dynamic range of $\|\mathbf{e}\|_2$ was much smaller for the Bayesian algorithm than the Tikhonov algorithm.

Table 4.2: Range of Reconstruction Errors in the Structured Optimization using the Deterministic and Bayesian Algorithms

Flow	Deterministic Range		Bayesian Range	
	Fan Beams	*Parallel Beams*	*Fan Beams*	*Parallel Beams*
Jet 1	0.23 (0.38 to 0.61)	0.10 (0.34 to 0.44)	0.04 (0.26 to 0.30)	0.02 (0.24 to 0.26)
Jet 2	0.36 (0.43 to 0.79)	0.19 (0.41 to 0.60)	0.04 (0.25 to 0.29)	0.02 (0.24 to 0.26)
Uniform	0.12 (0.13 to 0.25)	0.06 (0.13 to 0.19)	0.17 (0.12 to 0.29)	0.06 (0.13 to 0.19)

[64] The prior information implicit in the deterministic functions is accurate when the target is known to be isotropic, as was the case for the uniform phantom set.

Table 4.2 reports the spread of errors for the structured tests. Given this context, Figure 4.4 and Figure 4.5 demonstrate that F_{B1} captured more detailed information about variation in the reconstruction accuracy with α and ω than did F_{D1}, F_{D2}, or F_{D3}. The Bayesian approach to the design of structured CST arrays and reconstruction produced optimal, flow-specific arrangements and accurate estimates of the target distribution.

4.1.4.2 Unstructured array optimization

Measurement arrays in limited-data CST are typically constrained to some sort of regular arrangement, motivated by theoretical analyses [287,293] and practical considerations [286]. However, decreasing component costs have improved the feasibility of irregular arrays and sparse arrangements often provide the sole means for optical access into fluid enclosures, such as pistons [130,133,137] and exhaust systems [149]. In the numerical context, relaxing constraints on the path arrangement also elucidates the predictive capacity of DOE objective functions. For these reasons, unstructured beam paths are routinely employed to test DOE functions for CST [89,289–291,294].

First, an unstructured optimization was conducted to replicate the results of Twynstra and Daun [289], using F_{D1} to select the seed array. Candidate arrays were scored by F_{D1}, F_{D2}, and F_{D3} and errors were calculated for all three targets using 250 phantoms in each case. Figure 4.6 shows the relationship between F_{D1}, F_{D2}, and F_{D3} and Tikhonov-based reconstruction errors for each candidate array.[65] From this figure, it can be seen that the objective function of Twynstra and Daun [289] tracked errors most consistently among the deterministic criteria. The function of Song et al. [290] exhibited reasonable correlations, as well, while the collinearity metric of Yu et al. [291] was considerably less predictive than either F_{D1} or F_{D2}. Following the deterministic test, the optimization procedure was repeated using an A-optimal Bayesian function to select arrays for each phantom set with a target-specific prior. Measurements for every candidate array were reconstructed using both the Tikhonov and Bayesian algorithms. Correlations between the Bayesian functions and reconstruction error are shown alongside the deterministic correlations in Figure 4.6.

[65] Yu et al. [291] compare F_{D1}, F_{D2}, and F_{D3} with arrays selected by an annealing algorithm, scored by F_{D3}. They restrict the comparison to accepted arrays, limiting the space of candidates and biasing the correlation in favour of the selection function. Analyses in this chapter consider all of the randomly proposed arrangements to avoid this pitfall.

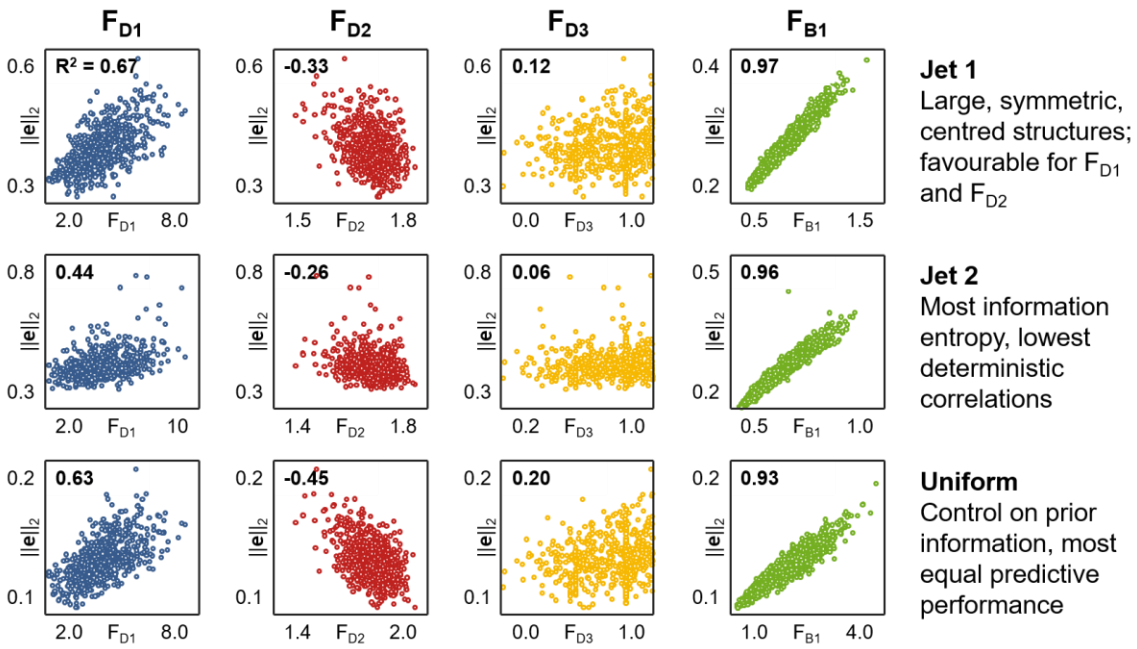

Figure 4.6: Comparison between objective function scores and average reconstruction errors for the unstructured array tests. Deterministic functions were compared to Tikhonov-based errors and the Bayesian metric was compared to sample-based reconstruction errors. The Bayesian function exhibited much stronger correlations for each flow.

Regardless of the phantom set, once beam positions were free to vary, the deterministic functions were less predictive of reconstruction accuracy than in the fan-beam and parallel-beam tests. All three objective functions performed worst for jet 2: a structured flow with asymmetric placement in the domain. Error correlations for F_{D2} and F_{D3} were greater for the uniform flow than for jet 1; and F_{D1} performed similarly-well for these phantoms. Deterministic DOE functions do not anticipate the location of structures in the flow field. Anisotropy in the target distributions thus caused lower correlations for jet 2. In general, as the information entropy of the target increases—i.e., with more complex shapes, less uniformly-distributed in the measurement plane—F_{D1}, F_{D2}, and F_{D3} become less predictive of reconstruction accuracy.

Correlations between the Bayesian function and reconstruction accuracy were high for all three phantom sets. Moreover, the correlations were equivalent to the best-case deterministic results from the structured optimization tests. The reason for this improvement can be understood by considering the range of possible arrays in the structured test. Structured candidates with projections that happened to align with the flow area scored well using F_{D1} and F_{D2}. Moreover, Bayesian reconstructions were relatively accurate for all of the structured arrays. When constraints on the beam positions were lifted, some of the candidates contained beams that did not intersect

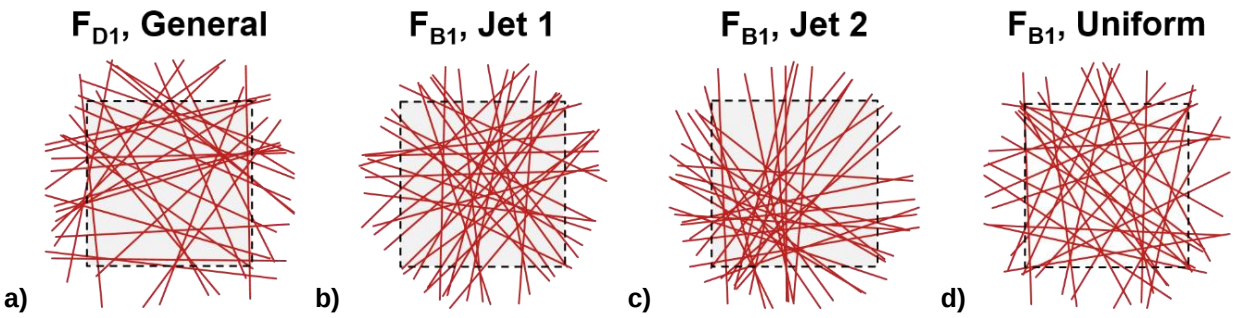

Figure 4.7: Unstructured arrays selected in a genetic optimization by a) F_{D1}, the resolution matrix function and (b-d) F_{B1}, the Bayesian function with a flow-specific prior for the b) jet 1, c) jet 2, and d) uniform phantom set.

the jet area, especially for the case of jet 2. These candidates performed poorly, irrespective of the reconstruction algorithm—such arrays were penalized by the Bayesian function but not by the deterministic functions. Bayesian scores were thus expected to track reconstruction error throughout the design space while the deterministic score was less appropriate for unrestricted beams and anisotropic targets.

Figure 4.7 shows unstructured arrays produced by the deterministic and Bayesian optimization tests. The arrangement in Figure 4.7a features fairly consistent coverage of the domain and is in good agreement with the isotropic information implicit in F_{D1}. (That is, no pixels or regions are preferred over others.) Moreover, this array strongly resembles that of Twynstra and Daun [289], which confirms that the metric was correctly implemented. The spatial information encoded in the Bayesian functions is immediately apparent in the optimized arrays. Beams for the jet phantoms are distributed in a circle around the centre of the flow, with a larger circle for jet 1 than jet 2; and F_{B1} selected evenly-distributed beams for the uniform phantoms, much like the F_{D1}. The Bayesian function selected beams in order to maximize linearly-independent sums of pixels with significant variance, neglecting low-activity pixels. Differences in the posterior variance of a pixel for two arrays reflects the relative uncertainty of that parameter. By constructing a prior with a rough estimate of the spatial distribution of variance, and incorporating that information into F_{B1}, the Bayesian approach to DOE can optimize CST measurement systems more acutely than can existing deterministic procedures. And when little information about the flow field is known, the Bayesian functions and best-practice deterministic functions converge.

Finally, Figure 4.8 shows sample reconstructions using arrays selected by the deterministic and Bayesian optimization tests. In each case, the Bayesian function procedure produced superior images of the target flow, though improvement was marginal in the uniform case. Tikhonov-based

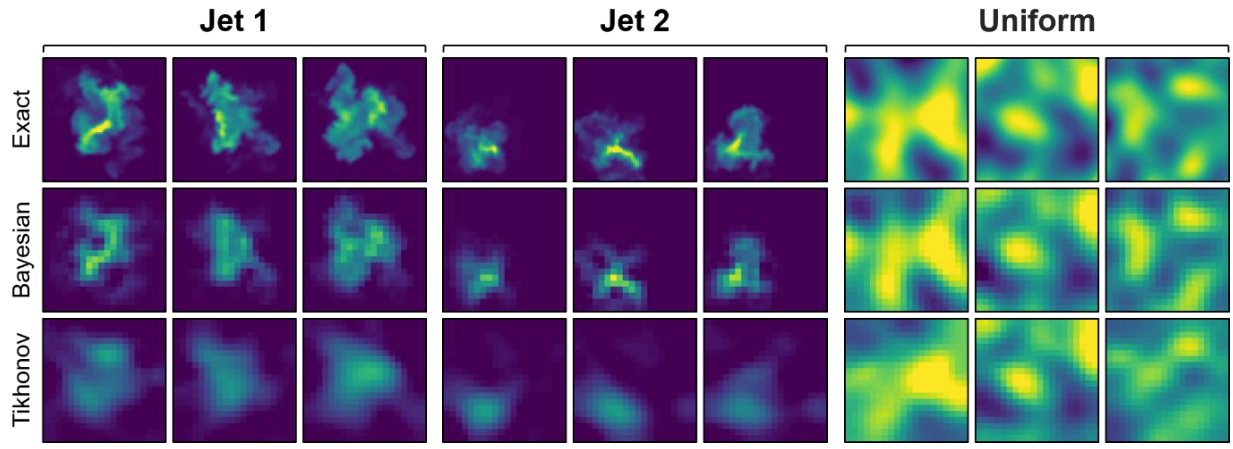

Figure 4.8: Random draws from each phantom set along with the corresponding reconstructions using the beam array optimized with F_{B1} and F_{D1}.

reconstructions of the jet phantoms were overly-smooth, distorting the periphery of the jet. Bayesian reconstructions featured realistic fluctuations, by contrast. These images illustrate the utility of the Bayesian framework for CST. Knowledge about the distribution of a flow in the measurement plane is helpful in positioning measurement paths to maximize their informative content; and the same framework can be used to generate superior reconstructions.

4.2 Bayesian Meshing, Basis Selection, and Prior Assignment

Prior information can be used to identify a suitable basis and beam arrangement for an experiment. Unfortunately, experiments do not always conform to the experimenter's expectations.[66] In gas-phase tomography, bulk motion of the ambient fluid can cause a gas jet to sway or flame to flicker; operating conditions in a piston are subject to change as parts wear and shift; injectors in a SCR system may be perturbed by vibrations in the exhaust manifold, altering the trajectory of a reacting species; and environmental monitoring scenarios are plagued by variation in wind conditions and atmospheric levels of the target molecule. All of these effects cause unexpected changes to the flow field and the aim of CST is precisely to observe such changes. While DOE procedures and fluid simulations are usefully employed to optimize the position of optical paths and selection of a basis prior to testing, actual measurement conditions may prove better-suited to some other model of the flow field.

Considerable research has been conducted on algorithms for gas-phase tomography (e.g., [86,90,235,293]) and the optimal design of CST experiments (e.g., [89,289–291,294]). Far less

[66] This is said tongue-in-cheek, of course, as scientific progress consists in large part in revising models to transform unexpected results into expected results.

attention has been trained on the relationship between the discretization scheme and utility of reconstructions. Ideally, a discretization scheme should be flexible enough to represent the "true" solution for a large set of measurements. At the same time, the model's degrees-of-freedom should be restricted in order to promote computational efficiency and limit parameter uncertainties, particularly in limited-data settings. The discretization scheme itself functions as a form of prior information, since the basis determines which attributes of the flow field can be represented. Select observational studies have investigated the effect of the basis on the visual quality of reconstructions, e.g., Mohri et al. [218], but none have proposed a general mathematical criterion for basis selection. There is therefore a need to systematically adjudicate between competing bases: in terms of the measurement model and density of basis functions, with respect to standard tomography metrics.

Bayesian model comparison is an approach to data analysis in which the model used to represent the data is itself an uncertain quantity. The parameters that specify a system state, the model relating those parameters to the data, and the prior used to regularize the inference are all free to vary. Numerous measures have been proposed to compare the inversion of a data set by different models. The practice of comparing models for inference is called *model selection* or *model comparison*. Models for gas-phase tomography comprise the basis used to represent a flow field, discrete approximation to the RTE, and prior pdf. In model comparison, these elements are adjusted and different combinations are judged on their ability to reconcile measurements and prior assumptions while minimizing uncertainty. This section develops Bayesian model comparison for tomography with joint-normal pdfs. Discretization schemes are proposed using the finite element method (FEM), and the section reports the first application of model selection to CST.

4.2.1 Model comparison for CST

Models in hard-field tomography are conceived as a discrete entity that consists of the measurement model/interpolation scheme; basis, Φ; and prior, $\pi_{\text{pr}}(\mathbf{x})$—where the ith model is designated M_i. The approach to model comparison presented in this chapter follows from the framework set out by Kaipio and Somersalo [295]. They developed a general analysis of discrete subspaces of a Hilbert space, comparing the subspaces' ability to represent solutions to a generic inverse problem in a Bayesian way. Sambrige et al. [296] conducted a similar analysis, using the evidence, $\pi(\mathbf{b})$, to quantify the performance of models for a trans-dimensional geophysical inverse problem. Bayesian model selection does not require knowledge of a ground truth distribution.

Instead, observational data are employed to calculate a model likelihood, derived from Bayes' equation. The technique is responsive to changes in experimental conditions and eliminates the need to simulate an experiment in order to pick an appropriate model.

The likelihood, prior, and posterior pdfs of Bayesian CST are repurposed for model selection, which quantifies the veridicality of a model [297].[67] Selection begins with the introduction of a model likelihood, $\pi(\mathbf{b}|M_i)$, akin to the likelihood from Chapter Two, $\pi(\mathbf{b}|\mathbf{x})$. The model likelihood is used to gauge the probability that M_i can explain a set of measurements based on the posterior variance of parameter estimates. Model comparison consists of evaluating model likelihoods for different grid resolutions, interpolation schemes, etc., to identify models that are substantially "more probable" (i.e., having a greater likelihood). By hypothesis, discretization schemes that produce a greater model likelihood should provide a superior trade-off between parameter uncertainty and model error compared to "less probable" schemes.

Standard Bayesian model selection employs Bayes factors, presented below, to compare $\underline{M_i}$ and M_j. Log-scale model likelihoods are commonly used in high-dimension scenarios to stabilize the selection. This chapter shows how the log-model likelihood can be decomposed into key terms that illustrate the role of grid resolution and prior information in the performance of a CST model.

4.2.1.1 Calculating model odds with Bayes factors

Take $\mathscr{M} = \{M_i\}$ to be the set of candidate models available to a CST practitioner. Bayesian model selection seeks the model that "most probably" generated the data set $\{\mathbf{b}^{(k)}\}$ [297]. The model $M_i \in \mathscr{M}$ that probably produced the data with minimal flexibility should, on average, yield the best inference because models that can reproduce measurements for a variety of conditions while minimizing posterior uncertainty are likely to bear a structural resemblance to the underlying physical system. This criterion amounts to maximizing the model posterior, which involves the inference of M_i,

$$\pi(M_i \,|\, \mathbf{b}) = \frac{\pi(\mathbf{b} \,|\, M_i)\pi_{\text{pr}}(M_i)}{\pi(\mathbf{b})} \propto \pi(\mathbf{b} \,|\, M_i)\,. \tag{4.20}$$

In principle, it is possible to define a prior on the model space, $\pi_{\text{pr}}(M_i)$, to incorporate additional information about the physical system into the inversion. However, developing a properly-scaled prior pdf requires comprehensive, formal knowledge about possible approximations to the RTE,

[67] *Veridicality of a model* meaning, under appropriate conditions: *How well do competing models map onto reality?*

bases, etc.—rarely available in CST. Models are thus treated as equally probable, a priori, which corresponds to the maximum likelihood formulation in Eq. (4.20) and ultimately gives rise to the Bayes factor.

Terms in Bayes' equation, as presented in Eq. (2.30), are implicitly contingent on a model of the flow field. This contingency can be made explicit,

$$\pi(\mathbf{x} \mid \mathbf{b}, M_i) = \frac{\pi(\mathbf{b} \mid \mathbf{x}, M_i)\pi_{\text{pr}}(\mathbf{x} \mid M_i)}{\pi(\mathbf{b} \mid M_i)}. \tag{4.21}$$

Equation (4.21) reveals that the model likelihood is already present in Bayesian CST in the form of the evidence.[68] Substituting Eq. (4.21) into Eq. (4.20) provides an expression for the model posterior and likelihood in terms of the original pdfs,

$$\pi(M_i \mid \mathbf{b}) \propto \pi(\mathbf{b} \mid M_i) = \frac{\pi(\mathbf{b} \mid \mathbf{x}, M_i)\pi_{\text{pr}}(\mathbf{x} \mid M_i)}{\pi(\mathbf{x} \mid \mathbf{b}, M_i)}. \tag{4.22}$$

The most probable model is found by maximizing Eq. (4.22) for models in $\mathscr{M}$.

Sampling methods are typically required to compute the model likelihood. However, the joint-normal likelihood and prior pdfs imply a joint-normal posterior and Section 4.1.2.1 demonstrated that $\pi(\mathbf{x}|\mathbf{b})$ can be expressed in terms of the parameters of $\pi(\mathbf{b}|\mathbf{x})$ and $\pi_{\text{pr}}(\mathbf{x})$. As a result, there are exact expressions for all of the terms in Eq. (4.22) and the model likelihood is directly computable. Equation (4.22) is independent of $\mathbf{x}$ and constant for any $\mathbf{b}$; evaluating Eq. (4.22) at the MAP estimate simplifies the expression, resulting in a closed-form formula for the model likelihood,

$$\pi(\mathbf{b} \mid M_i) = \sqrt{\frac{\det(\boldsymbol{\Gamma}_{\mathbf{x}|\mathbf{b}})}{\det(2\pi\boldsymbol{\Gamma}_{\mathbf{e}})\det(\boldsymbol{\Gamma}_{\mathbf{x}})}} \exp\left\{-\frac{1}{2}\left\|\begin{bmatrix}\mathbf{L}_{\mathbf{e}}\mathbf{A}\\ \mathbf{L}_{\mathbf{x}}\end{bmatrix}\mathbf{x}^{\text{MAP}} - \begin{bmatrix}\mathbf{L}_{\mathbf{e}}\mathbf{b}\\ \mathbf{L}_{\mathbf{x}}\boldsymbol{\mu}\end{bmatrix}\right\|_2^2\right\}. \tag{4.23}$$

Non-linear formulations of CST, such as that of Ma et al. [124], feature non-Gaussian likelihood and posterior pdfs, in which case sampling methods are required to compute the model likelihood. Sampling the posterior for a non-linear inversion with a large number of measurements quickly becomes computationally-intractable. Nevertheless, while the pdfs for non-linear CST are not strictly Gaussian, they are frequently well-approximated as such and non-Gaussianity may take a similar form from model to model. The Laplacian approximation is invoked under such

[68] Sambrige et al. [296] also exploit this relationship.

circumstances: the approximation holds that the posterior is roughly Gaussian about the MAP and the model likelihood is well-estimated by Eq. (4.23) [298].[69]

Models in $\mathscr{M}$, M_i and M_j, are compared by the ratio of model likelihoods, called a Bayes factor

$$B_{ij} = \frac{\pi(\mathbf{b} \mid M_i)}{\pi(\mathbf{b} \mid M_j)}. \tag{4.24}$$

Formally, B_{ij} gives the odds that M_i produced the data vs. M_j. The model likelihood implicitly marginalizes all parameters of a model so B_{ij} accounts for the fit of M_i and M_j to the data as well as the posterior uncertainty. Bayesian model selection concludes by identifying the model $M_i \in \mathscr{M}$ that maximizes Eq. (4.24) when set against the available alternatives. For CST of a turbulent target, no single measurement is representative of the process. Selection thus proceeds with average Bayes factors for a set of measurements.

4.2.1.2 Decomposition of the log-scale model likelihood

Equation (4.24) involves a ratio of exponentials that contain the norms of a high-dimension vector. The norm can be quite large such that the model likelihoods approaches zero, introducing numerical instabilities into the comparison. Log-scale model likelihoods are frequently employed to stabilize the calculation of a Bayes factor,

$$\begin{aligned} L_i &\equiv \ln\left[\pi(\mathbf{b} \mid M_i)\right] \\ &= \frac{1}{2}\ln\left[\det(\boldsymbol{\Gamma}_{\mathbf{x}|\mathbf{b}})\right] - \frac{1}{2}\ln\left[\det(\boldsymbol{\Gamma}_{\mathbf{e}})\right] - \frac{1}{2}\ln\left[\det(\boldsymbol{\Gamma}_{\mathbf{x}})\right]. \\ &\quad - \frac{1}{2}\left\|\mathbf{b} - \mathbf{A}\mathbf{x}^{\mathrm{MAP}}\right\|^2_{\mathbf{L}_{\mathbf{e}}} - \frac{1}{2}\left\|\mathbf{x}^{\mathrm{MAP}} - \boldsymbol{\mu}\right\|^2_{\mathbf{L}_{\mathbf{x}}} \end{aligned} \tag{4.25}$$

The model in $\mathscr{M}$ with the largest log-model likelihood will maximize Eq. (4.25). Alternatively, B_{ij} is explicitly calculated: $B_{ij} = \exp\{L_i - L_j\}$.

Given the linear formulation of CST (or Laplacian approximation to non-linear variants) and explicit expression of L_i, the log-model likelihood can be decomposed into meaningful sub-expressions. These factors illuminate the function of grid resolution and prior information in model accuracy. Four key components are defined. First, the *measurement credence*,

$$V = \frac{1}{2}\sum_{k=1}^{n} \ln\left[\frac{\lambda^{(k)}_{\mathbf{x}|\mathbf{b}}}{\lambda^{(k)}_{\mathbf{x}}}\right], \tag{4.26}$$

[69] See Sipkens et al. [373] for an example of non-linear Bayesian model selection using the Laplacian approximation.

where $\lambda_{\mathbf{x}|\mathbf{b}}^{(k)}$ and $\lambda_{\mathbf{x}}^{(k)}$ are the kth eigenvalues of $\mathbf{\Gamma}_{\mathbf{x}|\mathbf{b}}$ and $\mathbf{\Gamma}_{\mathbf{x}}$, respectively. V is half the log-scale difference between the constants that normalize the volume of the hyperellipses corresponding to $\mathbf{\Gamma}_{\mathbf{x}|\mathbf{b}}$ and $\mathbf{\Gamma}_{\mathbf{x}}$. The relative size of these "credibility ellipses" quantifies the differential knowledge about $\mathbf{x}$ due to measurement. The measurement credence is relative to the beam arrangement and covariance information specified in the prior. Next, a *data fit*

$$D = -\frac{1}{2}\left\|\mathbf{b} - \mathbf{A}\mathbf{x}^{\mathrm{MAP}}\right\|_{\mathbf{L}_e}^2 \tag{4.27}$$

and *prior fit*

$$P = -\frac{1}{2}\left\|\mathbf{x}^{\mathrm{MAP}} - \boldsymbol{\mu}\right\|_{\mathbf{L}_x}^2 \tag{4.28}$$

are introduced to quantify the capacity of a model to simulate the data set and support the prior, respectively. Remaining terms in Eq. (4.25) are grouped into a *system constant*, C_{sys}, which cancels out in the calculation of a Bayes factor. The sum of the measurement credence, data fit, and prior fit gives the log-model likelihood: $L_i = V + D + P + C_{\mathrm{sys}}$.

Results presented in Section 4.2.4 demonstrate that trends in V, D, and P are related to model efficacy. For instance, an accurate prior can enable the extraction of dense spatial information from a limited set of measurements (i.e., permitting a high grid-resolution), which is revealed by a relatively large credence. By contrast, when that prior is unspecific or incompatible with the target process, fit terms decrease as the grid is refined. The Bayes factor automatically weighs the trade-off between the marginal cost of additional parameter uncertainty and marginal benefits of added resolution, optimizing for predictive power.

4.2.2 Finite element method for CST

One way to adjust the model in CST is to increase or decrease the resolution of the pixel basis used thus far in this work. Indeed, square-pixel and cubic-voxel bases are the most common discretization schemes for gas-phase tomography [235,299]. The concept of FEM discretization for CST is introduced below, to reduce model error and enable the comparison of different approximations to the RTE.

Pixel and voxel grids split the flow field into square or cubic regions that roughly contain a uniform concentration of the target species. While this approach has merits, including its simple implementation and the easy enforcement of bound constraints, the coarse pixel/voxel structure introduces error into the measurement model relative to several alternatives. Polydorides et al.

[300] recently proposed a cosine basis for CST, constructed from an infinite set of functions; the authors derived an error bound to guide truncation of the series. Their method's performance depends on the compatibility between the first cosine function and mean gas concentration. Axisymmetric plumes, centred in the domain, are well-represented by a cosine basis, but this may not hold true for other flows such as asymmetric plumes, bifurcations, and the like.

Finite element meshes can easily accommodate complex geometries and support high-order approximations to the measurement physics. As a result, the FEM is common to numerous forms of tomography, including optical tissue [301], electrical impedance [302], and seismic [303] tomography. The classic uniform-pixel basis can be represented within the finite element framework. However, the assumption of spatially-uniform gas within the pixels leads to a coarse measurement model, especially in the context of low-resolution grids for limited-data tomography. This section presents the FEM for CST with three forms of piecewise polynomial support: constant, linear, and quadratic. While high-order bases account for the spatially-smooth variation expected of a gas, they also require more nodes per element than low-order bases. Furthermore, overly-smooth bases with dense support can exacerbate noise amplification, complicating the benefits of model error reduction. In view of these elaborate trade-offs, the finite element framework provides suitable proving grounds for model selection.

To begin, the CST domain is represented using a set of elements. Figure 4.9 shows a triangle element mesh for a 2D measurement plane, Ω, in global coordinates, (x, y). The domain is divided into triangular elements, $\delta\Omega$. Also shown in Figure 4.9 is a single element in local element coordinates, (ξ, η), with nodes that correspond to different shape functions. Shape functions are

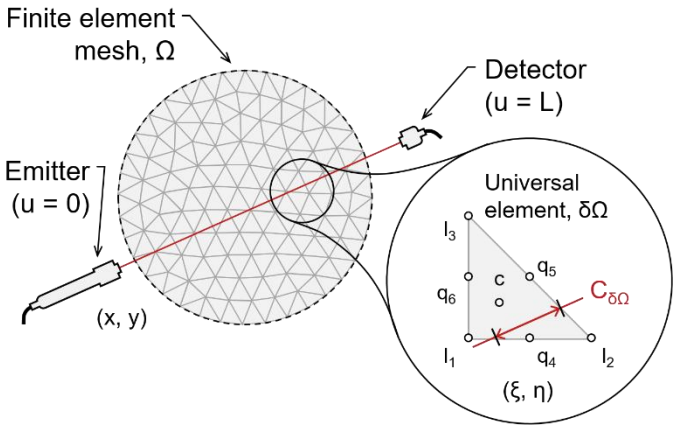

Figure 4.9: Finite element domain for CST: a) circular domain in global coordinates, (x, y), with a single LOS and b) a single element in element coordinates, (ξ, η), with piecewise constant, c, linear, l, and quadratic, q, nodes. (Linear nodes also serve as the first three quadratic nodes.)

defined over the element to interpolate the target (i.e., κ_η or S_η) between the nodes. The number of functions and placement of nodes in an element depend on the interpolation scheme.

Recall the ray-sum approximation to the absorption and emission IFKs from Chapter Two,

$$b_i \approx \sum_{j=1}^{n} \alpha_j \int_0^L \phi_j \left[\mathbf{r}_j(u) \right] du , \tag{4.29}$$

where u is a position from 0 to L along the ith LOS. Here $\mathbf{r}_j(u)$ is an indicator function that returns a position in local element coordinates for the element containing u. Each basis functions is associated with one of the triangle elements and the number of functions equals the number of nodes. (Functions are not specific to a node, however, as neighbouring elements share nodes in the linear and quadratic schemes.) The jth function has compact support and is equal to unity at the jth node such that α_j directly represents κ_η or S_η at that point. Therefore, unlike other forms of representation, the FEM preserves a close connection between the physical quantity of interest and inferred parameters.

Nodal placement for the piecewise constant, linear, and quadratic bases are shown in Figure 4.9. Global coordinates are related to local element coordinates by a linear transformation,

$$\begin{bmatrix} \xi(x,y) \\ \eta(x,y) \end{bmatrix} = \begin{bmatrix} x_{l2} - x_{l1} & x_{l3} - x_{l1} \\ y_{l2} - y_{l1} & y_{l3} - y_{l1} \end{bmatrix}^{-1} \begin{bmatrix} x - x_{l1} \\ y - y_{l1} \end{bmatrix}. \tag{4.30}$$

Basis functions for the triangle element mesh are

$$\phi_j(\xi,\eta) = \begin{cases} N_j(\xi,\eta), & \xi,\eta \in [0,1],\ \xi+\eta \le 1 \\ 0, & \text{otherwise} \end{cases}, \tag{4.31}$$

where N_j is a shape function, which depends on the mode of interpolation. The constant shape function, N_c, is one throughout the element containing node c, akin to a triangle formulation of the pixel basis. Linear shape functions are

$$N_{l1} = 1-\xi-\eta,\ N_{l2} = \xi, \text{ and } N_{l3} = \eta ; \tag{4.32}$$

and the quadratic shape functions are

$$\begin{aligned} &N_{l1} = (1-\xi-\eta)(1-2\xi-2\eta), \quad N_{l2} = \xi(2\xi-1), \quad N_{l3} = \eta(2\eta-1), \\ &N_{q4} = 4\xi(1-\xi-\eta), \qquad\quad N_{q5} = 4\xi\eta, \qquad\quad N_{q6} = 4\eta(1-\xi-\eta). \end{aligned} \tag{4.33}$$

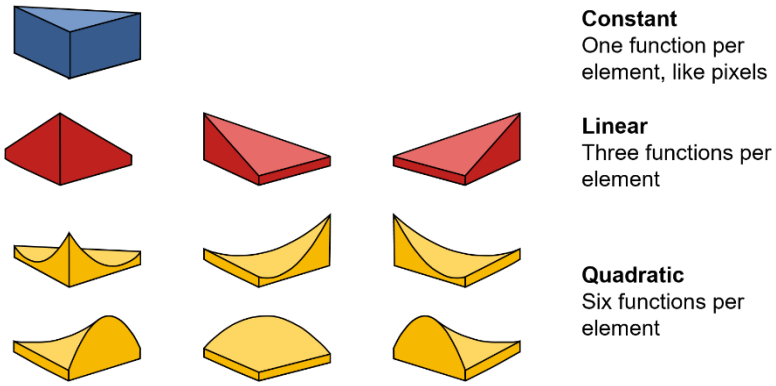

Figure 4.10: Shape functions for the constant, linear, and quadratic interpolation schemes for a triangle-element mesh.

Plots of the piecewise constant, linear, and quadratic shape functions for a single element are shown in Figure 4.10.

Integrals in Eq. (4.29) are easily computed because the basis functions are specific to an element and the sum of integrals along a LOS for an element, $\delta\Omega$, equals the chord length of that LOS through $\delta\Omega$, called $C_{\delta\Omega}$, pictured in Figure 4.9. Elements of the ray-sum matrix are

$$A_{ij} = \sum_{\delta\Omega \in \Omega} \frac{C_{\delta\Omega}}{S_{\delta\Omega}} \int_0^L \phi_j \left[\mathbf{r}_i(u) \right] du \,, \tag{4.34}$$

where $\mathbf{r}_i$ corresponds to $\delta\Omega$, the integral corresponds to the ith LOS, $C_{\delta\Omega}$ is the length of the ith LOS through $\delta\Omega$, and $S_{\delta\Omega}$ normalizes the line integral over Φ in $\delta\Omega$. The normalization constant is

$$S_{\delta\Omega} = \sum_{p \in \delta\Omega} \int_0^L N_p \left[\mathbf{r}_i(u) \right] du \,. \tag{4.35}$$

Given a mesh with n nodes and system of m optical paths, A_{ij} is computed for each node, for each LOS, to form the system $\mathbf{Ax} = \mathbf{b}$, as with the square-pixel and cubic-voxel bases.

4.2.3 Simulating a CST model selection scenario

4.2.3.1 Selective catalytic reduction phantoms

Bayesian model selection for CST is demonstrated with a simulated experiment. The target is the distribution of NH_3 in exhaust gases in the mixing pipe of a SCR after-treatment system. This scenario is motivated by the experiment of Stritzke et al. [149], in which the authors conducted CST on the exhaust system of a heavy-duty diesel engine. Their apparatus consisted of an array of tunable diode laser beams, which had a frequency aligned with a strong ro-vibrational transition of NH_3 (near 2,200.5 nm). Eight beams were shone through the mixing pipe towards a set of photodiodes; the absorption signal was measured with a lock-in detector and amplification system.

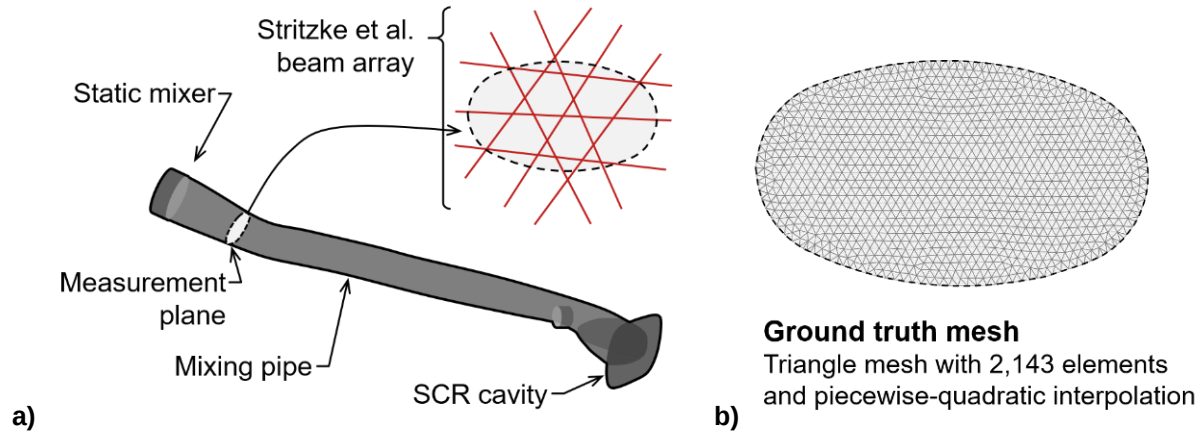

Figure 4.11: Geometry of a LES domain for a SCR simulation: a) domain from Zöchbauer et al. [304] and the measurement array of Stritzke et al. [149] and b) the 4422-node ground truth mesh.

Reconstructed distributions of NH_3 were used to gauge the quality of mixing.[70] CST of a SCR system is a good candidate for model selection as the number of measurements is limited by the geometry of the exhaust manifold ($m = 8$ in the case of Stritzke et al. [149]). Moreover, there are presently no such simulations in the literature to guide experimental mesh selection.

Chemical species tomography of NH_3 in a SCR system was simulated using realistic phantoms from a LES. The LES and CST domains are shown in Figure 4.11. Turbulent phantom data, obtained from the model of Zöchbauer et al. [304]; the authors simulated an underbody exhaust system with a three-hold injector and static mixer. Simulations were conducted with STAR-CCM+ v.8.06 using the segregated transient SIMPLE solver. The CFD grid consisted of 3.2 million polyhedral cells, and an experimental study was conducted to validate the turbulence model.

Data from the LES was collected for $K = 501$ timesteps, corresponding to a physical sampling rate of 2,000 Hz. Collection took place from $t = 0.1$ to 0.125 s, such that statistics of the phantom were stable. The measurement plane in Figure 4.11a was located 0.1 m downstream from the static mixer and the NH_3 volume fraction was obtained at each timestep for the quadratic nodes of the ground truth mesh, pictured in Figure 4.11b. Synthetic measurements were generated for the sparse array of Stritze et al. [149] to mimic the restrictive conditions of a limited-data CST experiment. Exact measurements were calculated by high-order integration over the ground truth domain and the data were corrupted with noise: $b_i = b_i^{\text{exact}} \cdot e$, where $e \sim \mathcal{N}(1, 0.03^2)$. This procedure is a conservative approximation to 3% shot noise, which follows a Poisson distribution.

[70] Urea-water solution, injected into the exhaust stream, reacts with combustion products and yields NH_3; treated gasses then enter the catalytic reduction chamber. Good performance is indicated by a large, even spread of NH_3.

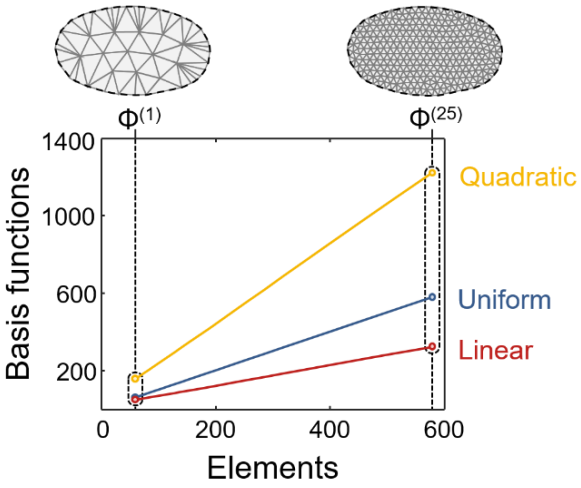

Figure 4.12: Number of basis functions for meshes in a CST model selection study.

4.2.3.2 Simulated model selection: meshing, testing, and scoring

Twenty-five triangle-element meshes of Ω with increasing resolution were generated to test Bayesian model selection. Node arrangements were designated $\Phi^{(i)}$ for $i = 1,\ldots,25$; the number of elements ranged from 59 to 580. Meshes $\Phi^{(1)}$ and $\Phi^{(25)}$ are shown in Figure 4.12 along with the number of nodes required for piecewise constant, linear, and quadratic bases. Placement of the corner nodes was executed with DistMesh [305], and Delaunay triangulation was used to generate the element graph.[71] Meshes in Figure 4.12 illustrate how triangle elements can easily accommodate an irregular domain.

Two model selection tests were conducted using the 25 meshes described above. First, tests were run to assess the utility of different priors. Priors were based on different combinations of two mean vectors, $\boldsymbol{\mu}^0$ and $\boldsymbol{\mu}^{smp}$, and two covariance matrices, $\boldsymbol{\Gamma}_{tk}$ and $\boldsymbol{\Gamma}_{sq}$. Vectors $\boldsymbol{\mu}^0$ and $\boldsymbol{\mu}^{smp}$ were a zeros vector and sample-based mean, respectively, and the covariance matrices had a zeroth-order Tikhonov and square-exponential structure. All four combinations of $\boldsymbol{\mu}$ and $\boldsymbol{\Gamma}_{\mathbf{x}}$ were tested using a piecewise linear basis. The second test of model comparison featured the piecewise constant, linear, and quadratic bases using $\boldsymbol{\mu}^{smp}$ and $\boldsymbol{\Gamma}_{tk}$. In each case, estimates were computed at all 501 timesteps. In order to provide a consistent baseline for comparison, reconstructions were compared to a projection of the ground truth using the SSIM index.

Results from of the model selection tests were used to select a mesh for the experiment. Finally, NH_3 distributions were reconstructed using a sample-based prior, with $\boldsymbol{\mu}^{smp}$ and $\boldsymbol{\Gamma}_{smp}$, to

[71] Note that the model space for this mesh scheme is infinite, and can be described by several hierarchical measures.

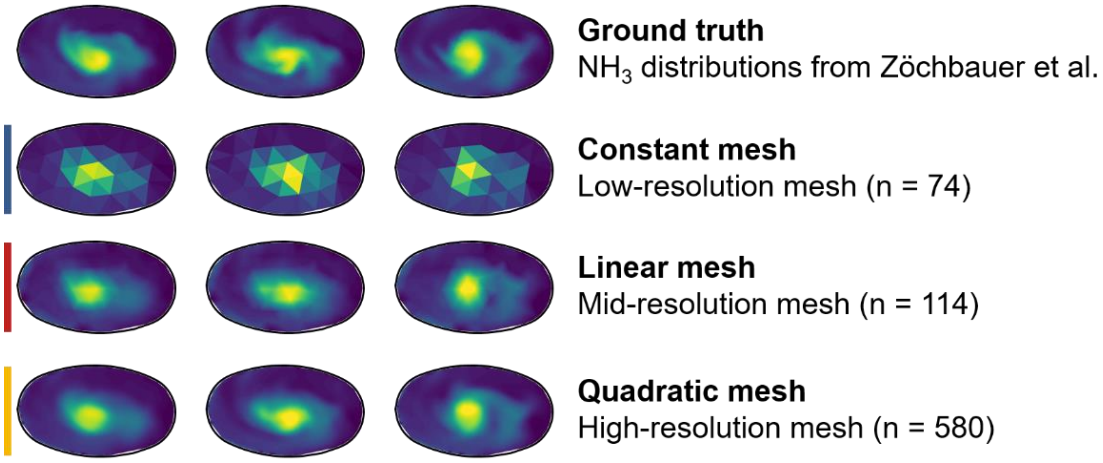

Figure 4.13: Ground truth distributions of NH_3 and the corresponding reconstructions on $\Phi^{(5)}$, $\Phi^{(15)}$ and $\Phi^{(25)}$ with a piecewise constant, linear, and quadratic basis. MAP estimates were computed with a sample-based prior to illustrate the quality of best-case reconstructions for each grid.

illustrate ideal reconstructions under noisy, limited-data imaging conditions. The sample-based covariance matrix is degenerate due to nodes that have no variance. This results in an infinite model credence and so $\boldsymbol{\Gamma}_{smp}$-based models cannot be included in the selection study. Nevertheless, the inference of $\mathbf{x}$ with $\boldsymbol{\mu}^{smp}$ and $\boldsymbol{\Gamma}_{smp}$ is full-rank and results in highly-accurate reconstructions.

4.2.4 Results and discussion

Figure 4.13 shows sample reconstructions from the simulated experiment. Piecewise constant, linear, and quadratic estimates were computed with $\Phi^{(5)}$, $\Phi^{(15)}$, and $\Phi^{(25)}$, respectively, using a sample-based prior, i.e., with $\boldsymbol{\mu}^{smp}$ and $\boldsymbol{\Gamma}_{smp}$. Sample-based estimates were highly-accurate despite the sparse structure of the measurement array and dense node arrangement of the meshes. Reconstructions captured the swirling motion in the concentration of NH_3 due to the action of the static mixer. Sample-based reconstructions on $\Phi^{(25)}$ had a mean SSIM index of 0.754 and standard

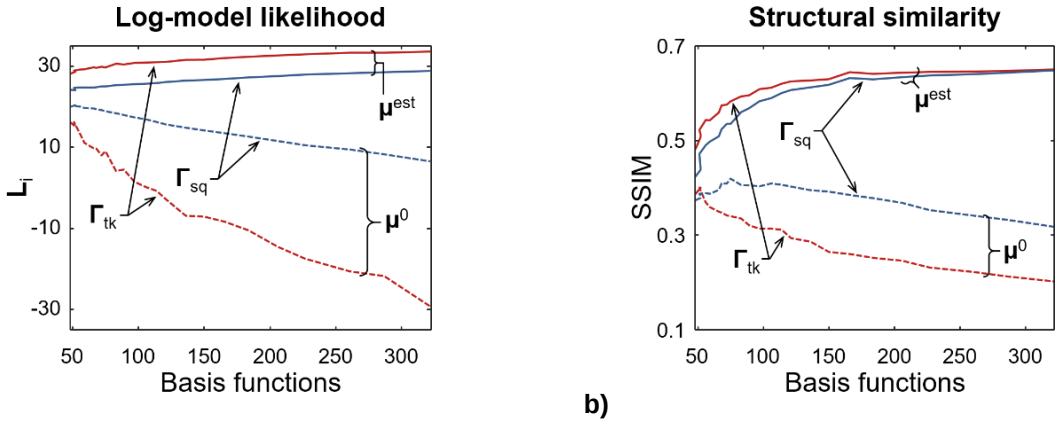

Figure 4.14: Model selection applied to prior information: trends in the a) log-model likelihood and b) SSIM index vs. the number of basis functions.

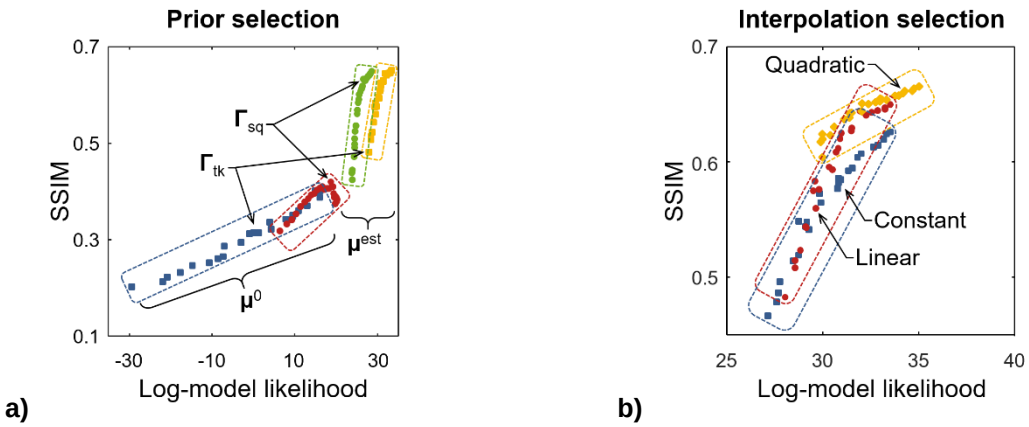

Figure 4.15: SSIM index vs. log model likelihood for a) different forms of prior information and b) piecewise constant, linear, and quadratic bases.

deviation of 0.033. The piecewise quadratic CST model and $\boldsymbol{\mu}^{smp}$ were selected based on an analysis of log model likelihoods, calculated using noise-laden data.

Figure 4.14 shows trends in the log-model likelihood and SSIM index compared to the number of basis functions for the four combinations of $\boldsymbol{\mu}^0$ and $\boldsymbol{\mu}^{smp}$ with $\boldsymbol{\Gamma}_{tk}$ and $\boldsymbol{\Gamma}_{sq}$. Predictably, the quality of standard Tikhonov reconstructions (with $\boldsymbol{\mu}^0$) degraded with increasing mesh resolution, as did $\boldsymbol{\mu}^0$-based estimates with the square-exponential covariance. Increasing the number of parameters introduced posterior uncertainty, reducing the accuracy of reconstructions. However, switching from $\boldsymbol{\mu}^0$ to $\boldsymbol{\mu}^{smp}$ improved the accuracy of estimates, reversing the trend of decreasing accuracy for higher-resolution grids. That is: including an estimate of the mean at additional nodes, along with an estimate of the covariance between nodes, was sufficient information to support the extra inference. As a result, for a stationary process with a smooth mean distribution, incorporating $\boldsymbol{\mu}^{smp}$ into the prior can permit the use of a high-resolution mesh such as $\Phi^{(25)}$. Notably, log-model likelihood and SSIM index trends in Figure 4.14 were consistent for each of the priors. It is therefore reasonable to expect the log-model likelihood to predict the quality of reconstructions.

Figure 4.15 confirms the relationship between the model likelihood and reconstruction accuracy. Accuracy improved from piecewise constant to linear to quadratic bases, and improved with increasing mesh resolution, as shown in Figure 4.15b. A caveat: more nodes are required to support a quadratic basis than a linear basis for the same mesh. For instance, the linear basis of $\Phi^{(25)}$ contains 322 nodes, compared to 1223 nodes for the quadratic basis. While the best results were obtained with a high-resolution quadratic mesh, it also required the greatest computation time. It may be desirable in some cases to select a coarser mesh to enable on-line imaging.

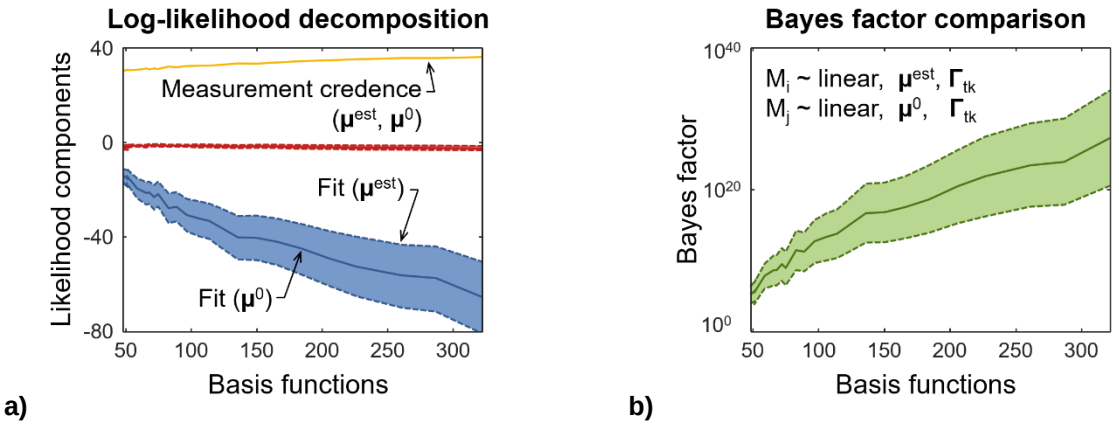

Figure 4.16: Comparison of $\boldsymbol{\mu}^0$ and $\boldsymbol{\mu}^{smp}$ for increasing mesh density in terms of the a) log-model likelihood components and b) Bayes factor. Fit terms are grouped together, D + P.

Another important feature of model selection is that the likelihood does not distinguish between model classes. A class refers to models that share a discretization scheme and prior; meshes in a class may differ in density. Model classes are grouped together in Figure 4.15 by a dashed line. The figure depicts a strong relationship between log-model likelihood and the structural-similarity of estimates, both within a class and, largely, between classes. Therefore, it is reasonable to use trends in L_i to choose the form of interpolation and prior information, as well as the optimal mesh density within a class. This procedure yields the CST model best-suited to a set of measurement data, without recourse to a simulated experiment.

Components of the log-model likelihood—V, D, and P—can inform on the trends in L_i with respect to the mesh resolution and competing priors. Figure 4.16 illustrates the measurement credence, V, and fit, $D + P$, for a comparison between $\boldsymbol{\mu}^{smp}$ (model M_i) and $\boldsymbol{\mu}^0$ (model M_j). Both models used the Tikhonov covariance and linear interpolation. The measurement credence is a deterministic function of the measurement array and finite basis. Loosely, the credence quantifies the information that can be extracted from a measurement using a given model, based on the expectations encoded in the prior. Since M_i and M_j employ the same basis and covariance, they share a measurement credence. Figure 4.16a shows the measurement credence increasing with mesh resolution. The trend is due to correlation structure of $\boldsymbol{\Gamma}_{tk}$: additional parameters relate to each existing parameter. This relationship increases the confidence in additional parameters relative to cases where added parameters are unrelated to existing parameters. Fit components fluctuate with each measurement, reflected in the spread of fit terms in Figure 4.16a. The sample-based mean improved the mean and variance of the fit compared to $\boldsymbol{\mu}^0$. Fit terms can be used to

check for model errors and the correspondence between the presumed and actual mean gas distribution.

Finally, Figure 4.16b shows the mean Bayes factor for each mesh resolution and the two sigma credibility interval. This figure clearly demonstrates that M_i is preferred to M_j, regardless of mesh density. There is also a significant upward trend in the Bayes factor, which follows from the relative log model likelihoods in Figure 4.14, supporting the claim that a robust estimate of the mean can enable CST imaging with a high-resolution mesh.

4.3 Conclusions

Tomographic images of a gas-phase target are sensitive to the measurement system and model used to represent the flow field. Limited-data CST experiments feature a small number of beams relative to the number of basis functions—commonly fewer than 100 LOS measurements for a system of several hundred variables, e.g., Refs. [89,136,149,224]. The arrangement of optical paths through the domain determines the spatial information that can be inferred about a target and the beam positions become increasingly important as the rank of a system decreases. As a result, optimal placement of the optical paths has been a focus of research on CST. This work reveals the complex relationship between the basis, reconstruction algorithm, measurement system, and reconstruction accuracy. Moreover, the basis is free to vary before and after an experiment, and can itself be optimized given a set of measurement data. The Bayesian framework for CST is naturally adapted to experimental design and selection of the basis, among other components of the tomography model. This chapter presents Bayesian functions to guide the design of gas-phase tomography arrays and model selection. Numerical tests were conducted to verify the performance of these procedures.

Deterministic methods for the design of CST experiments were reviewed to provide context for the Bayesian approach. Terzija et al. [89] proposed a heuristic for selecting a beam array. The authors argued that reconstruction amounts to interpolating CST data in sinogram space; it follows that for the best interpolation, arrangements should be selected to maximize the spread of sinogram coordinates. Quantitative assessment of the sinogram coverage hypothesis by Daun [288] found no relationship between the spread of coordinates and reconstruction accuracy. Three subsequent papers proposed objective functions for DOE in CST. Twynstra and Daun [289] developed a metric based on the resolution matrix for Tikhonov regularization; Song et al. [290] presented a grid weight function, motivated by the iterative action of the ART; and Yu et al. [291] devised an

operator to minimize the collinearity of the most similar pair of ray-sums. These criteria, denoted F_{D1}, F_{D2}, and F_{D3}, did not incorporate expectations about the flow field.

Bayesian CST features a posterior covariance matrix, which contains information about the variation and correlation of reconstructed parameters. The posterior covariance is a function of the measurement array, error model, and prior assumptions about the flow field. In DOE analyses, the prior is fixed so differences in $\mathbf{\Gamma_{x|b}}$ for different arrays reflect uncertainties due to the array, itself, as opposed to variance and correlations inherent to the flow field. Measures of $\mathbf{\Gamma_{x|b}}$ have been devised to quantify the spread of the posterior pdf, which explicitly relate to statistical attributes of the reconstructions. Two Bayesian functions were proposed for the design of CST experiments: an A-optimal function, F_{B1}, to minimize the variance of estimates, and a D-optimal function, F_{B2}, to minimize the volume of posterior credibility ellipses. Section 4.1.2.3 showed that F_{B1} and F_{B2} are structurally-similar to F_{D1}, F_{D2}, and F_{D3} given minimal prior assumptions about the flow field. However, the Bayesian metrics follow from a rigorous derivation, relating to confidence in the reconstructions, whereas the deterministic functions are essentially heuristic.[72] Moreover, F_{B1} and F_{B2} can incorporate knowledge about the flow field through the prior covariance matrix.

Design-of-experiment functions for CST were evaluated with three sets of turbulent phantoms and two optimization scenarios. Phantom sets comprised a large, centred free-shear jet; a small, off-centre jet; and isotropic draws of a Gaussian random field. Flow fields contained different levels of anisotropy in order to test the effect of target structures on the predictive capacity of DOE functions. Structured and unstructured optimization scenarios were investigated. In the structured tests, fan-beam and parallel-beam projections were parametrized by a spacing variable. The unstructured test used a genetic algorithm to minimize F_{D1} and F_{B1} for all three phantom sets. Targets were reconstructed using both a Tikhonov algorithm and Bayesian algorithm with a sample-based prior (because deterministic functions were not expected to track Bayesian reconstruction accuracy and vice versa).[73]

The deterministic functions of Twynstra and Daun [289] and Song et al. [290] were predictive of reconstruction accuracy in the structured scenario while the function of Yu et al. [291] was not.

[72] Ultimately, the norm of the resolution matrix, grid weight, and maximum collinearity each amounts to an arbitrary choice; whereas the Bayesian optimality criteria were derived from an analysis of the expected outcomes for a random variable [292].

[73] This was numerically verified. Correlations between F_{D1}, F_{D2}, F_{D3} and Bayesian reconstruction scores and the correlation between F_{B1} and Tikhonov reconstruction scores were similarly low.

Results from the unstructured test revealed that the predictive capacity of F_{D1} and F_{D2} for the fan-beam and parallel-beam arrays was specific to the particular combination of the structured projections and the 400-pixel basis. When beam positions were free to vary in the plane, F_{D1} and F_{D2} were only weakly correlated to reconstruction error. Correlations for the deterministic functions were weakest for jet 2, which underscores the importance of spatial information to the utility of DOE metrics.

Bayesian DOE functions were consistently predictive of reconstruction accuracy. Fan-beam and parallel-beam optimizations with F_{B1} featured a small range of error and non-linear relationships between the spacing parameter and reconstruction accuracy. Nevertheless, F_{B1} consistently approximated the optimal arrangement. Naturally, the range of error was greater in the unstructured test. The genetic algorithm explored a large space of beam arrays, revealing a strong, general relationship between the Bayesian objective function and reconstruction accuracy. Bayesian correlations exceeded 0.93 for all three phantom sets, compared to a maximum deterministic correlation of 0.67. Optimal arrangements for the Bayesian functions were intuitive. Beam arrays for the jet phantoms were distributed around areas of high variance in the domain, with a large circle of beams centred around jet 1 and a tight circle around jet 2. The optimal array for F_{B1} with a uniform prior had beams that were evenly-distributed throughout the measurement plane, which closely resembled the array that minimized F_{D1}. This result coheres with the comparison of F_{D1} and F_{B1} in Section 4.1.2.3. Absent flow-specific information, the Bayesian functions contain the same structural information as the deterministic functions. Reconstruction accuracy was consistently greater for the Bayesian estimates. And F_{B1} was the most predictive of error in the unconstrained scenario. These results suggest that the Bayesian framework for experimental design in CST is preferable to a deterministic approach.

Once a beam arrangement has been fixed and experimental measurements made, the model used to reconstruct a flow can optimized. CST models comprise the discretization scheme, measurement operator, and prior pdf. Bayesian inference is conditioned on the model, which is itself conceived as an unknown quantity. Models are compared using a Bayes factor that quantifies the odds of one model producing the data over another model, accounting for the effects of noise and uncertainty. The procedure assumes models that can generate the data from a constrained set of system states will yield robust parameter estimates. This chapter describes the first application of Bayesian model comparison to CST: to select a grid resolution, mode of interpolation, and prior.

Bayesian model selection begins with a statement of Bayes' equation where the model itself is an unknown quantity. In principle, a prior can be developed for the model space; but model priors require comprehensive information about the possible space of discretization schemes and priors. Absent detailed information about the model space (rarely available in the CST context), a uniform prior is selected and the model inference reduces to a maximum likelihood formulation. The model likelihood is equivalent to the evidence in the initial Bayesian formulation of CST; and the joint-normal pdfs, discussed in Chapter Two and Chapter Three, enable direct calculation of the evidence/model likelihood. Model selection involves the calculation of this likelihood for a set of candidate models and the model with the greatest likelihood for a set of measurements is said to have most probably generated the data—this model is selected, accordingly. Log-scale model likelihoods are used to stabilize the comparison and this chapter introduces a decomposition of the log-model likelihood. Three key components of the likelihood are related to model performance: the measurement credence, prior fit, and data fit.

Candidate models were generated using a finite element discretization scheme. Finite element meshes can support high-order interpolation and accommodate complex geometries. Meshes of increasing resolution were compared for three classes: using piecewise constant, linear, and quadratic interpolation. High-order bases approximate gas distributions better than low-order bases but require additional parameters, resulting in greater posterior uncertainty. Finite element meshes provide a good test case for model selection due to the trade-off between flexibility and uncertainty. The selection technique was demonstrated using a simulated SCR scenario. Phantoms were obtained from the LES of Zöchbauer et al. [304]; 25 meshes of increasing resolution were generated for the measurement plane; and absorption data were simulated for the eight-beam array of Stritzke et al. [149], which motivated the choice of a SCR scenario.

Models were constructed using the 25 meshes, three modes of interpolation, and four priors. Log-model likelihoods were calculated for each model and compared to the reconstruction statistics. Results of the model selection tests show that the model likelihood is a good predictor of reconstruction accuracy, both within a model class and between classes. The log-model likelihood can be used to select the form of mean and covariance information, resolution of the basis, and mode of interpolation. Moreover, the results illustrate how components of the model likelihood can be examined to explicate trends in the Bayes factor. In the SCR scenario, a sample-

based prior supported the use of a high-resolution mesh and high-order basis (piecewise quadratic), resulting in accurate reconstructions of the NH_3 concentration field.

This chapter demonstrated that Bayesian methods for DOE and model selection—derived from Bayes' equation—are powerful tools for gas-phase tomography. Both methods take advantage of prior information to improve the accuracy of CST: optimizing measurement systems, and selecting a form of representation for gas imaging.

Chapter Five
Broadband Absorption Chemical Species Tomography

Chapters One through Four presented the fundamentals of Bayesian CST and theoretical developments that follow from the Bayesian framework. The next two chapters concern novel applications of gas-phase tomography, motivated by emissions detection and combustion monitoring scenarios, in turn. Methodological improvements are introduced in both cases and reconstructions are carried out with a Bayesian algorithm. This chapter presents a new technique for low-cost tomographic detection of emissions called *broadband absorption CST*.

Simple hydrocarbon molecules and VOCs from upstream oil and gas facilities make up a considerable portion of Canada's greenhouse gas production [306]. VOCs from the Canadian energy sector grew by 24% from 1990 to 2013 due to increased production and now account for 10% of the sector's greenhouse inventory [307]. Gaseous emissions are released at each stage of fuel production, including by inefficient flare combustion; valve, seal, and pipe joint leaks; and evaporation from the surface of oil-water separators and tailings ponds. Methane from flaring is a primary contributor to the greenhouse warming effect and fugitive emissions such as benzene, toluene, ethylene, and xylene (BTEX) have an adverse influence on human health and ecological stability. Benzene is a potent carcinogen [308] and elevated BTEX levels near gas production facilities have been associated with symptoms including fatigue, headaches, dizziness, nausea, respiratory irritation and asthma [309,310]. Correspondingly, there is a strong interest in reducing CH_4 emissions and the release of VOCs, particularly BTEX molecules because of their prevalence and acute adverse health effects.

Canada, the United States, and other nations have enacted regulations that require polluters to quantify their emissions [311,312]. Accurate emissions inventories are needed to develop and enforce mitigation strategies and inform climate models. Flux totals from industrial sources are presently estimated using point-concentration measurements (e.g. flame ionizing detectors (FIDs) [313], catalytic pellistor sensors [312,314], semiconductor sensors [315], and closed-path absorption spectroscopy [316]) coupled with empirical emissions factors and mass balance calculations [317]. These practices are limited by the locality of point-concentration data—as discussed in the introduction—and yield markedly unreliable estimates [35,318]. Moreover, point-measurement surveys are costly, time-consuming, and often require personnel to work in hazardous conditions. Stand-off optical methods for quantifying fugitive emissions, such as gas-phase tomography, can generate the reliable, spatially-resolved measurements that are necessary to meet reporting requirements.

Chapter One provided a detailed overview of optical techniques for the remote sensing of emissions. These include DOAS, DIAL, TDL absorption spectroscopy by DAS or WMS, and broadband imaging with an IR camera. Industrial sources of fugitive emissions are typically anisotropic, distributed across a large area (e.g., the surface of an oil-water separator), and subject to change over time due to transient environmental conditions (temperature, humidity, wind speed, etc.). Many sources are characterized by bursts of activity that result in a thick-tailed distribution of mass flux over time. The bulk of emissions are released during short segments and it is important to develop diagnostics that are easily-adapted to long-term monitoring in order to properly characterize a VOC source.

Open path devices are well-suited to detect distributed fugitive emissions and broadband measurements can be safely conducted using low-cost commercial devices. Moreover, many of these devices are intrinsically safe, meaning they can be used at industrial facilities without modification. In principle, broadband LOS data contains the information necessary to carry out quantitative gas-phase tomography of an emissions source. However, the governing IFK for absorption CST is derived from the Beer-Lambert law, which applies to a monochromatic absorption coefficient. Broadband transmittances convolve spectral information; as a result, measurements are a non-linear function of the gas burden. An alternative procedure is required to reconstruct a gas-phase flow field from coupled open path broadband measurements.

This chapter reports the development of such a procedure, starting from the fundamental model of IR absorption. Results from the first broadband absorption CST experiment are presented along with a Bayesian uncertainty analysis. Thermal emission and broadband detection units used in the experiment were constructed by Roger Tsang, as described in his master's thesis [28]. Light from the emission unit was generated with an incandescent source (a silicon carbide globar) and transmittance measurements were made with photovoltaic detector equipped with a bandpass filter. The filter range was aligned with the main rovibrational C-H stretching band at 3.4 μm. While bandpass filters omit most incoming radiation, they combine light over a range that includes many spectral lines. The integral equation of interest is nested in an exponential function, which is convolved in broadband measurement, thereby producing a non-linear dependence on the emission burden. A transfer function was derived to infer the linear path-integrated concentration for a measurement line from the broadband transmittance. Transfer functions are specific to the target species over a set spectral range and this chapter presents functions for CH_4, C_2H_4, and C_3H_8 with bounds that corresponds to a commercial bandpass filter. Spectral data for CH_4 and C_2H_4 were calculated using a line-by-line model with parameters from the HITRAN database [228]. The C_3H_8 spectrum was obtained from a high-resolution spectral transmittance database [319].

Finally, the broadband reconstruction technique was demonstrated by imaging a momentum-driven C_3H_8 plume, perturbed by advection. LOS measurements were made with a 35-path array and linearized by the C_3H_8 transfer function. The Bayesian framework was employed to reconstruct the plume with a smoothness prior; and uncertainties were estimated in a Bayesian way by calculation of the posterior covariance matrix. Concentration measurements of the plume were made with a FID to validate the procedure. Tomographic data were in good agreement with the FID measurements. Results from this experiment support the development of broadband absorption CST for the quantification of anisotropic, time-varying hydrocarbon emissions.

5.1 Broadband infrared spectroscopy

Molecular spectra consist of lines, bands, and systems, which are convolved in broadband transmittance data. Narrow bandpass filters are selected to align with strong rovibrational transitions in a target species to generate a unique signal for tomographic reconstruction. Transfer functions that convert the signal into a linear measurement are derived from the filter bounds and spectroscopic features of the molecule of interest. In order to justify the form of the transfer function, it is necessary to understand the physical basis for optical gas detection.

Spectroscopy exploits the interaction between light and matter to identify and characterize a species. Atoms contain charged and uncharged particles (protons, electrons, neutrons), arranged in a stable unit. An electric dipole moment arises when the charge about an atom or molecule accelerates during electronic reconfiguration, the bulk motion of a polar molecule, or the relative motion of its atoms. The accelerating charge perturbs the surrounding electromagnetic field, which acts upon the molecule, in turn. This mode of exchange facilitates the absorption, emission, and scattering of radiation. Light-matter interactions occur between specific energy levels, E_i and E_j, which correspond to the quantum states i and j. The shift in energy represents a spectral line: $\Delta E = E_j - E_i = hc\eta_{ij}$, where η_{ij} is the central wavenumber of the transition.

Spectral features are described in terms of the position, strength, and shape of spectral lines, which are illuminated by simple spectroscopic models. The internal energy of a molecule is commonly specified with respect to electronic, rotational, and vibrational components, $E_i = E_{\text{elec}} + E_{\text{rot}} + E_{\text{vib}}$, each associated with a characteristic energy range and corresponding model. IR lines arise from combined rotational and vibrational—*rovibrational*—transitions, whereas electronic transitions are more energetic and fall outside the scope of IR spectroscopy. This section reviews some fundamentals of IR spectroscopy and demonstrates the calculation of spectral bands for broadband tomography. The semi-classical treatment of spectroscopy in this chapter can be found in texts such as Banwell and McCash [320] and Hanson et al. [321] and rigorous quantum mechanical derivations are provided by Struve [322].

5.1.1 Rotational transitions

5.1.1.1 Transition strength

The energy of rotational transitions be understood by introducing an ideal diatomic molecule and relaxing the simplifications to approximate more realistic behaviour. Rotation of the molecule is modelled with a rigid rotor system, shown in Figure 5.1, where the atoms are point masses, m_1 and m_2, connected by a bond of length $r_{\text{eq}} = r_1 + r_2$.[74] Classically, the moment of inertia is

$$I = \mu_{\text{rot}} r_{\text{eq}}^{\,2}, \tag{5.1}$$

where μ_{rot} is the reduced mass of the system,

[74] For real atoms, $m \sim 10^{-13}$ cm and $r \sim 10^{-8}$ cm, so the point-mass assumption is justified.

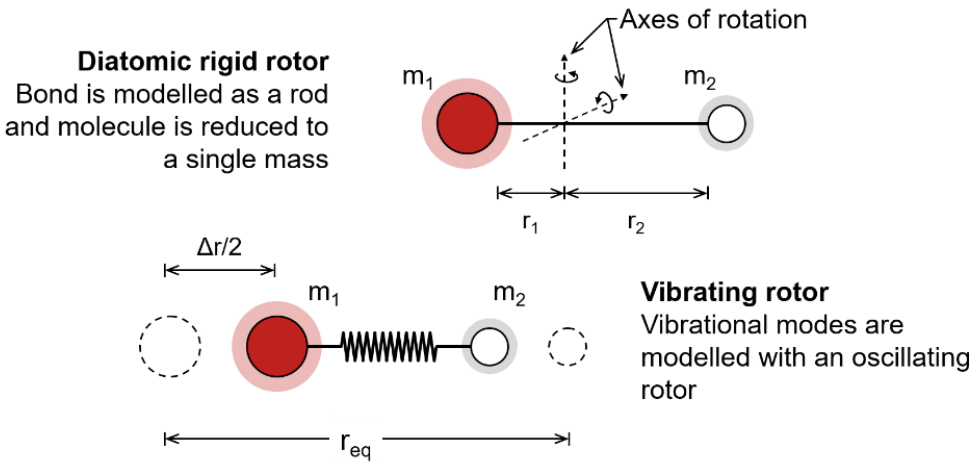

Figure 5.1: Models of a diatomic atom: a rigid rotor model for pure rotational transitions and a vibrating rotor model for rovibrational transitions.

$$\mu_{\text{rot}} = \frac{m_1 m_2}{m_1 + m_2}. \tag{5.2}$$

Molecules are represented by a wavefunction in quantum mechanics, and evolution of the wavefunction is governed by Schrödinger's equation.[75] Solving for the wavefunction of a diatomic rigid rotor yields the moment of inertia,

$$I\omega_{\text{rot}} = \frac{h}{2\pi}\sqrt{J(J+1)}, \tag{5.3}$$

where ω_{rot} is the angular velocity and J is the *rotational quantum number*. The rotor's wavefunction only satisfies Schrödinger's equation when J is an integer, meaning that the quantized nature of molecular states naturally follows from the governing equation. Rotational energy of a molecule in J, ε_J, is typically calculated in terms of the corresponding wavenumber. Since radiative energy equals $hc\eta$, the rotational energy in wavenumbers is

$$\varepsilon_J = \frac{E_{\text{rot}}}{hc} = \frac{1}{2hc} I\omega_{\text{rot}}^2 = \frac{1}{2hcI} J(J+1) = \left(\frac{h}{8\pi^2 cI}\right) J(J+1) = BJ(J+1), \tag{5.4}$$

where B is the rotational constant. Equation (5.4) says that rotational states which can be occupied by a rigid diatomic molecule—and which thereby give rise to rotational lines—are fully-determined by fundamental constants, the rotor's moment of inertia, and a quantum number, J. Transition probabilities can be calculated from the wavefunction, which reveals limitations on

[75] The time-independent form of Schrödinger's equation is $d^2\Psi/dx^2 + (8\pi^2 m/h^2)[E - U(x)]\Psi(x) = 0$, where Ψ is the wavefunction [374], which describes the motion of a particle of mass m moving through a potential field, U. The probability that the particle will be measured in $x + dx$ is given by $\Psi\Psi^*$, where Ψ^* is the complex conjugate of Ψ.

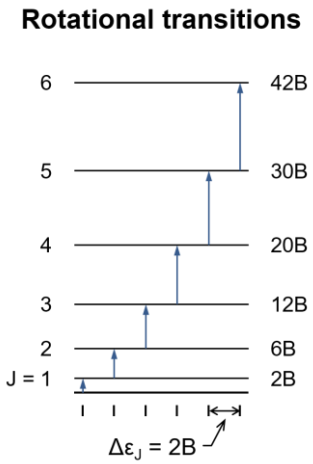

Figure 5.2: Energy levels for valid transitions of a diatomic rotor; pure rotational transitions in heteronuclear rotors generate microwave lines.

state transitions, resulting in so called *selection rules*.[76] For a diatomic rigid rotor, the selection rule is $\Delta J = \pm 1$; the allowable rotational transition energies are: $\Delta\varepsilon_{J \to J+1} = 2B(J+1)$. Energy levels and transitions of the rigid rotor are shown in Figure 5.2. While rotational transitions occur for all molecules, they are only observed by absorption or emission if rotation induces a dipole moment.

Simple molecules such as CO behave like a rigid rotor at low rotational energy levels. In reality, the bond length increases with rotational velocity and atomic vibrations affect the rotational momentum. Moreover, the rigid rotor only describes the rotation of diatomic molecules. Stretching effects are corrected with centrifugal and vibrational distortion terms; and the wavefunction for a non-rigid rotor relaxes the selection rules, permitting additional transitions. Similar analyses are conducted for triatomic linear molecules and 3D molecules with rotational symmetry [321].[77] These solutions are applied to predict the onset and spacing of rotational spectral lines in a wide array of molecules. Anomalies between predicted and observed transition energies are used to learn about molecular structures.

5.1.1.2 Transition intensity

Once the energy of a transition has been established, the probability of transition is calculated to determine the line strength. Rigid rotor transitions from J to $J + 1$ or $J - 1$ are equally probable for

[76] The probability of transition from i to j is proportional to the integral of $\Psi_i \mu_{\text{dip}} \Psi_j^*$ over the space elements, where μ_{dip} is the permanent electric dipole moment [374]. Valid transitions are indicated by a non-zero integral.

[77] Molecules have three principal axes of rotation, I_A, I_B, and I_C, and are classified as linear rotors ($I_A \approx 0$, $I_B = I_C$), symmetric tops ($I_A \neq 0$, $I_B = I_C$), spherical tops ($I_A = I_B = I_C$), and asymmetric tops ($I_A \neq I_B \neq I_C$). Non-rigid corrections have been developed for linear rotors and symmetric tops, spherical tops are rotationally inactive (i.e., rotation does not produce a dipole moment), and transitions for asymmetric tops are only identified numerically or empirically.

a given molecule but the line strength depends on the relative number of molecules in the lower and upper states. For a molecules in LTE, states are populated according to a Boltzmann distribution,

$$\frac{N_J}{N_0} = \exp\left\{-\frac{E_J}{k_B T}\right\} = \exp\left\{-\frac{BhcJ(J+1)}{k_B T}\right\}, \tag{5.5}$$

where N_J is the number of molecules in J and $J = 0$ is the ground rotational state. The probability of transition also depends on the degeneracy of states. For rotational states, degeneracy is determined by the number of valid directions of the angular momentum vector, $\mathbf{P} = I\omega_{\text{rot}}$, where the state corresponds to a constant magnitude, $|\mathbf{P}|$. Substituting Eq. (5.3) into the definition of **P** reveals that the magnitude of **P** will take quantized values,

$$|\mathbf{P}| = \frac{h}{2\pi}\sqrt{J(J+1)}\,. \tag{5.6}$$

The direction of **P** is also quantized. Integrating the rigid rotor wavefunction and its complex conjugate reveals that **P** may point in any direction such that the projection of **P** onto a reference vector is an integer multiple of $h/2\pi$ [320]. There are $2(J + 1)$ such directions for any state, which results in a modification to the state populations,

$$\frac{N_J}{N_0} = \frac{\sigma_{\text{sym}}\theta_{\text{rot}}}{T}(2J+1)\exp\left\{-\frac{\theta_{\text{rot}}J(J+1)}{T}\right\}, \tag{5.7}$$

where σ_{sym} is a symmetry factor and $\theta_{\text{rot}} = hcB/k_B$ is a characteristic temperature, usually on the order of 1 K, which relates to the spacing of rotational lines.[78] Pure rotational transitions reside in the microwave spectrum but rotational and vibrational transitions are intrinsically related and the rigid rotor model is thereby relevant to hydrocarbon spectra in the IR region.

5.1.2 Vibrational transitions

Vibrations in a diatomic molecule are modelled by replacing the rigid rotor with a simple harmonic oscillator. The mass-spring system features point-mass atoms, connected by a massless spring, oscillating in a frictionless plane; this model is depicted alongside the rigid rotor in Figure 5.1. Force due to atomic vibrations is given by Hooke's law,

[78] The symmetry factor describes the number of principle rotations for which the molecule appears identical. Consider the case of diatomic molecules: $\sigma_{\text{sym}} = 2$ for homonuclear rotors whereas $\sigma_{\text{sym}} = 1$ for heteronuclear rotors, since the molecule is asymmetric.

$$F_{\text{vib}} = -k_{\text{vib}}(r - r_{\text{eq}}), \tag{5.8}$$

where r is the separation of the atoms, r_{eq} is the bond length at equilibrium, and k_{vib} is the spring constant for the rotor (i.e., the bond energy). The potential energy of the system is

$$E_{\text{pot}} = \frac{1}{2} k_{\text{vib}}(r - r_{\text{eq}})^2. \tag{5.9}$$

Figure 5.3a shows the energy potential for a simple harmonic oscillator. The frequency of this system in wavenumbers is

$$\omega_{\text{vib}} = \frac{1}{2\pi c}\sqrt{\frac{k_{\text{vib}}}{\mu_{\text{rot}}}}. \tag{5.10}$$

Solving for the wavefunction of the harmonic oscillator yields the total vibrational energy,

$$E_{\text{vib}} = \omega_{\text{vib}}(v + 1/2), \tag{5.11}$$

where v is the *vibrational quantum number*. Interestingly, the lowest vibrational energy level is $\omega_{\text{vib}}/2$ (i.e., molecules always contain vibrational energy).

As with rigid rotors, the oscillator's wavefunction will only satisfy Schrödinger's equation when v is an integer. Discrete energy levels for the simple harmonic oscillator accompany the energy potential in Figure 5.3a. Potential and kinetic energy follow a continuous curve but the total energy is restricted to angular frequencies that correspond to an integer value of v. The selection rule for a diatomic oscillator is $\Delta v = \pm 1$, in which case

$$\Delta E_{v \to v+1} = \omega_{\text{vib}}(v + 1 + 1/2) - \omega_{\text{vib}}(v + 1/2) = \omega_{\text{vib}}. \tag{5.12}$$

Equation (5.12) holds for absorption and emission and predicts equally-spaced vibrational states.[79]

Real molecules deviate from the harmonic idealization in several ways, resulting in anharmonic vibrations. The most substantial correction is the altered potential—shown alongside the harmonic oscillator's potential in Figure 5.3b—which reflects the possibility of dissociation and impossibility of nucleic contact.[80] This potential modifies the wavefunction, resulting in the vibrational energy levels for an anharmonic oscillator,

[79] Note that these vibrations are only visible when they induce a dipole moment, which is only possible in the case of a heteronuclear diatomic molecule because homonuclear diatomic rotors are symmetrical.

[80] One common semi-empirical potential is the Morse function: $E = D_{\text{eq}}[1 - \exp\{a(r - r_{\text{eq}})\}]^2$, where D_{eq} is the dissociation energy and a is a molecular constant. Correction terms in Eq. (5.13) are found by substituting the Morse function into Schrödinger's equation.

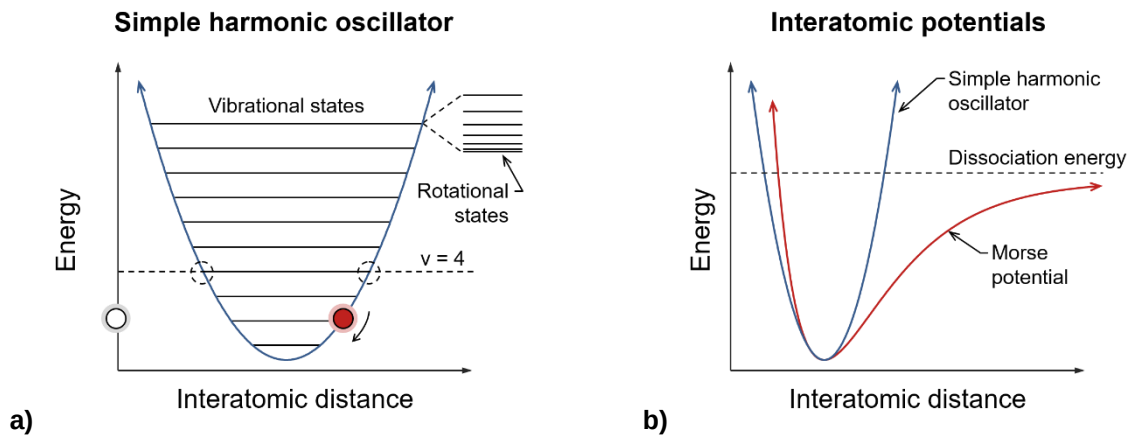

Figure 5.3: Vibrational states and energy potentials for a diatomic molecule: a) vibrational levels for a simple harmonic oscillator and b) a semi-empirical potential for a real diatomic rotor (i.e., a Morse potential).

$$E_{\text{vib}} = \omega_{\text{vib}}(v+1/2) - \omega_{\text{vib}} x_c (v+1/2)^2 + \mathcal{O}(v^3), \tag{5.13}$$

where the anharmonicity constant, x_c, is strictly positive. Selection rules are modified in the anharmonic case, introducing larger transitions (i.e., $\Delta v > 1$). However, since the population of molecules above ε_0 is minimal at equilibrium, dominant transitions are positive: $\Delta v = 1, 2$, etc. The first vibrational transition yields the fundamental absorption band and subsequent transitions generate overtone bands. (Overtone bands are forbidden for simple oscillators but ubiquitous among real molecules.)

Vibrational state populations for molecules in LTE follow a Boltzmann distribution,

$$\frac{N_v}{N_0} = \left[1 - \exp\left\{-\frac{\theta_{\text{vib}}}{T}\right\}\right] \exp\left\{-\frac{\theta_{\text{vib}} v}{T}\right\}, \tag{5.14}$$

where $\theta_{\text{vib}} = hc\omega_{\text{vib}}/k_{\text{B}}$ is a characteristic temperature that relates to the strength of vibrational transitions, analogous to θ_{rot}; θ_{vib} is usually on the order of 1,000 K. The difference in magnitude between θ_{rot} and θ_{vib} is reflected in the position of spectral lines. While rotational lines occupy the microwave spectrum, vibrational transitions are active at IR energies.

5.1.3 Rovibrational bands

So far, rotational and vibrational transitions have been discussed independently. However, these transitions are typically coupled and can be combined in a linear fashion, which amounts to the Born-Oppenheimer approximation. This simplification results in the vibrating rigid rotor model of

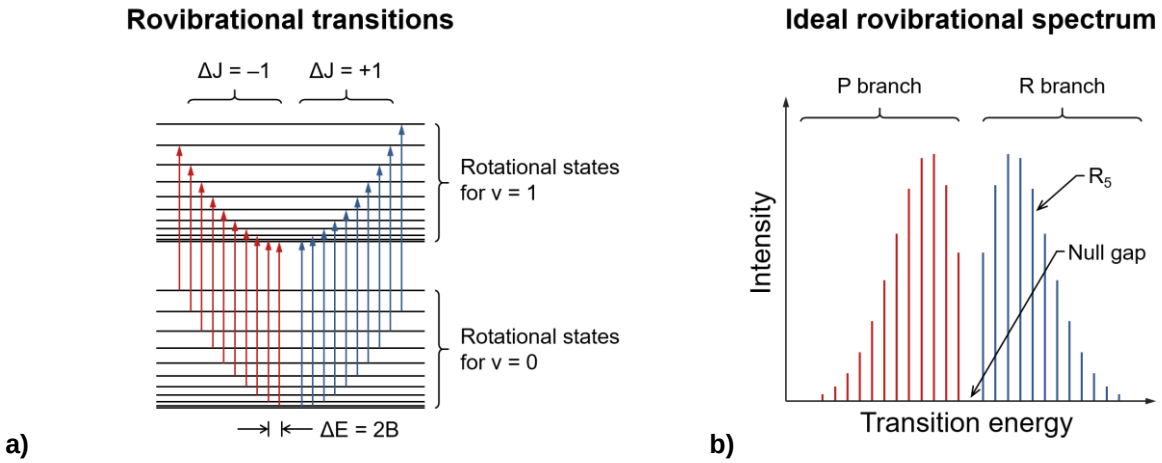

Figure 5.4: Rovibrational transitions for a diatomic rotor: a) transitions and line spacing for the fundamental band and b) an ideal rovibrational spectrum.

diatomic molecules.[81] Ignoring the minimal contribution of centrifugal distortion, the energy of a vibrating rigid rotor in the rotational state J and vibrational state v is

$$\varepsilon_{J,v} \approx BJ(J+1) + \omega_{\text{vib}}(v+1/2) - \omega_{\text{vib}}x_c(v+1/2)^2. \tag{5.15}$$

Anharmonic vibrations remain important to the spectrum and the quadratic correction term is retained in Eq. (5.15). Selection rules for coupled transitions are unchanged except that vibrational transitions with no rotational component (i.e., $\Delta J = 0$ and $\Delta v \neq 0$) are forbidden for diatomic rotors. As mentioned in the previous section, the dominant vibrational transition is $\Delta v = 1$ (the fundamental band). In general, for $\Delta v = 1$, the rovibrational transition from the lower rotational state, J_i, to the upper state, J_j, is

$$\begin{aligned}\Delta\varepsilon_{J=i,v=1\rightarrow J=j,v=0} &= BJ_j(J_j+1) + \frac{3}{2}\omega_{\text{vib}} - \frac{1}{2}\omega_{\text{vib}}x_c - \left[BJ_i(J_i+1) + \frac{1}{2}\omega_{\text{vib}} - \frac{1}{4}\omega_{\text{vib}}x_c\right] \\ &= \omega_{\text{vib}}(1-2x_c) + B(J_j - J_i)(J_j + J_i + 1)\end{aligned}. \tag{5.16}$$

Figure 5.4 shows rovibrational energy levels and transition intensities for the fundamental absorption band of a simple diatomic rotor. Line positions were calculated with Eq. (5.16) and relative line intensities were found by combining Eqs. (5.7) and (5.14) using a rotational constant of 5 cm^{-1} and temperature of 300 K. The absorption band is divided into two branches: the R branch for $\Delta J = 1$ and P branch for $\Delta J = -1$. Non-linear molecules can feature vibrational transitions with $\Delta J = 0$, resulting in a central branch called the Q branch. Otherwise, the distance between the R

[81] Of course, there is an inherent tension in the idea of vibration in a "rigid" rotor; nevertheless, the approximation is useful. Proper analysis of the dipole induced by a vibrating rotator increases the accuracy of line positions.

and P transitions is called the null gap. The line structure of overtone bands, where $\Delta v > 1$, is approximately the same as the fundamental band structure. Overtone lines are much less intense, however, typically reduced by a factor of 10 to 1,000. In the case of hydrocarbons R, Q, and P branches are evident in the rovibrational lines due to asymmetric stretching of C-H bonds.

Real molecules violate several of the assumptions used to construct the vibrating rigid rotor model. Correction terms are required to account for the energy of a non-rigid, anharmonically-vibrating rotor. Moreover, alternative models must be developed to obtain the spectrum of triatomic rotors, spherical tops (e.g., CH_4), and symmetric tops. Nevertheless, the basic band structure of a vibrating rigid rotor appears in the spectra of many molecules—including asymmetric tops such as C_2H_4 and C_3H_8. The onset, spacing, and relative strength of spectral lines determines the broadband absorption behaviour of a molecule and rotor analyses can structure observations of spectroscopic phenomena—including the position and strength of overtone bands. Hanson et al. [321] provide a complete treatment of spectroscopy models for engineers.

5.1.4 Line strength

5.1.4.1 Absorption probabilities

Spectral lines are observable by three mechanisms: absorption, where the molecule jumps from the lower state to an upper state; and spontaneous or stimulated emission, where the molecule relaxes from an upper state to a lower state. These events occur in proportion to the number density of molecules in the transition states, N_i (lower) and N_j (upper), moderated by incident light at the transition wavenumber. Emission and absorption are inherently stochastic and transitions are characterized by the probability of an event over time, quantified by Einstein A and B coefficients. The A coefficient relates to spontaneous emission and B coefficients relate to absorption and stimulated emission. Innate transition probabilities are combined with the local distribution of molecules to calculate the propensity of a gas to absorb or emit light. This propensity is summarized by the absorption coefficient, κ_η, which is the reconstructed quantity in monochromatic absorption CST and forms the basis of the transfer function, as described in Section 5.2.

For very simple systems, such as a single hydrogen atom, the probability of spontaneous emission can be computed from quantum theory. In complex systems, however, aggregate behaviour is described by the Einstein coefficients, which are innate properties of a transition but must be empirically determined. To understand the function of these coefficients, consider a

system with two states: a lower state, 1, and upper state, 2. The transition rate due to spontaneous emission (usually in molecules per time) is N_2A_{21}.[82] Absorption and stimulated emission depend on the amount of incident light at the transition wavenumber, I_η.[83] The rate of absorption is $N_1(I_\eta B_{12})$ and the rate of stimulated emission is $N_2(I_\eta B_{21})$. Since the system only has two states, rates of relaxation and excitation must be equal in equilibrium: $N_1 I_\eta B_{12} = N_2(A_{21} + I_\eta B_{21})$. Intensity depends on the environment and the coefficients are not yet known. However, the relationship between A_{21}, B_{21}, and B_{12} can be seen by applying an energy balance to an isolated medium in LTE. Intensity is a function of the transition rates,

$$I_\eta = \frac{N_2 A_{21}}{N_1 B_{12} - N_2 B_{21}} = \frac{A_{21}}{\frac{N_1}{N_2} B_{12} - B_{21}}; \tag{5.17}$$

the ratio of states, N_1/N_2, follows the Boltzmann distribution; and emission by the medium follows the Planck distribution. Substituting these distributions into Eq. (5.17) reveals a connection between A and B coefficients,

$$\frac{2h\eta^3}{c^2} \frac{1}{\exp\left\{\frac{hc\Delta\eta}{k_B T}\right\} - 1} = \frac{A_{21} / B_{12}}{\frac{g_1}{g_2} \exp\left\{-\frac{\Delta E_{21}}{k_B T}\right\} - \frac{B_{21}}{B_{12}}}, \tag{5.18}$$

where g_1 and g_2 are lower and upper statistical weights that account for degeneracy of the states. Note that the transition energy is related to the radiative energy, $\Delta E = hc\Delta\eta$. Hence, for I_η at $\Delta\eta$, Eq. (5.18) leads to the Einstein relations,

$$g_1 B_{12} = g_2 B_{21} \text{ and } A_{21} = \frac{2h\eta^3}{c^2} B_{21}. \tag{5.19}$$

Equation (5.19) indicates that any one of A_{21}, B_{21}, and B_{12} can fully characterize the innate probability of an absorption- or emission-based transition between two states. (For instance, a large decay rate suggests both substantial absorption and substantial spontaneous emission.) Next, this information is related to the abundance of a target molecule and used to construct a quantitative spectroscopic model.

[82] If the analysis is restricted to spontaneous emission then $dN_2/dt = -N_2A_{21}$ and $N_2 \propto \exp\{-A_{21}t\}$. That is, the Einstein A coefficient is directly related to the radiative lifetime and half-life of an excited state.

[83] Here, the incident intensity, I_η, represents an average over all directions as well as the spectral range about the broadened transition line.

5.1.4.2 Developing the spectral absorption coefficient

Einstein coefficients characterize the fundamental relationship between states—sometimes called the innate strength of a transition. The absorption coefficient from the Beer-Lambert law describes light attenuation due to absorption, minus the contribution of stimulated emission;[84] the coefficient can be expressed in terms of B_{12} and B_{21}. The energy balance of light over a differential path, of length du, is [323]

$$\delta I_\eta \delta\eta = \overbrace{\frac{N_2 B_{21} I_\eta}{c} du}^{\text{Emission probability}} \cdot h\eta - \overbrace{\frac{N_1 B_{12} I_\eta}{c} du}^{\text{Absorption probability}} \cdot h\eta = [N_2 B_{21} - N_1 B_{12}] \frac{h\eta}{c} (I_\eta du). \tag{5.20}$$

The differential wavenumber, $\delta\eta$, indicates that absorption occurs over a finite (albeit infinitesimal) spectral width. (The next section shows how to determine the energy distribution of a transition—given by f—but the distribution is not required to calculate the relationship between a transition strength and absorption coefficient.) Rearranging Eq. (5.20) reveals the absorption coefficient,

$$\kappa_\eta \equiv -I_\eta^{-1} \frac{dI_\eta}{du} = \frac{h\eta}{c} [N_1 B_{12} - N_2 B_{21}] \cdot \delta\eta^{-1}. \tag{5.21}$$

For molecules in LTE, the Boltzmann distribution relates the populations in states 1 and 2 and the ideal gas law is used to compute the target molecule's number density. Finally, the lineshape from Chapter Two accounts for the wavenumber differential,

$$\kappa_{\eta,ij} = \overbrace{\underbrace{h\eta_{ij}}_{\text{Energy}} \underbrace{\frac{g_i}{Q(T)} \exp\left\{-\frac{hcE_i}{k_B T}\right\}}_{\text{Relation between } n_i \text{ and } n} \underbrace{\frac{B_{ij}}{c}\left(1 - \exp\left\{-\frac{hc\eta_{ij}}{k_B T}\right\}\right)}_{\text{Fundamental transition probability}}}^{\text{Line intensity: } S_{ij}(T)} \cdot f(\eta) \cdot \frac{\chi p}{k_B T}, \tag{5.22}$$

where Q is the total internal partition sum. Separating the number density from the line intensity, S_{ij}, is convenient in CST since κ_η is used to infer χ. This form of S_{ij} is called the *number density normalized line intensity*.

[84] The direction of spontaneous emission is uniformly distributed and its contribution to a collimated beam is negligible. As such, while line intensity is often expressed in terms of A_{21}, the absorption coefficient, B_{12}, is a more natural choice for absorption spectroscopy

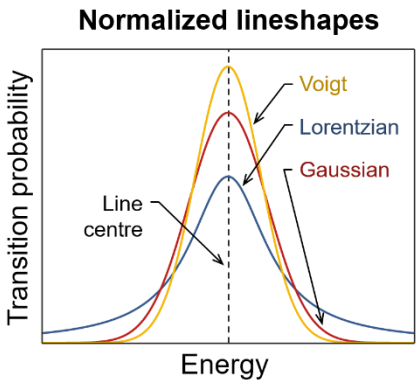

Figure 5.5: Normalized lineshapes with a Lorentzian, Doppler, and Voigt profile.

5.1.5 Lineshape

So far, transitions have been discussed in terms of a precise energy that corresponds to a single wavenumber. Transitions occur over a finite duration and have a finite energy due to the quantized nature of electromagnetic radiation, but these values are not infinitely precise. Instead, the uncertainty principle limits the combined precision of the time and energy associated with a transition. As a result, spectral lines have a natural width that is broadened by kinetic and electric effects. Lines are modelled in terms of their intensity and shape, which is itself a function of the state of the gas. The lineshape is normalized by the line such that *f* integrates to unity; the definition of the lineshape function is

$$f(\eta) \equiv \frac{\kappa_{\eta,ij}}{\int_{\mathbb{R}} \kappa_{\eta',ij} d(\eta - \eta_{ij})} \approx \frac{1}{\delta\eta}, \text{ where } \int_{\mathbb{R}} f(\eta') d(\eta - \eta_{ij}) = 1. \tag{5.23}$$

Thus *f* only describes the *distribution* of energy about the line centre, η_{ij}. Broadening mechanisms determine the shape of *f*. Dominant forms of broadening in CST are natural, collisional, and Doppler broadening, discussed below, which are collectively described by a Voigt profile. Lineshapes for these mechanisms can be seen in Figure 5.5.

5.1.5.1 Natural broadening

Spontaneous emission from *j* to *i* occurs over some duration, Δt, and releases some energy, $\Delta E = hc\Delta\eta$. The characteristic duration for an excited state is its *lifetime*, $\tau_{ji} = A_{ji}^{-1}$, and the uncertainty principle states that $\Delta E \Delta t \geq h/2\pi$. Therefore, transitions have an intrinsic spectral width, $\Delta\eta = A_{ji}/2\pi c$; this result is said to be a *lifetime limited* phenomenon. Another way to understand natural broadening is to observe that any process with duration in the temporal domain—required by the uncertainty principle, in this case—has width in the frequency domain.

The persistence of an excited state is characterized by an exponential decay, parametrized by the A coefficients for that state: $n_{\text{upper}} \propto \exp\{-At\}$.[85] Hendrik Lorentz modelled spontaneous emission as a damped oscillator. He took the Fourier transform of the system to determine the corresponding distribution in frequency space. The resulting lineshape function is said to have a Lorentzian profile,

$$f_{\text{L}}(\eta) = \frac{1}{\pi} \frac{\Delta\eta / 2}{(\eta - \eta_{ij})^2 + (\Delta\eta / 2)^2}. \tag{5.24}$$

where $\Delta\eta/2$ is the full width at half maximum; for natural broadening, $\Delta\eta_{\text{N}} = A_{ji}/2\pi c$. See Demtröder [324] for a derivation of f_{L}.

5.1.5.2 Collisional broadening

Molecular collisions can induce a rovibrational transition, where a large number of collisions will appreciably reduce the lifetime of an excited state. Faster decay in the temporal domain corresponds to a broader profile in the frequency domain. Collisional broadening is thus a lifetime limited phenomenon, derivative of natural broadening. Collisions effectively decrease Δt and the lineshape for collisional broadening is the Lorentzian profile of Eq. (5.24). The collision-broadened full width at half maximum depends on the chemical composition of a medium,

$$\Delta\eta_{\text{C}} = 2p \sum_k \chi_k \gamma_k(T), \tag{5.25}$$

where p is the total pressure and χ_k and γ_k are the mole fraction and collisional broadening coefficient of the kth species. Temperature effects are approximated with a correlation,

$$\gamma(T) = \gamma(T_0)\left(\frac{T_0}{T}\right)^n, \tag{5.26}$$

where n is an empirical, transition-specific factor that can vary from –0.3 to 1 [40].

Equation (5.25) is derived from analysis of the mean collision frequency between two arbitrary species. The derivation features a collisional cross-section that must be empirically determined. Complex models of collisional broadening for high-energy collisions account for changes to the potential wells of colliding particles. By contrast, Eq. (5.25) assumes a large interatomic distance at the point of transition, such that the energy difference is invariant to the shape of the potential. High-energy models are a function of the mixture composition and energy

[85] The overall A coefficient for an upper state is the sum of transition-specific coefficients for all valid lower states, i.

states involved in a transition. Furthermore, high-temperature effects (e.g., due to shifted state populations and velocity distributions) are accommodated with speed-dependent lineshapes.

Collisional broadening dominates the shape of hydrocarbon emissions at standard conditions.

5.1.5.3 Doppler broadening

The Doppler effect is a general phenomenon in which a wavelength is shifted due to the relative velocity between the wave source and an observer. Electromagnetic radiation has a constant velocity, irrespective of the frame of reference, but the wavelength/wavenumber is a function of perspective: molecules travelling towards a light source see photons with a different energy than molecules travelling away from the source. This effect manifests in gas spectra in two ways. Bulk motion of a fluid introduces a coherent Doppler shift, where the initial lineshape is preserved but the line centre is shifted. By contrast, thermal motion within the fluid is characterized by the random motion of particles. The combined effect of Doppler-shifted light for particles moving in all directions is a broadened lineshape that relates to the gas temperature.

Molecules see light at a shifted wavelength, $\Delta\eta = \eta(1 - v_p/c)$, where v_p is the component of a molecule's velocity in the direction of a colliding photon. The velocity distribution determines the width and shape of Doppler broadening. Kinetic theory dictates that molecular motion due to thermal energy follows a Maxwellian distribution. Substituting the shifted wavelength into this distribution for a given lower energy state and normalizing the result produces the Doppler lineshape [320],

$$f_D(\eta) = \sqrt{\frac{4\ln(2)}{\pi\Delta\eta_D^{\,2}}}\exp\left\{-4\ln(2)\frac{(\eta-\eta_{ij})^2}{\Delta\eta_D^{\,2}}\right\}. \tag{5.27}$$

Equation (5.27) is a Gaussian distribution about the line centre, characterized by the temperature-dependent Doppler width,

$$\Delta\eta_D = \sqrt{\frac{8kT\ln(2)}{m_0}}\eta_{ij}, \tag{5.28}$$

where m_0 is the molecular mass of the target species.

5.1.5.4 Voigt profiles

Natural, collisional, and Doppler broadening are all present in gas-phase LOS measurements. Near standard conditions, natural broadening is minuscule compared to collisional and Doppler effects

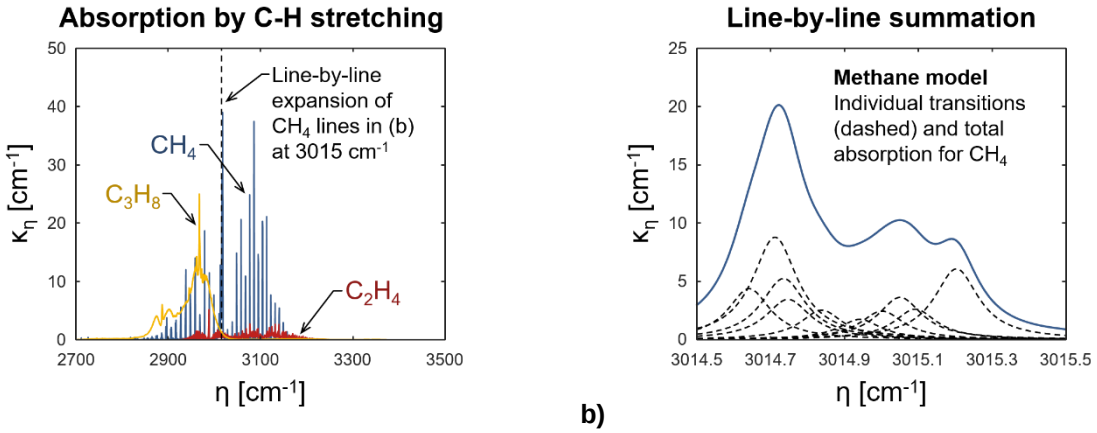

Figure 5.6: Mid-IR absorption spectra: a) spectra for CH_4, C_2H_4, and C_3H_8 and b) a line-by-line summation of individual CH_4 transitions. Line parameters for CH_4 and C_2H_4 were calculated using HITRAN parameters [228]; C_3H_8 spectra were inferred from PNNL absorbance data [319].

(natural broadening is observable primarily due to its participation in collisional broadening). The Gaussian profile of Doppler broadening is relatively important about the line centre and the Lorentzian profile of collision broadening dominates the wings, illustrated in Figure 5.5. However, these mechanisms act independently of one another and the resulting lineshape, called a Voigt profile, is given by the convolution of Eqs. (5.24) and (5.27),

$$f_V(\eta) = \int_{\mathbb{R}} f_D(\eta)\, f_L(\eta - \eta')\, d\eta' = \sqrt{\frac{4\ln(2)}{\pi \Delta\eta_D}} \overbrace{\frac{a}{\pi} \int_{\mathbb{R}} \frac{\exp\left\{-y^2\right\}}{a^2 + (w-y)^2}\, dy}^{\text{Voight function, } V(a,w)}, \tag{5.29}$$

where $a = \ln(2)^{1/2} \Delta\eta_C / \Delta\eta_D$ and $w = 2\ln(2)^{1/2} (\eta - \eta_{ij}) / \Delta\eta_D$. Equation (5.29) is solved using lookup tables or a correlation, such as that of Whiting [325].

5.1.6 Calculating absorption spectra

Absorption and emission events are independent and most optical diagnostics rely on a large number of transitions and a target fluid in LTE. Under these conditions, which prevail in the emissions detection context, the absorption coefficient is a simple summation of the transition-specific coefficients, $\kappa_{\eta,ij}$, for all valid transitions:

$$\kappa_\eta = \sum_{ij} \kappa_{\eta,ij} \,. \tag{5.30}$$

Parameters to calculate the position, strength, and shape of spectral lines for common molecules are available in databases such as the *hi*gh-resolution *tran*smission (HITRAN) database [228]. Line-by-line parameters for complex molecules, including C_3H_8, are often unavailable, but κ_η can be inferred in many such cases using an empirically-derived transmittance profile. This study

employs a line-by-line model of κ_η for CH_4 and C_2H_4 based on HITRAN parameters [228], and an empirical profile of κ_η for C_3H_8 using data from the vapour phase infrared spectral library [319]. Figure 5.6 shows absorption coefficient profiles for all three targets. Stretching of the C-H bond gives rise to rovibrational transitions in the mid-IR; the R/Q/P band structure derived from the rotor model is especially apparent in the CH_4 spectrum.

5.2 Broadband Absorption Transfer Function

Direct absorption and wavelength modulation spectroscopy generate a spectrally-resolved measurement of I_η (or its harmonics), used to determine κ_η across an absorption feature. These features are sensitive to the abundance, temperature, and pressure of an absorbing gas. Spectroscopic models of the targets can be used to infer the composition and state of a mixture from DAS or WMS data. Moreover, per Chapter Two, the logarithm of monochromatic measurements, $\ln[I_\eta(0)/I_\eta(L)]$, is a linear function of the absorption coefficient, which enables reconstruction of κ_η by computed tomography.

Broadband measurements for open path IR spectroscopy are typically made with a bandpass filter and photovoltaic detector. The result is one transmittance per LOS (as opposed to a spectral profile), which convolves spectral features and has a non-linear dependence on the emissions burden. However, κ_η can be decomposed into a shape factor, C_η, and emissions volume fraction, χ. This decomposition is substituted into the expression for broadband transmittance to isolate an integral equation of χ. An empirical transfer equation relates transmittance data to the integral, which forms the basis of broadband absorption CST. Derivation of this function and the calculation and verification of target-specific transfer equations are described in Sections 5.2.2 and 5.3, respectively.

5.2.1 Transmittance measurement

Absorption data for broadband tomography is generated by light from a thermal source, attenuated by the target, passed through a bandpass filter, and measured with a photovoltaic detector. Power incident on the detector, located some distance, L, from the source, is

$$P = C_{\text{cfg}} \int_0^\infty \overbrace{\varepsilon_\eta I_{b,\eta}(T_s)}^{\text{Thermal emission}} \overbrace{\exp\left\{-\int_0^L \kappa_\eta(u)du\right\}}^{\text{Absorption by the target}} \overbrace{\tau_\eta d_\eta}^{\text{Detection}} \, d\eta \,. \tag{5.31}$$

Terms in Eq. (5.31) can be categorized as relating to emission from the source, absorption by the gas, and spectral characteristics of the detector. Source terms include C_{cfg}, a geometric

configuration factor that accounts for the fraction of energy from the source that reaches the detector; ε_η, the spectral emissivity; and $I_{b,\eta}$, blackbody emission at the source temperature, T_s. Absorption by the gas is governed by the Beer-Lambert law and the detector is modelled using the product of τ_η, the filter's spectral transmissivity, and d_η, a function that describes the conversion of incident intensity into a voltage by the photodetector. Optics for collimation and focusing may have a spectral dependence, but the spectral effects of C_{cfg} are constant between the reference and absorption measurements and are neglected, accordingly. Thermal source materials are well-modelled as gray bodies and the blackbody spectrum and detector function are roughly constant over the active range of a narrow bandpass filter. The filter function approximates a top-hat profile and, as a result, Eq. (5.31) simplifies into

$$P \approx C_{\text{det}} \int_{\eta_1}^{\eta_2} \exp\left\{-\int_0^L \kappa_\eta(u)du\right\} d\eta\,, \tag{5.32}$$

where C_{det} is an aggregate system constant and η_1 and η_2 are the bounds of the bandpass window. The system constant is

$$C_{\text{det}} = C_{\text{cfg}} \overline{\varepsilon_\eta I_{b,\eta}(T)\tau_\eta d_\eta}\,, \tag{5.33}$$

where the product of ε_η, $I_{b,\eta}$, τ_η, and d_η is an average over the active range of the filter.

Broadband transmittance measurements, *Tr*, are defined as the ratio of power attenuated by the gas, P_{abs}, to a reference power, P_{ref}, made in the absence of the target (i.e., $\kappa_\eta = 0$):

$$P_{\text{ref}} = C_{\text{det}} \int_{\eta_1}^{\eta_2} \exp\left\{-\int_0^L (0)du\right\} d\eta = C_{\text{det}}(\eta_2 - \eta_1)\,. \tag{5.34}$$

The aggregate system constant cancels out in the calculation of *Tr*. Broadband transmittances are expressed in terms of Eq. (5.32),

$$Tr \equiv \frac{P_{\text{abs}}}{P_{\text{ref}}} = \frac{1}{\eta_2 - \eta_1} \int_{\eta_1}^{\eta_2} \exp\left\{-\int_0^L \kappa_\eta(u)du\right\} d\eta\,. \tag{5.35}$$

In contrast to the monochromatic measurements featured in preceding chapters, *Tr* smears the path-integrated absorption coefficients from a range of η. An additional step is thus required to deconvolve the target distribution from coupled broadband LOS data.

5.2.2 Transfer function

Targets in the context of ground-level emissions monitoring consist of a single species or well-mixed composition that quickly equilibrates to ambient conditions. This commonality enables a key simplification of Equation (5.35). The absorption coefficient of a gas mixture is naturally weighted by the mole fraction of the constituent species,

$$\kappa_\eta = \sum_k \left\{ \sum_{ij} \left(S_{ij}^{(k)}(T_0)\, f^{(k)}(\eta;\eta_{ij}) \right) \frac{\chi^{(k)} p_0}{k_\mathrm{B} T_0} \right\}, \tag{5.36}$$

where k refers to a species in the mixture and T_0 and p_0 are the ambient temperature and pressure. If the target composition is consistent throughout the imaging domain, the combined lineshapes can be isolated using a spectral shape factor,

$$C_\eta \equiv \frac{p_0}{k_\mathrm{B} T_0} \sum_k \left\{ \sum_{ij} \left(S_{ij}^{(k)}(T_0)\, f^{(k)}(\eta;\eta_{ij}) \right) \frac{\chi^{(k)}}{\chi^{\mathrm{mix}}} \right\}, \tag{5.37}$$

defined such that

$$\kappa_\eta = C_\eta \chi^{\mathrm{mix}}. \tag{5.38}$$

Equation (5.38) assumes the measurement plane contains a binary mixture of air and a target gas. The collisional broadening coefficients required to compute Eq. (5.37) are a mole fraction-weighted sum of the self- and air-broadened half widths at half maximum. From Eq. (5.25),

$$\Delta\eta_{\mathrm{C},ij} = 2p_0[\chi\gamma_{\mathrm{self}} + (1-\chi)\gamma_{\mathrm{air}}] \tag{5.39}$$

for each transition of the target, where $\chi = \chi^{\mathrm{mix}}$. The contribution of air to κ_η in the IR range is negligible since N_2 is effectively rovibrationally inactive. Substantial differences between γ_{self} and γ_{air} can invalidate Eq. (5.38), but these differences are naturally mitigated and the approximation is only problematic in special cases. Divergent γ_{self} and γ_{air} coefficients predominantly introduce errors into C_η when χ is small (i.e., when excited states in the target interact primarily with air molecules). Absolute errors in κ_η that stem from this difference are inherently minimized, since a small target volume fraction implies limited absorption.

Substituting Eq. (5.38) into Eq. (5.35) yields in the following expression for transmittance:

$$Tr = \frac{1}{\eta_2 - \eta_1} \int_{\eta_1}^{\eta_2} \left[\exp\left\{ -\int_0^L \chi(u)\, du \right\} \right]^{C_\eta} d\eta, \tag{5.40}$$

which features a path integral over the target concentration. The function G is defined as the path integral over χ,

$$G(L) \equiv \int_0^L \chi(u)du\,, \tag{5.41}$$

which is a Fredholm IFK. The transmittance is expressed in terms of G,

$$Tr = \frac{1}{\eta_2 - \eta_1} \int_{\eta_1}^{\eta_2} \left[\exp\left\{-G(L)\right\}\right]^{C_\eta} d\eta\,. \tag{5.42}$$

Equation (5.42) demonstrates that the spatial distribution of χ with respect to u does not affect the broadband transmittance because χ does not affect the number density-normalized line strength (except through the broadening effects discussed above). The relationship between the path-integrated emissions burden and Tr can be computed when the shape function of the target and spectral range of the bandpass filter are known. The inverse function, G^{-1}, is numerically tabulated and broadband absorption CST measurements are defined in terms of this inverse,

$$b \equiv G^{-1}(Tr, C_\eta) = \int_0^L \chi(u)du\,. \tag{5.43}$$

Here, b equals the path-integrated volume fraction of the target and $G^{-1}(Tr, C_\eta)$ is the linearizing "transfer function."

A linear system for broadband absorption CST is constructed as follows. The ray-sum matrix, **A**, is unchanged—elements of **A** are line integrals over the basis that correspond to measurement paths. Transmittances are transformed by Eq. (5.43) to acquire a data vector, **b**, and elements of the unknown vector, **x**, consist of the local volume fraction of emissions, projected onto the basis. Bayesian inference can be directly applied to this system to estimate the distribution of emissions, and C_η can be scaled using T_0 and p_0 to determine the emissions burden in standard units (e.g., ppm). Linearization of the broadband transmittance data is valid under the following conditions:

1. Absorption is the prevailing mode of radiative transfer;
2. Self- and air-broadened collision half widths at half maximum are comparable; and
3. Emissions are well mixed.

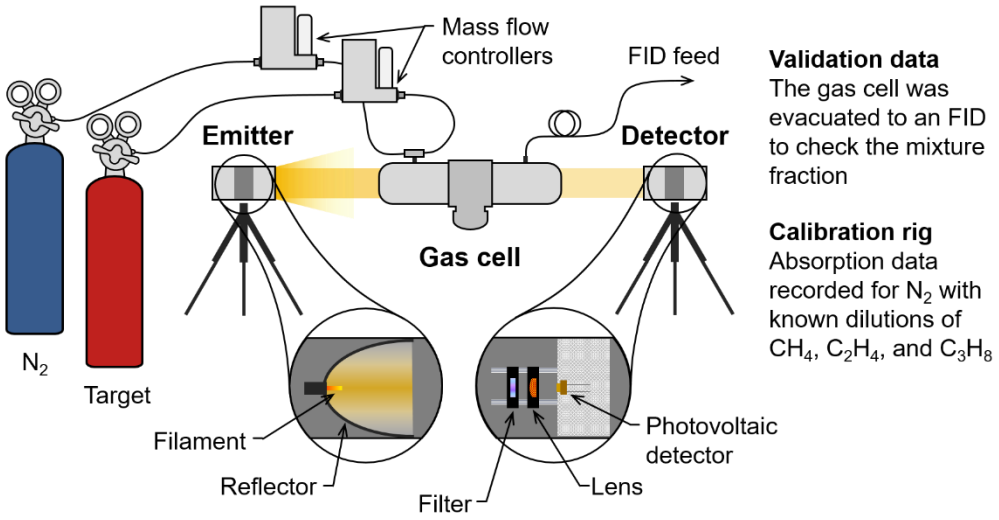

Figure 5.7: Thermal emitter and broadband detector units for open path broadband measurement and a calibration schematic. The setup features an absorption cell that contains a controlled mixture of N_2 and the target gas.

5.3 Constructing and calibrating measurement devices

5.3.1 Emission and detection units

A custom-built open path detection system was developed to make the multiple transmittance measurements needed to carry out broadband absorption CST. The prototype consisted of four transmitter-receiver pairs. Construction of these devices was headed by Roger Tsang, who selected the components and conducted calibration tests with assistance from the author of this thesis.[86] Transmission and detection units were assembled from low-cost, commercially-available components to facilitate the development of a large number of devices, capable of making time-resolved measurements in future tests. The objective of the experiment was to determine the spatial distribution of a single species concentration (or that of a homogeneous mixture), not to distinguish the components of a mixture, which requires multiple broadband signals, at a minimum—preferably spectrally-resolved data (e.g., using a TDL source or FTIR detector). Figure 5.7 shows a schematic of the transmitter and detector units, aligned with a gas cell for the calibration tests.

Transmitters were fitted with a 5 mm long, 1 mm diameter silicon nitride glowbar (HawkEye Technologies IR-Si243), positioned inside a parabolic reflector (Phoenix PA10.02) with an opening diameter of 97.8 mm. The assembly was housed in a cylindrical aluminum case and

[86] An early prototype of the open path gas detection device was built by Nick Bodd, Ali Jahed, Shari King, and Peter Robertson as part of their MTE 481/482 capstone design project. The project was conceived as a BTEX detection campaign in collaboration with Imperial Oil Ltd. See Roger Tsang's master's thesis for further technical specifications and details on the design process [28].

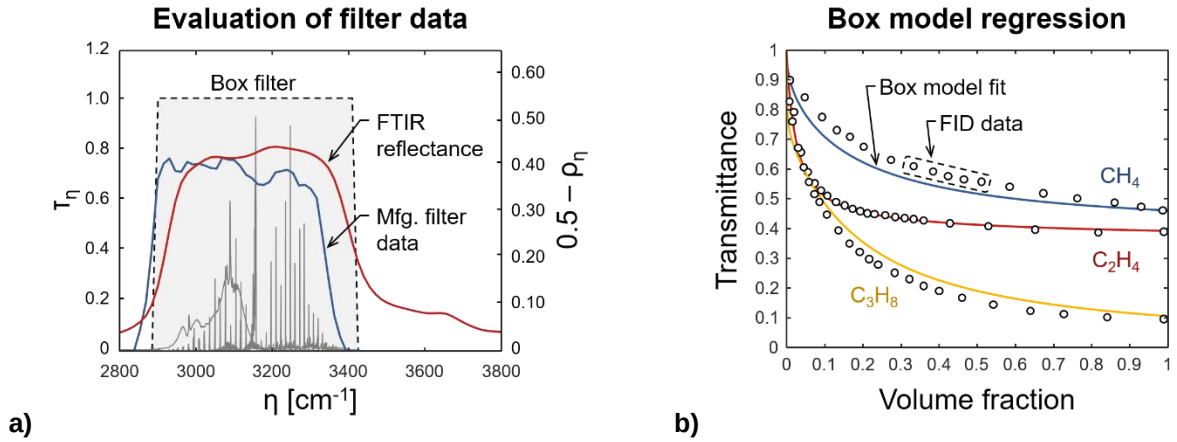

Figure 5.8: Calibration results: a) manufacturer-supplied filter transmittance data, FTIR-measured filter reflectance data (inverted, see second y axis), and the transmittance results of a box filter regression; and b) modelled and measured transmittances for CH_4, C_2H_4, and C_3H_8.

mounted on an adjustable tripod base. The filament was powered using a 12 V, 1.6 A supply, yielding a filament temperature of 1,443 K. Optimal positioning of the filament within the reflector was determined by a Monte Carlo ray-tracing procedure that maximized the fraction of collimated light.

Receivers consisted of a 25.4 mm (1") diameter CaF plano-convex lens (ThorLabs LA5470-E), which focused light through a bandpass filter (ThorLabs FB3250-500 IR) on to an uncooled InAs photovoltaic detector (Hamamatsu P10090-01). The detector had a near-uniform response over filter's spectral window (i.e., d_η was constant). Optical components were cage-mounted in an aluminum cylinder, itself mounted on an adjustable tripod. Detector voltages were amplified (TI LM358) and collected by a USB-6001 DAQ from National Instruments. Measurements made absent the target gas revealed normally-distributed noise with a standard deviation equal to 0.3% of the mean signal.

A removable assembly was designed to align the transmitter and receiver units. The device consisted of a visible diode laser, mounted over the transmitter, and mirror, mounted over the receiver. The assembly was removed prior to testing.

5.3.2 Calibration procedure

Transfer functions were established by examining the response of the transmitter/receiver system to controlled dilutions of CH_4, C_2H_4 and C_3H_8 in a N_2 atmosphere. Validation measurements were made using a gas cell, depicted in Figure 5.7, having a total path length of 81 cm between two sapphire windows, 38.1 mm (1.5") in diameter. For each measurement, a flow of N_2 and the target

were fed through two ports. Composition of the gas cell's contents was tuned using either a mass flow controller (CH_4: Brooks SLA-5850S) or rotameters (C_2H_4, C_3H_8: Cole Parmer N102-05; N_2: Cole Parmer N034-39). The volume fraction of the target species was adjusted from 0 (i.e., P_{ref}) to 1, with 16 to 22 intermediate fractions. Measurements were recorded once P_{abs} was observed to be constant for five minutes in order to ensure the gas mixture had stabilized. Absorption data was compared to point-concentration measurements, made with a FID (ThermoScientific TVA-1000A).

5.4 Proof-of-concept Emissions Detection Experiment

5.4.1 Developing the transfer functions

Line-by-line parameters for CH_4 and C_2H_4 are available in the HITRAN database [228]. Lineshapes were calculated with Eq. (5.22) using standard units of cm^{-1}. κ_η was divided by 10^6 ppm to obtain C_η. The shape factor function was calculated across η = 2,000 to 4,000 cm^{-1} at a resolution of 0.4 cm^{-1}. Absorbance data for C_3H_8 were inferred from the high-resolution FTIR measurements reported in the vapour phase infrared spectral library [319]. These measurements were made using a 1 ppm·m burden of C_3H_8 at 296 K and pressures ranging from 0.45 to 12.10 Torr. Absorbance data were scaled by $\ln(10)\cdot 10^6$ cm^{-1} to obtain κ_η, assuming a linear function of partial pressure and negligible differences between the self- and air-broadened half widths at half maximum.

Figure 5.8a shows manufacturer-supplied transmissivity data for the filter, imposed on absorption spectra for pure CH_4 at atmospheric conditions. The filter width is reported to a tolerance of ±0.10 μm and the centre wavelength to a tolerance of ±0.05 μm. Transmittance data

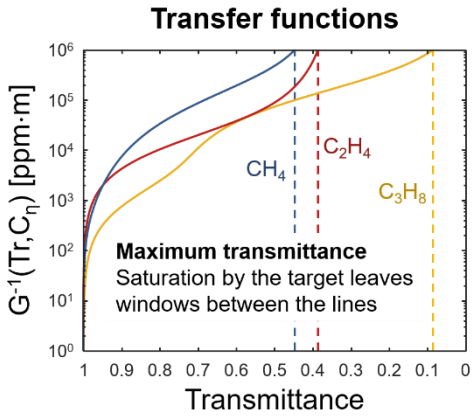

Figure 5.9: Transfer functions for broadband absorption tomography of CH_4, C_2H_4, and C_3H_8 for a 523 cm^{-1} wide box filter, centred at 3,163 cm^{-1}.

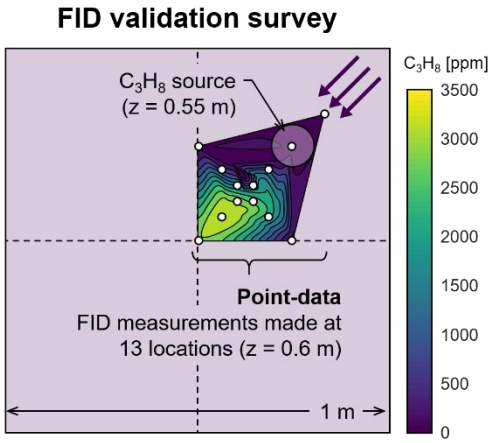

Figure 5.10: Domain geometry with the source location and FID measurement positions; contours of the interpolated C_3H_8 data are superimposed on the domain. Arrows indicate the fan position and direction of the advective flow.

are sensitive to the precise onset and slope of the window due to the large number of spectral lines close to the lower threshold (~2,850 cm^{-1}). Broadband transmittances are independent of the peak filter transmissivity, however, as the transmissivity is approximately constant for the bulk of the filter window. This observation justifies the inclusion of τ_η in the system constant, C_{det}, which cancels out in Tr, amounting to a box model of the bandpass filter.

Filter bounds for the box model were inferred by conducting a non-linear regression between modeled and measured transmittances for dilutions of CH_4, C_2H_4, and C_3H_8 in N_2, ranging from 0% to 100%. The regression produced a filter of width 523 cm^{-1}, centred at 3,163 cm^{-1}. This range was consistent with the filter's reflectance profile, measured with a FTIR reflectometer (Surface Optics Corp. SOC-400), also shown in Figure 5.8a. Corresponding measured and modeled transmittances are plotted in Figure 5.8b.

The box filter from the regression was used to compute a database of Tr for the target species via Eq. (5.42) over a path-integrated concentration range from 1 to 10^6 ppm·m. This database was employed in turn to construct the transfer functions, $G^{-1}(Tr, C_\eta)$, plotted in Figure 5.9. G^{-1} is a monotonic map of broadband measurements to a linear, path-integrated concertation, suitable for tomographic reconstruction.

5.4.2 Laboratory-scale tomography experiment

The broadband absorption CST technique was evaluated by reconstructing a plume of C_3H_8 in an enclosed test space. This target is representative of ground source fugitive emissions (e.g., [326,327]), except at a smaller scale. The domain was 1×1 m in size with its origin at the centre.

Propane was supplied at 2.44 L/min and released vertically into the domain through a 7.62 cm (3”) diffuser, located at $x = y = 0.21$ m and $z = 0.55$ m. A small fan, placed level with the plume at $x = y = 0.5$ m, provided an advective flow with a speed of 2 m/s. The domain size was selected to be proportional to the size of the emissions source. Individual single-path measurements were conducted over a 10 m distance to verify that the light was effectively collimated by the transmission unit, and hence that the open path system could operate over distances relevant to field measurements. An FID was used to measure the average concentration of C_3H_8 at 13 discrete locations in the domain. Twelve measurements were made over a five second interval at each location. The average standard deviation across these measurements was 480 ppm, with a maximum standard deviation of 1,603 ppm. Figure 5.10 shows contours of a spline interpolation over the average FID data.

Transmittance measurements were carried out for a four-projection, 35-beam array, depicted in Figure 5.11a. Each projection of the base arrangement contained nine beams, centred in the domain with a 10 cm spacing. A single beam was excluded from one of the projections to accommodate the fan and the adjacent beams were crossed to partially compensate for the loss of spatial information. Transmittance measurements began with a 600 s reference, recorded at 2 Hz, after which C_3H_8 flow was introduced through the diffuser. Attenuated signals were recorded for 600 s at 2 Hz. The transmittance data was transformed with the C_3H_8 transfer function.

The basis shown in Figure 5.11b comprised 40^2 square pixels and reconstruction was conducted using the Tikhonov smoothness prior in Eq. (2.35). A prior variance of $\lambda^{-2} = 100$ ppm^2 was selected according to the spectral technique of Daun [88]. This approach identifies the spatial uncertainty appropriate to a given measurement array and basis for single-shot reconstruction.

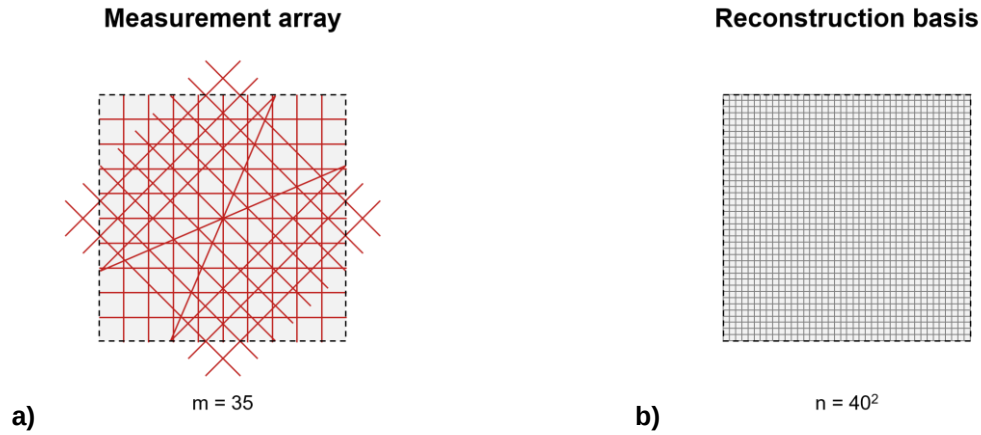

Figure 5.11: Schematic for broadband absorption CST: a) 35-path array and b) 40^2 pixel basis.

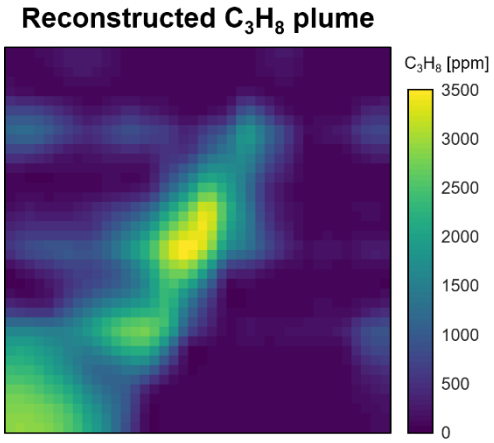

Figure 5.12: Reconstruction of an advected C_3H_8 plume using broadband absorption CST.

Figure 5.12 contains the reconstructed C_3H_8 emissions plume, which aligns with the interpolated FID data in Figure 5.10. Table 5.1 lists mean concentration data, uncertainties for the five largest FID measurements, and the corresponding uncertainties for the broadband absorption CST estimate. These results demonstrate that FID measurements of C_3H_8 were broadly consistent with the reconstruction. Integral-scale fluctuations in the concentration of C_3H_8 resulted in large uncertainties in the FID measurements, which took place over a 60 s interval. Uncertainties for the reconstruction were smaller due to the longer measurement interval (600 s) and because the latter uncertainties apply to a spatial average over a basis function instead of a point-concentration.

Table 5.1: Comparison of Concentration Data from FID Measurements and the Broadband Absorption CST Reconstruction

Location		**FID Data [ppm]**		**Reconstruction [ppm]**	
x [mm]	*y [mm]*	*Mean*	*Std. Dev.*	*Mean*	*Std. Dev.*
-0.10	+0.10	2,894	725	3,514	275
+0.00	+0.00	2,595	860	3,079	230
-0.15	+0.15	1,952	931	2,594	285
+0.20	+0.15	1,848	1,603	2,833	271
+0.25	+0.10	1,691	863	1,916	288

5.4.3 Uncertainty analysis

Error in broadband absorption CST is divided into four categories: measurement noise, model error in the transfer function, regularization error due to the incompatibility of the prior and ground truth distribution, and discretization error. Transmittance measurements are derived from the ratio of

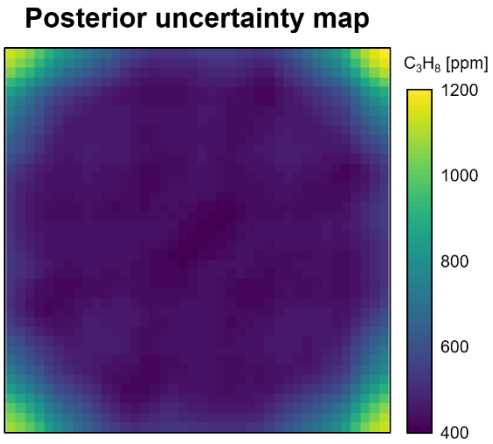

Figure 5.13: Map of the standard deviation from the posterior covariance estimate.

two random variables—the mean absorption and reference data—designated V_{abs} and V_{ref}. Figure 5.14 shows a typical voltage trace used to obtain a transmittance. The distribution of fluctuations in the reference, indicative of electronic noise, roughly follows a normal distribution. Increased variation in the absorption trace is attributed to turbulent fluctuations in the C_3H_8 plume. These large fluctuations indicate transient behaviour on a time-scale longer than the FID measurement interval, which could be imaged by a time-resolved broadband absorption CST system.

Mean voltage traces are normally distributed, according to the central limit theorem. Standard deviations for the trace in Figure 5.14 are $\sigma_{abs} = 1.9 \cdot 10^{-3}$ V and $\sigma_{ref} = 2.8 \cdot 10^{-4}$ V. Expanding the expression of variance for V_{abs}/V_{ref} and neglecting higher order terms gives an expression for the variance of Tr,

$$\sigma_{Tr} = \frac{V_{abs}^2 \sigma_{ref}^2 + V_{ref}^2 \sigma_{abs}^2}{V_{ref}^4}. \tag{5.44}$$

Equation (5.44) was used to estimate the standard deviation of Tr for the signal in Figure 5.14: $\sigma_{Tr} = 3.1 \cdot 10^{-5}$. The maximum standard deviation from the experiment was $1.6 \cdot 10^{-4}$ for a transmittance of 0.974. Therefore, mean transmittance data were known to a high degree of precision.

Another source of error was the transfer function. Discrepancies between modelled and experimental transmittance data arose from the assumptions used to construct Eq. (5.42) (e.g., modeling the bandpass filter as a box). Errors due to the transfer function were estimated from discrepancies observed in the calibration test: i.e., computing the difference between the path-averaged concentrations from G^{-1} for the measured and modelled transmittances with the largest residual. This procedure predicts a maximum discrepancy of 370 ppm·m for a C_3H_8 burden up to

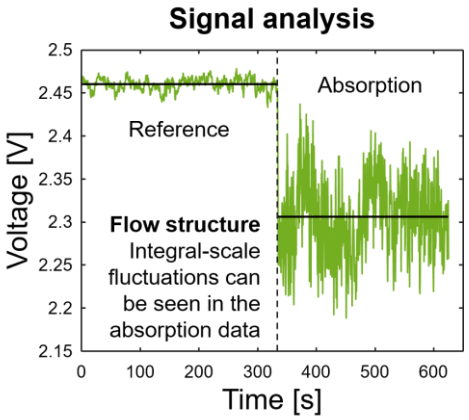

Figure 5.14: Voltages used to obtain a LOS transmittance measurement.

6,500 ppm·m (or 5.69%). Greater uncertainty is expected for higher burdens because partially-transmitted lines at the filter wings—excluded by the box model—become more prevalent as dominant lines are saturated.

Finally, the tomographic reconstruction process is subject to errors associated with the discretization scheme and incompatibility between the prior and ground truth distribution. The effect of this error on reconstructed structures is estimated by computing the posterior covariance matrix using Eq. (4.13), with uncertainties of the transmittance and transfer function included in the measurement covariance. Figure 5.13 shows a contour map of the resulting posterior standard deviation for C_3H_8. Regions of high uncertainty in Figure 5.13 align with artifacts in the reconstruction, primarily concentrated about the corner $x = y = -0.5$ m.

Figure 5.15 illustrates the sensitivity of reconstructions to the density and arrangement of measurement lines. Different subsets of the measurement lines were used to reconstruct the plume.

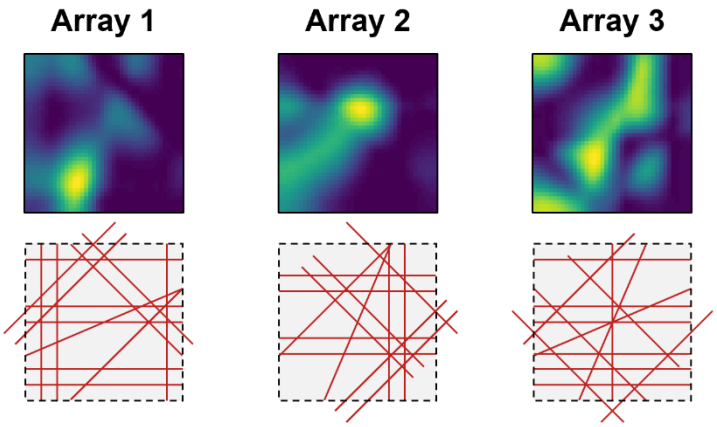

Figure 5.15: Alternative reconstructions using a subset of the projections: a) half of each projection; b) the compliment arrangement to (a); and c) 18 randomly-selected lines.

These reconstructions roughly capture the location and magnitude of the peak concentration but differ about the plume's margins. This limitation may be overcome with supplementary measurement lines or by developing a more sophisticated prior. A quantitative estimate of reconstruction uncertainty was obtained by analyzing the difference between ground truth plumes and tomographic reconstructions from Ref. [294], ensuring basis and regularization parameter parity. The mean net and maximum concentration errors were estimated to be 31% and 14%, respectively.

5.5 Conclusions

The need to develop stand-off measurement techniques for detecting and quantifying hydrocarbon emissions is motivated by their contributions to climate change and the numerous health and safety hazards presented to workers and the public at large. This chapter develops and applies the theory for broadband absorption CST, a novel approach to spatially-resolved emissions quantification. Previous deployments of CST were based on spectrally-resolved intensity data, in which the inferred absorption coefficient is related to a Fredholm IFK. Broadband measurements convolve this integral equation over the detector's spectral range. This chapter reviews the spectroscopic models used to calculate and interpret the absorption coefficient and develops a transfer function to linearize broadband absorption data. The transfer function employs a shape function, obtained from a line-by-line model of the target or empirical absorbance data from the literature. The development of a device for broadband tomography is described and the results of a proof-of-concept experiment are reported.

Tomographic imaging with broadband measurements occurs in three-stages. First, transmittance measurements are made. Next, these measurements are transformed into a path-integrated. Finally, transformed data are tomographically reconstructed. A laboratory-scale experiment demonstrated the concept by imaging a plume of C_3H_8 emissions, shown in Figure 5.12. The reconstruction was consistent with validation measurements from a FID survey, depicted in Figure 5.10, with numerical comparisons listed in Table 5.1. An analysis of errors in the reconstruction suggested similar levels of point-wise uncertainty in the extrapolated FID and CST estimates of C_3H_8. Uncertainty in the FID measurements arose due to the transient nature of the plume and inherent locality of the FID device. Tomographic uncertainties were primarily attributable to modelling errors in the transfer function and regularization error.

Transmittance measurements are procedurally-straightforward. Both the reference and absorption signals are average quantities, robust to the measurement duration at relevant timescales, which limits the uncertainty about the transmittance. Moreover, the simplicity and low cost of the detection apparatus enable the simultaneous measurements needed to capture integral-scale fluctuations over a large area. Real-time reference measurements could be established using a filter wheel or dual-band filter with a beam splitter and multiple detectors. Moreover, with the accumulation of measurement data over time, previous measurements could be used to improve the prior by way of covariance estimation.

Discrepancies between the theoretical and empirical transmittances, plotted in Figure 5.8b, underline the importance of filter selection. Modelling errors associated with the spectral dependencies in ε_η, τ_η, and I_η were the primary source of error in the technique. In particular, the onset of transmission in the filter—near 2,900 cm^{-1}—was not known with precision. This limitation was evidenced by the discrepancy between manufacturer-provided transmission data and the reflectance measurement in Figure 5.8a. Target gasses featured different levels of absorption in this region. The spectral lines of C_3H_8 are dense and overlap substantially near the filter's edge; CH_4 also absorbs light around the onset, but less so than C_3H_8; conversely, the bulk of the C_2H_4 band lies well within the filter window. The amount of absorption at the filter boundary corresponded to box filter errors: 6.2%, 4.7%, and 3.4% for C_3H_8, CH_4, and C_2H_4, respectively. In order to minimize this error, filter selection should minimize overlap between the transmission range and target absorption bands.

Uncertainties from the reconstruction procedure also contributed to errors in the recovered concentration distribution. Broadband absorption CST is based on a Fredholm IFK, identical to the monochromatic absorption equations, and general algorithmic improvements to limited-data CST can be applied to the broadband technique. One avenue for improvement lies in the development of flow-specific priors. Chapter Three demonstrated that estimates of the mean and covariance of a turbulent variable can notably improve reconstructions. Moreover, Chapter Four demonstrated that optimization of the measurement array using prior knowledge of the emissions distribution can also improve reconstructions.

Overall, results in this chapter demonstrate the potential for passive, open path, spatially-resolved, emissions quantification using broadband data. FID measurements of a time-varying flow do not necessarily represent average features and must be extrapolated, leading to

considerable spatial uncertainty. Collecting FID measurements was labour-intensive and required direct physical access to the measurement points. By contrast, open path broadband absorption data can be remotely collected, without immediate physical access to the measurement plane. Tomographic reconstruction yields spatially-resolved concentration estimates through deconvolution rather than extrapolating labour-intensive probe data. As such, broadband tomography is a promising approach to emissions detection.

Chapter Six
Background-Oriented Schlieren Tomography of Combustion

Hard-field tomography operators comprise a set of line integrals that follow a straight path through the measurement domain. Fluids with large density gradients have corresponding gradients in their refractive index field, causing beam steering. Curved ray paths deviate from the straight trajectory of ray-sums, as constructed in previous chapters, which is a source of error in CST, but alternative modalities for tomographic imaging have been developed to exploit refraction. The deflection of rays by a gradient index medium is measured with schlieren optics or a computer vision algorithm and the deflections are used to reconstruct the refractive index field. Estimates of the index of refraction can be related to key state variables, such as density and temperature. BOS tomography is an emerging diagnostic that has been deployed to estimate the 3D temperature field in heated gas jets and the density field of incompressible flows. This chapter reports the first application of BOS tomography to combustion imaging, conducted within the Bayesian framework developed in previous chapters.

Turbulent flames are common in industrial combustors and feature complex interactions between turbulent transport, chemical kinetic, and radiative heating mechanisms [328]. Combustion simulations are used to predict burner performance, optimize efficiency, and minimize the production of NO_x and soot. Simulations must be benchmarked against experimental measurements of temperature, velocity, species concentration, flame front geometry, and other parameters to ensure validity of the numerical model [17]. Data for benchmarking is obtained from physical probes or optical diagnostics. The latter are generally favoured since the former cannot provide sufficient spatial resolution to capture the structures of interest in a turbulent field.

Moreover, unlike physical probes, optical systems do not perturb reactions and transport processes in the flame. Optical combustion diagnostics often feature lasers, including LOS absorption spectroscopy, quantitative PLIF, and scattering techniques—Rayleigh/Raman thermometry and CARS—which have been combined to generate rich data sets for benchmarking. Laser diagnostics yield high-resolution measurements and advanced setups can simultaneously image multiple quantities [329]. At the same time, spatially-resolved laser-based measurements require intricate optics, controls, and data acquisition systems. Complex laser probes pose cost and safety concerns that limit the mobility of the apparatus and range of potential targets. More fundamentally, the vast majority of laser diagnostics are only capable of 2D measurement.[87]

Quantitative, volumetric measurements of combustion variables are required to obtain key statistics, including fluctuations in curvature, out-of-plane dissipation rates, and the destruction of flame wrinkling. The demand for instantaneous 3D data and the cost and complexity of laser diagnostics motivate the development of alternative devices for combustion sensing. Measurements of refraction have long been used to image temperature and density gradients in gases and liquids, and refraction-based tomography is an established approach for 3D fluid imaging [330]. Measurements are obtained by schlieren imaging or synthetic schlieren (BOS), which may be accomplished in several ways, outlined in Chapter One. Irrespective of the schlieren technique, rays pass through the probe volume along a curved path due to the variable speed of electromagnetic waves in the medium. Schlieren data consist of a pattern of light deflections relative to a reference image; visualizing the deflections provides a qualitative account of density and temperature. Quantitative data can be extracted from schlieren images through post-processing, most commonly by tomography [62].

Conventional schlieren rigs include an intricate arrangement of lenses and mirrors that focus light from a calibrated source onto a detector. These techniques pose similar cost and mobility challenges as laser sensors. BOS simplifies the optical setup required to infer the deflection data. In BOS imaging, a camera is focused on a background pattern, positioned behind the probe volume. Refraction, caused by the medium, distorts the scene and image processing tools identify the direction and magnitude of deflections from reference and deflected images. The resulting pixel-wise defections constitute a BOS image. Deflections are related to local variation of the

[87] Advances in volumetric LIF and 3D absorption tomography are recent exceptions.

optical density in a fluid by a Fredholm IFK, similar to other forms of gas-phase tomography. Multiple BOS images from a unique perspective can be combined to reconstruct the refractive index field with a computed tomography algorithm. Of particular interest in the combustion context: reconstructions can be used to determine the location of the flame front, characterized by steep gradients in the estimate.

Atcheson et al. [331] reported the first demonstration of BOS tomography, which they employed to estimate the density of an unsteady gas flow. Subsequent studies followed suit, using multi-camera arrays to reconstruct the instantaneous density distribution in a natural convection flow, turbomachine, and free-shear gas jet [332–340]. For heated jets of a known composition, temperature is obtained by the ideal gas law. The initial formulation of Atcheson et al. [331] requires three stages: identification of the deflections, reconstruction of the refractive index gradients, and inference of the refractive index field from its gradients by Poisson integration. Nicolas et al. [338] introduced gradient operators into the measurement model to combine the second and third stage. The authors directly reconstructed the refractive index from BOS deflections; with the Poisson integration implicit in the inversion.

Recently, Lang et al. [341] used a single camera and phase-averaged measurements to infer the temperature of a swirling gas jet, heated by a coil, intended as a surrogate for swirl combustion. However, the BOS literature contains no reports of 3D combustion tomography. This chapter presents the first such application of BOS tomography. The technique was prototyped with a LES phantom, consisting of a realistic optical density field for a turbulent swirl flame. Inversion of the deflection data is an ill-posed inverse problem, similar to other forms of gas-phase tomography, and a Bayesian approach was used to incorporate prior information. Two priors were evaluated: a smoothing prior, based on a first-order Tikhonov regularization, and TV prior, intended to promote sharp gradients about the flame front. A proof-of-concept experiment was conducted on an unsteady laboratory Bunsen flame using 23 cameras to resolve accurate, instantaneous, 3D combustion structures. This chapter conclusively shows that BOS tomography can be applied to volumetric flame imaging. Moreover, BOS tomography is readily extended to time-resolved reconstruction and can provide important information about the evolution of complex structures in turbulent combustion.

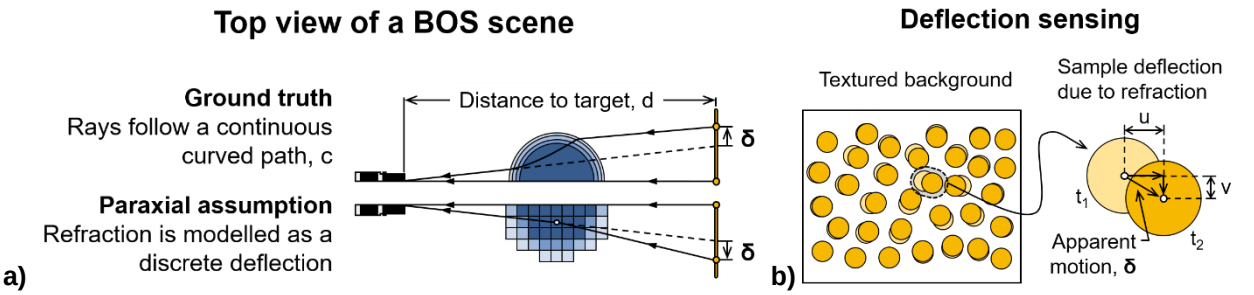

Figure 6.1: Schematic for BOS imaging: a) top view with a continuous curved path and discrete approximation and b) BOS scene with a reference pattern (light dots) and deflected pattern (dark dots).

6.1 Background-Oriented Schlieren Tomography

Background-oriented schlieren tomography reconstructs the refractive index field, *n*, in a transparent medium from deflection patterns caused by gradients in *n*. Spatial variation in *n* is an effect of variation in the temperature and composition of a medium. Data vectors consist of deflections that are inferred from a pair of images: a reference image, captured through a uniform refractive index field, and distorted image, where ray paths are refracted by the target. Figure 6.1 illustrates a BOS imaging scenario, highlighting the continuous and discrete models of refraction, and shows deflection sensing by BOS.

Reconstruction requires discretization of the probe volume, typically into cubic voxels that contain a uniform distribution of *n*, and a model that relates *n* to the deflections. The BOS equations act as a smoothing kernel and inversion amplifies noise in the deflection vectors, rendering reconstruction ill-posed. Supplemental information is required to generate physically-plausible estimates, as with absorption and emission CST. This section presents the imaging tool for deflection sensing, measurement model, and reconstruction algorithm for BOS tomography.

6.1.1 Deflection sensing

Absorption and emission CST employ measurements of intensity to reconstruct the target. BOS tomography is an optical diagnostic, usually applied to gas-phase fluids, based on radiative transport relations. However, measurements are the deflections observed in a background pattern, which must be identified by digital post-processing, as opposed to the raw intensity data required by absorption and emission modalities.[88]

[88] Strictly speaking, most absorption and emission CST experiments require post-processing of the measurements. In principle, however, intensity/voltage data are sufficient. By contrast, BOS imaging is an advanced inverse problem in and of itself—there is no direct measure of deflections in synthetic schlieren.

Several techniques have been proposed to obtain deflection data, including cross correlation methods [67,342], which form the basis of PIV, and optical flow algorithms from the computer vision literature [343]. This chapter employs the latter approach, using the closure of Horn and Schunck [344]. Atcheson et al. [345] compared the performance of PIV and optical flow algorithms for fluid imaging by BOS. They found that gradient-based optical flow techniques were superior to the variational approach of Brox et al. [346] and the open source MatPIV toolbox [347]. Two classical gradient-based optical flow algorithms—Horn-Schunck and Lucas-Kanade—feature a single regularization parameter, which limits the potential for over-tuning.

Optical flow determines the apparent motion in a sequence of images, illustrated by the moving dots in Figure 6.1b. Deflections relate successive frames, $I(x, y, t_1)$ and $I(x, y, t_2)$—or I_1 and I_2—the couplet (x, y) identifies a pixel, and $\Delta t = t_2 - t_1$. For convenience, visible features are identified with a pixel that is said to "move" between successive images. These algorithms were originally intended to sense the velocity of moving objects in a video, which requires the camera framerate, Δt. The quantity of interest in BOS is the 2D displacement field that transforms I_1 into I_2, resolved at each pixel (i.e., deflections); Δt is thus set to unity.[89]

Optical flow follows from two primary assumptions: the brightness of a pixel remains constant between the images, and displacements have a small magnitude. Apparent motion in the image is approximated with a Taylor series expansion that relates I_1 to I_2,

$$I(x,y,t_2) \approx I(x,y,t_1) + \left(I_x u + I_y v + I_t\right)\Delta t + \mathcal{O}(\Delta t^2), \tag{6.1}$$

where $I_x = \partial I/\partial x$, $I_y = \partial I/\partial y$, $I_t = \partial I/\partial t$, $u = \partial x/\partial t$, and $v = \partial y/\partial t$. Equation (6.1) yields an underdetermined system of linear equations with the two unknown velocities, u and v, and one equation per pixel. The Horn-Schunck method closes the system for an entire image, Ω, by adding a global penalty term that penalizes sharp gradients in the vector field,

$$u, v = \underset{u,v}{\arg\min}\left\{\int_\Omega \left[I_x u + I_y v - I_t + \alpha\left(\left|\nabla u\right|^2 + \left|\nabla v\right|^2\right)\right] d\Omega\right\}. \tag{6.2}$$

The Horn-Schunck parameter, α, controls the degree of smoothing, similar to λ in Tikhonov regularization. Equation (6.2) is approximately solved by taking its derivative with the Euler-

[89] Typically, the I_1 frame is captured prior to an experiment and I_2 frames are captured during the experiment. I_1 is often a composite image that averages many reference frames.

Lagrange equation, setting the derivative to zero, and solving for *u* and *v*. This procedure yields an iterative expression for the deflections,

$$u^{k+1} = \bar{u}^k - \frac{I_x(I_x\bar{u}^k + I_y\bar{v}^k + I_t)}{\alpha^2 + I_x^2 + I_y^2},\ v^{k+1} = \bar{v}^k - \frac{I_y(I_x\bar{u}^k + I_y\bar{v}^k + I_t)}{\alpha^2 + I_x^2 + I_y^2}, \tag{6.3}$$

where $\bar{u}^k$ and $\bar{v}^k$ are the average displacements, *u* and *v*, for the *k*th iteration. Equation (6.3) generates pixel-wise deflections, which are then scaled by the physical size of pixels in the background image plane,

$$\boldsymbol{\delta} = (s_x u)\mathbf{p}_u + (s_y v)\mathbf{p}_v . \tag{6.4}$$

The width and height of a pixel in the background plane are s_x and s_y, given in world coordinates. Unit vectors, $\mathbf{p}_u$ and $\mathbf{p}_v$, reside in the same plane and point in the direction of *u* and *v*, respectively.[90] The scaled deflection in Eq. (6.4) constitutes a BOS measurement for one pixel.

6.1.2 Deflection model

Refraction is modelled by the method of geometric optics.[91] Optical paths obey a partial differential equation. When total refraction is small, deflections are approximated with an integral equation via the paraxial assumption, shown in Figure 6.1a. This chapter employs a cubic voxel basis to support the deflection equations. The IFK is computed along each LOS to construct a linear operator that relates the target field, *n*, to a set of deflections—similar to absorption and emission CST operators.

6.1.2.1 Ray equation of geometric optics

Geometric optics represents visible light waves as a complex-valued wavefunction, which simplifies into a superposition of sinusoidal waves of monochromatic radiation [348]. Spatial evolution of the wavefront is governed by a Helmholtz equation, which can be approximated by the eikonal equation because visible wavelengths are short compared to the characteristic length of fluctuations in *n*. Using this formulation, rays propagate normal to surfaces of constant phase, described by the ray equation of geometric optics,

$$\frac{d}{ds}\left(n\frac{d\mathbf{u}}{ds}\right) = \nabla n . \tag{6.5}$$

[90] $\mathbf{p}_u$ and $\mathbf{p}_v$ are determined during camera calibration.

[91] Advanced forms of the RTE use the ray equation of geometric optics to incorporate beam steering; in a sense, BOS tomography can be said to derive from fundamental relations of radiative transport.

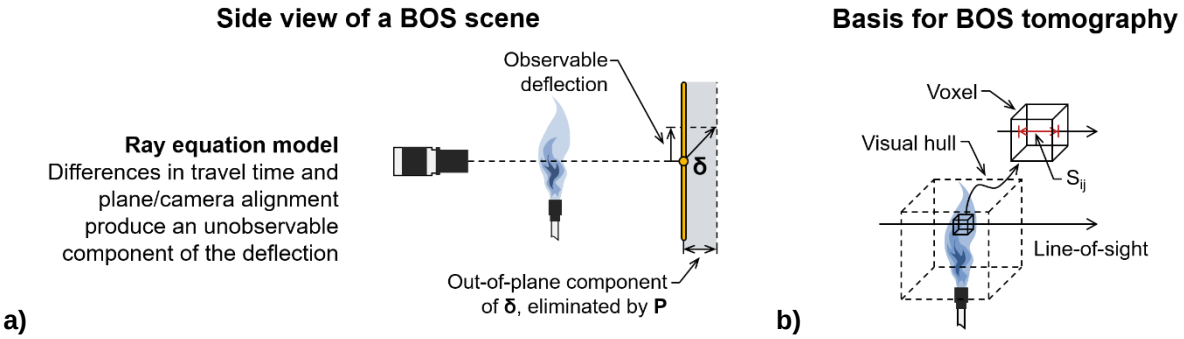

Figure 6.2: Side view of a BOS imaging scenario, featuring a) the coordinate system, distance to the target d, and a deflection with an out-of-plane component, which is not observable by deflection sensing; and b) a voxel and the path integral S_{ij} for a LOS.

The position of a hypothetical particle travelling along the ray path is $\mathbf{u}(x, y, z)$, ds is a differential distance along the path, and ∇ is the gradient operator. See Ref. [348] for a complete derivation of Eq. (6.5). The ray equation is reformulated as a system of first-order ODEs [349],

$$n\frac{d\mathbf{u}}{ds} = \mathbf{v}\,,\ \frac{d\mathbf{v}}{ds} = \nabla n\,, \tag{6.6}$$

where $\mathbf{v}$ is the local ray direction scaled by n. Typically, in gas-phase applications, $\|\mathbf{v}\|_2 \approx 1$ [332]. Forward Euler discretization of Eq. (6.6) yields an iterative solution,

$$\mathbf{u}^{i+1} = \mathbf{u}^{i} + \frac{\Delta s}{n}\mathbf{v}^{i}\,,\ \mathbf{v}^{i+1} = \mathbf{v}^{i} + \Delta s \nabla n\,, \tag{6.7}$$

where Δs is a discrete step size.

Curved ray paths through a variable index medium are governed by Eq. (6.5) and ray-traced with Eq. (6.7) to simulate schlieren imaging, where Δs is conservatively selected to be $1/10^{\text{th}}$ of the voxel length-scale. Fourth- and fifth-order Runge-Kutta approximations to Eq. (6.6) have also been employed to speed-up non-linear ray-tracing [350].[92]

The deflection vector in Figure 6.2a, $\boldsymbol{\delta} = [\boldsymbol{\delta}_x\ \boldsymbol{\delta}_y\ \boldsymbol{\delta}_z]^T$, is found by integrating Eq. (6.6) along the curved ray path, c, which can be seen in Figure 6.1a,

$$\boldsymbol{\delta} = \int_c \nabla n ds\,. \tag{6.8}$$

Equation (6.8) is a set of three Fredholm IFKs, with one equation per direction per LOS—each similar to the IFKs for emission and absorption CST, *except* that the integral is carried out over a

[92] Optical paths are straight in linear ray-tracing and curved in non-linear ray-tracing, travelling normal to surfaces of constant phase per the ray equation of geometric optics.

gradient of the quantity of interest. The gradient operator requires special attention in the reconstruction of n.

6.1.2.2 Discrete operator for BOS tomography

Atcheson et al. [331] proposed a two-step procedure to infer n by BOS tomography: first, obtain the deflection data; then independently reconstruct the refractive index gradients, $\nabla_x n$, $\nabla_y n$, and $\nabla_z n$; and, finally, conduct a Poisson integration over these fields to estimate the refractive index, itself. Nicolas et al. [338] recently introduced discrete gradient operators into the forward system to compute n, directly. The authors' approach implicitly carries out a Poisson integration during inversion of the augmented operator. This work adopts the direct method of Nicolas et al. [338] and introduces a general improvement to the BOS operator.

Estimates of n are defined over a finite basis (voxels, in this chapter) with a vector of coefficients, $\mathbf{x} \in \mathbb{R}^N$, where N is the number of voxels. Deflections in the plane of the background pattern are small and the fluid is small relative to the experimental domain so ray paths remain nearly straight within the probe volume [332]. As a result, the ray path, c, in Eq. (6.8) is assumed to follow the original (straight) trajectory. Path integration over the ith LOS in the jth voxel gives the product of the coefficient—i.e., the local gradient of x_j—and length of the LOS through that voxel—here called S_{ij} (shown in Figure 6.2b). Components of the ith deflection in Eq. (6.8) are

$$\boldsymbol{\delta}_i = \begin{bmatrix} \delta_{ix} \\ \delta_{iy} \\ \delta_{iz} \end{bmatrix} \approx d \sum_{j=1}^{N} S_{ij} \begin{bmatrix} (\nabla_x n)_j \\ (\nabla_y n)_j \\ (\nabla_z n)_j \end{bmatrix}, \tag{6.9}$$

where d is the distance from the centre of the probe volume to the background pattern, which can be seen in Figure 6.2a, and the $(\nabla n)_j$ terms are 1D gradients of n at the jth voxel. The distance d slightly differs for each LOS and should be individually calculated to properly scale the ray-sums.

Data for all three gradients are arranged into a single vector, $\mathbf{b} \in \mathbb{R}^{3M}$, where M is the total number of rays, with one ray per pixel per camera.[93] The deflections are grouped together by direction, $\mathbf{b} = [\boldsymbol{\delta}_x{}^T \; \boldsymbol{\delta}_y{}^T \; \boldsymbol{\delta}_z{}^T]^T$, and the system, $\mathbf{S} \in \mathbb{R}^{M \times N}$, consists of chord lengths for each voxel along each LOS, scaled by the distance to the corresponding background, d.[94] Using the technique

[93] The number of pixels is an upper bound on the number of optical paths. However, the pixel trajectories are close together and deflection sensing is very noise-laden. Pixels and pixel-wise deflections are usually downsampled as a result.

[94] In effect, **S** is a scaled version of the ray-sum matrix for absorption and emission CST.

of Nicolas et al. [338], 1D finite difference matrices, $\mathbf{D}_x$, $\mathbf{D}_y$, and $\mathbf{D}_z$, are included in the operator such that the relationship between the discrete index of refraction field, **x**, and deflections, **b**, is

$$\begin{bmatrix} \mathbf{S}\mathbf{D}_x \\ \mathbf{S}\mathbf{D}_y \\ \mathbf{S}\mathbf{D}_z \end{bmatrix} \mathbf{x} = \mathbf{b}\,. \tag{6.10}$$

Central differences are applied within the domain to generate the **D** matrices, with forward and backward differences applied at the boundaries.

Deflections computed with Eq. (6.8) and modelled with Eq. (6.10) contain a component that is orthogonal to the background plane, as depicted in Figure 6.2a. These components are unobservable, in principle, meaning the deflection model does not correspond to the measurement procedure. This shortcoming can be eliminated with a projection matrix, $\mathbf{P} \in \mathbb{R}^{3M\times 3M}$, which projects ray-sum components into the plane of the corresponding background image. **P** is constructed from individual projection matrices for each LOS, $\mathbf{P}_i$. To generate $\mathbf{P}_i$, first recall that the *i*th LOS is associated with a single background pattern. Two orthogonal unit vectors that lie in the plane of this background pattern are selected, $\hat{\mathbf{v}}_1$ and $\hat{\mathbf{v}}_2$.[95] A matrix, $\mathbf{V} \in \mathbb{R}^{3\times 2}$, is constructed from the couplet, $\mathbf{V} = [\hat{\mathbf{v}}_1\ \hat{\mathbf{v}}_2]$, such that $\mathbf{P}_i = \mathbf{V}(\mathbf{V}^T\mathbf{V})^{-1}\mathbf{V}^T$. The *x*, *y*, and *z* components of these 3×3 matrices are grouped together to match the arrangement of the system in Eq. (6.10). Finally, the operator is

$$\mathbf{A} \equiv \mathbf{P}\begin{bmatrix} \mathbf{S}\mathbf{D}_x \\ \mathbf{S}\mathbf{D}_y \\ \mathbf{S}\mathbf{D}_z \end{bmatrix}, \tag{6.11}$$

where *observable* deflections, **b**, are directly computed from a discrete distribution of optical density, **x**: $\mathbf{A}\mathbf{x} = \mathbf{b}$.

6.1.3 Reconstruction

Background-oriented schlieren tomography is an ill-posed inverse problem, akin to absorption and emission CST. The amplification of high-frequency components by the ray-sums is increased due to the presence of the 1D gradient operators. Supplemental information about the optical density

[95] In practice, these vectors are the calibration vectors used to scale deflections for a LOS, $\mathbf{p}_u$ and $\mathbf{p}_v$. However, any orthogonal unit vectors that lie in the plane of the background pattern will suffice.

field is included in the inversion using a Bayesian algorithm. The likelihood for BOS tomography is identical to the likelihood discussed in previous chapters.[96]

Two priors were considered for BOS tomography of flames: the Tikhonov smoothing prior from Chapter Two, $\pi_{tk}(\mathbf{x})$, and a TV prior, $\pi_{tv}(\mathbf{x})$—introduced below—which permits sharp discontinuities in $\mathbf{x}$. The bases considered in Sections 6.2 and 6.3 contain a very large number of voxels so reconstruction of the deflection data poses a unique set of computational challenges. Following discussion of the TV prior, this section reviews the method used to compute 3D estimates of the refractive index field.

6.1.3.1 Priors for BOS tomography

Classical Tikhonov regularization was developed to filter out high-frequency features that arise from inversion, attributable to noise and model errors. The Tikhonov prior pdf, based on the same operator, follows from the assumption that turbulent flow and combustion variables are subject to random fluctuations that follow a predictable distribution. Sets of turbulent flow quantities typically follow a joint-skew-normal distribution, modelled with a joint-normal pdf. The Tikhonov prior is given by Eq. (2.34), with $\boldsymbol{\mu} = 0$ and the $\mathbf{L}$ matrix defined in Eq. (2.35).

Total variation regularization, originally developed for image denoising [351], is intended to preserve the contrast of $\mathbf{x}$: promoting smooth distributions—much like Tikhonov regularization—but also permitting sharp discontinuities between distinct regions of the domain [352]. Flames feature large gradients at the periphery of reacting zones. The concept of a TV limit has thus been applied to discretize numerical simulations of combustion in order to generate high-contrast features that are characteristic of flame fronts [353]. Following from this motivation, TV regularization has been employed in flame tomography, e.g., in Ref. [207], but has not been used in the BOS context.

Total variation regularization is based on the TV norm. For a continuous 3D distribution of n in the probe volume, Ω, this norm is

$$\|n\|_{\mathrm{TV}} = \int_{\Omega} |\nabla n| \, d\Omega \,. \tag{6.12}$$

González et al. [354] proposed a Bayesian interpretation of TV regularization for discrete 3D inverse problems. In their formulation, the TV functional is

[96] Full Bayesian treatment of the deflection sensing procedure could be developed to produce an advanced likelihood.

$$G(\mathbf{x}) = \beta^2 \sum_i \sqrt{(\mathbf{D}_x\mathbf{x})_i^2 + (\mathbf{D}_y\mathbf{x})_i^2 + (\mathbf{D}_z\mathbf{x})_i^2}\ , \tag{6.13}$$

where the parameter, β, operates as a diffusion constant. The corresponding pdf is

$$\pi_{\text{tv}}(\mathbf{x}) \propto \exp\{-G(\mathbf{x})\}\ . \tag{6.14}$$

The Tikhonov prior penalizes large, isolated gradients in **x** relative to continuous, small gradients. By contrast, Eq. (6.14) only penalizes the total sum of gradients. In this way, the TV prior allows for sharp discontinuities between relatively-smooth regions of **x**, which is the behaviour expected of scalar fields in combustion.

A final source of prior information is the concentration range function, which restricts the solution to [1, n_{atm}], where n_{atm} is the refractive index of air at atmospheric conditions. This value is expected to be the maximum since n decreases with increasing temperature and combustion products remain hot within the probe volume. The concentration range prior is

$$\pi_{\text{cr}}(\mathbf{x}) = \begin{cases} 1, & x_i \in [1, n_{\text{atm}}]\ \forall\ i \in 1, \ldots, N \\ 0, & \text{otherwise} \end{cases}\ . \tag{6.15}$$

Posterior pdfs for the Tikhonov prior and TV prior are proportional to $\pi(\mathbf{b}|\mathbf{x})\pi_{\text{tk}}(\mathbf{x})\pi_{\text{cr}}(\mathbf{x})$ and $\pi(\mathbf{b}|\mathbf{x})\pi_{\text{tv}}(\mathbf{x})\pi_{\text{cr}}(\mathbf{x})$, respectively.

6.1.3.2 Computational considerations

Maximum a posteriori estimates for the Tikhonov and TV priors are denoted $\mathbf{x}^{\text{TK}}$ and $\mathbf{x}^{\text{TV}}$. Calculation of the MAP estimate follows a unique procedure for the priors. For the Tikhonov prior, determining $\mathbf{x}^{\text{TK}}$ is straightforward, whereas an iterative approach is required to compute $\mathbf{x}^{\text{TV}}$.

The posterior pdf for the Tikhonov prior is proportional to the product of Eqs. (2.36) and (6.15), which is maximized by $\mathbf{x}^{\text{TK}}$,

$$\mathbf{x}^{\text{TK}} = \arg\max_{\mathbf{x}} \{\pi(\mathbf{x}\,|\,\mathbf{b})\} = \arg\min_{1 \le \mathbf{x} \le n_{\text{atm}}} \left\{ \left\| \begin{bmatrix} \mathbf{L_e A} \\ \mathbf{L_x} \end{bmatrix} \mathbf{x} - \begin{bmatrix} \mathbf{L_e b} \\ \mathbf{0} \end{bmatrix} \right\|_2^2 \right\}. \tag{6.16}$$

Equation (6.16) is solved by constrained least squares minimization of the augmented system.

The posterior pdf for the TV prior includes Eq. (6.13) in the exponential, resulting in a non-linear system,

$$\pi(\mathbf{b}\,|\,\mathbf{x})\pi_{\text{tv}}(\mathbf{x}) \propto \exp\left\{ -\frac{1}{2} \|\mathbf{Ax} - \mathbf{b}\|_{\mathbf{L_e}}^2 - G(\mathbf{x}) \right\} \tag{6.17}$$

for $\mathbf{x}$ in [1, n_{atm}]. González et al. [354] directly maximized Eq. (6.17) using a Gauss-Newton optimization routine. However, the dimension of 3D tomography problems is typically well above 100,000 and the direct approach can be prohibitively slow. One alternative is to employ a fast, iterative approximation to the TV norm, preserving the problem's linear form [351]. Similar to the iterative Horn-Schunck approximation, the unique extrema of Eq. (6.17) is found by taking its derivative with the Euler-Lagrange equation, setting the derivative to zero, and solving for $\mathbf{x}$. MAP estimates for the TV prior are thus approached by repeatedly solving a linear system,

$$\begin{bmatrix} \mathbf{L_e A} \\ \beta^2 \nabla \cdot \dfrac{\nabla}{\left|\nabla \mathbf{x}^{(k)}\right|} \end{bmatrix} \mathbf{x}^{(k+1)} = \begin{bmatrix} \mathbf{L_e b} \\ \mathbf{0} \end{bmatrix}. \tag{6.18}$$

In Eq. (6.18), ∇ is the discrete 3D gradient operator and $\mathbf{x}^{(k+1)}$ is found by constrained least squares inversion of the augmented system. Steps of Eq. (6.18) quickly approach $\mathbf{x}^{TV}$. Convergence is accelerated further by setting $\mathbf{x}^{(0)}$ to $\mathbf{x}^{TK}$. The effect of the TV norm is apparent in the structure of Eq. (6.18), which suggests that $\nabla^2\mathbf{x}$ should be zero at positions where the derivative of $\mathbf{x}$ is small—smoothing out these regions of the estimate. Areas of $\mathbf{x}$ where the derivative is large are relatively-unaffected by the iteration.

Constrained least squares solutions to Eqs. (6.16) and (6.18) are computationally-expensive due to the size of the systems. While the operators for BOS tomography are sparse, the pseudoinverse of the augmented systems in Eqs. (6.16) and (6.18) are not and the memory required to store and manipulate these matrices can render direct inversion intractable. The simultaneous iterative reconstruction technique (SIRT) does not require explicit inversion and can generate constrained least squares estimates for high-resolution BOS tomography [355].

6.2 Numerical Evaluation of BOS Tomography

6.2.1 Simulating deflection imaging

Validation of the deflection model and evaluation of the Tikhonov and TV priors were conducted by numerical simulation. Two scenes were constructed to test the algorithms, both shown in Figure 6.3. In the first scene, a single camera was positioned 2.5 m from the background plane, which was rotated by 20°. The second scene had a system of 12 cameras, equally-spaced around a 165° arc at a radial distance of 0.5 m from the burner. Background images, 1.189×1.682 m in size, were located 2 m from the burner, opposite the cameras. The cameras were simulated with a 659×494 pixel sensor (with 9.9×9.9 μm pixels) and assigned a focal length of 12 mm. A cubic hull with

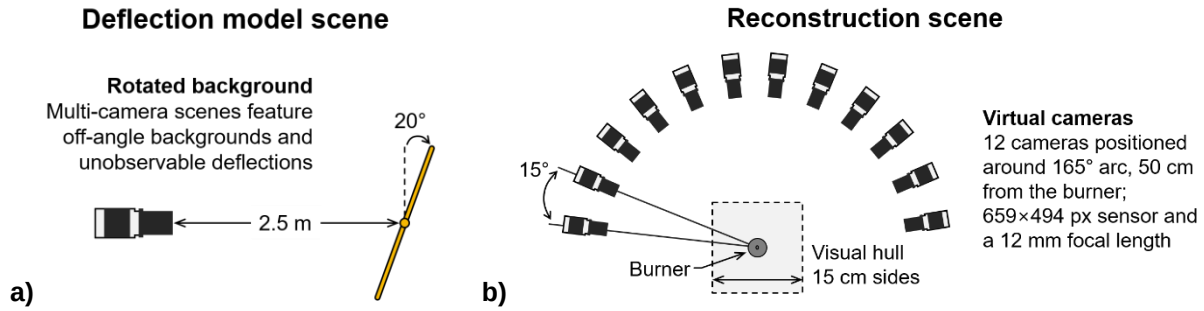

Figure 6.3: Virtual BOS tomography scenarios: a) single-camera scene to test the projection matrix and deflection sensing tools and b) 12-camera scene to test reconstructions.

0.15 m sides was placed at the centre of the domain to house refractive index distributions (i.e., phantoms). Five discretizations were tested, with 15^3, 30^3, 45^3, 60^3, and 75^3 voxels. Ground truth data in the domain was obtained by high-order interpolation of 75^3-voxel phantoms.

Reference images were generated by linear ray-tracing of the scene and deflection images were generated by non-linear ray-tracing through an inhomogeneous distribution of n. The latter procedure was carried out using Eq. (6.7) with a step size of $\Delta s = 1.33 \cdot 10^{-4}$ m. Diffraction-limited optics were simulated by applying a Gaussian blur kernel with a standard deviation of 0.85 px. Images from this procedure were stored as png files, which were then used as inputs to the optical flow algorithm.

6.2.2 Refractive index phantoms

Two phantoms were developed in order to i) test the impact of the projection matrix on model errors, ii) identify an appropriate regularization parameter for Horn-Schunck deflection sensing, and iii) benchmark the performance of Tikhonov and TV estimates. The first phantom was a 3D Gaussian bead of hot air, which produced highly-regular deflections to highlight systematic deviations in the discrete model. The second phantom was a turbulent swirl flame, generated by LES, with intricate small-scale features and substantial large-scale variation. Turbulent structures in this phantom were considerably more complex than those expected of a Bunsen flame. The swirl flame phantom was designed to provide a conservative sense of the potential to reconstruct an unsteady Bunsen flame.

The Gaussian phantom was composed of air at standard pressure with a temperature distribution given by

$$T(x,y,z) = 296.15 + 703.85 \cdot \exp\left\{-\frac{1}{2}\frac{x^2+y^2+z^2}{0.025^2}\right\}. \tag{6.19}$$

Equation (6.19) yields a maximum temperature of 1,000 K at the centre of the domain, which quickly decays to standard conditions within the probe volume. The density of air throughout the sphere was calculated using the ideal gas law. In general, the local density of a gas mixture is related to the local index of refraction by the Gladstone-Dale equation [356],

$$n = 1 + \rho G \,, \tag{6.20}$$

where the Gladstone-Dale coefficient for air over visible wavelengths is $G = 2.26 \cdot 10^{-4}$ m^3/kg [357]. Equation (25) can be combined with the ideal gas law and a model of combustion products to infer the temperature field of reconstructions. Using this approach, temperature in the *j*th voxel is

$$T_j = \frac{p}{R(x_j - 1)} \sum_i (Y_i M_i G_i)_j \,, \tag{6.21}$$

where p is pressure, R is the universal gas constant, and x_j is the reconstructed value of n in j. The sum is a volume fraction-weighted product of molecular mass and the Gladstone-Dale coefficient of the *i*th species in the *j*th voxel.

Table 6.1: Molecular Weights and Gladstone-Dale Coefficients of Select Gases [357]

Species	Molecular Weight [kg/kmol]	$G \times 10^{-4}$ [m^3/kg]
CH_4	16.04	6.15
CO	28.00	2.67
CO_2	44.01	2.26
H_2	2.02	1.54
H_2O	18.02	3.12
O_2	32.00	1.89
N_2	28.01	2.38

The LES was developed by Andreas Rittler of the University of Duisburg-Essen to simulate combustion from the turbulent premixed TECFLAM swirl burner [358]. This flame features intricate, stochastic structures, representative of swirled premixed combustion, and has been compared to experimental data in the literature [358–360]. LES was carried out using PsiPhi [361], with an equivalence ratio of 0.83, swirl number of 0.75, and cold flow Reynolds number of 10,000. The domain was discretized into 30 million cells and required 50,000 core hours for a simulated time of 1.6 s. Combustion was modelled with the premixed flamelet-generated manifold, coupled with an artificial flame thickening method. Results were compared to experimental measurements

from Schneider et al. [362] and Gregor et al. [363] and the LES of Butz et al. [364]. The flame shape and recirculation zone at the centreline were representative of those reported in the aforementioned studies. Agreement between the LES data and experimental results support the use of this phantom as a test case to validate the BOS tomography procedure.

In order to compute the refractive index of the swirl flame, temperature and density of the flame and mass fraction of CH_4, CO, CO_2, H_2, H_2O, O_2, and N_2 were recorded. The volume fraction-weighted Gladstone-Dale coefficient throughout the domain was calculated with the species-specific values of G reported by Qin et al. [357], shown in Table 6.1.

6.2.3 Model performance

Figure 6.4 shows ground truth deflection vectors for the hot air sphere and swirl flame phantoms. Per Figure 6.3a, the camera was positioned 0.5 m from the centre of the phantom and aimed towards the centre of a background plane, located 2.5 m away. Space-related concerns generally restrict the number and orientation of background planes in BOS tomography and most cameras end up facing their target pattern at an angle. Therefore, the plane was rotated 20° clockwise about the image plane to generate the out-of-plane deflections that arise from the standard BOS model. After ray-tracing ground truth deflections for each phantom, measurement operators from Section 6.1.2 were used to model the scene. This procedure was repeated with and without the projection matrix, $\mathbf{P}$, resulting in two systems: $\mathbf{A}^{\text{prj}}$ and $\mathbf{A}^{\text{std}}$, respectively, where $\mathbf{A}^{\text{prj}} = \mathbf{P}\mathbf{A}^{\text{std}}$ and $\mathbf{A}^{\text{std}}$ is the operator of Nicolas et al. [338] from Eq. (6.10).

Exact deflections were arranged as a measurement vector with the directional components grouped together: $\mathbf{b}^{\text{exact}} = [\boldsymbol{\delta}_x{}^T\ \boldsymbol{\delta}_y{}^T\ \boldsymbol{\delta}_z{}^T]^T$. Modelled deflections were calculated with the 75^3-voxel

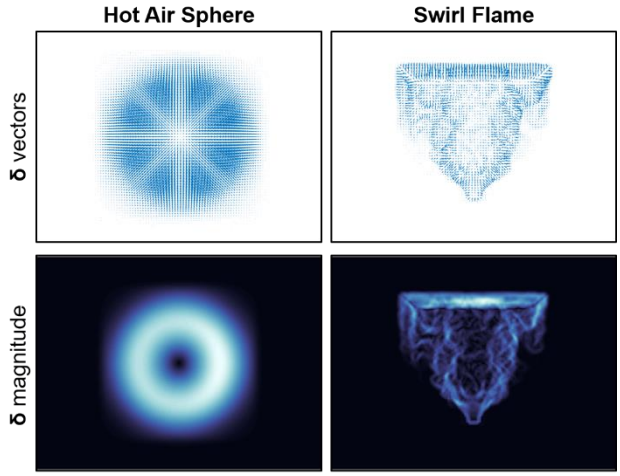

Figure 6.4: Ground truth deflection vectors for the hot air sphere and swirl flame phantoms. Vectors are scaled by a factor of 2.5 to emphasize apparent motion in the visual field.

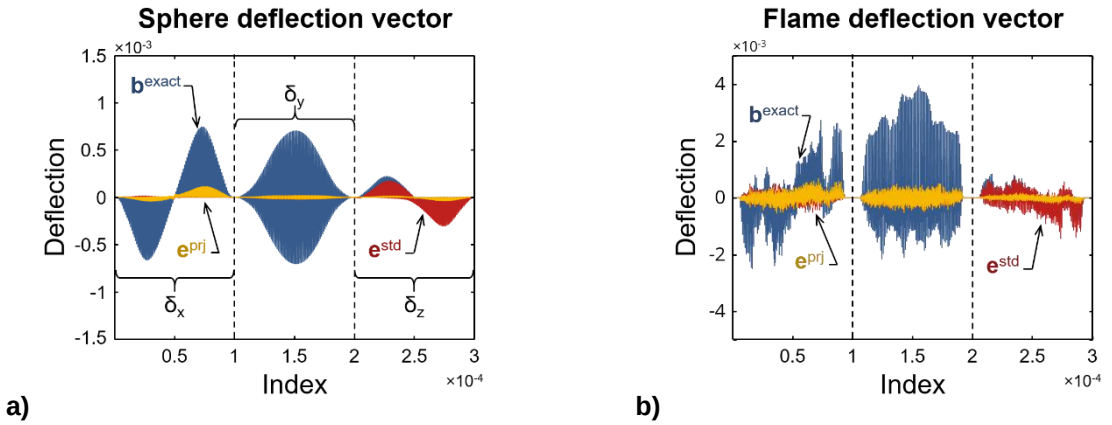

Figure 6.5: Exact measurements and model error for phantoms with 75^3 voxel support: a) the hot air sphere (error reduced by 63% due to the projection matrix) and b) the TECFLAM swirl flame (error reduced by 42% due to the projection matrix).

hull and errors were defined as the Euclidean distance of the residual, $\mathbf{b}^{\text{exact}} - \mathbf{A}\mathbf{x}^{\text{exact}}$, normalized by the magnitude of $\mathbf{b}^{\text{exact}}$. Measurement vectors and model errors for both phantoms are shown in Figure 6.5. Deflections computed with $\mathbf{A}^{\text{prj}}$ exhibited limited error throughout the vector, with an error of 9.3% for the hot sphere phantom and 15.4% for swirl flame phantom. Corresponding errors for $\mathbf{A}^{\text{std}}$ were 25.1% and 26.6%. Model discrepancies were greater for the flame than the sphere—both with and without the projection matrix—due to the relative complexity of the flame phantom. This difference occurs because gradients in the discrete approximation to the sphere were more accurate than gradients in the discrete approximation to the flame.

The standard model generated accurate data in the *x* and *y* directions but produced significant error in the *z* direction. By contrast, the performance of $\mathbf{A}^{\text{prj}}$ was more uniform, with lower overall error. The projection matrix accounts for the pose of the camera relative to the plane and thereby reduces model errors. To illustrate: in this case, while $\mathbf{A}^{\text{std}}$ computes vectors that lie primarily in the image plane, deflections apparent in the background pattern contain a considerable *z* component, which can be seen in Figure 6.5. In addition, there are small components of $\boldsymbol{\delta}$ in the *z* direction due to the path integrals over $\nabla_z n$. These components are caused by inhomogeneous gradients in *n* along the *z* direction, which bend the phase front relative to the plane, regardless of its orientation. $\mathbf{P}$ eliminates unobservable deflections due to both effects and $\mathbf{A}^{\text{prj}}$ predicts more accurate deflections for $\mathbf{x}^{\text{exact}}$ than $\mathbf{A}^{\text{std}}$ as a result.

Any discrepancies between the measurement model and underlying physics will introduce errors into reconstructions. These errors are amplified in tomography due to the inherently ill-posed nature of inverting coupled IFKs. The standard BOS model does not restrict deflections to

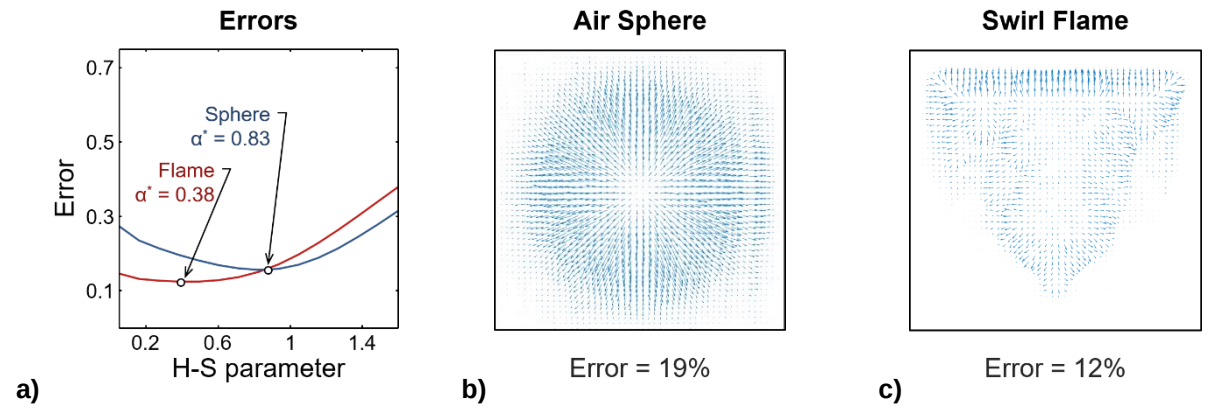

Figure 6.6: Optimizing deflection sensing: a) errors in the Horn-Schunck vectors and vector plots for the b) heated air sphere and c) swirl flame phantoms.

the plane of the background pattern, resulting in the out-of-plane errors described above. However, a matrix, **P**, can be constructed to project modelled deflections into the target plane. It was found that the product $\mathbf{PA}^{std}$ reduced model error by 63% and 42% compared to $\mathbf{A}^{std}$ for the air sphere phantom and swirl flame phantom, respectively. The use of $\mathbf{A}^{prj}$ thus reduces the uncertainty in reconstructed parameters relative to $\mathbf{A}^{std}$.

6.2.4 Deflection sensing

The same ray-tracing simulation was employed in order to evaluate the performance of Horn-Schunck deflection sensing. Tests were run with both the Horn-Schunck and Lucas-Kanade algorithms to compare these techniques. Figure 6.6 shows errors in the optical flow deflections vs. α for both phantoms. Error ranged from 15.5% to 31.4% for the hot air sphere and 12.4% to 37.8% for the swirl flame for α in [0.05, 1.60]. The optimal value of α was 0.83 for the sphere test and 0.38 for the swirl flame test. The trend in error vs. α followed a shallow trough around the minimum in both cases, which supports the use of a Horn-Schunck algorithm. By comparison, the Lucas-Kanade algorithm was less accurate and more sensitive to the regularization parameter. Minimum error in the Lucas-Kanade tests was 42.2% for a window size of 25 px; the error trace featured a steep well near the minimum (i.e., results were quite sensitive to the window size). Therefore, the Horn-Schunck algorithm was used for deflection sensing in the remainder of simulations and post-processing of experimental images.

Also shown in Figure 6.6 are Horn-Schunck-based vector plots for the phantoms. These were calculated from the blurred png images from the non-linear ray-tracing simulation using α = 0.8. Both plots exhibit a strong resemblance to the ground truth structures in Figure 6.4, with errors primarily distributed around the edge of the structures. Measurements in Figure 6.6 were calculated

for a 400×400 px window in the centre of the sensor, which fully contained both phantoms, and downsampled by linear interpolation to a resolution of 100×100 px. The same treatment was applied to the LOS vectors used to generate the forward operator, **A**.

6.2.5 Evaluation of Bayesian priors

Following evaluation of the measurement model, the swirl flame phantom was reconstructed using the 12-camera setup in Figure 6.3b. First, the Tikhonov prior was tested using each discretization scheme, from 15^3 to 75^3 voxels, varying λ from $1{\cdot}10^{-4}$ to 500. Reconstructions were computed with the SIRT algorithm to avoid explicit calculation of the inverse operator. The SIRT is often used for iterative regularization in tomographic reconstruction due to its semi-convergence behaviour [355]. However, since the augmented system in Eq. (6.16) already incorporates a priori information, the system is not ill-conditioned. As such, the SIRT algorithm was run for 15,000 steps, which was sufficient to ensure convergence to a tolerance of 10^{-8}.

Reconstruction accuracy was scored with respect to the 75^3-voxel ground truth phantom to control for the effects of dimension on inter-grid comparisons. The measurement model assumes uniform concentration in the voxels, which, accordingly, was the mode of interpolation used to upsample data from the coarse grids. Accuracy was measured with the SSIM index.

Figure 6.7 shows the results of the Tikhonov parameter study. All SSIM scores were above 0.99, indicating a high degree of structural similarity throughout the tests. The range of indices in the study was $3.8{\cdot}10^{-7}$, this small range was due to the very high dimension of **x** (i.e., 75^3 variables). Scores in Figure 6.7 are scaled to the range of scores in the study to emphasize relative trends. Reconstructions improved with increasing resolution of the discretization scheme and peaked in

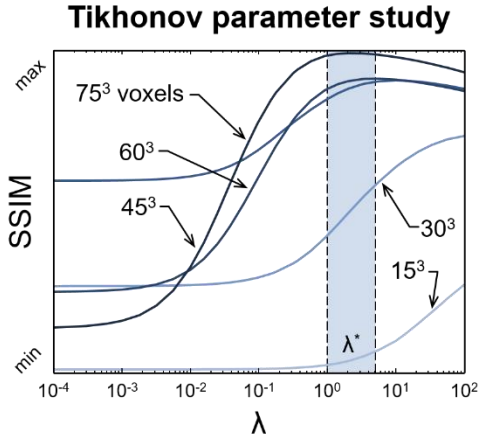

Figure 6.7: SSIM index scores for reconstructions based on the Tikhonov prior, calculated for smoothing parameters from $\lambda = 1{\cdot}10^{-4}$ to 500.

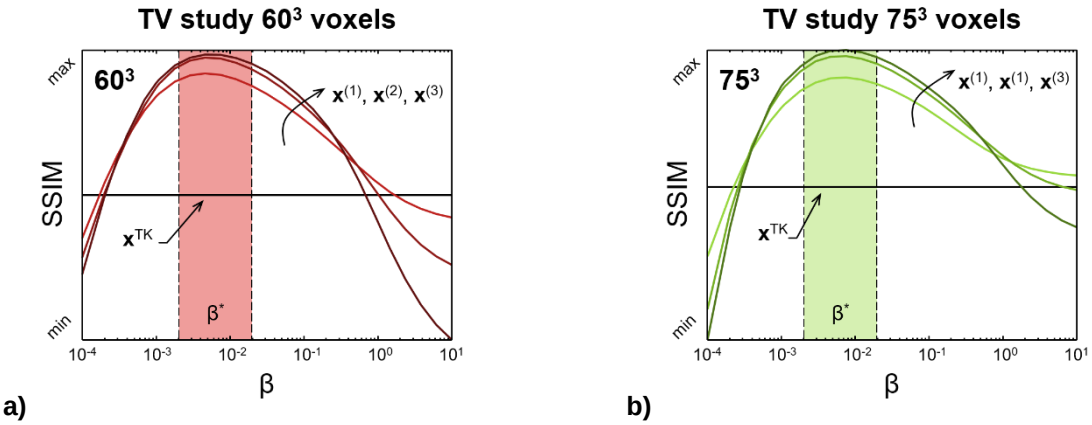

Figure 6.8: SSIM index scores for reconstructions based on three iterations of the TV prior, calculated for β = 1·10^{-4} to 10. Results are shown for the a) 60^3 voxel hull and b) 75^3 voxel hull.

the range of λ = 1 to 10 for the 45^3-, 60^3-, and 75^3-voxel schemes. Optimal values of λ decreased with increasing grid resolution, which is consistent with the Bayesian interpretation of Tikhonov regularization. That is, the variance of voxels should increase with the grid resolution.

The TV prior parameter study was conducted using the swirl flame phantom and all five grids. The diffusion parameter, β, was varied from 1·10^{-4} to 10. Iterations of the TV prior were computed with Eq. (6.18), which was initialized using a Tikhonov reconstruction (i.e., $\mathbf{x}^{(0)} = \mathbf{x}^{TK}$), itself computed with the optimal value of λ indicated in Figure 6.7. Three iterations of $\mathbf{x}^{(k)}$ were computed with 15,000 steps of the SIRT algorithm and reconstructions were scored by the SSIM index.

Figure 6.8 shows results of the TV parameter study for the 60^3 and 75^3 voxel hulls. These tests featured a range of SSIM scores of 8.4·10^{-8} and 8.0·10^{-8}, respectively. The Euler-Lagrange approximation to the TV prior improved reconstructions relative to the Tikhonov prior for each iteration across several orders of magnitude of β for all five hulls. Continued iteration of the prior produced diminishing returns, with effective convergence after three steps. These results suggest that the TV prior provides robust improvement over the Tikhonov prior in the reconstruction of a flame scalar by permitting sharp gradients in the estimate. However, values of β that are very small effectively eliminate the influence of the prior, and values that are very large over-smooth the distribution, as with Tikhonov regularization.

Figure 6.9 illustrates the effect of Tikhonov and TV iterations with slices of the 3D swirl flame reconstructions on the 75^3-voxel grid. Measurement data for the reconstructions were obtained by Horn-Schunck deflection sensing; reference and deflection images were generated by the linear and non-linear ray-tracing algorithms. MAP estimates were computed with the Tikhonov prior,

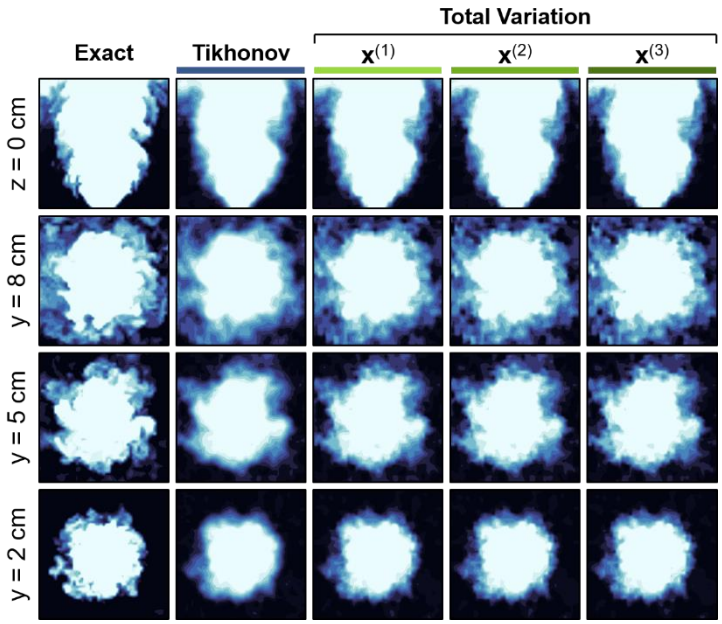

Figure 6.9: Index of refraction slices from the TECFLAM swirl flame phantom and the corresponding reconstructions. Iterations were initialized with a Tikhonov reconstruction ($\mathbf{x}^{(0)} = \mathbf{x}^{TK}$, $\lambda = 5$). Subsequent reconstructions, $\mathbf{x}^{(k)}$, were computed with the TV prior ($\beta = 0.01$).

using $\lambda = 1$, followed by three iterations of the TV prior, with $\beta = 0.01$. Accuracy trends in Figure 6.8 align with the visual quality of reconstructions in Figure 6.9. The initial Tikhonov estimate was itself accurate, capturing large-scale variation in the flame but over-predicting the extent of hot gases outside the flame. Iterative TV estimates preserved the large-scale structures and progressively refined small-scale features at the flame front. As a result, variation apparent in the third iteration of the TV prior was much closer to variation in the ground truth flame front than the Tikhonov reconstruction. This result was anticipated because the TV prior promotes information that is more compatible with combustion physics than the Tikhonov prior. Implementation of the iterative, linear approximation to the TV norm is straightforward. Therefore, the TV prior was employed to reconstruct experimental deflection data in Section 6.3.

Large-scale structures in the final TV reconstruction in Figure 6.9 appear substantially similar to those of the ground truth phantom, and the SSIM index assigned a large value (indicating similar residuals) to all of the reconstructions. Nevertheless, certain discrepancies are visible in the estimates and it is crucial to develop the means to assess the accuracy of optical density field estimates. Figure 6.10 shows a voxel-by-voxel comparison of the TV reconstruction and ground truth distribution in Figure 6.9, i.e., $\mathbf{x}^{(3)}$ and $\mathbf{x}^{exact}$. As with the SSIM index, a simple correlation metric shows substantial similarity between the two vectors, with an observed correlation of 0.94.

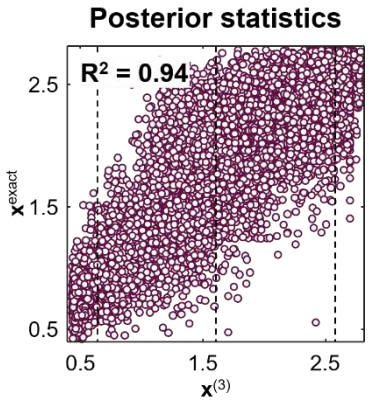

Figure 6.10: Voxel-by-voxel comparison of $x^{(3)}$ and x^{exact}; axes report a transformation of the refractive index, $(n - 1)\cdot 10^4$, and dashed lines indicate joint-comparison values: the 10th, 50th, and 90th percentile of the range of n.

However, close inspection of Figure 6.9 reveals that the reconstructed index of refraction is prone to some non-physical variation, contributing to posterior uncertainties.

Joint-statistics for the reconstruction and ground truth phantom can elucidate the accuracy and precision of quantitative estimates from tomographic BOS. Figure 6.11 shows distributions of $\mathbf{x}^{\text{exact}}$ conditioned on the estimate. The range of $\mathbf{x}^{(3)}$ and $\mathbf{x}^{\text{exact}}$ was divided into 1,000 bins and conditional distributions of $\mathbf{x}^{\text{exact}}$ were obtained for $\mathbf{x}^{(3)}$ = 1.00006, 1.00016, and 1.00026, corresponding to the 10th, 50th, and 90th percentile of the range. The resulting pdfs, $\pi(\mathbf{x}^{\text{exact}}|\mathbf{x}^{(3)} = P)$, are plotted in Figure 6.11, which also lists the corresponding mean conditional-percentile of $\mathbf{x}^{\text{exact}}$. Tenth percentile estimates (at n = 1.00006) corresponded to a true optical density of 1.00005 on average, which equates to a temperature difference of 300 K. Estimates of $\mathbf{x}$ at the 50th and 90th percentile of the range were within 1.6 and 0.9 percentiles of the true mean density. These estimates exhibited a greater spread than the first distribution but implied a less substantial temperature difference. One standard deviation of the distributions in Figure 6.11b and c corresponded to 122 K and 28 K, respectively. Additional temperature sensitivity at the lower optical densities arose because Eq. (6.21) is singular for n = 1, which suggests a temperature of infinity.

Ideally, the distribution of n conditional on an estimate would be a delta function about the estimate (i.e., with no posterior uncertainty). At present, errors from the optical flow algorithm are the primary source of uncertainty in the reconstructions, as illustrated by the posterior distributions in Figure 6.11. These errors can obscure important features of the flame and reduce the spatial resolution of BOS tomography. However, reconstructed structures were clearly representative of the true distribution, as evidenced by the SSIM index, correlation, and visual similarity between

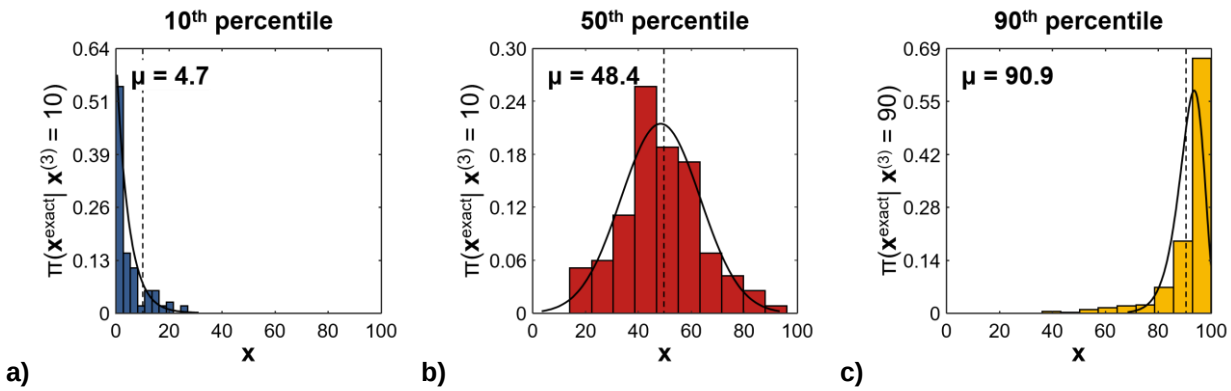

Figure 6.11: Joint-statistics of the TV reconstruction and ground truth phantom, $\pi(\mathbf{x}^{exact}|\mathbf{x}^{(3)} = P)$, where P is a percentile of $\mathbf{x}^{(3)}$. Joint-comparisons include the a) 10th, b) 50th, and c) 90th percentile. Dashed lines are the conditional value of $\mathbf{x}^{(3)}$.

$\mathbf{x}^{exact}$ and $\mathbf{x}^{(3)}$. Probability distributions of *n*, conditional on the reconstruction, gave a reasonably-bounded temperature range, suggesting BOS tomography can be usefully employed for flame imaging.

6.3 Instantaneous 3D Imaging of a Laboratory Bunsen Flame

6.3.1 Laboratory setup

A Bunsen burner with an exit diameter of 15 mm and height of 88 mm was operated with open intake slots at the base to generate a premixed natural gas/air flame. The flame was neither encased in a housing nor co-flow and was left to flicker and drift due to ambient fluid motion. Figure 6.12 depicts the laboratory setup and a photo of the flame set against a black background. Apparent in this photo are the wrinkled reacting zone and envelope of hot gases.

Twenty-three Basler acA645-100gm cameras were equally-spaced around a 165° arc surrounding the flame, focused on five background patterns, shown in Figure 6.12a. The cameras include a ½" Sony ICX414 659×494 px monochromatic sensor with a pixel size of 9.9×9.9 μm

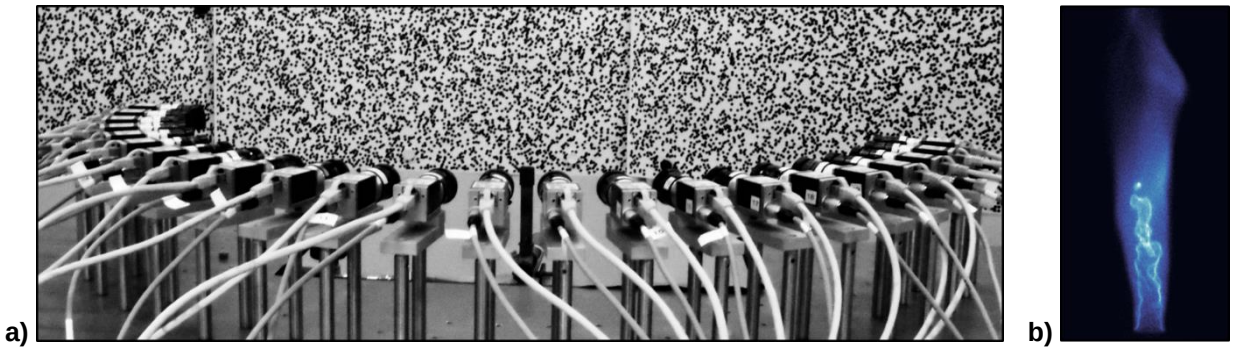

Figure 6.12: Laboratory setup for BOS tomography: a) the 23-camera laboratory array, centred on a Bunsen burner and focused on textured background images, and b) image of the Bunsen flame against a black background, captured with a 300 μs exposure time.

Cameras were fixed in position by mounting them onto a single base plate at a fixed radius from a common origin, roughly corresponding to the burner's outlet. This arrangement was previously used in an emission CST experiment with a swirl flame target [218]. A Kowa C-mount lens having a focal length of 12 mm was attached to each camera. The cameras' peak spectral response was in the visible range, from 400 to 680 nm, and the aperture size was toggled between a maximum and minimum setting to achieve an f-stop of f/1.4 and f/16, respectively. Emission from the flame was negligible compared to the intense illumination of the background patterns.

Five dot speckle patterns, shown in Figure 6.12a, were printed on white A0 poster paper. The patterns each contained 7,500 black dots, 8 mm in diameter, positioned by a Poisson-disc sampling algorithm. Posters were arranged in a semicircle, approximately 2 m away from the burner. The background planes were lit, homogeneously, by twelve 200 W LED floodlights, resulting in 240,000 lumens of illumination. Deflections in the BOS patterns due to refraction through the flame were visible to the human eye during the tests.

An emission CST experiment and simple LES of the Bunsen flame were conducted to validate the optical density estimates. The room was darkened for the CST test and the flame was imaged with the 23-camera setup using an f-stop of f/16 and long exposure time. Emission data was reconstructed according to the procedure of Floyd et al. [206].

6.3.2 Camera calibration

Ray trajectories for each pixel were calculated using an idealized pinhole model. The pinhole camera system comprises an intrinsic matrix, $\mathbf{K} \in \mathbb{R}^{3\times3}$, and extrinsic matrix, $\mathbf{M} \in \mathbb{R}^{3\times4}$. $\mathbf{M}$ is constructed by augmenting a rotation matrix, $\mathbf{R}$, and translation vector, $\mathbf{t}$: $\mathbf{M} = [\mathbf{R}\ -\mathbf{t}]$, which describes the camera's pose and location. The beam for the ith pixel was approximated by its primary ray,

$$\mathbf{r}_i = \mathbf{R}_i^T \mathbf{K}_i^{-1} \mathbf{q}_i \,, \tag{6.22}$$

where $\mathbf{R}_i$ and $\mathbf{K}_i$ are the rotation and intrinsic matrix for the camera containing i and $\mathbf{q}_i$ is the location of the pixel on the sensor in homogeneous sensor coordinates. The translation vector is $\mathbf{t} = \mathbf{Rc}$, where $\mathbf{c}$ is the camera position (i.e., the origin of the ray in world coordinates). $\mathbf{K}$ consists of a homogeneous sensor origin, skew parameter, and u and v direction focal lengths. Given the matrices $\mathbf{M}$ and $\mathbf{K}$, the equation for the ith ray is $\mathbf{c}_i + u\mathbf{r}_i$, where u is a non-negative scalar.

Stereo calibration of the 23-camera setup was conducted with MATLAB's Computer Vision System Toolbox. A procedure was developed to obtain synchronous camera parameters and plane equations for the background patterns. Calibration was conducted in two steps. First, the cameras were fixed in place to determine their extrinsic parameters. For this step, the cameras were aimed at a small target, positioned above the burner. Next, the cameras were refocused on a larger target, placed directly in front of the speckle dot posters, and a second image set was recorded to determine the intrinsic parameters and plane equations. Calibration codes were written by Andreas Unterberger of the University of Duisburg-Essen, in collaboration with the author of this thesis, and photos of the target boards were captured with the assistance of Ying Jin of the Nanjing University of Science and Technology.

6.3.2.1 Extrinsic parameters

The target for extrinsic calibration was a checkerboard with 12 rows of 17 squares, 8×8 mm in size. Parameters were computed for a set of at least 20 images that were accepted by the calibration toolbox, each featuring a random orientation of the target. MATLAB's stereo calibration algorithm [67] generates extrinsic matrices, $\mathbf{M}_a$ and $\mathbf{M}_b$, for simultaneous images of the target from two cameras. The rotation matrices for the first pair of cameras were denoted $\mathbf{R}_1 = \mathbf{R}_a$ and $\mathbf{R}_2 = \mathbf{R}_b$. Subsequent pairs were calibrated and rotated into the global system as follows:

$$\mathbf{R}_{i+1} = \mathbf{R}_b \mathbf{R}_a \mathbf{R}_i, \tag{6.23}$$

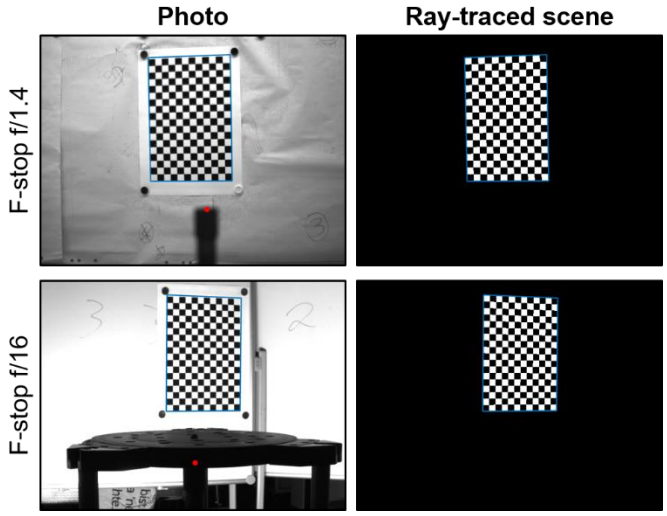

Figure 6.13: Calibration photos from camera 11 for the f/1.4 and f/16 f-stop settings and corresponding ray-traced scenes. Outlines of the simulated target in the ray-traced scenes are superimposed on the calibration photos in blue and the global origin is plotted in red.

where $\mathbf{R}_a$ and $\mathbf{R}_b$ were extracted from $\mathbf{M}_i$ and $\mathbf{M}_{i+1}$, respectively. Translation vectors were similarly transformed,

$$\mathbf{t}_{i+1} = \mathbf{t}_i + \mathbf{R}_i(\mathbf{t}_b - \mathbf{t}_a)\,. \tag{6.24}$$

Finally, the whole system was rotated and translated such that the primary ray of camera 12 pointed along z = -1 with the origin located approximately at the centre of the burner exit.

6.3.2.2 Intrinsic parameters

Intrinsic calibration was conducted to correct for lens aberrations and small differences in the focus of individual cameras. The first target was a checkerboard with 18 rows of 12 squares, 27.5×27.5 mm in size. Calibration of the intrinsic parameters was conducted twice, once for each f-stop setting.

Figure 6.13 shows a sample set of second-stage calibration photos. Also shown are simulated images of the same scene, ray-traced with the calibration parameters and plane equations. The edge of the target (as determined by the ray-tracing procedure) is outlined in blue in the photo to highlight the close correspondence between the true and simulated target positions; the global origin is plotted in red. The aperture size had a considerable influence on the apparent focus of the images. As the aperture size was decreased from f/1.4 to f/16, the volume of rays for a single pixel was decreased. Moreover, the volume shape transitioned from conical to cylindrical. The edge of the burner appears blurry in the f/1.4 photo and sharp in the f/16 case, accordingly. It is desirable to minimize this bokeh effect in BOS imaging.

Small discrepancies between the plane equations were observed between estimates from different cameras, indicative of calibration errors. The magnitude of this error was greatest for ray-traced positions in the background plane (i.e., furthest away from the camera); discrepancies within the visual hull were expected to be small. Camera-specific plane equations were used for each background, to minimize the effects of misalignment between the location of optical flow data and ray-sum trajectories. The mean and standard deviation of reprojection errors from the camera calibration was 0.18 px and 0.007 px. A previous study of the tomography system showed increasing accuracy with an increasing number of views for up to 24 cameras [218]. While these results support the accuracy of the calibration and ray tracing procedures, further study is required to quantify the relationship between reconstruction accuracy and calibration uncertainties in BOS tomography.

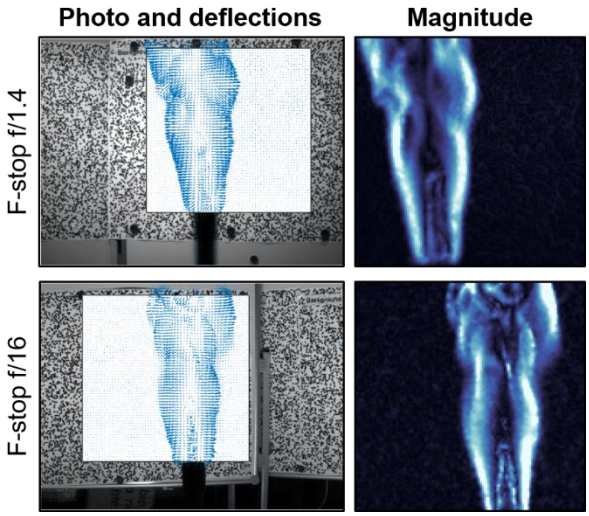

Figure 6.14: Photos from camera 11 for the small and large aperture tests, with measurement region and deflections superimposed, and downsampled deflection plots for the same measurements.

6.3.3 Results and discussion

Two proof-of-concept experiments were conducted to establish the viability of BOS tomography as a practical combustion diagnostic. Both tests featured a premixed natural gas/air flame from a Bunsen burner with no coflow. The aperture size was varied between the tests to illustrate the effect of the blur in the probe volume on reconstruction accuracy. Images for the cameras were captured, simultaneously, with an exposure time of 300 μs at a sampling rate of 5 Hz.

Sub-regions of each sensor were selected to eliminate degenerate deflection vectors at the edge of the burner and minimize unnecessary ray-tracing, since the flame did not fill the cameras' field-of-view. These regions, roughly 350×350 px in size, were downsampled to 125×125 LOS arrays, resulting in measurement vectors of dimension $3 \cdot 125^2$. A cubic hull with 0.1 m sides, which fully contained the flame front, was discretized into a 60^3 voxel system. This system had a grid resolution of 1.67 mm, similar to the resolution of the 75^3 voxel system from the numerical study. Based on the results in Section 6.2.5, the flame was reconstructed using three iterations of the TV prior, with $\beta = 0.01$, starting from a Tikhonov reconstruction, with $\lambda = 1$. Each iteration was computed by 15,000 steps of the SIRT solver to ensure adequate convergence.

Figure 6.14 contains sample photos of the distorted background from camera 11 for both f-stop settings. Deflections from the optical flow algorithm, downsampled to the 125×125 LOS array, are plotted in blue. The measurement sub-region is superimposed on the photo in white to highlight the deflections. Also shown are plots of the magnitude of downsampled deflections, which illustrate the position of refractive index gradients in the flame. The primary gradient is

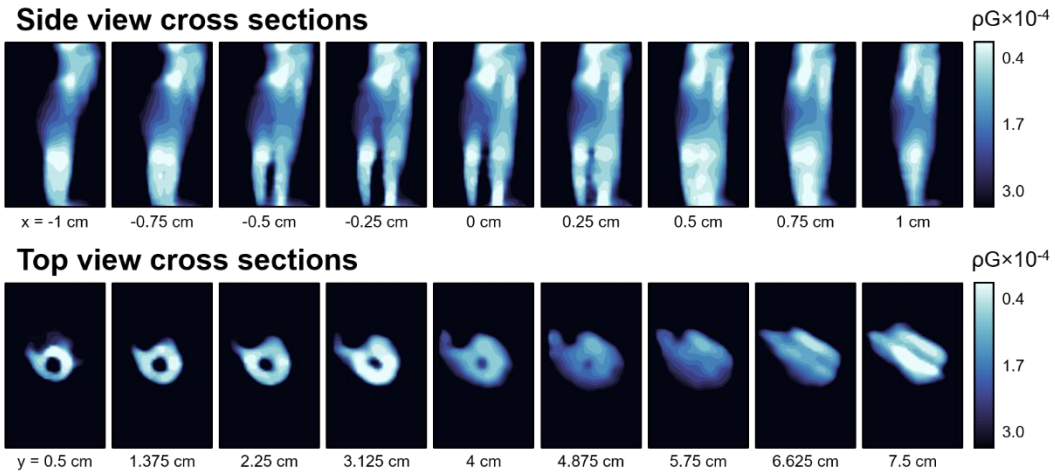

Figure 6.15: Cross sections of an instantaneous reconstruction from the f/16 test, computed with three iterations of the TV prior ($x^{(0)} = x^{TK}$ with $\lambda = 1$, and $\beta = 0.01$ for $x^{(1)}$ to $x^{(3)}$).

located about the edge of the hot gas envelope, with the flame front clearly visible within the inner structure, directly above the burner. Deflection magnitudes for the f/1.4 and f/16 apertures emphasize the effect of blur in the probe volume on the optical flow algorithm, established in Figure 6.13. Although the background is in focus at both f-stop settings, f/1.4 images feature larger, more conical ray bundles in the probe volume than f/16 images. The former setting thus obscures fine features within the flame and the wrinkled reacting zone appears clearer in the f/16 test.

Horizontal and vertical cross sections of an instantaneous reconstruction from the f/16 test are shown in Figure 6.15. Structures in this figure align with structures apparent in the photo in Figure 6.12b and deflection vector magnitudes in Figure 6.14. The reconstruction features a hollow core within the flame front due to the high optical density of the cold, unburned gases. This mixture consisted primarily of N_2, O_2, and CH_4 (roughly, 72%, 22%, and 5%, respectively), with an approximate density of 1.14 kg/m^3 and ambient optical density of 1.000283. The envelope of hot products surrounding the flame front consisted mainly of N_2, CO_2, and H_2O, along with CO and other trace gases. Density of the mixture was lower in this region because of heat released by the combustion process, thereby lowering the optical density, per Eq. (6.19). Figure 6.16 shows corresponding mean reconstructions. The measurement vector for mean estimates was obtained by averaging Horn-Schunck deflections for 50 successive frames. The horizontal cross sections are circular, reflecting the axisymmetric burner configuration.

Mean results from the f/16 experiment are compared to the Bunsen flame simulation and emission CST estimate in Figure 6.17. The LES was run using the same combustion model as the

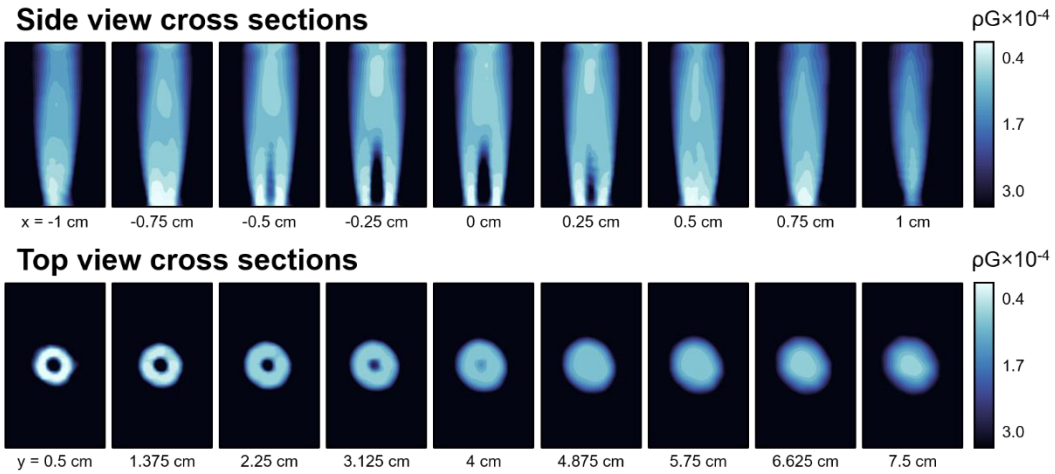

Figure 6.16: Cross sections of the mean reconstruction from the f/16 test, computed with three iterations of the TV prior ($x^{(0)} = x^{TK}$ with $\lambda = 1$, and $\beta = 0.01$ for $x^{(1)}$ to $x^{(3)}$).

LES in Section 6.2.2 to provide a baseline for qualitative comparison to the experimental reconstructions. Instantaneous optical density fields from the simulated Bunsen flame exhibited a reacting zone with wrinkles on the same scale as those of the estimates in Figure 6.15. Emission from the flame peaked about the flame front and then quickly tapered off, resulting in a thin profile. By contrast, optical density is elevated far away from the reaction zone due to the extent of hot products and convective heating of the surrounding air. Regardless, mean reconstructions from the BOS and chemiluminescence tests suggest a common underlying flame structure. The height and width of flame fronts from the LES and CST test match the BOS reconstructions, which supports the use of BOS tomography to visualize 3D features of an unsteady flame.

Figure 6.18 shows instantaneous reconstructions from the f/1.4 test. Blurring effects are clearly apparent in the over-smoothed core and enlarged envelope of hot products. Furthermore, the peak magnitude of refractive index near the base of the flame is lower than that of f/16 reconstructions, reflecting a lower overall magnitude of deflection vectors in the f/1.4 test. The

Figure 6.17: Comparison of the Bunsen flame profiles from LES, BOS tomography for f/16 images, and chemiluminescence tomography. Side and top view cross sections are presented for x = 0 cm and y = 2 cm, respectively, showing close correspondence of the flames.

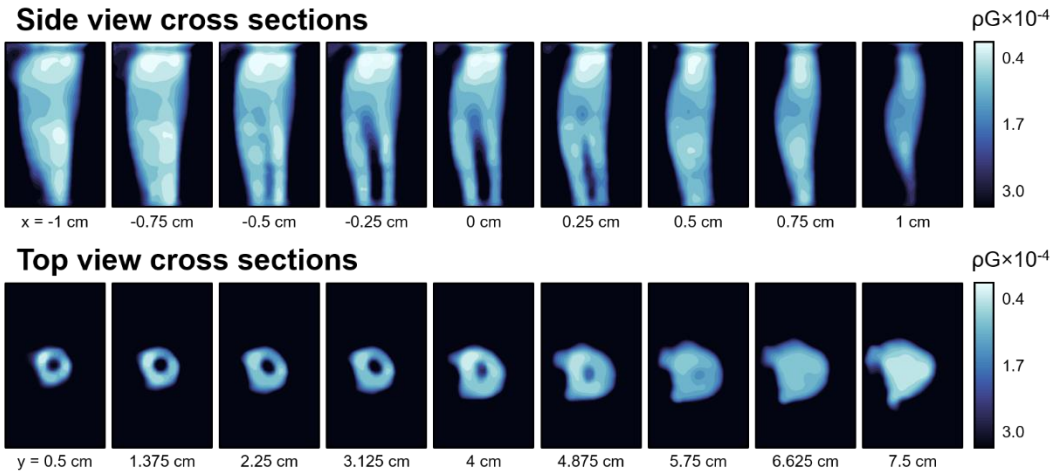

Figure 6.18: Cross sections of an instantaneous reconstruction from the f/1.4 test, computed with three iterations of the TV prior ($x^{(0)} = x^{TK}$ with $\lambda = 1$, and $\beta = 0.01$ for $x^{(1)}$ to $x^{(3)}$).

larger aperture reduced the exposure time required to obtain a clear image of the posters but blur in the probe volume, produced by the larger, more conical ray bundles accepted by the aperture, limited the accuracy of f/1.4 reconstructions. The aperture size should therefore be set to a minimum feasible value.

Local flame temperatures are extracted from the optical density field via the Gladstone-Dale relation, but temperature inference is complicated by the fact that G varies throughout the flame. There are three effective regimes of n within the probe volume: unburned gases, a thin reaction zone, and the envelope of combustion products. Variation of G within these regimes is negligible and the variation in between may sometimes be neglected, as well, depending on the mode of combustion [357]. In order to transform the estimates in Figure 6.15 into a temperature, one would need to either model the distribution of G or infer this parameter from the distribution of n with a segmentation algorithm, which is a topic for future research. Preliminary results were obtained for an optical density immediately outside the flame front in Figure 6.15, $n = 1.0004$. Substituting this value and a presumed combustion product mixture into Eq. (26) yields a maximum temperature of roughly 2,150 K and ambient temperature of 300 K. The latter value was in good agreement with the temperature of air in the lab and the peak value was consistent with prior expectations about the Bunsen flame.

6.4 Conclusions

Three-dimensional measurements of scalar fields in turbulent flames are vital to the development and validation of combustion simulations, which enable engineering solutions to numerous energy

and climate challenges. Present optical diagnostics are either spatially-limited, such as 2D laser diagnostics, or qualitative, such as 3D emission CST. Emerging alternatives, including volumetric LIF, promise quasi-instantaneous, quantitative 3D data. VLIF systems require intricate, highly-expensive setups that pose safety risks and suffer from limited mobility. Novel 3D diagnostics are thus of considerable interest to the combustion community.

Schlieren imaging responds to gradients in a refractive index medium, such as a flame, and can be used for quantitative tomography. BOS uses computer vision tools to identify the deflections, which greatly simplifies the technique. BOS tomography is a form of gas-phase tomography, previously employed to reconstruct the temperature and density of a gas-phase fluid. This chapter reports the first application of BOS tomography to combustion imaging. Moreover, the deflection model was improved with a projection matrix, shown here to reduce model errors by up to 63%. Tomography was conducted in the Bayesian framework developed in previous chapters; Tikhonov and TV priors were employed to reconstruct the flame front. A parametric study of the priors was conducted on a turbulent swirl flame phantom. Results showed that the TV prior yields improved reconstructions for a large range of the diffusion coefficient. Conditional statistics were employed to quantify posterior uncertainties. Numerical evaluation of BOS tomography supported its viability in the combustion imaging context.

Lastly, this chapter concludes with reconstructions of an unsteady, premixed natural gas/air flame from a Bunsen burner. Three iterations of the TV prior were conducted to generate accurate instantaneous 3D estimates of the flame's refractive index field, used to infer the peak temperature. Such reconstructions reveal the evolution of turbulent structures in 3D and BOS tomography can provide quantitative data for benchmarking simulations. Benchmarking data will be obtained in future experiments by thermometry or post-processing the simulation to obtain a refractive index field.

Chapter Seven
Progress and Outlook for Bayesian Gas-Phase Tomography

Modelling turbulent phenomena, simulating combustion, and monitoring emissions are scientifically interesting tasks that play a critical role in major social challenges. Turbulence consists in multiscale motion in which energy is dissipated from large coherent structures to smaller and smaller swirls and vortices, ultimately exhausted by viscous forces at the molecular level. Continuum models of fluid flow require a dense computational grid, impractical in application-driven scenarios, or semi-empirical closure that approximates subgrid behaviour. Spatially-resolved measurements of turbulence are needed in the latter case in order to observe phenomena, develop models, and identify coefficients. Combustion further complicates matters since turbulent transport occurs at length- and time-scales that are common to chemical kinetics and radiative transport, thereby giving rise to non-linear interactions. Three-dimensional temperature and concentration data are used to validate flame simulations. Simulations are employed to engineer efficient burners and predict the combustion attributes of alternative fuels. Finally, emissions from oil and gas facilities, landfills, and industrial plants contribute to long-term climate risks and can cause respiratory morbidity, cancer, and other ailments. Quantitative gas diagnostics are increasingly necessary to inform climate models and devise and enforce emissions mitigation strategies.

Each of these areas demonstrates a clear need for diagnostics that deliver robust, spatially-resolved measurements of a gas-phase target. Numerous tools have been developed to serve this purpose, including LOS absorption spectroscopy, LIF, and gas-correlation imaging, among others. The present work concerns gas-phase tomography, a fast-growing class of imaging technologies

that can provide accurate estimates of a gas distribution when optical access is limited, and can resolve intricate turbulent structures in open laboratory conditions. Gas-phase tomography transforms measurements of light, made around the periphery of a domain, into a 2D or 3D image of key quantities, including the concentration of a target species, temperature, and pressure. The measurement model is derived from the RTE, in the case of CST, and the ray equation of geometric optics, for BOS tomography. CST is further divided into absorption and emission scenarios and the governing equations for all of these modalities—absorption and emission CST as well as BOS tomography—simplifies to a Fredholm IFK. Tomographic imaging, or *reconstruction*, is conducted by inverting the coupled IFKs for a series of measurements to estimate the unknown distribution with a finite representation of the flow field, called a *basis*. The inversion is necessarily ill-posed for one of two reasons: either the measurement array is too sparse to determine a unique estimate or the damping action of the IFK amplifies noise in inversion, giving rise to non-physical artifacts. Gas-phase tomography is thus an ill-posed inverse problem and requires supplemental information to generate physically-plausible estimates.

Statistical inversion uses Bayes' equation to incorporate prior information into inverse problems like tomography. This dissertation applies the Bayesian framework to gas-phase tomography, drawing on the implications of Bayes' equation to construct a sophisticated prior for a turbulent target, improve the design of limited-data CST systems, and select an optimal discretization scheme. Following these developments, two novel applications of gas-phase tomography were carried out in the Bayesian framework: a broadband form of absorption CST, for emissions monitoring; and the first application of BOS tomography to flame imaging. This chapter reviews the advances in Bayesian tomography, presented in Chapters Three and Four, and novel tomography experiments, reported in Chapters Five and Six. Finally, the dissertation concludes with some remarks on the implications of the Bayesian framework for tomography and avenues for future research.

7.1 Developments in the Bayesian Framework for CST

The Bayesian approach to reconstruction conceives measurements, quantities of interest, and physical parameters as random variables, characterized by a probability density function. The pdf represents one's state of knowledge about a variable, accounting for both the variation intrinsic to a process—e.g., random fluctuations in a turbulent quantity—and uncertainties that arise from the inference. A likelihood pdf is constructed to quantify the chance of observing a data vector for an

arbitrary target, based on attributes of the noise and model errors; the prior quantifies the relative likelihood of different distributions, based on what was known before measurement. The latter function reflects expectations about a flow field, typically derived from transport equations or a simulation. Bayes' equation relates the likelihood and prior pdfs to a posterior distribution, and statistical inversion amounts to working out the posterior pdf for a given data vector. Reconstruction culminates in calculating a point estimate to represent the posterior. Estimates can take several forms but reconstructions are typically defined to be the MAP estimate, which is the most probable distribution of gas given the observed data, subject to noise, modelling errors, and prior assumptions about the target. Tomographic imaging is carried out following one or more measurements and the specification of a likelihood and prior.

Measurements and physical parameters in Bayesian tomography are frequently modelled as joint-normal random variables. Per Chapters Two and Three, the joint-normal form is a good approximation to the true distributions. Given a joint-normal likelihood and prior, the posterior is also joint-normal. Several important developments in Bayesian tomography follow from this common functional form. Most fundamentally, arguments in the joint-normal likelihood, prior, and posterior pdf reside in an exponential function; MAP estimation is formulated accordingly as the least squares solution to a linear system. In addition, explicit representation of the posterior enables estimation of a summary statistic, used to improve the arrangement of optical paths, as well as the evidence (i.e., the probability density of a data vector), which is the key quantity in model selection. Chapter Three justifies the joint-normal prior pdf and develops priors for turbulent free-shear flows in limited-data and full-rank CST. Chapter Four derives Bayesian objective functions for DOE in CST as well as a model likelihood, later used for model selection. These contributions are reviewed, below.

7.1.1 Turbulence modelling and advanced priors

Constructing an appropriate prior pdf is a key task in Bayesian tomography. Reconstruction accuracy depends on the correspondence between true variation in the measurement domain and the functional form of the prior. Turbulent jets and flames are common targets in CST and, ideally, the prior should encode the distribution of fluctuations present in the flow field. Joint-normal pdfs are often employed to model turbulent quantities in CST but this choice is rarely questioned. Chapter Three includes an analysis of turbulent fluctuations and argues that they are adequately-modelled as Gaussian. It was noted that reconstructions are represented in terms of a finite basis

that effectively averages fluctuations over a region of space, thereby suppressing non-Gaussianity; and non-Gaussian features are most prevalent in the tails, which have a limited effect on MAP estimates. Theoretical arguments for Gaussianity were supported with experimental results, showing scalar fluctuations in turbulent flows. Finally, epistemic uncertainty about the flow conditions and effect of projection onto the basis further justifies the choice of a high-entropy prior, especially since it leads to an analytically-tractable posterior.

The joint-normal pdf includes two arguments: a mean vector and covariance matrix. Typically, minimal assumptions about the flow field are used to derive these quantities, as in first-order Tikhonov regularization. However, flow-specific information about the mean and covariance can be extracted from the measurements, subject to constraints that are motivated by the governing equations. Towards this end, scale profiles were derived for the first two moments of the pdf of a passive scalar in a round jet. The first profile operates as a subspace restriction during reconstruction of the mean concentration. A novel expression was presented for the second function, in which the variance profile is given in terms of the mean. The covariance matrix consists of the spatial distribution of variance combined with a spatial autocorrelation function. Separate techniques were developed to estimate this matrix for limited-data and full-rank CST.

Limited-data covariance estimation begins with reconstruction of the mean distribution from an average measurement vector. If the target is a free-shear jet, or combination of jets, the mean estimate is found in terms of the analytical scale function. Otherwise, the mean is reconstructed with a smoothness prior, given that advection-diffusion transport should yield a spatially-smooth average field. Once the mean is determined, the distribution of variance is calculated using the established relationship between the first two moments of the concentration pdf. Square-exponential correlation structure is added to the variance and the resulting matrix is scaled to match the variance observed in the measurements.

Absent measurement noise and model error, full-rank covariance data can be directly obtained by inversion of the ray-sum matrix. Corruption by noise is unavoidable, of course, and individual measurements are always affected by noise. But the influence of unbiased noise diminishes in average quantities—including the observed measurement covariance—as the measurement duration is increased. The effects of model error, and the interactions between model error and noise, are determined using an approximation error method. Approximation errors are found by reconstructing the flow with a smoothing prior, projecting estimates onto a high-order basis, and

computing the expected difference between ideal measurements over a reconstruction and simulated "ground truth" measurement over the projected estimate. Interaction models obtained from this procedure stabilize direct estimates of the target covariance. Finally, the correlation structure is replaced with a square-exponential correlation function and the covariance matrix is scaled by the observed measurement covariance, as in the limited-data method.

Numerical tests were conducted to verify the performance of covariance estimation for tomography of turbulent flows. Phantoms were obtained by LES of two targets. The first flow was a round, turbulent, free-shear CH_4 jet; the second was a turbulent CH_4/air flame in hot coflow. Reconstructions computed with a data-based covariance estimate were consistently more accurate than first-order Tikhonov estimates. Results reported in Chapter Three strongly support the Bayesian interpretation of tomographic imaging. Selecting prior information that reflects genuine variation in the flow field improves the accuracy of reconstructions. Furthermore, the covariance estimation techniques in Chapter Three are applicable to a range of industrially-relevant targets and compatible with real-time imaging algorithms for limited-data gas-phase tomography.

7.1.2 Design of limited-data arrays

The amount of information that can be extracted from CST data is a strong function of the arrangement of optical paths in the domain. Physical enclosures that restrict optical access and the rise of inexpensive opto-electronic components motivate and enable the use of irregular beam arrays in CST. Recent research has focused on developing techniques to optimize beam positions in limited-data systems. Prior DOE work applied to CST was carried out in a deterministic framework, without attention to prior expectations about the flow field. The Bayesian approach to inverse analysis naturally lends itself to the design of measurement systems, with explicit reference to prior knowledge about the target. Bayesian DOE is a statistical approach to experimental design in which the information extracted from the data is maximized, subject to an analysis of measurement uncertainties.

Deterministic methods to optimize the array were universally motivated by the mathematics of reconstruction, though not all followed a strict derivation. For instance, the sinogram coordinate criterion was initially proposed as a qualitative metric. "Uniform coverage" of the sinogram space by the beam coordinates was recommended, based on a Fourier analysis of back projection. Later testing of this method found no correspondence between the spread of coordinates and accuracy of reconstructions. Three subsequent metrics were shown to predict the performance of CST

systems: the resolution matrix, grid weight, and collinearity objective functions. Respectively, these relate to the minimization of regularization error, maximum coverage of the measurement plane, and minimum overlap between components of the ray-sum matrix. However, none of the deterministic techniques included specific information about the flow field, nor were they related to statistical properties of the reconstructions.

Bayesian reconstruction with joint-normal pdfs entails an analytical expression for the posterior covariance matrix, which is a function of the measurement array and prior covariance. As noted in Chapter Four, measurement vectors are not required to compute this estimate. The posterior covariance describes the expected variance and covariance of reconstructed parameters due to inherent variation, encoded in the prior, and uncertainties that arise from the arrangement of optical paths. In a design context, expectations about the flow field are fixed and differences between the posterior covariance matrix for candidate arrays stem from interactions between the ray-sum matrix and prior. However, the posterior covariance can be difficult to interpret due to its high-dimension and complex correlation structures. Summary statistics have been derived to relate the posterior covariance matrix to average reconstruction outcomes. In particular, the A-optimal function minimizes the total variance of reconstructions and the D-optimal function minimizes posterior uncertainty, accounting for correlated parameters. Bayesian objective functions for DOE are based on a summary measure of the posterior covariance matrix. Limited-data CST arrays are constructed to minimize the A- or D-optimal function, depending on the rank of the prior.

One significant insight presented in Chapter Four concerns the functional similarity between Bayesian and deterministic objective functions. Deterministic functions implicitly rely upon minimal assumptions about the flow field. These assumptions were encoded in the Bayesian prior to compare the frameworks. The resolution norm was derived for Tikhonov regularization, which has a direct analog in Bayesian CST, and the combination of a zero-mean vector and a diffuse IID covariance matrix corresponds to the assumptions that underpin the grid weight and collinearity functions. Generating a posterior covariance matrix with these priors revealed substantial correspondence between the Bayesian and deterministic metrics. (Though Chapter Four notes the lack of a direct relationship between the grid weight or collinearity function and the accuracy of reconstructions.) This connection suggests that, absent information about a specific flow, both frameworks should achieve similar performance. However, some information about the distribution of variance in a given scenario is almost always known; the Bayesian function

incorporates this knowledge in a statistically-robust manner. Bayesian design metrics imply that accurate prior information should improve the accuracy of reconstructions and yield a superior measurement system when used to design an experiment.

Phantoms sets from the round jet in Chapter Three and an isotropic Gaussian random field were used to evaluate the DOE functions. Three types of phantoms were constructed: the unmodified jet; an affine transformation of the jet, scaled by 50% and repositioned in the domain; and the isotropic (or *uniform*) field. Two optimization scenarios were considered, having structured projections (fan and parallel) and unstructured arrays; a genetic algorithm was designed to explore a large space of beam arrangements in the latter case. Uniform tests effectively served as a control on the prior since the minimal a priori information implicit in the deterministic functions was accurate for these phantoms.

Bayesian reconstruction with a flow-specific prior produced estimates that were consistently more accurate than the Tikhonov reconstructions, having a smaller mean and range of errors. The deterministic functions performed well for the structured projections (excluding the collinearity metric), though this was in part coincidental, due to the position and size of the target in the domain and grid resolution. Performance of the deterministic functions was worst for the small, shifted jet, while the Bayesian function captured unique, flow-specific trends in each test. Results for the unstructured beam arrangements evidenced the strong connection between the Bayesian objective function and reconstruction statistics, whereas the deterministic functions performed poorly in this setting. Beams arrays that minimized the Bayesian function were intuitively distributed about regions of high variance for the jets and uniformly-distributed for the uniform phantoms. The latter arrangement was similar to that selected by the resolution matrix function, confirming the analytical comparison of the frameworks. From these tests it can be concluded that a Bayesian approach to DOE will properly adapt a measurement array to the prior and accurate priors can be used to optimize the design of CST systems.

7.1.3 Model selection in gas-phase tomography

At the point of reconstruction, beam positions are fixed but the discretization scheme, measurement model, and prior are not. Together, these elements constitute a model of the flow field and each plays a major role in the accuracy of CST estimates. The choice of basis and prior used to reconstruct a flow are often heuristic in nature or based on a simple simulation of the gas. However, measurements can reveal unexpected features in the target and a mathematically-

rigorous approach to model selection—one which incorporates the data—is desirable in CST. Bayesian tomography is implicitly conditioned on a model of the flow; Bayesian model comparison makes this contingency explicit and derives an expression for the odds that a data set was produced by one model over an alternative model. Chapter Four develops Bayesian model comparison for gas-phase tomography for the first time and reports the results of a numerical experiment demonstrating the technique.

Numerous discretization schemes are available to CST practitioners. The most obvious degree of freedom is the grid resolution; the functional form of the basis is also open to selection. Traditionally, square pixels and cubic voxels are employed for CST; whereas general finite element schemes, with triangular or quadrilateral elements (prisms in 3D), are more common in other forms of tomography. Chapter Four employs the FEM with triangular elements for CST using piecewise constant, linear, and quadratic modes of interpolation. The number of nodes in an element depends on the interpolation scheme—hence, the same mesh will have a different number of basis functions for different modes of interpolation. Triangle-element meshes across a range of resolutions are easily adapted to oddly-shaped domains and this flexibility enables multiple forms of comparison, ideal for testing model selection in CST.

Bayesian model comparison treats the model as an unknown quantity, analogous to the gas distribution, measurement vector, and nuisance parameters. Statistical inversion is applied to the model. It is not normally possible to construct a proper prior pdf on the model space. Absent a specific model prior, it is appropriate to adopt a uniform pdf over the set of candidate models, leading to a maximum likelihood formulation of the model inference. The ratio of model likelihoods for a data set, called a *Bayes factor*, gives the odds that the first model produced the data relative to the second. This procedure accounts for the complicated trade-offs between the ability of high-resolution bases to mimic the data and the uncertainties associated with additional nodes. By hypothesis, models that are likely to have produced a set of data will feature parameters and measurement equations that correspond to true variation in the system. The use of such models should lead to a more reliable inference. Model likelihoods are implicit in the evidence of the Bayesian formulation of CST and can be explicitly calculated due to the joint-normal pdfs.

The model likelihood is typically cast in logarithmic scale because of the numerical instabilities associated with calculating a Bayes factor. In addition to this computational advantage, the analytical expression of the log-model likelihood suggests a useful decomposition. The log-

model likelihood comprises four terms: a measurement credence, data fit, and prior fit, and system constant (which cancels out in the Bayes factor). The credence describes the information that can be extracted from a measurement and the fit terms quantify the correspondence between MAP estimates and the data and prior. These terms can supply CST practitioners with useful information about why some models outperform others.

Chapter Four concludes with a CST simulation to test model selection, designed to resemble a recent experiment featuring a very-limited set of measurements (with eight lines-of-sight), large number of basis functions (over 2,000), and triangle elements with linear interpolation. LES data was obtained for the distribution of NH_3 in an exhaust flow, downstream from a urea injector and static mixer (part of a SCR system). Gas distributions were highly turbulent and the numerical model was verified with experimental measurements. Components of the log-model likelihood were calculated for all three modes of interpolation, meshes of increasing resolution, and priors with different mean vectors and covariance matrices. There was a strong relationship between the log-model likelihood and average structural similarity index for the reconstructions; trends in the component terms also matched key aspects of model performance. As with the advanced prior for turbulent flows in Chapter Three, and the DOE procedure in Chapter Four, model selection is a straightforward derivative of the Bayesian formulation of CST. Results of the model comparison tests further evidence the versatility and benefits of the Bayesian approach to inverse analysis applied to gas-phase tomography.

7.2 Novel Applications of Gas-Phase Tomography

Two experiments were conducted to expand the range of viable uses for gas-phase tomography. Specifically, techniques were developed to address the demand for low-cost, stand-off emissions diagnostics and instantaneous 3D flame data. First, a transfer function was devised to linearize broadband open path absorption measurements for CST, using a spectroscopic model of well-mixed emissions at atmospheric conditions. Subsequently, the measurement model for BOS tomography was improved and the technique was applied to a combustion imaging scenario for the first time. Both experiments were carried out in the Bayesian framework, drawing on the advances from Chapters Two through Four.

7.2.1 Broadband absorption CST

Industrial hydrocarbon emissions cause adverse health and environmental effects and have hence drawn considerable interest from regulatory bodies. Ground source emissions quickly equilibrate

to atmospheric conditions and frequently feature well-mixed components. Moreover, such flows are dispersive and highly transient, making them difficult to characterize by point-concentration surveys. These conditions are ideal for CST diagnostics but the measurement equations for absorption CST are formulated for monochromatic intensity data. Monochromatic measurements either require a laser source or a spectrally-resolved detector, posing numerous cost and/or safety concerns at industrial sites. By comparison, broadband IR spectroscopy is conducted with low-cost, commercially-available devices—often intrinsically safe—motivating the development of a measurement model for broadband absorption CST.

Radiation is absorbed and emitted by molecules as part of their transition between energy states. IR lines involve coupled transitions between rotational and vibrational modes of internal energy. Atomic arrangements determine which states may be occupied by a molecule and which transitions are valid. The shape and intensity of IR lines follow regular patterns, forming bands and overtone bands with distinct branches. These features are described by an absorption coefficient, defined in terms of a molecule's quantum mechanical properties. Chemically-similar molecules have co-located bands. For instance, stretching of the H-C bond gives rise to a hydrocarbon absorption band at 3.4 μm, which is of particular interest in broadband spectroscopy and optical leak detection. As a result, while common targets such as CH_4 are transparent in the visible spectrum, they are often observable with mid-IR radiation.

Broadband transmittances are defined as the ratio of the transmitted spectral intensity, integrated over the range of the detector, measured with and without the absorbing species. The intensity at each wavelength is the source intensity attenuated by Beer-Lambert-type absorption, which depends on the absorption coefficient described above. Chapter Five shows how the path-integrated absorption coefficient for well-mixed atmospheric emissions can be decomposed into a path-integrated volume fraction and spectral shape function. Substituting this expression into the transmittance equation relates spectrally-convolved broadband data to an integral over the local emissions burden—isolated from the spectral shape. The integral is a Fredholm IFK, identical in form to the measurement equations for monochromatic absorption tomography. A transfer function relates broadband data to the IFK, which is the measurement equation for broadband absorption CST. Spectral shape functions are computed with a line-by-line model for simple molecules (and combinations thereof) or derived from an empirical absorbance profile for complex

targets. Shape functions are combined with the filter bounds to determine a transfer function, which may then be deployed to linearize transmittance measurements.

Broadband absorption CST was verified with a laboratory-scale emissions detection experiment. A series of open path detectors were constructed, with a collimated thermal source and broadband detector, equipped with a mid-IR bandpass filter. Transfer functions for CH_4, C_2H_4 and C_3H_8 were benchmarked with absorption measurements through a gas cell, filled with controlled mixtures of the target species. Bounds for a box model of the filter were determined by non-linear regression and confirmed with an FTIR reflectance measurement. A plume of C_3H_8, perturbed by advection, was imaged with a 35-path array; point-concentration measurements for validation were made with a FID.

Chapter Five concludes with a Bayesian analysis of posterior uncertainties in the reconstruction. An estimate of the posterior covariance matrix for the tomographic image was computed, along with standard errors for the FID data. The reconstructed C_3H_8 field was in agreement with the FID measurements. Uncertainty in the point-concentration data was large, due to integral scale fluctuations in the target and the spatial uncertainty associated with extrapolation. By comparison, broadband absorption CST is based on spatially-integrated data, recorded over a long interval, which mitigates the primary errors that accompany point-based emissions surveys. Broadband absorption CST was shown to be a promising technique for low-cost quantitative emissions detection.

7.2.2 BOS tomography for combustion imaging

Benchmarking procedures are required to build trust in numerical models of combustion. High-resolution, high-frequency 2D data for validation is measured with laser diagnostics (often tracer LIF); but turbulent combustion is inherently 3D and measurements of flame structures and key combustion scalars—especially temperature—remain elusive. Recently, precision optics have been combined with a modulated laser source to obtain 3D temperature fields by volumetric LIF. However, this approach requires an intricate, expensive, and relatively immobile apparatus. Schlieren imaging is compatible with tomographic reconstruction and can resolve temperature fields through post-processing. Developments in BOS imaging have enabled schlieren-type tomography through the use of simple, low-cost devices. Pictures from commercial cameras are combined with a computer vision algorithm to extract deflections and reconstruct the refractive index field, which may then be used to infer the distribution of temperature or density in a fluid.

Chapter Six reports the first use of BOS tomography in the combustion context, setting the stage for low-cost 3D flame thermometry.

Background-oriented schlieren imaging employs pictures of a textured background, taken with and without the target, to determine the deflection of light by refraction in the probe volume. Deflections are related to refractive index gradients by the ray equation of geometric optics, which simplifies into a Fredholm IFK. Coupled IFKs form a tomographic operator in the same manner as absorption and emission CST; the optical density field is computed either indirectly, by conducting a Poisson integration over reconstructed gradient fields, or directly, by including gradient operators in the measurement model. Deflection sensing operates by image correlation or the method of optical flow. Horn-Schunck optical flow was chosen for this work; the technique is derived from a Taylor expansion of the deflections, assuming a small magnitude, and closed by integration over the image to regularize the field. Background planes for BOS tomography should fill the image and textured patterns are thus printed on large posters. Cameras outnumber the background planes and, as a result, most cameras face their target poster at an angle. Due to this offset, deflections contain a component that is orthogonal to the poster (realized as a difference in travel time). Chapter Six introduces a projection matrix that corrects for this effect such that the operator only describes deflection components that can be observed in the background plane.

Reconstructing the refractive index field from deflection data is ill-posed and requires supplemental information. The Bayesian framework for gas-phase tomography was applied in the BOS setting, using smoothness (Tikhonov) and TV priors. TV regularization promotes smooth regions, similar to the Tikhonov prior, but the TV norm also permits sharp discontinuities between distinct regions. Turbulent combustion features a wrinkled flame front and scalar fields exhibit large gradients about this region, suggesting the suitability of a TV prior. Computation of the TV norm is non-linear so an iterative approximation was adapted for the BOS operator, which constitutes the first use of TV regularization in BOS tomography. MAP estimates for both priors were computed with a SIRT routine to avoid explicit representation of the inverse operator.

Performance of the projection matrix and priors was assessed by simulating the BOS diagnostic. Two refractive index phantoms were developed, consisting of a Gaussian ball of hot air and a highly-turbulent swirl flame from a LES. Index of refraction fields were calculated from the Gladstone-Dale relation; and linear and non-linear ray-tracing was conducted to determine the ground truth deflections. The projection matrix reduced model errors by up to 63% by eliminating

unobservable deflection components. Synthetic images from a 12-camera system were used to evaluate the reconstruction procedure. Deflections produced by the flame phantom were inferred with Horn-Schunck optical flow and reconstructed using the Tikhonov prior, followed by three iterations of the TV prior. Five grid resolutions were tested—with 15^3 to 75^3 voxels—using a large range of smoothness and diffusion parameters. Reconstruction accuracy was highest following three iterations of the TV prior with the 75^3-voxel grid. An analysis of the posterior joint-statistics was conducted in order to compare best estimates of the refractive index to ground truth values. Reconstructions of the phantom by BOS tomography accurately captured structures in the flame and could be used to assess evolution of the reacting zone.

Finally, a flame-imaging experiment was performed to demonstrate the potential of BOS tomography as a combustion diagnostic. The target was an unsteady premixed natural gas/air flame from a Bunsen burner, simultaneously imaged by a 23-camera array. Radiative emission from the flame was minimal compared to the intense illumination of the speckle dot posters. The aperture size was toggled between two settings to test the influence of the bokeh effect on reconstructions, caused by thicker beams in the probe volume. Instantaneous and mean distributions were estimated using three iterations of the TV prior. Chemiluminescence tomography and a LES were conducted to verify the mean refractive index field. Bunsen flame structures imaged by the BOS system were in good agreement with the emission field and LES. Moreover, estimates of the ambient and peak temperatures—300 and 2,100 K, respectively—were calculated from the reconstruction using the Gladstone-Dale relation. Temperature estimates were in-line with expected values for the laboratory air and operating conditions of the Bunsen burner.

7.3 Future Research on Gas-Phase Tomography

Researchers' interest in gas-phase tomography has increased since the advent of laser-based gas diagnostics in the 1970s, with a marked inflection in the mid-2000s and sustained growth since then. The cost of lasers, lenses, cameras, and computers dramatically decreased over this period, and the demand for rich data sets that describe internal flow structures rose, thanks to experiments in combustion, environmental monitoring, and basic research. These trends are expected to continue over the coming decades, ensuring future developments in CST technology, and an increasing range of applications. Notable recent progress includes the administration of large-scale tomographic surveys of hydrocarbon emissions, small-scale measurements of intricate flame dynamics, and real-time imaging of engine exhaust for on-line feedback and control purposes.

Cutting-edge demonstrations such as these are sensitive to the accuracy and precision of estimates and are therefore ideally-suited to Bayesian methods for gas-phase tomography.

This section focuses on two specific avenues for CST research: a two-step reconstruction procedure for hyperspectral data; and high-precision flame thermometry using BOS tomography. Both of which represent a natural progression of the work described in this thesis.

7.3.1 Two-step hyperspectral CST with linear reconstruction

Hyperspectral data comprise quasi-instantaneous, spectrally-resolved signals for several lines-of-sight, measured by direct absorption or wavelength modulation spectroscopy. This data is used to reconstruct multiple parameters—usually the temperature and concentration of a target such as water vapour or CO_2. Parameter estimates are obtained by non-linear regression of the hyperspectral data. The measurement model calculates the absorption coefficient at each pixel for a pair of temperature and concentration parameters and then takes ray-sums across the local spectra. Standard minimization algorithms are employed to identify the temperature and concentration distributions that minimize the residual. In principle, spectral information can supplement spatial information, decreasing the lines-of-sight needed to obtain a quality image of the flow field. However, non-linear hyperspectral reconstruction is computationally expensive, which limits the achievable resolution. For instance, 8×8 and 10×10 pixel grids are common, even for systems that have several dozen optical paths.

This thesis amply demonstrates that the joint-normal form of Bayesian CST can achieve accurate reconstructions using a large number of basis functions despite limited measurement information. Hyperspectral data can be reconstructed by the linear method for each wavenumber, independently, producing local spectra for a dense array of pixels. Following linear reconstruction, a spectroscopic regression could be conducted on a pixel-by-pixel basis. Each regression would minimize the residual between the local spectra—i.e., all of the reconstructed wavenumbers at the current pixel—and the modelled absorption coefficient, in terms of the temperature and partial pressure of one or more species. Wavenumber-specific priors could potentially be developed to exploit the unique spectral signatures of multiple targets and posterior uncertainties could be calculated to incorporate additional information into the spectroscopic inference.

The two-step technique for hyperspectral tomography relocates the spectroscopic model to a post-processing stage, thereby preserving the linear form of reconstruction. As a result, high-resolution reconstructions can be generated without much computational effort. Moreover,

additional parameters can be calculated with the spectroscopic model at minimal cost since the local regression is overdetermined. (That is, there are only a handful of parameters—temperature and a partial pressure for each species—while both DAS and WMS can resolve many lines over a short interval.) These advantages suggest that hyperspectral CST with a two-step reconstruction is a promising alternative to non-linear methods.

7.3.2 Flame thermometry by BOS tomography

Background-oriented schlieren tomography serves as a simple, economical diagnostic for measuring instantaneous 3D flow structures with an array of cameras. The technique has been employed to resolve the temperature field of heated gas jets and this work used the mean reconstruction of an unsteady Bunsen flame to estimate its peak temperature. However, there is a non-linear relationship between optical density and temperature and the conversion becomes more susceptible to small artifacts at higher temperatures. (An optical density of one indicates an infinite temperature such that a constant level of noise implies a greater temperature uncertainty near one than at ambient conditions.) High-temperature applications such as flame imaging therefore require a precise reconstruction to generate instantaneous estimates of temperature and density.

The primary source of error observed in the BOS system was the optical flow procedure. Optical flow is an advanced inverse problem in itself and further attention to this step could improve the accuracy of deflection data, improving the quality of reconstructions, in turn. Research on optical flow algorithms in the computer vision literature has employed convolutional neural nets (a deep learning technique) to obtain accurate and precise results. This approach poses simulation and data-management challenges for BOS tomography. A large library of ground truth deflections would be needed for various flow and combustion fields. However, the principle is straightforward and existing techniques could be employed to improve deflection sensing. Moreover, given a library of deflection data, neural nets could be trained for each camera using the reference images from an experiment. The present work employs a simple implementation of an established algorithm for optical flow. Adopting modern methods represents low-hanging fruit for future research.

References

[1] Markatos, N. C., 1986, "The Mathematical Modelling of Turbulent Flows," Appl. Math. Model., **10**(3), pp. 190–220.

[2] Pope, S. B., 2001, "Turbulent Flows."

[3] Tennekes, H., Lumley, J. L., Lumley, J. L., and others, 1972, *A First Course in Turbulence*, MIT press.

[4] Pope, S. B., 1994, "Lagrangian PDF Methods for Turbulent Flows," Annu. Rev. Fluid Mech., **26**(1), pp. 23–63.

[5] Batten, P., Goldberg, U., and Chakravarthy, S., 2004, "Interfacing Statistical Turbulence Closures with Large-Eddy Simulation," AIAA J., **42**(3), pp. 485–492.

[6] Adrian, R. J., 1979, "Conditional Eddies in Isotropic Turbulence," Phys. Fluids, **22**(11), pp. 2065–2070.

[7] Heath, J., 2016, "Caring about Climate Change Implies Caring about Economic Growth."

[8] Nordhaus, W. D., 2007, "A Review of the Stern Review on the Economics of Climate Change," J. Econ. Lit., **45**(3), pp. 686–702.

[9] Stern, D. I., and others, 2004, "Economic Growth and Energy," Encycl. Energy, **2**(00147), pp. 35–51.

[10] Li, X., Zheng, L., Qiu, H., and Chen, J., 2013, "Experimental Investigations on the Power Extraction of a Turbine Driven by a Pulse Detonation Combustor," Chinese J. Aeronaut., **26**(6), pp. 1353–1359.

[11] Watanabe, H., and Otaka, M., 2006, "Numerical Simulation of Coal Gasification in Entrained Flow Coal Gasifier," Fuel, **85**(12–13), pp. 1935–1943.

[12] Arcoumanis, C., Bae, C., Crookes, R., and Kinoshita, E., 2008, "The Potential of Di-Methyl Ether (DME) as an Alternative Fuel for Compression-Ignition Engines: A Review," Fuel, **87**(7), pp. 1014–1030.

[13] Bilger, R. W., Pope, S. B., Bray, K. N. C., and Driscoll, J. F., 2005, "Paradigms in Turbulent Combustion Research," Proc. Combust. Inst., **30**(1), pp. 21–42.

[14] Pope, S. B., 1991, "Computations of Turbulent Combustion: Progress and Challenges," *Symposium (International) on Combustion*, pp. 591–612.

[15] Pope, S. B., 1997, "Turbulence Combustion Modeling: Fluctuations and Chemistry," Adv. Comput. Anal. Combust. Moscow ENAS, pp. 310–320.

[16] Coelho, P. J., 2007, "Numerical Simulation of the Interaction between Turbulence and Radiation in Reactive Flows," Prog. Energy Combust. Sci., **33**(4), pp. 311–383.

[17] Kempf, A. M., 2008, "LES Validation from Experiments," Flow, Turbul. Combust., **80**(3), pp. 351–373.

[18] Hewitt, C. N., 2001, "The Atmospheric Chemistry of Sulphur and Nitrogen in Power Station Plumes," Atmos. Environ., **35**(7), pp. 1155–1170.

[19] Wright, R. F., and Schindler, D. W., 1995, "Interaction of Acid Rain and Global Changes: Effects on Terrestrial and Aquatic Ecosystems," Water. Air. Soil Pollut., **85**(1), pp. 89–99.

[20] Civerolo, K. L., Brankov, E., Rao, S. T., and Zurbenko, I. G., 2001, "Assessing the Impact of the Acid Deposition Control Program," Atmos. Environ., **35**(24), pp. 4135–4148.

[21] Myhre, G., Shindell, D., Bréon, F.-M., Collins, W., Fuglestvedt, J., Huang, J., Koch, D., Lamarque, J.-F., Lee, D., Mendoza, B., and others, 2013, "Anthropogenic and Natural Radiative Forcing," Clim. Chang., **423**, pp. 658–740.

[22] US Environmental Protection Agency, 2017, "Oil and Natural Gas Sector: Emission Standards for New, Reconstructed, and Modified Sources: Stay of Certain Requirements."

[23] Eckbreth, A. C., 1996, *Laser Diagnostics for Combustion Temperature and Species*, CRC Press.

[24] McKeon, B. J., Li, J., Jiang, W., Morrison, J. F., and Smits, A. J., 2003, "Pitot Probe Corrections in Fully Developed Turbulent Pipe Flow," Meas. Sci. Technol., **14**(8), p. 1449.

[25] Buttafuoco, G., Tallarico, A., and Falcone, G., 2007, "Mapping Soil Gas Radon Concentration: A Comparative Study of Geostatistical Methods," Environ. Monit. Assess., **131**(1–3), pp. 135–151.

[26] Mackie, K. R., and Cooper, C. D., 2009, "Landfill Gas Emission Prediction Using Voronoi Diagrams and Importance Sampling," Environ. Model. Softw., **24**(10), pp. 1223–1232.

[27] Smith, S., Vass, A., Karpushko, F., Hardaway, H., and Crowder, J. G., 2001, "The Prospects of LEDs, Diode Detectors and Negative Luminescence in Infrared Sensing of Gases and Spectroscopy," Philos. Trans. R. Soc. London A Math. Phys. Eng. Sci., **359**(1780), pp. 621–634.

[28] Tsang, R., 2017, "Development and Characterization of Infrared Broadband Open-Path Hydrocarbon Detectors for Chemical Species Tomography," University of Waterloo.

[29] Platt, U., and Stutz, J., 2008, "Differential Absorption Spectroscopy," *Differential Optical Absorption Spectroscopy*, Springer, pp. 135–174.

[30] Weibring, P., Edner, H., Svanberg, S., Cecchi, G., Pantani, L., Ferrara, R., and Caltabiano, T., 1998, "Monitoring of Volcanic Sulphur Dioxide Emissions Using Differential Absorption Lidar (DIAL), Differential Optical Absorption Spectroscopy (DOAS), and Correlation Spectroscopy (COSPEC)," Appl. Phys. B Lasers Opt., **67**(4), pp. 419–426.

[31] Mount, G. H., Rumburg, B., Havig, J., Lamb, B., Westberg, H., Yonge, D., Johnson, K., and Kincaid, R., 2002, "Measurement of Atmospheric Ammonia at a Dairy Using Differential Optical Absorption Spectroscopy in the Mid-Ultraviolet," Atmos. Environ., **36**(11), pp. 1799–1810.

[32] Lee, C., Choi, Y. J., Jung, J. S., Lee, J. S., Kim, K. H., and Kim, Y. J., 2005, "Measurement of Atmospheric Monoaromatic Hydrocarbons Using Differential Optical Absorption Spectroscopy: Comparison with on-Line Gas Chromatography Measurements in Urban Air," Atmos. Environ., **39**(12), pp. 2225–2234.

[33] Dooly, G., Fitzpatrick, C., and Lewis, E., 2008, "Deep UV Based DOAS System for the Monitoring of Nitric Oxide Using Ratiometric Separation Techniques," Sensors Actuators B Chem., **134**(1), pp. 317–323.

[34] Cheng, A. Y. S., and Chan, M. H., 2004, "Acousto-Optic Differential Optical Absorption Spectroscopy for Atmospheric Measurement of Nitrogen Dioxide in Hong Kong," Appl. Spectrosc., **58**(12), pp. 1462–1468.

[35] Chambers, A., Strosher, M., Wootton, T., Moncrieff, J., and McCready, P., 2006, "DIAL Measurements of Fugitive Emissions from Natural Gas Plants and the Comparison with

Emission Factor Estimates," *15th Annual Emission Inventory Conference, US Environmental Protection Agency New Orleans*, pp. 15–18.

[36] Frisch, L., 2003, "Fugitive VOC-Emissions Measured at Oil Refineries in the Province of Västra Götaland in South West Sweden."

[37] Robinson, R., Gardiner, T., Innocenti, F., Woods, P., and Coleman, M., 2011, "Infrared Differential Absorption Lidar (DIAL) Measurements of Hydrocarbon Emissions," J. Environ. Monit., **13**(8), pp. 2213–2220.

[38] Allen, M. G., 1998, "Diode Laser Absorption Sensors for Gas-Dynamic and Combustion Flows," Meas. Sci. Technol., **9**(4), p. 545.

[39] Moses, E. I., and Tang, C. L., 1977, "High-Sensitivity Laser Wavelength-Modulation Spectroscopy," Opt. Lett., **1**(4), pp. 115–117.

[40] Goldenstein, C. S., 2014, "Wavelength-Modulation Spectroscopy for Determination of Gas Properties in Hostile Environments," Stanford University.

[41] Miller, M. F., Kessler, W. J., and Allen, M. G., 1996, "Diode Laser-Based Air Mass Flux Sensor for Subsonic Aeropropulsion Inlets," Appl. Opt., **35**(24), pp. 4905–4912.

[42] Liu, X., Jeffries, J. B., Hanson, R. K., Hinckley, K. M., and Woodmansee, M. A., 2006, "Development of a Tunable Diode Laser Sensor for Measurements of Gas Turbine Exhaust Temperature," Appl. Phys. B, **82**(3), pp. 469–478.

[43] Lyle, K. H., Jeffries, J. B., and Hanson, R. K., 2007, "Diode-Laser Sensor for Air-Mass Flux 1: Design and Wind Tunnel Validation," AIAA J., **45**(9), pp. 2204–2212.

[44] Witzel, O., Klein, A., Wagner, S., Meffert, C., Schulz, C., and Ebert, V., 2012, "High-Speed Tunable Diode Laser Absorption Spectroscopy for Sampling-Free in-Cylinder Water Vapor Concentration Measurements in an Optical IC Engine," Appl. Phys. B, **109**(3), pp. 521–532.

[45] Zhou, X., Liu, X., Jeffries, J. B., and Hanson, R. K., 2005, "Selection of NIR H2O Absorption Transitions for In-Cylinder Measurement of Temperature in IC Engines," Meas. Sci. Technol., **16**(12), p. 2437.

[46] Wu, Y., Xu, W., Lei, Q., and Ma, L., 2015, "Single-Shot Volumetric Laser Induced Fluorescence (VLIF) Measurements in Turbulent Flows Seeded with Iodine," Opt. Express, **23**(26), pp. 33408–33418.

[47] Wellander, R., Richter, M., and Aldén, M., 2014, "Time-Resolved (KHz) 3D Imaging of OH PLIF in a Flame," Exp. Fluids, **55**(6), p. 1764.

[48] Li, T., Pareja, J., Becker, L., Heddrich, W., Dreizler, A., and Böhm, B., 2017, "Quasi-4D Laser Diagnostics Using an Acousto-Optic Deflector Scanning System," Appl. Phys. B, **123**(3), p. 78.

[49] Tanahashi, M., Murakami, S., Choi, G.-M., Fukuchi, Y., and Miyauchi, T., 2005, "Simultaneous CH--OH PLIF and Stereoscopic PIV Measurements of Turbulent Premixed Flames," Proc. Combust. Inst., **30**(1), pp. 1665–1672.

[50] Zhou, B., Brackmann, C., Li, Z., and Aldén, M., 2015, "Development and Application of CN PLIF for Single-Shot Imaging in Turbulent Flames," Combust. Flame, **162**(2), pp. 368–374.

[51] Lee, T., Jeffries, J. B., and Hanson, R. K., 2007, "Experimental Evaluation of Strategies for Quantitative Laser-Induced-Fluorescence Imaging of Nitric Oxide in High-Pressure Flames (1--60 Bar)," Proc. Combust. Inst., **31**(1), pp. 757–764.

[52] Michael, J. B., Venkateswaran, P., Miller, J. D., Slipchenko, M. N., Gord, J. R., Roy, S., and Meyer, T. R., 2014, "100 KHz Thousand-Frame Burst-Mode Planar Imaging in Turbulent Flames," Opt. Lett., **39**(4), pp. 739–742.

[53] Kulatilaka, W. D., Patterson, B. D., Frank, J. H., and Settersten, T. B., 2008, "Comparison of Nanosecond and Picosecond Excitation for Interference-Free Two-Photon Laser-Induced Fluorescence Detection of Atomic Hydrogen in Flames," Appl. Opt., **47**(26), pp. 4672–4683.

[54] Frank, J. H., Chen, X., Patterson, B. D., and Settersten, T. B., 2004, "Comparison of Nanosecond and Picosecond Excitation for Two-Photon Laser-Induced Fluorescence Imaging of Atomic Oxygen in Flames," Appl. Opt., **43**(12), pp. 2588–2597.

[55] Mathews, G. C., and Goldenstein, C. S., 2017, "Wavelength-Modulated Planar Laser-Induced Fluorescence for Imaging Gases," Opt. Lett., **42**(24), pp. 5278–5281.

[56] Pearman, W. F., Carter, J. C., Angel, S. M., and Chan, J. W. J., 2008, "Quantitative Measurements of CO 2 and CH 4 Using a Multipass Raman Capillary Cell," Appl. Opt., **47**(25), pp. 4627–4632.

[57] Martyshkin, D. V, Ahuja, R. C., Kudriavtsev, A., and Mirov, S. B., 2004, "Effective Suppression of Fluorescence Light in Raman Measurements Using Ultrafast Time Gated Charge Coupled Device Camera," Rev. Sci. Instrum., **75**(3), pp. 630–635.

[58] Fourguette, D. C., Zurni, R. M., and Long, M. B., 1986, "Two-Dimensional Rayleigh Thermometry in a Turbulent Nonpremixed Methane-Hydrogen Flame," Combust. Sci. Technol., **44**(5–6), pp. 307–317.

[59] Dibble, R. W., Stårner, S. H., Masri, A. R., and Barlow, R. S., 1990, "An Improved Method of Data Aquisition and Reduction for Laser Raman-Rayleigh and Fluorescence Scattering from Multispecies," Appl. Phys. B, **51**(1), pp. 39–43.

[60] Meier, W., Barlow, R. S., Chen, Y.-L., and Chen, J.-Y., 2000, "Raman/Rayleigh/LIF Measurements in a Turbulent CH4/H2/N2 Jet Diffusion Flame: Experimental Techniques and Turbulence--Chemistry Interaction," Combust. Flame, **123**(3), pp. 326–343.

[61] Roy, S., Gord, J. R., and Patnaik, A. K., 2010, "Recent Advances in Coherent Anti-Stokes Raman Scattering Spectroscopy: Fundamental Developments and Applications in Reacting Flows," Prog. Energy Combust. Sci., **36**(2), pp. 280–306.

[62] Hargather, M. J., and Settles, G. S., 2012, "A Comparison of Three Quantitative Schlieren Techniques," Opt. Lasers Eng., **50**(1), pp. 8–17.

[63] Hargather, M. J., Lawson, M. J., Settles, G. S., and Weinstein, L. M., 2011, "Seedless Velocimetry Measurements by Schlieren Image Velocimetry," AIAA J., **49**(3), pp. 611–620.

[64] Schardin, H., 1934, "Das Toeplersche Schlierenverfahren: Grundlagen Fur Seine Anwendung Und Quantitative Auswertung," VDI Forschungsh., **367**(5), pp. 1–32.

[65] Howes, W. L., 1984, "Rainbow Schlieren and Its Applications," Appl. Opt., **23**(14), pp. 2449–2460.

[66] Dalziel, S. B., Hughes, G. O., and Sutherland, B. R., 2000, "Whole-Field Density Measurements by 'Synthetic Schlieren,'" Exp. Fluids, **28**(4), pp. 322–335.

[67] Elsinga, G. E., Van Oudheusden, B. W., Scarano, F., and Watt, D. W., 2004, "Assessment and Application of Quantitative Schlieren Methods: Calibrated Color Schlieren and Background Oriented Schlieren," Exp. Fluids, **36**(2), pp. 309–325.

[68] Kolhe, P. S., and Agrawal, A. K., 2009, "Density Measurements in a Supersonic Microjet Using Miniature Rainbow Schlieren Deflectometry," AIAA J., **47**(4), pp. 830–838.

[69] Flynn, M. R., Onu, K., and Sutherland, B. R., 2003, "Internal Wave Excitation by a Vertically Oscillating Sphere," J. Fluid Mech., **494**, pp. 65–93.

[70] Li, X., and Ma, L., 2015, "Capabilities and Limitations of 3D Flame Measurements Based on Computed Tomography of Chemiluminescence," Combust. Flame, **162**(3), pp. 642–651.

[71] Karhunen, K., Seppänen, A., Lehikoinen, A., Blunt, J., Kaipio, J. P., and Monteiro, P. J. M., 2010, "Electrical Resistance Tomography for Assessment of Cracks in Concrete.," ACI Mater. J., **107**(5).

[72] McIntosh, R., Nicastro, D., and Mastronarde, D., 2005, "New Views of Cells in 3D: An Introduction to Electron Tomography," Trends Cell Biol., **15**(1), pp. 43–51.

[73] Gross, D., Liu, Y.-K., Flammia, S. T., Becker, S., and Eisert, J., 2010, "Quantum State Tomography via Compressed Sensing," Phys. Rev. Lett., **105**(15), p. 150401.

[74] Radon, J., 1986, "On the Determination of Functions from Their Integral Values along Certain Manifolds," IEEE Trans. Med. Imaging, **5**(4), pp. 170–176.

[75] Bracewell, R. N., and Riddle, Ac., 1967, "Inversion of Fan-Beam Scans in Radio Astronomy," Astrophys. J., **150**, p. 427.

[76] Ramachandran, G. N., and Lakshminarayanan, A. V, 1971, "Three-Dimensional Reconstruction from Radiographs and Electron Micrographs: Application of Convolutions Instead of Fourier Transforms," Proc. Natl. Acad. Sci., **68**(9), pp. 2236–2240.

[77] Shepp, L. A., and Logan, B. F., 1974, "The Fourier Reconstruction of a Head Section," IEEE Trans. Nucl. Sci., **21**(3), pp. 21–43.

[78] Herman, G. T., 2009, *Fundamentals of Computerized Tomography: Image Reconstruction from Projections*, Springer Science & Business Media.

[79] Deans, S. R., 2007, *The Radon Transform and Some of Its Applications*, Courier Corporation.

[80] Kaczmarz, S., "1379 Angenäherte Auflösung von Systemen Linearer Gleichungen," Bull. Int. Acad. Pol. Sci. Lett. Class. Sci. Math. Nat, pp. 355–357.

[81] Gordon, R., Bender, R., and Herman, G. T., 1970, "Algebraic Reconstruction Techniques (ART) for Three-Dimensional Electron Microscopy and X-Ray Photography," J. Theor. Biol., **29**(3), pp. 471–481.

[82] Shepp, L. A., and Vardi, Y., 1982, "Maximum Likelihood Reconstruction for Emission Tomography," IEEE Trans. Med. Imaging, **1**(2), pp. 113–122.

[83] Herman, G. T., and Meyer, L. B., 1993, "Algebraic Reconstruction Techniques Can Be Made Computationally Efficient (Positron Emission Tomography Application)," IEEE Trans. Med. Imaging, **12**(3), pp. 600–609.

[84] Lent, A., 1977, "A Convergent Algorithm for Maximum Entropy Image Restoration, with a Medical x-Ray Application," Image Anal. Eval., pp. 249–257.

[85] Ravichandran, M., and Gouldin, F. C., 1988, "Reconstruction of Smooth Distributions from a Limited Number of Projections," Appl. Opt., **27**(19), pp. 4084–4097.

[86] Verkruysse, W., and Todd, L. A., 2005, "Novel Algorithm for Tomographic Reconstruction of Atmospheric Chemicals with Sparse Sampling," Environ. Sci. Technol., **39**(7), pp. 2247–2254.

[87] Hartl, A., Song, B. C., and Pundt, I., 2006, "2-D Reconstruction of Atmospheric

Concentration Peaks from Horizontal Long Path DOAS Tomographic Measurements: Parametrisation and Geometry within a Discrete Approach," Atmos. Chem. Phys., **6**(3), pp. 847–861.

[88] Daun, K. J., 2010, "Infrared Species Limited Data Tomography through Tikhonov Reconstruction," J. Quant. Spectrosc. Radiat. Transf., **111**(1), pp. 105–115.

[89] Terzija, N., Davidson, J. L., Garcia-Stewart, C. A., Wright, P., Ozanyan, K. B., Pegrum, S., Litt, T. J., and McCann, H., 2008, "Image Optimization for Chemical Species Tomography with an Irregular and Sparse Beam Array," Meas. Sci. Technol., **19**(9), p. 94007.

[90] Terzija, N., and McCann, H., 2011, "Wavelet-Based Image Reconstruction for Hard-Field Tomography with Severely Limited Data," IEEE Sens. J., **11**(9), pp. 1885–1893.

[91] Twynstra, M. G., Daun, K. J., and Waslander, S. L., 2014, "Line-of-Sight-Attenuation Chemical Species Tomography through the Level Set Method," J. Quant. Spectrosc. Radiat. Transf., **143**, pp. 25–34.

[92] Nadir, Z., Brown, M. S., Comer, M. L., and Bouman, C. A., 2017, "A Model-Based Iterative Reconstruction Approach to Tunable Diode Laser Absorption Tomography," IEEE Trans. Comput. Imaging, **3**(4), pp. 876–890.

[93] Cai, W., Ewing, D. J., and Ma, L., 2008, "Application of Simulated Annealing for Multispectral Tomography," Comput. Phys. Commun., **179**(4), pp. 250–255.

[94] Chen, F. P., and Goulard, R., 1976, "Retrieval of Arbitrary Concentration and Temperature Fields by Multiangular Scanning Techniques," J. Quant. Spectrosc. Radiat. Transf., **16**(10), pp. 819–827.

[95] Wang, J. Y., 1976, "Laser Absorption Methods for Simultaneous Determination of Temperature and Species Concentrations through a Cross Section of a Radiating Flow," Appl. Opt., **15**(3), pp. 768–773.

[96] Emmerman, P. J., Goulard, R., Santoro, R. J., and Semerjian, H. G., 1980, "Multiangular Absorption Diagnostics of a Turbulent Argon-Methane Jet," J. Energy, **4**(2), pp. 70–77.

[97] Santoro, R. J., Semerjian, H. G., Emmerman, P. J., and Goulard, R., 1981, "Optical Tomography for Flow Field Diagnostics," Int. J. Heat Mass Transf., **24**(7), pp. 1139–1150.

[98] Bennett, K. E., Faris, G. W., and Byer, R. L., 1984, "Experimental Optical Fan Beam Tomography," Appl. Opt., **23**(16), pp. 2678–2685.

[99] Ray, S. R., and Semerjian, H. G., 1984, "Laser Tomography for Simultaneous Concentration and Temperature Measurement in Reacting Flows," Combust. Diagnostics by Nonintrusive Methods, **92**, pp. 490–501.

[100] Hall, R. J., and Bonczyk, P. A., 1990, "Sooting Flame Thermometry Using Emission/Absorption Tomography," Appl. Opt., **29**(31), pp. 4590–4598.

[101] Ouyang, X., Varghese, P. L., and Howell, J. R., 1992, "Tomographic Absorption Spectroscopy of Combustion Gases Using Tunable Infrared Diode Lasers," *Environmental and Process Monitoring Technologies*, pp. 163–173.

[102] Kauranen, P., Hertz, H. M., and Svanberg, S., 1994, "Tomographic Imaging of Fluid Flows by the Use of Two-Tone Frequency-Modulation Spectroscopy," Opt. Lett., **19**(18), pp. 1489–1491.

[103] Beiting, E. J., 1992, "Fiber-Optic Fan-Beam Absorption Tomography," Appl. Opt., **31**(9), pp. 1328–1343.

[104] Shimizu, S., and Sakai, S., 1994, "High-Speed Tomography for Simultaneous Measurement

of the Histories of Two-Dimensional Distributions of Temperature and Density of Burnt Gases," JSME Int. J. Ser. B Fluids Therm. Eng., **37**(3), pp. 596–603.

[105] Chung, K. B., Gouldin, F. C., and Wolga, G. J., 1995, "Experimental Reconstruction of the Spatial Density Distribution of a Nonreacting Flow with a Small Number of Absorption Measurements," Appl. Opt., **34**(24), pp. 5492–5500.

[106] Torniainen, E. D., and Gouldin, F. C., 1998, "Tomographic Reconstruction of 2-D Absorption Coefficient Distributions from a Limited Set of Infrared Absorption Data," Combust. Sci. Technol., **131**(1–6), pp. 85–105.

[107] McNesby, K. L., Daniel, R. G., Morris, J. B., and Miziolek, A. W., 1995, "Tomographic Analysis of CO Absorption in a Low-Pressure Flame," Appl. Opt., **34**(18), pp. 3318–3324.

[108] Baum, R. T., McGrattan, K. B., and Nyden, M. R., 1998, "An Examination of the Applicability of Computed Tomography for the Measurement of Component Concentrations in Fire-Generated Plumes," Combust. Flame, **113**(3), pp. 358–372.

[109] Kessler, W., Allen, M., Lo, E., and Miller, M., 1995, "Tomographic Reconstruction of Air Temperature and Density Profiles Using Tunable Diode Laser Absorption Measurements on O2," *26th Plasmadynamics and Lasers Conference*, p. 1953.

[110] Greenberg, P. S., and Ku, J. C., 1997, "Soot Volume Fraction Imaging," Appl. Opt., **36**(22), pp. 5514–5522.

[111] Wondraczek, L., Khorsandi, A., Willer, U., Heide, G., Schade, W., and Frischat, G. H., 2004, "Mid-Infrared Laser-Tomographic Imaging of Carbon Monoxide in Laminar Flames by Difference Frequency Generation," Combust. Flame, **138**(1–2), pp. 30–39.

[112] Villarreal, R., and Varghese, P. L., 2005, "Frequency-Resolved Absorption Tomography with Tunable Diode Lasers," Appl. Opt., **44**(31), pp. 6786–6795.

[113] Kasyutich, V. L., and Martin, P. A., 2011, "Towards a Two-Dimensional Concentration and Temperature Laser Absorption Tomography Sensor System," Appl. Phys. B, **102**(1), pp. 149–162.

[114] Bryner, E., Busa, K., McDaniel, J., Goyne, C., and Diskin, G., 2011, "Spatially Resolved Temperature and Water Vapor Concentration Distributions in a Flat Flame Burner by Tunable Diode Laser Absorption Tomography," *49th AIAA Aerospace Sciences Meeting Including the New Horizons Forum and Aerospace Exposition*, p. 1291.

[115] Busa, K., Bryner, E., McDaniel, J., Goyne, C., Smith, C., and Diskin, G., 2011, "Demonstration of Capability of Water Flux Measurement in a Scramjet Combustor Using Tunable Diode Laser Absorption Tomography and Stereoscopic PIV," *49th AIAA Aerospace Sciences Meeting Including the New Horizons Forum and Aerospace Exposition*, p. 1294.

[116] Song, J., Hong, Y., Wang, G., and Pan, H., 2013, "Algebraic Tomographic Reconstruction of Two-Dimensional Gas Temperature Based on Tunable Diode Laser Absorption Spectroscopy," Appl. Phys. B, **112**(4), pp. 529–537.

[117] Wang, F., Wu, Q., Huang, Q., Zhang, H., Yan, J., and Cen, K., 2015, "Simultaneous Measurement of 2-Dimensional H2O Concentration and Temperature Distribution in Premixed Methane/Air Flame Using TDLAS-Based Tomography Technology," Opt. Commun., **346**, pp. 53–63.

[118] Liu, C., Cao, Z., Lin, Y., Xu, L., and McCann, H., 2018, "Online Cross-Sectional Monitoring of a Swirling Flame Using TDLAS Tomography," IEEE Trans. Instrum. Meas.,

67(6), pp. 1338–1348.

[119] Mohamad, E. J., Rahim, R. A., Ibrahim, S., Sulaiman, S., and Manaf, M. S., 2006, "Flame Imaging Using Laser-Based Transmission Tomography," Sensors Actuators A Phys., **127**(2), pp. 332–339.

[120] Liu, C., Xu, L., Chen, J., Cao, Z., Lin, Y., and Cai, W., 2015, "Development of a Fan-Beam TDLAS-Based Tomographic Sensor for Rapid Imaging of Temperature and Gas Concentration," Opt. Express, **23**(17), pp. 22494–22511.

[121] Zhang, G., Liu, J., Xu, Z., He, Y., and Kan, R., 2016, "Characterization of Temperature Non-Uniformity over a Premixed CH 4--Air Flame Based on Line-of-Sight TDLAS," Appl. Phys. B, **122**(1), p. 3.

[122] Zhang, Z., Sun, P., Pang, T., Xia, H., Cui, X., Li, Z., Han, L., Wu, B., Wang, Y., Sigrist, M. W., and others, 2016, "Reconstruction of Combustion Temperature and Gas Concentration Distributions Using Line-of-Sight Tunable Diode Laser Absorption Spectroscopy," Opt. Eng., **55**(7), p. 76107.

[123] Xia, H., Kan, R., Xu, Z., He, Y., Liu, J., Chen, B., Yang, C., Yao, L., Wei, M., and Zhang, G., 2017, "Two-Step Tomographic Reconstructions of Temperature and Species Concentration in a Flame Based on Laser Absorption Measurements with a Rotation Platform," Opt. Lasers Eng., **90**, pp. 10–18.

[124] Ma, L., Cai, W., Caswell, A. W., Kraetschmer, T., Sanders, S. T., Roy, S., and Gord, J. R., 2009, "Tomographic Imaging of Temperature and Chemical Species Based on Hyperspectral Absorption Spectroscopy," Opt. Express, **17**(10), pp. 8602–8613.

[125] An, X., Kraetschmer, T., Takami, K., Sanders, S. T., Ma, L., Cai, W., Li, X., Roy, S., and Gord, J. R., 2011, "Validation of Temperature Imaging by H 2 O Absorption Spectroscopy Using Hyperspectral Tomography in Controlled Experiments," Appl. Opt., **50**(4), pp. A29--A37.

[126] An, X., Brittelle, M. S., Lauzier, P. T., Gord, J. R., Roy, S., Chen, G.-H., and Sanders, S. T., 2015, "Demonstration of Temperature Imaging by H 2 O Absorption Spectroscopy Using Compressed Sensing Tomography," Appl. Opt., **54**(31), pp. 9190–9199.

[127] Rahim, R. A., Pang, J. F., and San Chan, K., 2005, "Optical Tomography Sensor Configuration Using Two Orthogonal and Two Rectilinear Projection Arrays," Flow Meas. Instrum., **16**(5), pp. 327–340.

[128] Wang, F., Cen, K. F., Li, N., Jeffries, J. B., Huang, Q. X., Yan, J. H., and Chi, Y., 2010, "Two-Dimensional Tomography for Gas Concentration and Temperature Distributions Based on Tunable Diode Laser Absorption Spectroscopy," Meas. Sci. Technol., **21**(4), p. 45301.

[129] Halls, B. R., Gord, J. R., Meyer, T. R., Thul, D. J., Slipchenko, M., and Roy, S., 2017, "20-KHz-Rate Three-Dimensional Tomographic Imaging of the Concentration Field in a Turbulent Jet," Proc. Combust. Inst., **36**(3), pp. 4611–4618.

[130] Carey, S. J., McCann, H., Hindle, F. P., Ozanyan, K. B., Winterbone, D. E., and Clough, E., 2000, "Chemical Species Tomography by near Infra-Red Absorption," Chem. Eng. J., **77**(1–2), pp. 111–118.

[131] McCann, H., Carey, S. J., Hindle, F. P., Ozanyan, K. B., Winterbone, D. E., and Clough, E., 2001, "Near-Infrared Absorption Tomography System for Measurement of Gaseous Hydrocarbon Distribution," *Process Imaging for Automatic Control*, pp. 141–151.

[132] Hindle, F. P., Carey, S. J., Ozanyan, K. B., Winterbone, D. E., Clough, E., and McCann, H., 2001, "Measurement of Gaseous Hydrocarbon Distribution by a Near-Infrared Absorption Tomography System," J. Electron. Imaging, **10**(3), pp. 593–601.

[133] Wright, P., Garcia-Stewart, C. A., Carey, S. J., Hindle, F. P., Pegrum, S. H., Colbourne, S. M., Turner, P. J., Hurr, W. J., Litt, T. J., Murray, S. C., and others, 2005, "Toward In-Cylinder Absorption Tomography in a Production Engine," Appl. Opt., **44**(31), pp. 6578–6592.

[134] Wright, P., Ozanyan, K. B., Murray, S. C., Litt, T. J., Pegrum, S., Colbourne, S., and McCann, H., 2005, "First Optical Attenuation Measurements across the Cylinder of a Production IC Engine," *Proceedings of the 4th World Congress on Industrial Process Tomography*, pp. 165–170.

[135] Wright, P., Terzija, N., Davidson, J. L., Garcia-Castillo, S., Garcia-Stewart, C., Pegrum, S., Colbourne, S., Turner, P., Crossley, S. D., Litt, T., and others, 2010, "High-Speed Chemical Species Tomography in a Multi-Cylinder Automotive Engine," Chem. Eng. J., **158**(1), pp. 2–10.

[136] Terzija, N., Karagiannopoulos, S., Begg, S., Wright, P., Ozanyan, K., and McCann, H., 2015, "Tomographic Imaging of the Liquid and Vapour Fuel Distributions in a Single-Cylinder Direct-Injection Gasoline Engine," Int. J. Engine Res., **16**(4), pp. 565–579.

[137] Tsekenis, S. A., Wilson, D., Lengden, M., Hyvönen, J., Leinonen, J., Shah, A., Andersson, Ö., and McCann, H., 2017, "Towards In-Cylinder Chemical Species Tomography on Large-Bore IC Engines with Pre-Chamber," Flow Meas. Instrum., **53**, pp. 116–125.

[138] Kawazoe, H., and Whitelaw, J. H., 2002, "Computer Tomography of Infra-Red Absorption and Its Application to Internal-Combustion Engines," *Laser Techniques for Fluid Mechanics*, Springer, pp. 465–482.

[139] Gillet, B., Hardalupas, Y., Kavounides, C., and Taylor, A., 2004, "Infrared Absorption for Measurement of Hydrocarbon Concentration in Fuel/Air Mixtures (MAST-B-LIQUID)," Appl. Therm. Eng., **24**(11–12), pp. 1633–1653.

[140] Lindstrom, C., Tam, C.-J., Givens, R., Davis, D., and Williams, S., 2008, "Diode Laser Absorption Tomography Using Data Compression Techniques," *Computational Imaging VI*, p. 68140W.

[141] Busa, K., Ellison, E., McGovern, B., McDaniel, J., Diskin, G., DePiro, M., Capriotti, D., and Gaffney, R., 2013, "Measurements on NASA Langley Durable Combustor Rig by TDLAT: Preliminary Results," *51st AIAA Aerospace Sciences Meeting Including the New Horizons Forum and Aerospace Exposition*, p. 696.

[142] Busa, K. M., Rice, B. E., McDaniel, J. C., Goyne, C. P., Rockwell, R. D., Fulton, J. A., Edwards, J. R., and Diskin, G. S., 2016, "Scramjet Combustion Efficiency Measurement via Tomographic Absorption Spectroscopy and Particle Image Velocimetry," AIAA J., pp. 2463–2471.

[143] Kamimoto, T., and Deguchi, Y., 2015, "2D Temperature Detection Characteristics of Engine Exhaust Gases Using CT Tunable Diode Laser Absorption Spectroscopy," Int. J. Mech. Syst. Eng., **1**, p. 109.

[144] Ma, L., Li, X., Sanders, S. T., Caswell, A. W., Roy, S., Plemmons, D. H., and Gord, J. R., 2013, "50-KHz-Rate 2D Imaging of Temperature and H 2 O Concentration at the Exhaust Plane of a J85 Engine Using Hyperspectral Tomography," Opt. Express, **21**(1), pp. 1152–1162.

[145] Wright, P., Fisher, E., and McCann, H., 2014, "Optical Design Considerations for Chemical Species Tomography in a Jet Exhaust Plume," *Propagation Through and Characterization of Distributed Volume Turbulence*, p. JTu4A--2.

[146] Wright, P., McCormick, D., Ozanyan, K., Johnson, M., Black, J., Fisher, E., Chighine, A., Polydorides, N., McCann, H., Feng, Y., and others, 2015, "Progress towards Non-Intrusive Optical Measurement of Gas Turbine Exhaust Species Distributions," *Aerospace Conference, 2015 IEEE*, pp. 1–14.

[147] Chighine, A., Tsekenis, S.-A., Fisher, E., Polydorides, N., Wilson, D., Lengden, M., Johnstone, W., and McCann, H., 2015, "TDLAS Using FPGA-Based Lock-in Detection for Multi-Channel Chemical Species Tomography," *SENSORS, 2015 IEEE*, pp. 1–4.

[148] Polydorides, N., Tsekenis, A., Fisher, E., Chighine, A., McCann, H., Dimiccoli, L., Wright, P., Lengden, M., Benoy, T., Wilson, D., and others, 2018, "Constrained Models for Optical Absorption Tomography," Appl. Opt., **57**(7), pp. B1--B9.

[149] Stritzke, F., van der Kley, S., Feiling, A., Dreizler, A., and Wagner, S., 2017, "Ammonia Concentration Distribution Measurements in the Exhaust of a Heavy Duty Diesel Engine Based on Limited Data Absorption Tomography," Opt. Express, **25**(7), pp. 8180–8191.

[150] Cuccoli, F., Facheris, L., Tanelli, S., and Giuli, D., 2000, "Infrared Tomographic System for Monitoring the Two-Dimensional Distribution of Atmospheric Pollution over Limited Areas," IEEE Trans. Geosci. Remote Sens., **38**(4), pp. 1922–1935.

[151] Belotti, C., Cuccoli, F., Facheris, L., and Vaselli, O., 2003, "An Application of Tomographic Reconstruction of Atmospheric CO/Sub 2/over a Volcanic Site Based on Open-Path IR Laser Measurements," IEEE Trans. Geosci. Remote Sens., **41**(11), pp. 2629–2637.

[152] Pundt, I., and Mettendorf, K. U., 2005, "Multibeam Long-Path Differential Optical Absorption Spectroscopy Instrument: A Device for Simultaneous Measurements along Multiple Light Paths," Appl. Opt., **44**(23), pp. 4985–4994.

[153] General, S., Pöhler, D., Sihler, H., Bobrowski, N., Frieß, U., Zielcke, J., Horbanski, M., Shepson, P. B., Stirm, B. H., Simpson, W. R., and others, 2014, "The Heidelberg Airborne Imaging DOAS Instrument (HAIDI) A Novel Imaging DOAS Device for 2-D and 3-D Imaging of Trace Gases and Aerosols," Atmos Meas Tech, **7**(10), pp. 3459–3485.

[154] Heue, K.-P., Wagner, T., Broccardo, S. P., Walter, D., Piketh, S. J., Ross, K. E., Beirle, S., and Platt, U., 2008, "Direct Observation of Two Dimensional Trace Gas Distributions with an Airborne Imaging DOAS Instrument," Atmos. Chem. Phys., **8**(22), pp. 6707–6717.

[155] Frins, E., Bobrowski, N., Platt, U., and Wagner, T., 2006, "Tomographic Multiaxis-Differential Optical Absorption Spectroscopy Observations of Sun-Illuminated Targets: A Technique Providing Well-Defined Absorption Paths in the Boundary Layer," Appl. Opt., **45**(24), pp. 6227–6240.

[156] Frins, E., Platt, U., and Wagner, T., 2008, "High Spatial Resolution Measurements of NO 2 Applying Topographic Target Light Scattering-Differential Optical Absorption Spectroscopy (ToTaL-DOAS)," Atmos. Chem. Phys., **8**(24), pp. 7595–7601.

[157] Louban, I., Píriz, G., Platt, U., and Frins, E., 2008, "Measurement of SO2 and NO2 Applying ToTaL-DOAS from a Remote Site," J. Opt. A Pure Appl. Opt., **10**(10), p. 104017.

[158] Frins, E., Bobrowski, N., Osorio, M., Casaballe, N., Belsterli, G., Wagner, T., and Platt, U., 2014, "Scanning and Mobile Multi-Axis DOAS Measurements of SO2 and NO2 Emissions from an Electric Power Plant in Montevideo, Uruguay," Atmos. Environ., **98**, pp. 347–356.

[159] Kazahaya, R., Mori, T., Kazahaya, K., and Hirabayashi, J., 2008, "Computed Tomography Reconstruction of SO2 Concentration Distribution in the Volcanic Plume of Miyakejima, Japan, by Airborne Traverse Technique Using Three UV Spectrometers," Geophys. Res. Lett., **35**(13).

[160] Wright, T. E., Burton, M., Pyle, D. M., and Caltabiano, T., 2008, "Scanning Tomography of SO2 Distribution in a Volcanic Gas Plume," Geophys. Res. Lett., **35**(17).

[161] Johansson, M., Galle, B., Rivera, C., and Zhang, Y., 2009, "Tomographic Reconstruction of Gas Plumes Using Scanning DOAS," Bull. Volcanol., **71**(10), pp. 1169–1178.

[162] Krueger, A., Stremme, W., Harig, R., and Grutter, M., 2012, "Volcanic SO2 and SiF4 Visualization Using 2-D Thermal Emission Spectroscopy-Part 2: Wind Propagation and Emission Fluxes," Atmos. Meas. Tech. Discuss., **5**, pp. 4599–4633.

[163] Krueger, A., Stremme, W., Harig, R., and Grutter, M., 2013, "Volcanic SO 2 and SiF 4 Visualization Using 2-D Thermal Emission Spectroscopy--Part 2: Wind Propagation and Emission Rates," Atmos. Meas. Tech., **6**(1), pp. 47–61.

[164] Queißer, M., Granieri, D., and Burton, M., 2016, "2-D Tomography of Volcanic CO 2 from Scanning Hard-Target Differential Absorption Lidar: The Case of Solfatara, Campi Flegrei (Italy)," Atmos. Meas. Tech.

[165] Harig, R., Matz, G., Rusch, P., Gerhard, H.-H., Gerhard, J.-H., and Schlabs, V., 2005, "New Scanning Infrared Gas Imaging System (SIGIS 2) for Emergency Response Forces," *Chemical and Biological Standoff Detection III*, p. 59950J.

[166] Rusch, P., and Harig, R., 2010, "3-D Reconstruction of Gas Clouds by Scanning Imaging IR Spectroscopy and Tomography," IEEE Sens. J., **10**(3), pp. 599–603.

[167] Harig, R., and Matz, G., 2001, "Toxic Cloud Imaging by Infrared Spectrometry: A Scanning FTIR System for Identification and Visualization," F. Anal. Chem. Technol., **5**(1–2), pp. 75–90.

[168] Dobler, J., Braun, M., Blume, N., and Zaccheo, T. S., 2013, "A New Laser Based Approach for Measuring Atmospheric Greenhouse Gases," Remote Sens., **5**(12), pp. 6284–6304.

[169] Dobler, J., Blume, N., Braun, M., Zaccheo, T. S., Pernini, T., and Botos, C., 2016, "Greenhouse Gas Laser Imaging Tomography Experiment (GreenLITE)," *EPJ Web of Conferences*, p. 26003.

[170] Seidel, A., Wagner, S., Dreizler, A., and Ebert, V., 2015, "Robust, Spatially Scanning, Open-Path TDLAS Hygrometer Using Retro-Reflective Foils for Fast Tomographic 2-D Water Vapor Concentration Field Measurements," Atmos. Meas. Tech., **8**(5), pp. 2061–2068.

[171] Levine, Z. H., Pintar, A. L., Dobler, J. T., Blume, N., Braun, M., Zaccheo, T. S., and Pernini, T. G., 2016, "The Detection of Carbon Dioxide Leaks Using Quasi-Tomographic Laser Absorption Spectroscopy Measurements in Variable Wind," Atmos. Meas. Tech., **9**, p. 1627.

[172] Garay, M. J., Davis, A. B., and Diner, D. J., 2016, "Tomographic Reconstruction of an Aerosol Plume Using Passive Multiangle Observations from the MISR Satellite Instrument," Geophys. Res. Lett., **43**(24).

[173] Zhang, F.-Y., Fujiwara, T., and Komurasaki, K., 2001, "Diode-Laser Tomography for Arcjet Plume Reconstruction," Appl. Opt., **40**(6), pp. 957–964.

[174] Salem, K., Tsotsas, E., and Mewes, D., 2005, "Tomographic Measurement of Breakthrough

in a Packed Bed Adsorber," Chem. Eng. Sci., **60**(2), pp. 517–522.

[175] An tSaoir, M. N., Fernandes, D. L. A., Sá, J., McMaster, M., Kitagawa, K., Hardacre, C., and Aiouache, F., 2011, "Visualization of Water Vapour Flow in a Packed Bed Adsorber by Near-Infrared Diffused Transmittance Tomography," Chem. Eng. Sci., **66**(24), pp. 6407–6423.

[176] An tSaoir, M. N., Fernandes, D. L. A., McMaster, M., Kitagawa, K., Hardacre, C., and Aiouache, F., 2012, "Transient Distributions of Composition and Temperature in a Gas--Solid Packed Bed Reactor by near-Infrared Tomography," Chem. Eng. J., **189**, pp. 383–392.

[177] Schleicher, E., Da Silva, M. J., Thiele, S., Li, A., Wollrab, E., and Hampel, U., 2008, "Design of an Optical Tomograph for the Investigation of Single-and Two-Phase Pipe Flows," Meas. Sci. Technol., **19**(9), p. 94006.

[178] Chen, J., Hou, D., Zhang, T., and Zhou, Z., 2005, "Near Infrared Laser Computed Tomography Test--System Design and Application," Flow Meas. Instrum., **16**(5), pp. 321–325.

[179] Uchiyama, H., Nakajima, M., and Yuta, S., 1985, "Measurement of Flame Temperature Distribution by IR Emission Computed Tomography," Appl. Opt., **24**(23), pp. 4111–4116.

[180] Hino, M., Aono, T., Nakajima, M., and Yuta, S., 1987, "Light Emission Computed Tomography System for Plasma Diagnostics," Appl. Opt., **26**(22), pp. 4742–4746.

[181] Wan, X., Yu, S., Cai, G., Gao, Y., and Yi, J., 2004, "Three-Dimensional Plasma Field Reconstruction with Multiobjective Optimization Emission Spectral Tomography," JOSA A, **21**(7), pp. 1161–1171.

[182] Fischer, W., and Burkhardt, H., 1990, "Three-Dimensional Temperature Measurement in Flames by Multispectral Tomographic Image Analysis," *Applications of Digital Image Processing XIII*, pp. 96–106.

[183] Ha, K., and Choi, S., 1994, "Interpretation of Emission Image of an Axisymmetric Diffusion Flame into 2-Dimensional Temperature Data Using a Simplified Computed Tomography," KSME J., **8**(1), p. 94.

[184] Best, P. E., Chien, P. L., Carangelo, R. M., Solomon, P. R., Danchak, M., and Ilovici, I., 1991, "Tomographic Reconstruction of FT-IR Emission and Transmission Spectra in a Sooting Laminar Diffusion Flame: Species Concentrations and Temperatures," Combust. Flame, **85**(3–4), pp. 309–318.

[185] Bates, S. C., Carangelo, R., Knight, K., and Serio, M., 1993, "Fourier Transform Infrared Hadamard Tomography of Sooting Flames," Rev. Sci. Instrum., **64**(5), pp. 1213–1221.

[186] Correia, D. P., Ferrao, P., and Caldeira-Pires, A., 2000, "Flame Three-Dimensional Tomography Sensor for in-Furnace Diagnostics," Proc. Combust. Inst., **28**(1), pp. 431–438.

[187] Correia, D. P., Ferrao, P., and Caldeira-Pires, A., 2001, "Advanced 3D Emission Tomography Flame Temperature Sensor," Combust. Sci. Technol., **163**(1), pp. 1–24.

[188] Lou, C., and Zhou, H.-C., 2005, "Deduction of the Two-Dimensional Distribution of Temperature in a Cross Section of a Boiler Furnace from Images of Flame Radiation," Combust. Flame, **143**(1–2), pp. 97–105.

[189] Huajian, W., Zhifeng, H., Dundun, W., Zixue, L., Yipeng, S., Qingyan, F., Chun, L., and Huaichun, Z., 2009, "Measurements on Flame Temperature and Its 3D Distribution in a 660 MWe Arch-Fired Coal Combustion Furnace by Visible Image Processing and Verification

by Using an Infrared Pyrometer," Meas. Sci. Technol., **20**(11), p. 114006.

[190] Ihrke, I., and Magnor, M., 2004, "Image-Based Tomographic Reconstruction of Flames," *Proceedings of the 2004 ACM SIGGRAPH/Eurographics Symposium on Computer Animation*, pp. 365–373.

[191] Bheemul, H. C., Lu, G., and Yan, Y., 2002, "Three-Dimensional Visualization and Quantitative Characterization of Gaseous Flames," Meas. Sci. Technol., **13**(10), p. 1643.

[192] Bheemul, H. C., Brisley, P. M., Lu, G., Yan, Y., and Cornwell, S., 2003, "Three-Dimensional Quantitative Characterisation of Luminous Properties of Gaseous Flames."

[193] Bheemul, H. C., Lu, G., and Yan, Y., 2005, "Digital Imaging-Based Three-Dimensional Characterization of Flame Front Structures in a Turbulent Flame," IEEE Trans. Instrum. Meas., **54**(3), pp. 1073–1078.

[194] Brisley, P. M., Lu, G., Yan, Y., and Cornwell, S., 2005, "Three-Dimensional Temperature Measurement of Combustion Flames Using a Single Monochromatic CCD Camera," IEEE Trans. Instrum. Meas., **54**(4), pp. 1417–1421.

[195] Gilabert, G., Lu, G., and Yan, Y., 2005, "Three Dimensional Visualisation and Reconstruction of the Luminosity Distribution of a Flame Using Digital Imaging Techniques," *Journal of Physics: Conference Series*, p. 167.

[196] Gilabert, G., Lu, G., and Yan, Y., 2007, "Three-Dimensional Tomographic Reconstruction of the Luminosity Distribution of a Combustion Flame," IEEE Trans. Instrum. Meas., **56**(4), pp. 1300–1306.

[197] Huang, Q., Wang, F., Yan, J., and Chi, Y., 2012, "Simultaneous Estimation of the 3-D Soot Temperature and Volume Fraction Distributions in Asymmetric Flames Using High-Speed Stereoscopic Images," Appl. Opt., **51**(15), pp. 2968–2978.

[198] Hertz, H. M., and Faris, G. W., 1988, "Emission Tomography of Flame Radicals," Opt. Lett., **13**(5), pp. 351–353.

[199] Leipertz, A., Obertacke, R., and Wintrich, F., 1996, "Industrial Combustion Control Using UV Emission Tomography," *Symposium (International) on Combustion*, pp. 2869–2875.

[200] Obertacke, R., Wintrich, H., Wintrich, F., and Leipertz, A., 1996, "A New Sensor System for Industrial Combustion Monitoring and Control Using UV Emission Spectroscopy and Tomography," Combust. Sci. Technol., **121**(1–6), pp. 133–151.

[201] Ishino, Y., and Ohiwa, N., 2005, "Three-Dimensional Computerized Tomographic Reconstruction of Instantaneous Distribution of Chemiluminescence of a Turbulent Premixed Flame," JSME Int. J. Ser. B Fluids Therm. Eng., **48**(1), pp. 34–40.

[202] Anikin, N., Suntz, R., and Bockhorn, H., 2010, "Tomographic Reconstruction of the OH*-Chemiluminescence Distribution in Premixed and Diffusion Flames," Appl. Phys. B, **100**(3), pp. 675–694.

[203] Anikin, N. B., Suntz, R., and Bockhorn, H., 2012, "Tomographic Reconstruction of 2D-OH*-Chemiluminescence Distributions in Turbulent Diffusion Flames," Appl. Phys. B, **107**(3), pp. 591–602.

[204] Worth, N. A., and Dawson, J. R., 2012, "Tomographic Reconstruction of OH* Chemiluminescence in Two Interacting Turbulent Flames," Meas. Sci. Technol., **24**(2), p. 24013.

[205] Floyd, J., and Kempf, A. M., 2011, "Computed Tomography of Chemiluminescence (CTC): High Resolution and Instantaneous 3-D Measurements of a Matrix Burner," Proc. Combust.

Inst., **33**(1), pp. 751–758.

[206] Floyd, J., Geipel, P., and Kempf, A. M., 2011, "Computed Tomography of Chemiluminescence (CTC): Instantaneous 3D Measurements and Phantom Studies of a Turbulent Opposed Jet Flame," Combust. Flame, **158**(2), pp. 376–391.

[207] Cai, W., Li, X., Li, F., and Ma, L., 2013, "Numerical and Experimental Validation of a Three-Dimensional Combustion Diagnostic Based on Tomographic Chemiluminescence," Opt. Express, **21**(6), pp. 7050–7064.

[208] Kang, M., Wu, Y., and Ma, L., 2014, "Fiber-Based Endoscopes for 3D Combustion Measurements: View Registration and Spatial Resolution," Combust. Flame, **161**(12), pp. 3063–3072.

[209] Li, X., and Ma, L., 2014, "Volumetric Imaging of Turbulent Reactive Flows at KHz Based on Computed Tomography," Opt. Express, **22**(4), pp. 4768–4778.

[210] Xu, W., Wickersham, A. J., Wu, Y., He, F., and Ma, L., 2015, "3D Flame Topography Obtained by Tomographic Chemiluminescence with Direct Comparison to Planar Mie Scattering Measurements," Appl. Opt., **54**(9), pp. 2174–2182.

[211] Ma, L., Wu, Y., Xu, W., Hammack, S. D., Lee, T., and Carter, C. D., 2016, "Comparison of 2D and 3D Flame Topography Measured by Planar Laser-Induced Fluorescence and Tomographic Chemiluminescence," Appl. Opt., **55**(20), pp. 5310–5315.

[212] Wang, J., Song, Y., Li, Z., Kempf, A., and He, A., 2015, "Multi-Directional 3D Flame Chemiluminescence Tomography Based on Lens Imaging," Opt. Lett., **40**(7), pp. 1231–1234.

[213] Jin, Y., Song, Y., Qu, X., Li, Z., Ji, Y., and He, A., 2016, "Hybrid Algorithm for Three-Dimensional Flame Chemiluminescence Tomography Based on Imaging Overexposure Compensation," Appl. Opt., **55**(22), pp. 5917–5923.

[214] Jin, Y., Song, Y., Wang, W., Ji, Y., Li, Z., and He, A., 2016, "An Improved Calculation Model of Weight Coefficient for Three-Dimensional Flame Chemiluminescence Tomography Based on Lens Imaging Theory," *Real-Time Photonic Measurements, Data Management, and Processing II*, p. 1002612.

[215] Jin, Y., Song, Y., Qu, X., Li, Z., Ji, Y., and He, A., 2017, "Three-Dimensional Dynamic Measurements of CH* and C2* Concentrations in Flame Using Simultaneous Chemiluminescence Tomography," Opt. Express, **25**(5), pp. 4640–4654.

[216] Wan, M., Xie, H., Zhuang, J., and Xu, K., 2015, "Three-Dimensional Reconstruction Method for Flame Chemiluminescence Distribution with Complicated Structure," Appl. Opt., **54**(31), pp. 9071–9081.

[217] Lv, L., Tan, J., and Hu, Y., 2016, "Numerical and Experimental Investigation of Computed Tomography of Chemiluminescence for Hydrogen-Air Premixed Laminar Flames," Int. J. Aerosp. Eng., **2016**.

[218] Mohri, K., Göers, S., Schöler, J., Rittler, A., Dreier, T., Schulz, C., and Kempf, A., 2017, "Instantaneous 3D Imaging of Highly Turbulent Flames Using Computed Tomography of Chemiluminescence," Appl. Opt., **56**(26), pp. 7385–7395.

[219] Wiseman, S. M., Brear, M. J., Gordon, R. L., and Marusic, I., 2017, "Measurements from Flame Chemiluminescence Tomography of Forced Laminar Premixed Propane Flames," Combust. Flame, **183**, pp. 1–14.

[220] Alviso, D., Mendieta, M., Molina, J., and Rolón, J. C., 2017, "Flame Imaging

Reconstruction Method Using High Resolution Spectral Data of OH*, CH* and C2* Radicals," Int. J. Therm. Sci., **121**, pp. 228–236.

[221] Herding, G., Snyder, R., Rolon, C., and Candel, S., 1998, "Investigation of Cryogenic Propellant Flames Using Computerized Tomography of Emission Images," J. Propuls. power, **14**(2), pp. 146–151.

[222] Sivathanu, Y. R., Lim, J., Reinhart, L. E., and Bowman, R. C., 2007, "Structure of Plumes from Burning Aluminized Propellant Estimated Using Fan Beam Emission Tomography," AIAA J., **45**(9), pp. 2259–2266.

[223] Ma, L., Lei, Q., Wu, Y., Xu, W., Ombrello, T. M., and Carter, C. D., 2016, "From Ignition to Stable Combustion in a Cavity Flameholder Studied via 3D Tomographic Chemiluminescence at 20 KHz," Combust. Flame, **165**, pp. 1–10.

[224] Grauer, S. J., Tsang, R. W., and Daun, K. J., 2017, "Broadband Chemical Species Tomography: Measurement Theory and a Proof-of-Concept Emission Detection Experiment," J. Quant. Spectrosc. Radiat. Transf., **198**.

[225] Grauer, S. J., Unterberger, A., Rittler, A., Daun, K. J., Kempf, A. M., and Mohri, K., 2018, "Instantaneous 3D Flame Imaging by Background-Oriented Schlieren Tomography," Combust. Flame, **196**, pp. 284–299.

[226] Zhao, J. M., and Liu, L. H., 2018, "Radiative Transfer Equation and Solutions," Handb. Therm. Sci. Eng., pp. 933–978.

[227] Howell, J. R., Menguc, M. P., and Siegel, R., 2015, *Thermal Radiation Heat Transfer*, CRC press.

[228] Gordon, I. E., Rothman, L. S., Hill, C., Kochanov, R. V, Tan, Y., Bernath, P. F., Birk, M., Boudon, V., Campargue, A., Chance, K. V, and others, 2017, "The HITRAN2016 Molecular Spectroscopic Database," J. Quant. Spectrosc. Radiat. Transf., **203**, pp. 3–69.

[229] Farooq, A., Jeffries, J. B., and Hanson, R. K., 2008, "In Situ Combustion Measurements of H2O and Temperature near 2.5 $μ$m Using Tunable Diode Laser Absorption," Meas. Sci. Technol., **19**(7), p. 75604.

[230] Wood, M. P., and Ozanyan, K. B., 2015, "Simultaneous Temperature, Concentration, and Pressure Imaging of Water Vapor in a Turbine Engine," IEEE Sens. J., **15**(1), pp. 545–551.

[231] Chang, H., and Charalampopoulos, T. T., 1990, "Determination of the Wavelength Dependence of Refractive Indices of Flame Soot," Proc. R. Soc. Lond. A, **430**(1880), pp. 577–591.

[232] Bond, T. C., and Bergstrom, R. W., 2006, "Light Absorption by Carbonaceous Particles: An Investigative Review," Aerosol Sci. Technol., **40**(1), pp. 27–67.

[233] Nori, V., and Seitzman, J., 2008, "Evaluation of Chemiluminescence as a Combustion Diagnostic under Varying Operating Conditions," *46th AIAA Aerospace Sciences Meeting and Exhibit*, p. 953.

[234] Smith, G. P., Luque, J., Park, C., Jeffries, J. B., and Crosley, D. R., 2002, "Low Pressure Flame Determinations of Rate Constants for OH (A) and CH (A) Chemiluminescence," Combust. Flame, **131**(1–2), pp. 59–69.

[235] Cai, W., and Kaminski, C. F., 2017, "Tomographic Absorption Spectroscopy for the Study of Gas Dynamics and Reactive Flows," Prog. Energy Combust. Sci.

[236] Elfving, T., Hansen, P. C., and Nikazad, T., 2014, "Semi-Convergence Properties of Kaczmarz's Method," Inverse Probl., **30**(5), p. 55007.

[237] Gilbert, P., 1972, "Iterative Methods for the Three-Dimensional Reconstruction of an Object from Projections," J. Theor. Biol., **36**(1), pp. 105–117.

[238] Hadamard, J., 1902, "Sur Les Problèmes Aux Dérivées Partielles et Leur Signification Physique," Princet. Univ. Bull., pp. 49–52.

[239] Hansen, P. C., 2010, *Discrete Inverse Problems: Insight and Algorithms*, Siam.

[240] Kaipio, J., and Somersalo, E., 2006, *Statistical and Computational Inverse Problems*, Springer Science & Business Media.

[241] Lins, B., Zinn, P., Engelbrecht, R., and Schmauss, B., 2010, "Simulation-Based Comparison of Noise Effects in Wavelength Modulation Spectroscopy and Direct Absorption TDLAS," Appl. Phys. B, **100**(2), pp. 367–376.

[242] Barry, J. R., Lee, E. A., and Messerschmitt, D. G., 2012, *Digital Communication*, Springer Science & Business Media.

[243] George, W. K., 1989, "The Self-Preservation of Turbulent Flows and Its Relation to Initial Conditions and Coherent Structures," Adv. Turbul., **3973**.

[244] Roberts, P. J. W., and Abessi, O., 2014, "Optimization of Desalination Diffusers Using Three-Dimensional Laser-Induced Fluorescence," Agreem. Number R11 AC81, **535**.

[245] Ball, C. G., Fellouah, H., and Pollard, A., 2012, "The Flow Field in Turbulent Round Free Jets," Prog. Aerosp. Sci., **50**, pp. 1–26.

[246] Sami, S., Carmody, T., and Rouse, H., 1967, "Jet Diffusion in the Region of Flow Establishment," J. Fluid Mech., **27**(2), pp. 231–252.

[247] Townsend, A. A., 1980, *The Structure of Turbulent Shear Flow*, Cambridge university press.

[248] Richards, C. D., and Pitts, W. M., 1993, "Global Density Effects on the Self-Preservation Behaviour of Turbulent Free Jets," J. Fluid Mech., **254**, pp. 417–435.

[249] Dowling, D. R., and Dimotakis, P. E., 1990, "Similarity of the Concentration Field of Gas-Phase Turbulent Jets," J. Fluid Mech., **218**, pp. 109–141.

[250] Nathan, G. J., Mi, J., Alwahabi, Z. T., Newbold, G. J. R., and Nobes, D. S., 2006, "Impacts of a Jet's Exit Flow Pattern on Mixing and Combustion Performance," Prog. Energy Combust. Sci., **32**(5–6), pp. 496–538.

[251] Uddin, M., and Pollard, A., 2007, "Self-Similarity of Coflowing Jets: The Virtual Origin," Phys. fluids, **19**(6), p. 68103.

[252] Lubbers, C. L., Brethouwer, G., and Boersma, B. J., 2001, "Simulation of the Mixing of a Passive Scalar in a Round Turbulent Jet," Fluid Dyn. Res., **28**(3), p. 189.

[253] Dahm, W. J. A., and Dimotakis, P. E., 1990, "Mixing at Large Schmidt Number in the Self-Similar Far Field of Turbulent Jets," J. Fluid Mech., **217**, pp. 299–330.

[254] Mi, J., Nobes, D. S., and Nathan, G. J., 2001, "Influence of Jet Exit Conditions on the Passive Scalar Field of an Axisymmetric Free Jet," J. Fluid Mech., **432**, pp. 91–125.

[255] Carazzo, G., Kaminski, E., and Tait, S., 2006, "The Route to Self-Similarity in Turbulent Jets and Plumes," J. Fluid Mech., **547**, pp. 137–148.

[256] Shin, D., Aspden, A. J., and Richardson, E. S., 2017, "Self-Similar Properties of Decelerating Turbulent Jets," J. Fluid Mech., **833**.

[257] Prandtl, L., 1925, "Bericht Uber Untersuchungen Zur Ausgebildeten Turbulenz," Zs. angew. Math. Mech., **5**, pp. 136–139.

[258] Tollmien, W., 1926, “Berechnung Turbulenter Ausbreitungsvorgänge,” ZAMM-Journal Appl. Math. Mech. für Angew. Math. und Mech., **6**(6), pp. 468–478.

[259] von Görtler, H., 1942, “Berechnung von Aufgaben Der Freien Turbulenz Auf Grund Eines Neuen Näherungsansatzes.,” ZAMM-Journal Appl. Math. Mech. für Angew. Math. und Mech., **22**(5), pp. 244–254.

[260] Howarth, L., 1938, “Concerning the Velocity and Temperature Distributions in Plane and Axially Symmetrical Jets,” *Mathematical Proceedings of the Cambridge Philosophical Society*, pp. 185–203.

[261] Reichardt, H., 1943, “On a New Theory of Free Turbulence,” Aeronaut. J., **47**(390), pp. 167–176.

[262] Alexander, L. G., Baron, T., and Comings, E. W., 1953, *Transport of Momentum, Mass, and Heat in Turbulent Jets*.

[263] Chatwin, P. C., and Sullivan, P. J., 1990, “A Simple and Unifying Physical Interpretation of Scalar Fluctuation Measurements from Many Turbulent Shear Flows,” J. Fluid Mech., **212**, pp. 533–556.

[264] Antoine, Y., Lemoine, F., and Lebouché, M., 2001, “Turbulent Transport of a Passive Scalar in a Round Jet Discharging into a Co-Flowing Stream,” Eur. J. Mech., **20**(2), pp. 275–301.

[265] Birch, A. D., Brown, D. R., Dodson, M. G., and Thomas, J. R., 1978, “The Turbulent Concentration Field of a Methane Jet,” J. Fluid Mech., **88**(3), pp. 431–449.

[266] Panchapakesan, N. R., and Lumley, J. L., 1993, “Turbulence Measurements in Axisymmetric Jets of Air and Helium. Part 2. Helium Jet,” J. Fluid Mech., **246**, pp. 225–247.

[267] Batchelor, G. K., 1953, *The Theory of Homogeneous Turbulence*, Cambridge university press.

[268] Jimenez, J., 1998, “Turbulent Velocity Fluctuations Need Not Be Gaussian,” J. Fluid Mech., **376**, pp. 139–147.

[269] Townnsend, A. A., 1948, “Local Isotropy in the Turbulent Wake of a Cylinder,” Aust. J. Chem., **1**(2), pp. 161–174.

[270] Brun, C., and Pumir, A., 2001, “Statistics of Fourier Modes in a Turbulent Flow,” Phys. Rev. E, **63**(5), p. 56313.

[271] Mouri, H., Takaoka, M., Hori, A., and Kawashima, Y., 2002, “Probability Density Function of Turbulent Velocity Fluctuations,” Phys. Rev. E, **65**(5), p. 56304.

[272] Lockwood, F. C., and Moneib, H. A., 1980, “Fluctuating Temperature Measurements in a Heated Round Free Jet,” Combust. Sci. Technol., **22**(1–2), pp. 63–81.

[273] Sreenivasan, K. R., and Antonia, R. A., 1997, “The Phenomenology of Small-Scale Turbulence,” Annu. Rev. Fluid Mech., **29**(1), pp. 435–472.

[274] Holzer, M., and Siggia, E. D., 1994, “Turbulent Mixing of a Passive Scalar,” Phys. Fluids, **6**(5), pp. 1820–1837.

[275] Warhaft, Z., 2000, “Passive Scalars in Turbulent Flows,” Annu. Rev. Fluid Mech., **32**(1), pp. 203–240.

[276] Pumir, A., Shraiman, B. I., and Siggia, E. D., 1991, “Exponential Tails and Random Advection,” Phys. Rev. Lett., **66**(23), p. 2984.

[277] Tong, C., and Warhaft, Z., 1995, “Passive Scalar Dispersion and Mixing in a Turbulent Jet,” J. Fluid Mech., **292**, pp. 1–38.

[278] Vecherin, S. N., Ostashev, V. E., Ziemann, A., Wilson, D. K., Arnold, K., and Barth, M., 2007, "Tomographic Reconstruction of Atmospheric Turbulence with the Use of Time-Dependent Stochastic Inversion," J. Acoust. Soc. Am., **122**(3), pp. 1416–1425.

[279] Arridge, S. R., Kaipio, J. P., Kolehmainen, V., Schweiger, M., Somersalo, E., Tarvainen, T., and Vauhkonen, M., 2006, "Approximation Errors and Model Reduction with an Application in Optical Diffusion Tomography," Inverse Probl., **22**(1), p. 175.

[280] Upton, T. D., Verhoeven, D. D., and Hudgins, D. E., 2011, "High-Resolution Computed Tomography of a Turbulent Reacting Flow," Exp. Fluids, **50**(1), pp. 125–134.

[281] McGrattan, K., Hostikka, S., Floyd, J., Baum, H., Rehm, R. G., Mell, W., and McDermott, R., 2010, "Fire Dynamics Simulator (Version 5), Technical Reference Guide," NIST Spec. Publ., **1018**(5).

[282] Labahn, J. W., and Devaud, C. B., 2016, "Large Eddy Simulations (LES) Including Conditional Source-Term Estimation (CSE) Applied to Two Delft-Jet-in-Hot-Coflow (DJHC) Flames," Combust. Flame, **164**, pp. 68–84.

[283] Oldenhof, E., Tummers, M. J., Van Veen, E. H., and Roekaerts, D., 2011, "Role of Entrainment in the Stabilisation of Jet-in-Hot-Coflow Flames," Combust. Flame, **158**(8), pp. 1553–1563.

[284] Wang, Z., Bovik, A. C., Sheikh, H. R., and Simoncelli, E. P., 2004, "Image Quality Assessment: From Error Visibility to Structural Similarity," IEEE Trans. image Process., **13**(4), pp. 600–612.

[285] Wang, Z., Simoncelli, E. P., and Bovik, A. C., 2003, "Multiscale Structural Similarity for Image Quality Assessment," *The Thrity-Seventh Asilomar Conference on Signals, Systems & Computers, 2003*, pp. 1398–1402.

[286] Tsekenis, S.-A., and Polydorides, N., 2017, "Optical Access Schemes for High Speed and Spatial Resolution Optical Absorption Tomography in Energy Engineering," IEEE Sens. J., **17**(24), pp. 8072–8080.

[287] Rattey, P., and Lindgren, A., 1981, "Sampling the 2-D Radon Transform," IEEE Trans. Acoust., **29**(5), pp. 994–1002.

[288] Daun, K. J., 2009, "Infrared Species Limited Data Tomography through Tikhonov Reconstruction," *ASME 2009 Heat Transfer Summer Conference Collocated with the InterPACK09 and 3rd Energy Sustainability Conferences*, pp. 187–196.

[289] Twynstra, M. G., and Daun, K. J., 2012, "Laser-Absorption Tomography Beam Arrangement Optimization Using Resolution Matrices," Appl. Opt., **51**(29), pp. 7059–7068.

[290] Song, J., Hong, Y., Pan, H., and Wang, G., 2013, "Beam Arrangement on Two-Dimensional Temperature Reconstruction Based on Laser Absorption Spectroscopy," *International Symposium on Photoelectronic Detection and Imaging 2013: Infrared Imaging and Applications*, p. 89070K.

[291] Yu, T., Tian, B., and Cai, W., 2017, "Development of a Beam Optimization Method for Absorption-Based Tomography," Opt. Express, **25**(6), pp. 5982–5999.

[292] Atkinson, A., Donev, A., and Tobias, R., 2007, *Optimum Experimental Designs, with SAS*, Oxford University Press.

[293] Verhoeven, D., 1993, "Limited-Data Computed Tomography Algorithms for the Physical Sciences," Appl. Opt., **32**(20), pp. 3736–3754.

[294] Grauer, S. J., Hadwin, P. J., and Daun, K. J., 2016, "Bayesian Approach to the Design of

Chemical Species Tomography Experiments," Appl. Opt., **55**(21).

[295] Kaipio, J., and Somersalo, E., 2007, "Statistical Inverse Problems: Discretization, Model Reduction and Inverse Crimes," J. Comput. Appl. Math., **198**(2), pp. 493–504.

[296] Sambridge, M., Gallagher, K., Jackson, A., and Rickwood, P., 2006, "Trans-Dimensional Inverse Problems, Model Comparison and the Evidence," Geophys. J. Int., **167**(2), pp. 528–542.

[297] Penny, W. D., 2012, "Comparing Dynamic Causal Models Using AIC, BIC and Free Energy," Neuroimage, **59**(1), pp. 319–330.

[298] Kass, R. E., and Raftery, A. E., 1995, "Bayes Factors," J. Am. Stat. Assoc., **90**(430), pp. 773–795.

[299] Daun, K. J., Grauer, S. J., and Hadwin, P. J., 2016, "Chemical Species Tomography of Turbulent Flows: Discrete Ill-Posed and Rank Deficient Problems and the Use of Prior Information," J. Quant. Spectrosc. Radiat. Transf., **172**.

[300] Polydorides, N., Tsekenis, S.-A., McCann, H., Prat, V.-D., and Wright, P., 2016, "An Efficient Approach for Limited-Data Chemical Species Tomography and Its Error Bounds," Proc. R. Soc. A, **472**(2187), p. 20150875.

[301] Schweiger, M., Arridge, S. R., and Delpy, D. T., 1993, "Application of the Finite-Element Method for the Forward and Inverse Models in Optical Tomography," J. Math. Imaging Vis., **3**(3), pp. 263–283.

[302] Vauhkonen, M., Vadasz, D., Karjalainen, P. A., Somersalo, E., and Kaipio, J. P., 1998, "Tikhonov Regularization and Prior Information in Electrical Impedance Tomography," IEEE Trans. Med. Imaging, **17**(2), pp. 285–293.

[303] Tape, C., Liu, Q., Maggi, A., and Tromp, J., 2010, "Seismic Tomography of the Southern California Crust Based on Spectral-Element and Adjoint Methods," Geophys. J. Int., **180**(1), pp. 433–462.

[304] Zöchbauer, M., Smith, H., and Lauer, T., 2015, *Advanced SCR Flow Modeling with a Validated Large Eddy Simulation*.

[305] Persson, P.-O., and Strang, G., 2004, "A Simple Mesh Generator in MATLAB," SIAM Rev., **46**(2), pp. 329–345.

[306] Environment and Climate Change Canada, 2017, "Canadian Environmental Sustainability Indicators: Greenhouse Gas Emissions."

[307] Environment and Climate Change Canada, 2018, "National Inventory Report 1990-2016: Greenhouse Gas Sources and Sinks in Canada."

[308] Krewski, D., Snyder, R., Beatty, P., Granville, G., Meek, B., and Sonawane, B., 2000, "Assessing the Health Risks of Benzene: A Report on the Benzene State-of-the-Science Workshop," J. Toxicol. Environ. Heal. Part A, **61**(5–6), pp. 307–338.

[309] Baltrėnas, P., Baltrėnaitė, E., Serevičienė, V., and Pereira, P., 2011, "Atmospheric BTEX Concentrations in the Vicinity of the Crude Oil Refinery of the Baltic Region," Environ. Monit. Assess., **182**(1–4), pp. 115–127.

[310] Yang, C.-Y., Wang, J.-D., Chan, C.-C., Chen, P.-C., Huang, J.-S., and Cheng, M.-F., 1997, "Respiratory and Irritant Health Effects of a Population Living in a Petrochemical-Polluted Area in Taiwan," Environ. Res., **74**(2), pp. 145–149.

[311] Government of Canada, 1999, "Canadian Environmental Protection Act."

[312] US Environmental Protection Agency, 2007, "Method 21: Determination of Volatile

Organic Compound Leaks."

[313] US Environmental Protection Agency, 2007, "Method 25A: Determination of Total Gaseous Organic Concentration Using a Flame."

[314] Jones, E., 1987, "The Pellistor Catalytic Gas Detector," Tech. Mech. gas Sens., pp. 17–31.

[315] Bakker, E., and Telting-Diaz, M., 2002, "Electrochemical Sensors," Anal. Chem., **74**(12), pp. 2781–2800.

[316] Fiddler, M. N., Begashaw, I., Mickens, M. A., Collingwood, M. S., Assefa, Z., and Bililign, S., 2009, "Laser Spectroscopy for Atmospheric and Environmental Sensing," Sensors, **9**(12), pp. 10447–10512.

[317] Watson, J. G., Chow, J. C., and Fujita, E. M., 2001, "Review of Volatile Organic Compound Source Apportionment by Chemical Mass Balance," Atmos. Environ., **35**(9), pp. 1567–1584.

[318] Cuclis, A., 2006, "Why Emission Factors Don't Work at Refineries and What to Do about It," *Workshop in Research Triangle Park Hosted by EPA In*, p. 9.

[319] Johnson, T. J., Sams, R. L., and Sharpe, S. W., 2004, "The PNNL Quantitative Infrared Database for Gas-Phase Sensing: A Spectral Library for Environmental, Hazmat, and Public Safety Standoff Detection," *Chemical and Biological Point Sensors for Homeland Defense*, pp. 159–168.

[320] Banwell, C. N., McCash, E. M., and others, 1994, *Fundamentals of Molecular Spectroscopy*, McGraw-Hill New York.

[321] Hanson, R. K., Spearrin, R. M., and Goldenstein, C. S., 2016, *Spectroscopy and Optical Diagnostics for Gases*, Springer.

[322] Struve, W. S., 1989, *Fundamentals of Molecular Spectroscopy*, Wiley New York.

[323] Šimečková, M., Jacquemart, D., Rothman, L. S., Gamache, R. R., and Goldman, A., 2006, "Einstein A-Coefficients and Statistical Weights for Molecular Absorption Transitions in the HITRAN Database," J. Quant. Spectrosc. Radiat. Transf., **98**(1), pp. 130–155.

[324] Demtröder, W., 2014, "Widths and Profiles of Spectral Lines," *Laser Spectroscopy 1*, Springer, pp. 75–111.

[325] Whiting, E. E., 1968, "An Empirical Approximation to the Voigt Profile," J. Quant. Spectrosc. Radiat. Transf., **8**(6), pp. 1379–1384.

[326] Hashmonay, R. A., Natschke, D. F., Wagoner, K., Harris, D. B., Thompson, E. L., and Yost, M. G., 2001, "Field Evaluation of a Method for Estimating Gaseous Fluxes from Area Sources Using Open-Path Fourier Transform Infrared," Environ. Sci. Technol., **35**(11), pp. 2309–2313.

[327] Hashmonay, R. A., and Yost, M. G., 1999, "Localizing Gaseous Fugitive Emission Sources by Combining Real-Time Optical Remote Sensing and Wind Data," J. Air Waste Manage. Assoc., **49**(11), pp. 1374–1379.

[328] Veynante, D., and Vervisch, L., 2002, "Turbulent Combustion Modeling," Prog. energy Combust. Sci., **28**(3), pp. 193–266.

[329] Cabra, R., Myhrvold, T., Chen, J. Y., Dibble, R. W., Karpetis, A. N., and Barlow, R. S., 2002, "Simultaneous Laser Raman-Rayleigh-LIF Measurements and Numerical Modeling Results of a Lifted Turbulent H2/N2 Jet Flame in a Vitiated Coflow," Proc. Combust. Inst., **29**(2), pp. 1881–1888.

[330] Settles, G. S., 2002, "Schlieren and Shadowgraph Techniques: Visualizing Phenomena in

Transparent Media."

[331] Atcheson, B., Ihrke, I., Heidrich, W., Tevs, A., Bradley, D., Magnor, M., and Seidel, H.-P., 2008, "Time-Resolved 3d Capture of Non-Stationary Gas Flows," *ACM Transactions on Graphics (TOG)*, p. 132.

[332] Goldhahn, E., and Seume, J., 2007, "The Background Oriented Schlieren Technique: Sensitivity, Accuracy, Resolution and Application to a Three-Dimensional Density Field," Exp. Fluids, **43**(2–3), pp. 241–249.

[333] Goldhahn, E., Alhaj, O., Herbst, F., and Seume, J., 2009, "Quantitative Measurements of Three-Dimensional Density Fields Using the Background Oriented Schlieren Technique," *Imaging Measurement Methods for Flow Analysis*, Springer, pp. 135–144.

[334] Zeb, M. F., Ota, M., and Maeno, K., 2011, "Quantitative Measurement of Heat Flow in Natural Heat Convection Using Color-Stripe Background Oriented Schlieren (CSBOS) Method," J. Japanese Soc. Exp. Mech., **11**(Special_Issue), pp. s141--s146.

[335] Sourgen, F., Leopold, F., and Klatt, D., 2012, "Reconstruction of the Density Field Using the Colored Background Oriented Schlieren Technique (CBOS)," Opt. Lasers Eng., **50**(1), pp. 29–38.

[336] Hartmann, U., Adamczuk, R., and Seume, J., 2015, "Tomographic Background Oriented Schlieren Applications for Turbomachinery," *53rd AIAA Aerospace Sciences Meeting*, p. 1690.

[337] Tan, D. J., Edgington-Mitchell, D., and Honnery, D., 2015, "Measurement of Density in Axisymmetric Jets Using a Novel Background-Oriented Schlieren (BOS) Technique," Exp. Fluids, **56**(11), p. 204.

[338] Nicolas, F., Todoroff, V., Plyer, A., Le Besnerais, G., Donjat, D., Micheli, F., Champagnat, F., Cornic, P., and Le Sant, Y., 2016, "A Direct Approach for Instantaneous 3D Density Field Reconstruction from Background-Oriented Schlieren (BOS) Measurements," Exp. Fluids, **57**(1), p. 13.

[339] Nicolas, F., Donjat, D., Léon, O., Le Besnerais, G., Champagnat, F., and Micheli, F., 2017, "3D Reconstruction of a Compressible Flow by Synchronized Multi-Camera BOS," Exp. Fluids, **58**(5), p. 46.

[340] Donjat, D., Nicolas, F., Plyer, A., Micheli, F., Cornic, P., Le Besnerais, G., Champagnat, F., Le Sant, Y., and Deluc, J.-M., 2015, "Study of a Co-Flowing Hot Jet: An Application of Direct 3DBOS Technique in Research Wind Tunnel," *10th Pacific Symposium on Flow Visualization and Image Processing, Naples, Italy Google Scholar*.

[341] Lang, H. M., Oberleithner, K., Paschereit, C. O., and Sieber, M., 2017, "Measurement of the Fluctuating Temperature Field in a Heated Swirling Jet with BOS Tomography," Exp. Fluids, **58**(7), p. 88.

[342] Westerweel, J., 1997, "Fundamentals of Digital Particle Image Velocimetry," Meas. Sci. Technol., **8**(12), p. 1379.

[343] Venkatakrishnan, L., and Meier, G. E. A., 2004, "Density Measurements Using the Background Oriented Schlieren Technique," Exp. Fluids, **37**(2), pp. 237–247.

[344] Horn, B. K. P., and Schunck, B. G., 1981, "Determining Optical Flow," Artif. Intell., **17**(1–3), pp. 185–203.

[345] Atcheson, B., Heidrich, W., and Ihrke, I., 2009, "An Evaluation of Optical Flow Algorithms for Background Oriented Schlieren Imaging," Exp. Fluids, **46**(3), pp. 467–476.

[346] Brox, T., Bruhn, A., Papenberg, N., and Weickert, J., 2004, "High Accuracy Optical Flow Estimation Based on a Theory for Warping," *European Conference on Computer Vision*, pp. 25–36.

[347] Sveen, J. K., 2004, "An Introduction to MatPIV v. 1.6.1," Prepr. Ser. Mech. Appl. Math. http//urn. nb. no/URN NBN no-23418.

[348] Stam, J., and Languénou, E., 1996, "Ray Tracing in Non-Constant Media," *Rendering Techniques '96*, Springer, pp. 225–234.

[349] Ihrke, I., Ziegler, G., Tevs, A., Theobalt, C., Magnor, M., and Seidel, H.-P., 2007, "Eikonal Rendering: Efficient Light Transport in Refractive Objects," ACM Trans. Graph., **26**(3), p. 59.

[350] Sakamoto, T., 1987, "Ray Trace Algorithms for GRIN Media," Appl. Opt., **26**(15), pp. 2943–2946.

[351] Rudin, L. I., Osher, S., and Fatemi, E., 1992, "Nonlinear Total Variation Based Noise Removal Algorithms," Phys. D nonlinear Phenom., **60**(1–4), pp. 259–268.

[352] Strong, D., and Chan, T., 2003, "Edge-Preserving and Scale-Dependent Properties of Total Variation Regularization," Inverse Probl., **19**(6), p. S165.

[353] Sethian, J. A., 1987, "Numerical Methods for Propagating Fronts," *Variational Methods for Free Surface Interfaces*, Springer, pp. 155–164.

[354] González, G., Kolehmainen, V., and Seppänen, A., 2017, "Isotropic and Anisotropic Total Variation Regularization in Electrical Impedance Tomography," Comput. Math. with Appl., **74**(3), pp. 564–576.

[355] Trampert, J., and Leveque, J.-J., 1990, "Simultaneous Iterative Reconstruction Technique: Physical Interpretation Based on the Generalized Least Squares Solution," J. Geophys. Res. Solid Earth, **95**(B8), pp. 12553–12559.

[356] Vest, C. M., 1979, "Holographic Interferometry," New York, John Wiley Sons, Inc., 1979. 476 p.

[357] Qin, X., Xiao, X., Puri, I. K., and Aggarwal, S. K., 2002, "Effect of Varying Composition on Temperature Reconstructions Obtained from Refractive Index Measurements in Flames," Combust. Flame, **128**(1–2), pp. 121–132.

[358] Meier, W., Keck, O., Noll, B., Kunz, O., and Stricker, W., 2000, "Investigations in the TECFLAM Swirling Diffusion Flame: Laser Raman Measurements and CFD Calculations," Appl. Phys. B, **71**(5), pp. 725–731.

[359] Freitag, M., Klein, M., Gregor, M., Nauert, A., Geyer, D., Schneider, C., Dreizler, A., and Janicka, J., 2005, "Mixing Analysis of a Swirling Recirculating Flow Using DNS and Experimental Data," *TSFP DIGITAL LIBRARY ONLINE*.

[360] Röder, M., Dreier, T., and Schulz, C., 2013, "Simultaneous Measurement of Localized Heat-Release with OH/CH2O--LIF Imaging and Spatially Integrated OH* Chemiluminescence in Turbulent Swirl Flames," Proc. Combust. Inst., **34**(2), pp. 3549–3556.

[361] Pettit, M. W. A., Coriton, B., Gomez, A., and Kempf, A. M., 2011, "Large-Eddy Simulation and Experiments on Non-Premixed Highly Turbulent Opposed Jet Flows," Proc. Combust. Inst., **33**(1), pp. 1391–1399.

[362] Schneider, C., Dreizler, A., and Janicka, J., 2005, "Fluid Dynamical Analysis of Atmospheric Reacting and Isothermal Swirling Flows," Flow, Turbul. Combust., **74**(1), pp.

103–127.

[363] Gregor, M. A., Seffrin, F., Fuest, F., Geyer, D., and Dreizler, A., 2009, "Multi-Scalar Measurements in a Premixed Swirl Burner Using 1D Raman/Rayleigh Scattering," Proc. Combust. Inst., **32**(2), pp. 1739–1746.

[364] Butz, D., Gao, Y., Kempf, A. M., and Chakraborty, N., 2015, "Large Eddy Simulations of a Turbulent Premixed Swirl Flame Using an Algebraic Scalar Dissipation Rate Closure," Combust. Flame, **162**(9), pp. 3180–3196.

[365] Moin, P., and Mahesh, K., 1998, "Direct Numerical Simulation: A Tool in Turbulence Research," Annu. Rev. Fluid Mech., **30**(1), pp. 539–578.

[366] Ren, T., and Modest, M. F., 2015, "Temperature Profile Inversion from Carbon-Dioxide Spectral Intensities through Tikhonov Regularization," J. Thermophys. Heat Transf., **30**(1), pp. 211–218.

[367] Schulz, C., and Sick, V., 2005, "Tracer-LIF Diagnostics: Quantitative Measurement of Fuel Concentration, Temperature and Fuel/Air Ratio in Practical Combustion Systems," Prog. Energy Combust. Sci., **31**(1), pp. 75–121.

[368] John, F., 1981, "The Initial Value Problem for Hyperbolic Homogeneous Equations with Constant Coefficients," *Plane Waves and Spherical Means*, Springer, pp. 15–41.

[369] York, T., McCann, H., and Ozanyan, K. B., 2011, "Agile Sensing Systems for Tomography," IEEE Sens. J., **11**(12), pp. 3086–3105.

[370] Varghese, P. L., and Hanson, R. K., 1984, "Collisional Narrowing Effects on Spectral Line Shapes Measured at High Resolution," Appl. Opt., **23**(14), pp. 2376–2385.

[371] Hussein, H. J., Capp, S. P., and George, W. K., 1994, "Velocity Measurements in a High-Reynolds-Number, Momentum-Conserving, Axisymmetric, Turbulent Jet," J. Fluid Mech., **258**, pp. 31–75.

[372] Tavoularis, S., and Corrsin, S., 1981, "Experiments in Nearly Homogenous Turbulent Shear Flow with a Uniform Mean Temperature Gradient. Part 1," J. Fluid Mech., **104**, pp. 311–347.

[373] Sipkens, T. A., Hadwin, P. J., Grauer, S. J., and Daun, K. J., 2018, "Predicting the Heat of Vaporization of Iron at High Temperatures Using Time-Resolved Laser-Induced Incandescence and Bayesian Model Selection," J. Appl. Phys., **123**(9).

[374] Townes, C. H., and Schawlow, A. L., 2013, *Microwave Spectroscopy*, Courier Corporation.